Observations of Be X-ray Binaries: Spin Period and Spectral Evolution

Beobachtungen von Be-Röntgendoppelsternen: Rotationsperioden und spektrale Entwicklung

Der Naturwissenschaftlichen Fakultät
der Friedrich-Alexander-Universität
Erlangen-Nürnberg

zur

Erlangung des Doktorgrades Dr. rer. nat.

vorgelegt von

Matthias Bissinger
aus Wiesbaden

FRIEDRICH-ALEXANDER
UNIVERSITÄT
ERLANGEN-NÜRNBERG
NATURWISSENSCHAFTLICHE
FAKULTÄT

ERLANGEN CENTRE
FOR ASTROPARTICLE
PHYSICS

Als Dissertation genehmigt
von der Naturwissenschaftlichen Fakultät
der Friedrich-Alexander-Universität Erlangen-Nürnberg

Tag der mündlichen Prüfung: 19. Oktober 2016

Vorsitzender des Promotionsorgans: Prof. Dr. Georg Kreimer

Gutacher: Prof. Dr. Jörn Wilms
Gutacher: Dr. Vanessa McBride, University of Cape Town

Meine in der folgenden Arbeit zitierten Veröffentlichungen sind unter meinem Geburtsnamen Kühnel vermerkt.

Within the following thesis my cited publications are noted using my former family name Kühnel.

Zusammenfassung

Ein Neutronenstern entsteht durch die Supernova-Explosion eines massiven Sterns und entspricht dem kollabierten Überrest des Kerns. Diese kompakten Objekte konzentrieren mehr Masse als die Sonne innerhalb ihres Durchmessers von ∼23 km, wodurch Dichten vergleichbar mit nuklearer Materie entstehen. Auf Grund der Erhaltung des Drehimpulses und der magnetischen Flussdichte rotieren Neutronensterne mit Perioden zwischen einem Bruchteil einer Sekunde bis zu wenigen Stunden und besitzen Magnetfelder mit Stärken um 10^{12} G, welche neben anderen zu den stärksten Magnetfeldern im Universum zählen.

Sobald sich ein Neutronenstern in einem Orbit um einen Hauptreihenstern befindet, kann Materietransfer zwischen dessen stellarer Hülle und dem kompakten Objekt stattfinden. Innerhalb einer bestimmten Distanz zum Neutronenstern ist diese Materie gezwungen, dessen magnetischen Feldlinien zu folgen. Dies führt zu einer Kanalisierung des akkretierten Materials auf die magnetischen Pole des Neutronensterns, an denen sich sogenannte Akkretionssäulen auf der Oberfläche bilden. Innerhalb dieser Säulen wird das mit nahezu Lichtgeschwindigkeit einfallende Material durch verschiedene, physikalische Prozesse abgebremst. Dies führt zu einer intensiven Emission an Röntgenstrahlen, weswegen diese Systeme als sogennante Röntgendoppelsterne klassifiziert werden. Durch die Eigenrotation des Neutronensterns ändert sich Beobachtungswinkel auf die Akkretionssäulen periodisch, wodurch diese Objekte scheinbar pulsieren. Durch die orbitale Bewegung im Doppelsternsystem wird die Pulseperiode Doppler-verschoben, woraus die Parameter des Orbits bestimmt werden können. Zur gleichen Zeit erhöht sich die Rotationsfrequenz des Neutronensterns (ein sogenannter *spin-up*) auf Grund des Drehimpulsübertrags des akkretierten Materials.

Die extremen physikalischen Bedingungen um einen Neutronenstern stellen Jahrzehnte nach ihrer Entdeckung noch immer Herausforderungen für das wissenschaftliche Verständnis dar. Selbst-konsistente Modelle für die Emission der Röntgenstrahlung, d.h. für das Röntgenspektrum, die Form der Pulsationen (bekannt als Pulsprofil) oder die Änderung der intrinsischen Rotationsperiode sind noch immer in der Entwicklung. Auch wenn das Verständnis des Akkretionsprozesses auf Neutronensterne zur Zeit stark zunimmt, erzielen die aufkommenden theoretischen Modelle nur unzureichende Ergebnisse. Daher ist es äußerst wichtig existierende physikalische Modelle an Hand von Beobachtungen zu überprüfen und die Theorien durch die Ergebnisse weiter zu entwickeln. Des Weiteren sollten große Strichproben an Daten analysiert werden, um noch bisher unbekannte, beobachtbare Fakten über den Akkretionsprozess zu entdecken.

Ein fundamentaler Parameter in vielen Theorien ist die Menge an Material, das in einer bestimmten Zeitspanne vom Neutronenstern akkretiert wird: Die sogenannte Massenakkretionsrate, die grob mit dem beobachteten Röntgenfluss einer Quelle skaliert. Daher können Theorien am besten weiterentwickelt werden, indem Quellen untersucht werden, deren Fluss um Größenordnungen variiert. Tatsächlich existiert eine Unterklasse an Röntgendoppelsternen, die dieses Verhalten zeigt. Diese Systeme zeichnen sich durch einen weiten und exzentrischen Orbit des Neutronensterns um seinen Begleiter des Typs Be aus, welcher eine zirkumstellare Scheibe aus Materie besitzt. Entsprechend werden diese Systeme als Be-Röntgendoppelsterne bezeichnet. Der Neutronenstern befindet sich die meiste Zeit über in einer großen Entfernung zum Begleitstern, so dass er nicht im Röntgenlicht

nachweisbar ist. In der Nähe des Periastrons kann nun Material von der Scheibe des Be-Sterns auf den Neutronenstern akkretiert werden, was einen starken Röntgenausbruch zur Folge hat. Tatsächlich können diese Quellen während ihrer typischerweise wenige Wochen langen Ausbrüche zu den hellsten Objekten am Röntgenhimmel werden.

Eine Analyse der Doppler-verschobenen Pulsperiode wird auf Grund des intrinsischen *spin-up* des Neutronensterns, welcher durch die hohe Variabilität und Stärke der Massenakkretionsrate während dieser Ausbrüche ein komplexes Verhalten zeigt, erschwert. Wie in der vorliegenden Arbeit gezeigt ist, kann die Annäherung der Änderung der intrinsischen Rotationsperiode durch eine Taylorreihe, wie es häufig in der Literatur zu finden ist, zu falsch abgeleiteten orbitalen Parametern führen. Anstelle dessen sollten theoretische Modelle benutzt werden, die die Leuchtkraft, L, eines Neutronensterns mit seinem *spin-up*, $\dot{P}$, verbindet.

In dieser Arbeit wurde solch ein Modell an die zeitliche Entwicklung der Rotationsperiode des Röntgendoppelsterns XTE J1946+274 angewandt, wie sie mit *Fermi*-GBM gemessen wurde. Das Modell war in der Lage, die Beobachtungen erfolgreich zu beschreiben, und die Orbitalparameter wurden verlässlich bestimmt, welche bisher nur sehr vage bekannt waren. Die orbitalen Parameter von RX J0520.5−6932 und XTE J1859+083 wurden durch Anpassen dieses Modells an deren *Fermi*-GBM-Daten zum ersten Mal überhaupt bestimmt. Von der Stärke des *spin-up* wurden Rückschlüsse auf die Entfernung zu XTE J1859+083 gezogen. Des Weiteren wurde eine zweite Modulation der beobachteten Pulsperiode, eine sogenannte "superorbitale Periode", in diesem System detektiert. Durch eine Analyse der Pulsperiodenentwicklung von GRO J1008−57, wie sie mit *RXTE*, *Swift* und *Suzaku* gemessen wurde, konnten die orbitalen Parameter, insbesondere der Zeitpunkt der Periastronpassage und die Umlaufdauer, mit Hilfe einer Taylorreihenentwicklung verbessert werden. Ausgehend von diesen Parametern wurden die Orbitalphasen während der Röntgenausbrüche dieses Systems präzise für die letzten Jahrzehnte berechnet. Es zeigte sich, dass die Quelle regelmäßig und immer zur gleichen Orbitalphase ausbricht, wodurch ihre Ausbrüche vorhergesagt werden können. Durch Vergleichen der gemessenen *spin-ups* aller vier analysierten Quellen in dieser Arbeit zeigte sich, dass die Entwicklung der Rotationsperiode hauptsächlich von der Massenakkretionsrate bestimmt wird. Dies bestätigt die Theorie von Ghosh & Lamb (1979b) zum Drehimpulsübertrag auf Neutronensterne.

Die spektrale Entwicklung von GRO J1008−57 wurde in dieser Arbeit unter Benutzung *aller* verfügbaren *RXTE*-Daten analysiert, wobei Breitband-Beobachtungen mit *Suzaku* und punktierte Beobachtungen mit *Swift* und *NuSTAR* hinzugezogen wurden. Dasselbe phänomenologische Spektralmodell wurde auf all diese Daten angewandt, wofür eigens eine spezielle Software zur Analyse von großen Datenmengen entwickelt wurde. Es zeigte sich, dass gewisse spektrale Parameter unabhänging vom Fluss der Quelle und konsistent unter den Ausbrüchen sind. Durch eine simultane Analyse aller Spektren wurde die Entwicklung der übrigen Parameter mit sehr hoher Genauigkeit bestimmt. Eine weitere Untersuchung dieser Entwicklung mündete in der bemerkenswerten Erkenntnis, dass die spektrale Form von GRO J1008−57 einzig und allein durch dessen Röntgenfluss bestimmt ist. Dies ist ein wichtiges Ergebnis für die Theorie der Akkretion auf starkmagnetische Neutronensterne, da dies nahelegt, dass die Höhe und der Radius der Akkretionssäulen Funktionen der Massenakkretionsrate sind. Dieses Ergebniss wird durch eine vorläufige Untersuchung von GX 304−1 unterstützt. Nach einer Analyse *aller RXTE*-Daten dieser Quelle scheint ihre spektrale Form nur vom Fluss abzuhängen, ähnlich zu den Beobachtungen von GRO J1008−57.

Zusammengefasst bestimmt hauptsächlich die Massenakkretionsrate die Entwicklungen der Rotationsperiode und die spektrale Form von Neutronensternen in Röntgendoppelsternen mit Be-Begleitern.

Abstract

A neutron star is the collapsed relic of a massive star's core after its supernova explosion. These compact objects are concentrated to more than a solar mass within their $\sim$23 km diameter, resulting in a density as high as that of nuclear matter. Due to conservation of angular momentum and magnetic flux neutron stars spin with periods from fractions of a second up to a few hours and feature magnetic field strengths around 10^{12} G, which are among the strongest fields in the known universe.

Once a neutron star is on an orbit around a main-sequence star, mass transfer from its envelope onto the compact objects becomes possible. The material is forced to follow the magnetic field lines of the neutron star below a certain distance. Consequently, the accreted material is channeled onto the magnetic poles where it forms so-called accretion columns on top of the neutron star's surface. In these columns the infalling plasma is decelerated from nearly the speed of light by various physical processes, which results in the emission of intense X-ray radiation. These systems are therefore known as X-ray binaries. As the neutron star rotates, the viewing angle onto the accretion columns change periodically, which results in apparent X-ray pulsations. The pulsation period is Doppler shifted due to the orbital motion of the binary, which can be used to derive the orbital parameters of a system. At the same time, the neutron star spins up due to angular momentum transfer from the accreted material.

The extreme physics in the vicinity of neutron stars challenge our scientific knowledge even decades after their discovery. Self-consistent models for the X-ray continuum emission, i.e., the X-ray spectrum, the shape of the pulsations (called the pulse profile), and the intrinsic spin period evolution are still under development. Although a strong gradient in our understanding of accretion onto neutron stars is ongoing, applying emerging theoretical expectations result in only marginal success. Thus, it is of particular importance to check existing models with observational data and to feed the results back into theory. Furthermore, large samples of data should be analyzed to reveal yet unknown observational facts about the accretion process.

A key parameter in most theories is the amount of matter accreted by the neutron star during a certain time: the mass accretion rate, which scales roughly with the observed X-ray flux of a source. Consequently, the highest feedback to theory is achieved by investigating sources whose fluxes vary by orders of magnitude. Indeed, there is a subclass of X-ray binaries showing this behavior. These binaries are characterized by a wide eccentric orbit of the neutron star and a circumstellar disk of material around the main-sequence companion, a Be star, giving the name Be X-ray binaries. The sources are undetected in X-rays most of the time when the neutron star is far away from the Be star. Once it approaches periastron, mass accretion from the Be star's disk onto the neutron star becomes possible which results in strong X-ray outbursts. In fact, these sources can become the brightest objects in the X-ray sky during their outbursts, which typically last for a few weeks.

Due to the highly variable and strong mass accretion during these outbursts, the intrinsic spin-up of the neutron star complicates the analysis of its Doppler shifted pulse period. As shown in this thesis, approximating the spin period evolution by a Taylor series, as commonly used in the literature, can result in erroneously derived orbital parameters.

Instead, theoretical models should be used which connect the X-ray luminosity, L, of a neutron star with its spin-up rate, $\dot{P}$.

In this work such a model was applied to the spin period evolution of the X-ray binary XTE J1946+274 as measured by *Fermi*-GBM. The model was able to successfully describe the observations and reliable orbital parameters were derived, which were known only roughly before. The orbital parameters of RX J0520.5−6932 and XTE J1859+083 were determined for the first time by fitting the *Fermi*-GBM data with this model. From the strength of the spin-up in XTE J1859+083, conclusions about its yet unknown distance were drawn. Furthermore, a secondary modulation of the observed pulse period, a so-called "superorbital period", was detected in this system. Analyzing the pulse period evolution of GRO J1008−57 as measured with *RXTE*, *Swift*, and *Suzaku* using a Taylor series resulted in improved orbital parameters of the system, especially its time of periastron passage and orbital period. From these parameters the orbital phases of the system's X-ray outbursts during the last decades were calculated precisely. This reveals that almost all outbursts occurred regularly and at the same orbital phase, which enables the ability to predict outbursts of the source. Comparing the measured spin-up rates among the four sources analyzed in this thesis revealed that the spin period evolution is mainly driven by the mass accretion rate. This confirms the angular momentum theory by Ghosh & Lamb (1979b).

The spectral evolution of GRO J1008−57 with its flux was analyzed within this thesis using *all* available *RXTE* data, in addition to broad band observations by *Suzaku*, and pointed observations by *Swift* and *NuSTAR*. Using data analysis software specifically developed here to handle large datasets, the same phenomenological model was applied to all these spectra. It was found that certain spectral parameters are independent of the source's flux and are consistent among the outbursts of the source. By performing a simultaneous fit of all these spectra, the evolution of the remaining parameters was revealed with very high precision. Investigating these parameter evolutions further resulted in the remarkable conclusion that the spectral shape of GRO J1008−57 is determined by knowing its flux only. This is an important input for the theory of accretion onto magnetized neutron stars, as it suggests that the accretion column's height and radius are functions of the mass accretion rate. This conclusion is supported by preliminary results of an analysis of GX 304−1. Using *all RXTE* data of this source showed that its spectral shape seems to depend on the source's flux only, similar to what was observed in GRO J1008−57.

In summary, the mass accretion rate is the key driver for the evolutions of the spin period and the spectral shape in neutron star X-ray binaries with Be-type companion.

Contents

Yet Unanswered Questions

or Thesis Outline

> *" 'Exactly!', said Deep Thought. 'So once you know what the question actually is, you'll know what the answer means.' "*
>
> The Hitchhiker's Guide To The Galaxy
> by Douglas Adams

Usually, when you decide to do your Ph.D., you first define your thesis aims, i.e., the research questions. This might take a long time because they should be of scientific importance, i.e., their answers generate knowledge and they should not have been asked before. After having found the questions, methods to find the answers are developed, such as experiments in laboratories or questionnaires for subjects. In the research phase the methods are applied and the results will, finally, answer your research questions hopefully. In astronomy, however, there are no laboratories in their classical meaning: *"Most laboratories are characterized by controlled uniformity of conditions (constant temperature, humidity, cleanliness)."*[1] That is because the objects of interest, e.g., stars, are out of human control and experiments cannot be repeated under the same conditions. Consequently, the work flow of a Ph.D. thesis in observational astrophysics is the other way around: once you have analyzed the data you know which questions you can answer. Of course, this might lead to further questions, but designing and scheduling an observation which is able to provide answers at the first place is almost impossible.

Having analyzed some observational data at the beginning of my Ph.D. thesis, I have discussed the results with people from collaborations and at conferences around the globe. During these discussions, several specific questions have been asked based on the answers I had got already, for instance[2]

S1: *Why is there an outburst every orbit in GRO J1008−57?* — myself

S2: *Are there spectral differences between the rise and decline of an outburst?* — myself

S3: *Why happen the outbursts of GRO J1008−57 before periastron?* — Atsuo T. Okazaki

S4: *How is the column changing at this particular luminosity?* — Dmitry Klochkov

S5: *Can you measure the baryon to electron density at the shock?* — George Fuller

S6: *Is there a way to model the angular momentum transfer?* — Katja Pottschmidt

S7: *Do we need precise orbital solutions?* — Peter Kretschmar

S8: *I don't understand why this kind of analysis cannot be done...* — Jörn Wilms

[1] *Encyclopædia Britannica Online*, retrieved 02 September, 2015, from http://www.britannica.com/topic/laboratory-science

[2] The questions are not quoted verbatim and are reduced to their physical statement.

In my Ph.D. thesis, I will provide answers to most of these and further questions. However, looking at my work in total I am able to define two major subjects[3]:

THE DETERMINATION OF X-RAY BINARY ORBITS
and
THE SPECTRAL EVOLUTION OF BE X-RAY BINARY OUTBURSTS WITH LUMINOSITY

The results and, especially, the conclusions allow me to investigate three general questions:

G1: *Can the angular momentum transfer theory by Ghosh & Lamb (1979b) successfully explain observed pulse period evolutions?*

G2: *What drives the evolution of the spectral parameters during and between Be X-ray binary outbursts?*

G3: *Is there observational evidence for the accretion regimes theoretically proposed by Becker et al. (2012)?*

As one can see these questions connect the theoretical work on neutron star accretion with observational data. Our knowledge of accreting neutron stars is, however, yet insufficient to explain the observations with self-consistent models. This leads to the aim of my thesis:

PROVIDE OBSERVATIONAL INPUT TO IMPROVE OUR UNDERSTANDING OF NEUTRON STAR ACCRETION PHYSICS

But before I present the answers to the above questions I will give an introduction into accreting neutron stars and their physics in Chapter 1. Having a basic knowledge of this kind of objects is crucial to understand why some simple-sounding questions are impossible to answer yet. Again driven by first results I have developed and implemented new analysis methods, which are presented in Chapter 2. After an overview about X-ray detection mechanisms and used detectors in this thesis in Chapter 3, these methods are then applied to determine the orbits of neutron stars in Chapter 4 and to reveal their spectral evolution during outbursts in Chapter 5. Finally, I will answer the general questions above in Chapter 6 and conclude my Ph.D. thesis by raising further questions, which have to be answered in the future.

Sometimes, found answers are difficult to interpret, and the conclusions even might get turned around decades later:

'*With the designation "neutron star" we do not wish to imply, however, that such a star is to be regarded as a giant nucleus composed of separate neutrons of precisely the same character as free neutrons.*' (Zwicky, 1938)

'*Although there is no evidence for (and possibly some evidence against) quasi-stellar radio sources occurring inside ordinary galaxies,* [...]' (Salpeter, 1964)

'*It has been shown* [by Strom & Strom, 1961, who assumed 10^{21} atoms cm^{-2}] *that x rays in this wavelength region are not appreciably absorbed over interstellar distances.*' (Giacconi et al., 1962)

[3]For work which does not fit into these subjects please have a look on my list of publications.

Chapter 1

Introduction to Accretion Powered Neutron Stars

1.1 The Birth of Neutron Stars

Astronomers were puzzled as in 1962 the Geiger counters onboard a Aerobee rocket discovered the first extraterrestrial X-ray source Sco X-1 (Giacconi et al., 1962), named after its position in constellation Scorpius. In the following I will briefly argue why this discovery has astonished people, which finally led to the idea of accreting neutron stars, i.e., the birth in terms of knowledge. After having discussed the idea behind the actual birth of a neutron star I will end this Chapter with basic properties of neutron stars.

1.1.1 Historic Puzzles

Let us imagine we would live back in the 1960's and have followed the discovery of Sco X-1. Our goal is to derive physical properties of the newly discovered "star", like its temperature and radius, using basic physical laws[1]. Therefore, we will use the observational facts of Giacconi et al. (1962) and Sandage et al. (1966). From the sensitivity curves of the Geiger counters Giacconi et al. have estimated that the X-ray source had emitted photons with a wavelength of $\lambda \sim 3\,\text{Å}$ and a flux F of $5\,\text{photons}\,\text{s}^{-1}\,\text{cm}^{-2}$ (Giacconi et al., 1962).

Assuming that the star's spectrum is a pure black body and its flux peaks at the measured wavelength λ_{max} of 3 Å, we can use Wien's displacement law (Wien, 1893, 1896),

$$\lambda_{\text{max}} = \frac{b}{T} \quad , \tag{1.1}$$

to estimate the temperature T of the object. Together with Wien's displacement constant[1] $b = 0.29\,\text{cm}\,\text{K}$ we derive a temperature of $T = 2.34 \times 10^6\,\text{K}$.

A few years after the discovery, Sandage et al. (1966) identified the optical counterpart of Sco X-1 and estimated its distance d to be $250\,\text{pc}$ (a modern estimate is 2.8(3) kpc, Bradshaw et al., 1999). If we assume the object to radiate isotropically, its flux F translates to the intrinsic luminosity L via

$$L = 4\pi d^2 F \quad , \tag{1.2}$$

which results in $L = 2.5 \times 10^{35}\,\text{erg}\,\text{s}^{-1}$ or around ∼100 solar luminosities. If we consider the X-ray source to be a sphere and its full surface to radiate in X-rays, we can estimate its radius R using the Stefan-Boltzmann law, (Stefan, 1879; Boltzmann, 1884),

$$L = 4\pi R^2 \sigma T^4 \quad , \tag{1.3}$$

[1] All physical constants have been taken from "The 2010 CODATA Recommended Values of the Fundamental Physical Constants" (P. J. Mohr, B. N. Taylor, and D. B. Newell, 2011), web-client http://physics.nist.gov/cuu/Constants/ version of 2011 June 02 developed by J. Baker, M. Douma, and S. Kotochigova.

with the Stefan-Boltzmann constant $\sigma = 5.67 \times 10^{-5}\,\mathrm{erg\,cm^{-2}\,s^{-1}\,K^{-4}}$. This yields a radius of $R \sim 34\,\mathrm{km}$ only.

People realized that within this small volume the steady production of X-rays over decades can not be provided by a black body without further energy production. Furthermore, the physical processes leading to X-ray emission, like thermal bremsstrahlung emission from hot plasmas or inverse Compton effects by relativistic electrons, do not explain the observed spectra of the various X-ray sources, which had been detected within a few years after the discovery of Sco X-1 (see, e.g., Morrison, 1967, for a review and references therein).

A solution to the energy production issue was first proposed by Hayakawa & Matsuoka (1964) and later picked up by Shklovsky (1967) and Prendergast & Burbidge (1968). These authors considered mass accretion of the primary star in a binary to be a powerful energy source. This idea was of great interest since it has been discovered that Sco X-1 (Westphal et al., 1968) and Cyg X-2 (Lynds, 1967, and references to it) are indeed binary systems (derived from optical spectral analyses). A gas stream ejected from the secondary star is falling into the gravitational well of the primary with mass M and radius R. The released potential energy ΔE per accreted mass m is then given by

$$\frac{\Delta E}{m} = \frac{GM}{R} = 1.9 \times 10^{15}\,\frac{M/\mathrm{M_\odot}}{R/\mathrm{R_\odot}}\,\mathrm{erg\,g^{-1}} \quad , \tag{1.4}$$

where G is the gravitational constant. Once the ratio of the object's mass to radius, both in solar units, is much larger than unity a huge amount of energy is released even when only 1 g of material is accreted. Using the above equation and a given luminosity, L, one can estimate the so-called accretion rate,

$$\dot{M} = \frac{L}{\Delta E/m} = \frac{LR}{GM} \quad , \tag{1.5}$$

which is the amount of material accreted per unit time (often given in $\mathrm{g\,s^{-1}}$ or $\mathrm{M_\odot\,yr^{-1}}$). Apparently, one can solve this equation to the luminosity once the accretion rate is known from theory.

The objects, which have been under discussion, were white dwarfs (e.g., Cameron & Mock, 1967) and neutron stars (Morton, 1964, and references therein). White dwarfs typically have a mass of about $0.6\,\mathrm{M_\odot}$ (Tremblay et al., 2013) and a radius of $0.013\,\mathrm{R_\odot}$ (Shipman, 1972), i.e., their mass to radius ratio is ∼46. They are the end-product of stellar evolution of stars with an initial mass of less than $8\,\mathrm{M_\odot}$ and were already known from theory (see, e.g., Fowler, 1926; Stoner, 1929) triggered by the mass of Sirius-B (see, e.g., Plummer, 1881; Adams, 1915, and references therein). To release the observed luminosity of X-ray sources of $L \sim 10^{36}\,\mathrm{erg\,s^{-1}}$, a mass accretion rate of $\dot{M} \sim 10^{-7}\,\mathrm{M_\odot\,yr^{-1}}$ is needed, following Eq. (1.4). The accreting object might also be a neutron star, originally discussed theoretically by Oppenheimer & Volkoff (1939) as degenerated neutron cores within stars[2], after Baade & Zwicky (1934) proposed this kind of object being involved in supernovae (see the following Sect. 1.1.2), although at this time supernovae were believed to be a nova-like reaction, as known from white dwarfs, on the surface of massive stars. With a mass of about $1.4\,\mathrm{M_\odot}$ and a radius around 12 km (Lattimer, 2012) the neutron star's mass to radius ratio of ∼80 000 is much higher than that of a white dwarf. Consequently, the needed mass accretion rate is $\dot{M} \sim 10^{-10}\,\mathrm{M_\odot\,yr^{-1}}$.

[2]Landau (1938) considered neutron cores as the energy source for main sequence stars. Around the same time Bethe (1939) and Bethe & Critchfield (1938) proposed nuclear reactions, the pp-chain and CNO-cycle, as the well established primary energy source.

Figure 1.1: The type II supernova SN 2011dh in the nearby galaxy M 51. The yellow circle marks its position. In both images North is up. **Left:** Two years before the report of the supernova no bright object was visible at its position (image taken by H. Hirsch and M. Hanke on 2009 May 02, Dr. Karl Remeis-observatory Bamberg). **Right:** The supernova is clearly visible even one month after its discovery. The other bright point-like objects in the images are stars in the Milky Way (image taken by M. Wille on 2011 June 27, Dr. Karl Remeis-observatory Bamberg).

The key observations to distinguish whether white dwarfs or neutron stars are the majority among the accreting objects were the discovery of strong X-ray pulsations with timescales of several seconds in duration in Cen X-3 (Giacconi et al., 1971) and Her X-1 (Tananbaum et al., 1972). Lamb et al. (1973) showed that only a strong magnetized star (with $B \sim 10^{12}$ G), such as a neutron star, is able to focus the accreting material beyond its surface, which results in an anisotropy in the emitted radiation and, thus, leads to pulsations with the rotation period of the star.

With the launch of the first X-ray mission *UHURU* in 1970 the era of X-ray astronomy was basically born. The mission discovered over 400 X-ray sources, listed in the fourth Uhuru-catalog (Forman et al., 1978). Various X-ray missions followed until now and 301 confirmed compact X-ray sources in the Milky Way and Magellanic Clouds are known today (Liu et al., 2006, 2007). Among them, however, are not only neutron stars, but also black holes or white dwarfs in binary systems. Further sources of X-rays are cluster of galaxies, supernova remnants, or active galactic nuclei. They are, however, not described further in the present thesis, as it focuses on accreting neutron stars.

1.1.2 Supernova Explosion

As already mentioned in the previous Section neutron stars have been originally proposed to be formed in supernovae, although what is actually happening in a supernova was not fully understood (Baade & Zwicky, 1934; Zwicky, 1938). In the following decades the implosion of a star due to an exhausted fuel for nuclear reactions in its core was investigated, which would results in a dramatic increase of the core's density and, finally,

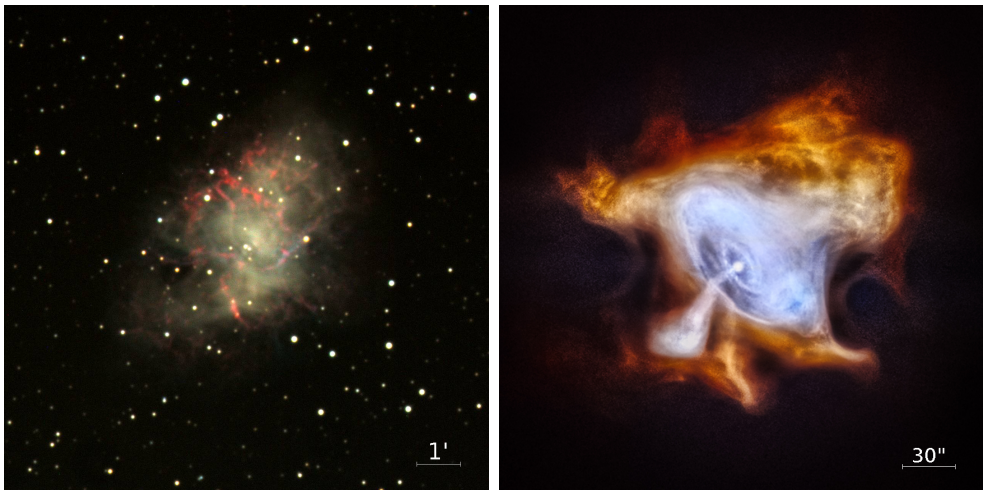

Figure 1.2: Left: Messier 1, the Crab nebula, as seen in optical wavelengths. While the nebula contains all kinds of elements, produced during the supernova explosion, the reddish regions are rich in fluorescent hydrogen (image taken by F. Fürst and M. Wille on 2011 January 28, Dr. Karl Remeis-observatory Bamberg). **Right:** The light of the nebula is powered by its central engine, a neutron star, which is seen as bright spot in this *Chandra*-image. Here, the X-ray energies are color coded, ranging from 0.5 keV (red) to 7 keV (blue) (taken from NASA/CXC/SAO).

give birth to a neutron star (see, e.g., Burbidge et al., 1957; Colgate & White, 1966; Colgate, 1971, and references therein). In this Section I will give an overview about supernovae, from observations of the explosion and their remnants, their connection to other important fields of astronomy, and the physical processes during the implosion of the star's core and the actual explosion of the rest of the star.

Neutron stars are believed to be born during the collapse of a massive star $\gtrsim 8$ times heavier than our Sun (Verbunt & van den Heuvel, 1995). This collapse further releases a lot of energy, partly in form of radiation. In fact, its luminosity of $10^{42-48}\,\mathrm{erg\,s^{-1}}$ (Bethe, 1990) can exceed the luminosity of the host galaxy the star is belonging to. That is the reason why this collapse is rather called a type II supernova explosion (SN). As an example, Fig. 1.1 shows the SN 2011dh, which happened in the nearby spiral galaxy M51 and was discovered by Silverman et al. (2011). The marked object on the right picture is not one of the visible foreground stars within the Milky Way. On the earlier picture on the left the object is not seen and the location right within one of the spiral arms of M51 is strong evidence for this object being a supernova. Of course, further investigations of, e.g., its electromagnetic spectrum are necessary to clarify its nature.

With a rate of only a few events per century in the Milky Way, supernovae explosions are rare events on human timescales (Ando et al., 2005). Studying their time evolution, detailed spectrum, and spatial distribution are important ingredients in order to understand, e.g., the cosmological parameters of the universe, such as the Hubble constant or mass density (see, e.g., Perlmutter et al., 1999, and references therein), or the chemical composition of our galaxy (see, e.g., Chiappini et al., 2001, and references therein), since these explosions eject a large amount of matter into the interstellar medium (ISM). One of the main scientific goals of the hard X-ray and gamma-ray mission *INTEGRAL* (Winkler et al., 2003) is to observe a nearby supernova within 15 Mpc distance (Knödlseder & Vedrenne, 2001) to achieve a good signal to noise ratio (S/N) between 20 keV and 8 MeV photon energy as provided by *INTEGRAL*-SPI (Vedrenne et al., 2003). Studying the emission lines of radioactive isotopes are important keys to understand the galactic nucleosynthesis processes. It is expected that during the estimated lifetime of *INTEGRAL* one supernova will be detected (Timmes & Woosley, 1997). In fact, such an event was detected during

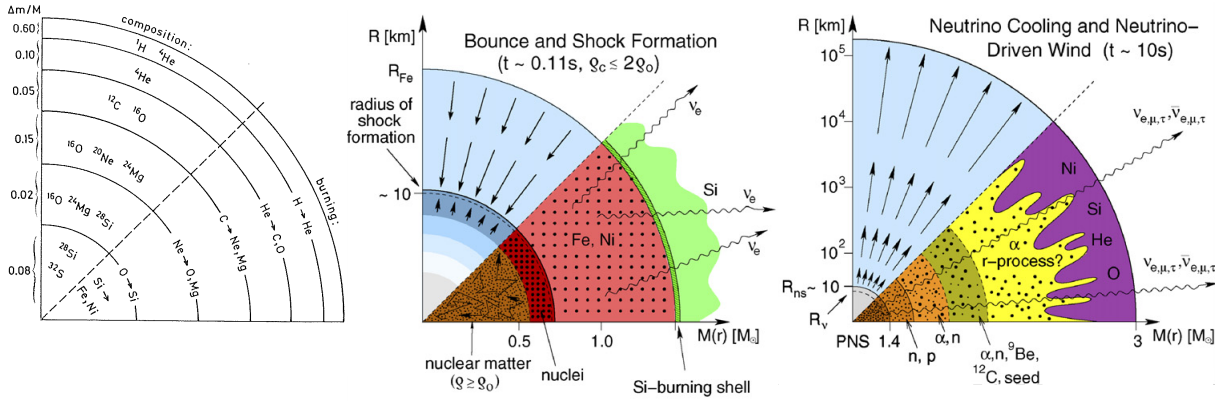

Figure 1.3: Schematic sketch of a supernova process. **Left:** The onion-like structure of a massive star before its explosion. The iron core is surrounded by the products of the different burning stages from silicon- to hydrogen-burning (taken from Kippenhahn & Weigert, 1990). **Middle:** During the collapse of the iron core a proto-neutron star is formed, at which surface the infalling matter is reflected forming an outwards shock (taken from Janka et al., 2007). **Right:** The shock has lost its energy by dissipating the core of the collapsing star. The neutrino wind revives this shock, which finally leads to the disruption of the star (taken from Janka et al., 2007).

the time of this Ph.D. thesis on 2014 January 22 (Fossey et al., 2014) and the analysis of its data is ongoing (see, e.g., Diehl et al., 2014, for first results).

Besides the study of the actual explosion, the supernova remnants (SNR) are another important field, which will improve our understanding of the nuclear reactions and asymmetries during the explosion (see, e.g., Vink, 2012, for a recent review). The first Messier object (M1), also known as the Crab nebula, is such a remnant and a picture in the optical is shown in Fig. 1.2 (left). The whole nebula is rich in atomic hydrogen, which fluorescence light at 656.3 nm can be detected. The energy source powering these filaments and the whole nebula is seen in the X-rays: a neutron star located in the central region of M1 (see right picture of Fig. 1.2). This object is surrounded by a torus and features an energetic jet. The jet and torus are the result of an interaction of the pulsar wind, which is an anisotropic outflow from the pulsars magnetosphere, with the ambient medium (see Kargaltsev & Pavlov, 2008, for a review). This structure seen in the X-rays is known as a pulsar wind nebula (PWN). In our galaxy 54 PWN are known from which 40 harbor a neutron star in their central regions (Kargaltsev & Pavlov, 2008). Compared to the 294 known SNRs (Green, 2014), however, only ∼10% have associated PWN and ∼ 30% have confirmed (radio or X-ray) point sources in its center[3]. For instance, in the remnant of the famous SN 1987A, no central object has yet been confirmed in the X-rays (see Burrows et al., 2012, for a recent review; Manchester, 2007). Several scenarios exist explaining the lack of a detection, such as a weak magnetic field, which needs decades to evolve, or an obscuration by a fall-back of material. Thus, studies of young neutron stars are important to constrain those models. A young population can be found, for example, in the Small Magellanic Cloud (SMC; see Sect. 4.2 for such an object).

From these facts it is clear that supernovae and neutron stars are related. How neutron stars form in detail during the collapse are not yet clear. Furthermore, the knowledge of the physical processes involved during a supernova explosion is incomplete. In fact, most simulations of core collapse supernovae did not result in a successful explosion until ∼1990 (Baron & Cooperstein, 1990). In the following a brief schematic sketch of the needed

[3]Green D. A., 2014, "A Catalogue of Galactic Supernova Remnants (2014 May version)", Cavendish Laboratory, Cambridge, United Kingdom (available at http://www.mrao.cam.ac.uk/surveys/snrs/)

physical effects of a supernova explosion is provided, based on Janka et al. (2007).

At the end of star's life it has produced various elements by fusion during several burning stages. Each stage has lead to a contraction of its core, i.e., an increase in temperature, such that the next burning process could be ignited. The resulting temperature and density gradient within the star defines zones where different burning processes take place, called shell burning. Thus, the produced elements are located within an onion-like structure of the star (see left sketch of Fig. 1.3). The inner most burning process fuses silicon to iron, which nucleus has the highest binding energy[4]. Thus, no net energy can be gained by burning iron any more. The iron core is growing until its mass exceeds the so-called Chandrasekhar mass limit, which is around $1.44\,\mathrm{M}_\odot$ (Chandrasekhar, 1931a,b, 1935; see Koester & Chanmugam, 1990 for a review). At this point the Fermi pressure of the degenerated electrons of the iron core is no longer capable to counteract the gravitation; the core collapses suddenly. As the density and temperature increases by orders of magnitude within a few milliseconds (Bethe, 1990) the Fermi energy of the electrons increases up to nuclear energies. At this point electron capture by the nuclei gets probable, which is also known as the inverse β-decay:

$$\mathrm{e}^- + (\mathrm{N}, \mathrm{Z}) \longrightarrow (\mathrm{N}+1, \mathrm{Z}-1) + \nu_\mathrm{e} \quad , \tag{1.6}$$

where N is the number of neutrons the nucleus consists of and Z is the atomic number, i.e., the number of protons. Once the resulting nuclei is too rich of neutrons, β-decay takes place,

$$(\mathrm{N}, \mathrm{Z}) \longrightarrow (\mathrm{N}-1, \mathrm{Z}+1) + \mathrm{e}^- + \bar{\nu}_\mathrm{e} \quad , \tag{1.7}$$

and the two processes are in equilibrium. This does not, however, stabilize the collapse and as the Fermi energy of the electrons exceeds the energy of the released energy from the β-decay, this process gets blocked by the Pauli Principle. Consequently, electron capture is the dominant process in the collapsing core and most of its protons are converted into neutrons. As the produced neutrons are not charged electromagnetic forces are not present, leading to densities in the order of $10^{15}\,\mathrm{g\,cm^{-3}}$, which is comparable to nuclear matter. Since neutrons are fermions the Pauli-principle leads to a Fermi pressure, which finally is able to counteract gravity and stabilizes the collapsing core; a proto neutron star (PNS) has formed inside the dying star. However, the outer layers of the star are still there and are now falling onto the PNS. Due to its high density it is nearly incompressible, leading to a full inelastic reflection of the infalling matter, that is a shock is forming which is traveling *outwards* (middle sketch of Fig. 1.3). While the shock is moving outwards it is quickly losing energy by dissipating the nuclei into neutrons and protons ($\sim 10^{51}$ erg per $0.1\,\mathrm{M}_\odot$ dissipated material, Woosley et al., 2002, and references therein). In fact, the shock energy is lost before it reaches the star's surface, preventing the star from an explosions. However, in last decades people investigated the role of the neutrinos produced during the inverse β-decay (Eq. 1.6), which finally lead to the key to a successful explosion (see Baron & Cooperstein (1990) for first results and Bethe, 1990, for a summary): due to the high density in the PNS the produced neutrinos are trapped. As soon as the matter sufficiently cooled down all of these neutrinos are released at nearly the same time, leading to a neutrino burst. The density in the shock region, still traveling outwards, is high enough such that the neutrinos can scatter off the matter (right sketch of Fig. 1.3). The shock is gaining energy by this neutrino wind, which finally is sufficient to disrupt the star completely. What is left behind is the PNS, a neutron star has formed.

[4]The nucleus with with a higher binding energy than ^{56}Fe is ^{63}Ni, which is, however, not reached in stellar fusion cycles (Fewell, 1995).

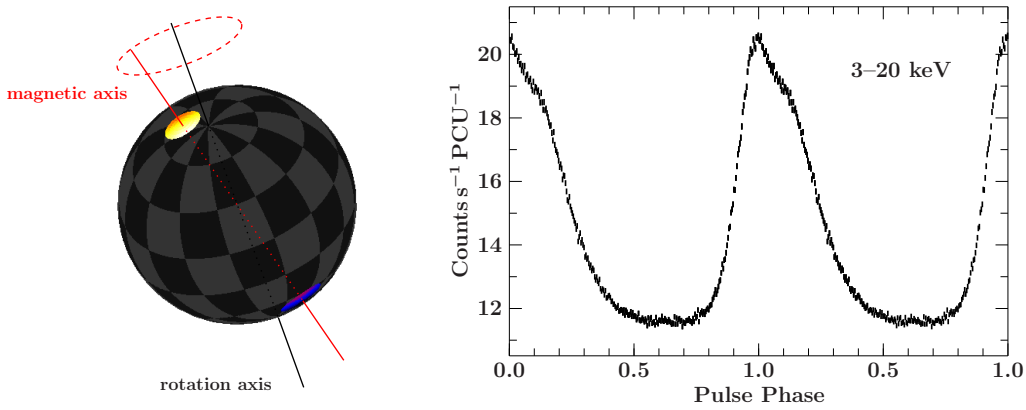

Figure 1.4: Left: Due to the misalignment between the neutron star's magnetic (red) and rotation axis (black) any emission from near the magnetic poles leads to observable pulsations. The colored area at the magnetic poles indicate the observed flux level from bright (yellowish) to dark (blueish). Lightbending effects project the surface to the observer in a non-linear way (Falkner et al., 2016, in prep.). **Right:** pulse profile of the pulsar PSR B1509−58 as measured with *RXTE*-PCA ($P_{\rm spin} \sim 150\,$ms; E. Fink, priv. comm.). The profile is shown twice for clarity. The main peak originates from one of the two poles, while the beam of the second pole is not detected.

It is interesting to note that while the shock is moving outwards starting at the star's core, the elements, which have been produced by the various burning processes during the lifetime of the star, are dissociated into neutrons and protons (Woosley et al., 2002). It is believed that from this neutron-proton-plasma heavier elements than iron form due to a rapid capture of neutrons, which is known as the r-process (Woosley et al., 1994, and references therein; see Hansen et al., 2012, for a discussion about a second r-process). The rate of neutron capture even exceeds the β-decay rate leading to neutron-rich nuclei. These nuclei are on an excited state in the beginning, which decay to the ground level by the emission of γ-rays, which can be detected by *INTEGRAL* (Winkler et al., 2003, and references therein). Thus, analyzing these emission lines will improve our understanding of the r-process. Finally, the unstable neutron-rich nuclei decay to stable high Z-elements within the chart of nuclides by the β-decay.

1.1.3 General Properties of Neutron Stars

Lamb et al. (1973) argued that due to the observed X-ray pulsations a neutron star has to be the compact object and the duration of the pulses, the pulse period, is equal to its spin (or rotational) period. Folding the X-ray light curve of an observation on this pulse period reveals the so-called pulse profile, i.e., the mean X-ray flux over the pulse (or spin) phase. As an example, the pulse profile of PSR B1509−58 is shown in Fig 1.4 (right). This neutron star is, however, not a member of a binary system. Rather that it is a radio pulsar, i.e., an isolated neutron star, which was born during a supernova ∼10 ky ago[5] derived from the associated SNR MSH 15−5*2* (Seward et al., 1983). The radio emission originates from synchrotron radiation, which is produced by electrons which are accelerated in the magnetic field around the neutron star (Michel, 1991). Most of the known isolated neutron stars are detected as radio pulsars, but PSR B1509−58 is also showing X-ray pulsations due to its high magnetic field in the order of $10^{12}\,$G. Its pulse profile, however, is a good example to explain the origin of pulsations in detail. Imagine

[5]From the spin-down of the pulsar one derives, however, an age of 1.7 ky, see Gvaramadze (2001) for a discussion.

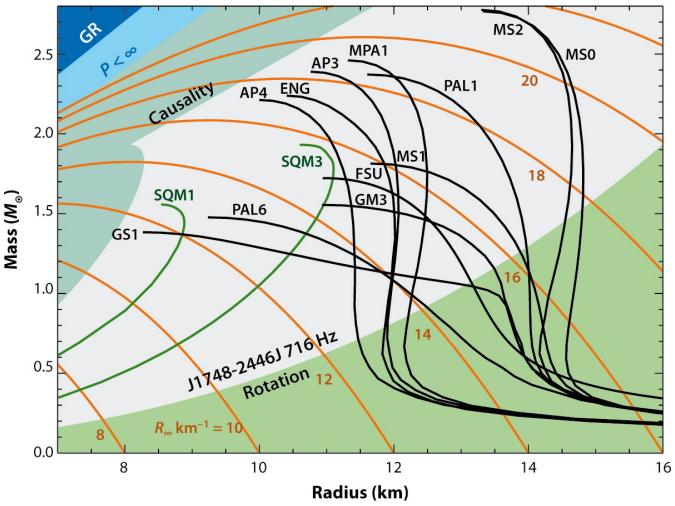

Figure 1.5: Relationship between mass and radius of a neutron star as predicted by different theoretical models. The black curves represent models for hadronic equations of state while the green ones are for strange quark matter. For the definition of the orange lines, which show contours of R_∞, please see Lattimer (2012). The blue shaded regions in the upper left corner are forbidden as predicted by general relativity (GR), finite pressure ($P < \infty$), and causality. The green region is the limit derived by the rotation frequency of PSR J1748−2446J, which is the fastest rotating pulsar known to date (taken from Lattimer, 2012).

two hot spot on the surface of the neutron star, which are located at the magnetic poles (as shown in Fig. 1.4). Because the rotation axis is inclined to the line of sight to the observer (the Earth) only one pole is visible in the classical picture. If the rotation axis is misaligned to the magnetic axis, like on Earth, the hot spot moves periodically into and out of the line of sight of the observer. Consequently, the X-rays emitted from the hot spot are observed modulated with the spin period. Accordingly, this effect is also known as the lighthouse effect. However, this simple picture is complicated due to the strong gravitational field close to the neutron star, which requires general relativity (GR) effects to be taken into account. As has been shown by calculations (see, e.g., Kraus et al., 2003, and references therein) the geometry is distorted such that light emitted under a certain angle to the normal of the neutron star's surface gets bent. That has the interesting consequence that an observer sees more surface area of the neutron star than in Euclidean geometry. Thus, in most cases *both* poles are visible over one rotation, which leads to double-peaked pulse profiles (for an example of pulse profile calculations see, e.g., Kraus et al., 2003, and references therein). Thus, from fitting the pulse profile one would be able, in principle, to derive the geometry and, consequently, the mass and radius of a neutron star (Falkner et al., 2016, in prep.). In case of an accreting pulsar the pulse profiles are much more complicated, however, due to the formation of accretion columns above the neutron star surface (see Sect. 1.3.2 for details).

In fact, deriving masses and radii from observations of neutron stars is still one of the most challenging quests in todays X-ray astronomy (see Özel & Freire, 2016, for a recent review). Furthermore, measuring the mass-radius-relationship of neutron stars is probably the most important input for Quantum chromodynamics (QCD) at extreme particle densities at high gravitational pressures, where effects of general relativity can no longer be neglected. That is, the equation of state (EoS) of neutron star matter is yet unknown. Figure 1.5 shows the theoretical mass-radius-relation as resulting from the different models for the EoS (Lattimer, 2012). Knowing the EoS would allow us, for instance, to derive the limiting mass of a neutron star. Above this limit, which is known as the Oppenheimer-Volkov-limit based on early EoS-calculations by Oppenheimer & Volkoff (1939), the degenerated neutron star matter is no longer able to resist gravity and, consequently, collapses. Since no physical mechanism is known (yet) to stabilize the collapse the density increases to infinity, i.e., a black hole forms. The most sophisticated

estimation for the critical mass so far is around $2.7\,\mathrm{M}_\odot$ (for the Müller & Serot (1996) (MS2) EoS, see Lattimer, 2012, for an overview) and the heaviest known neutron star has a mass of $2.74(21)\,\mathrm{M}_\odot$ (PSR 1748−2021B; Freire et al., 2008).

Thus, as explained above, it is of particular importance to derive masses and radii of neutron stars by observations to improve our understanding of physics at its extremes.

Despite the extreme density within a neutron star, theoretical calculations of, e.g., the EoS or the X-ray spectrum (see Sect. 1.3.2) the magnetic field needs to be known as well since it is extreme as well. Usually, the B-field strength of neutron stars is on the order of $10^{12}\,\mathrm{G}$. In the most extreme cases B-fields up to $10^{14}\,\mathrm{G}$ have been measured (Kouveliotou et al., 1998), which is why these neutron stars are called magnetars. These object gain their X-ray energy directly from their magnetic field. What causes all these strong magnetic fields is still under debate and, especially, the internal and external magnetic field configurations (see Turolla et al., 2015, for a recent review). It can be shown, however, that magnetic fields are enhanced during supernova explosions due to magnetic flux conservation (Ginzburg, 1964; Woltjer, 1964). Let the collapsing core of radius R_c has an magnetic field of strength B_c, then

$$\frac{\mathrm{d}}{\mathrm{d}t} B_\mathrm{c} R_\mathrm{c}^2 = 0 \quad \Longrightarrow \quad B = B_\mathrm{c} \frac{R_\mathrm{c}^2}{R^2} \quad , \tag{1.8}$$

with the magnetic field strength B and radius R of the remaining neutron star. If we assume $B_\mathrm{c} = 10^3\,\mathrm{G}$ and $R_\mathrm{c} \sim \mathrm{R}_\odot = 7 \times 10^{10}\,\mathrm{cm}$ similar to the Sun right before the collapse down to $R = 10^6\,\mathrm{cm}$, the magnetic field strength of the newborn neutron star would be $B = 4.9 \times 10^{12}\,\mathrm{G}$. However, R_c is actually the size of the collapsing *core* and not the full size of the star. Thus, the resulting field strength is much weaker than what is observed. If dynamo effects are included during the early evolutionary stage of a neutron star, Bonanno et al. (2005) could show that the magnetic field strength increases by a few orders of magnitude.

Finally, using the same argument as above, we can show that the rotation period of a neutron star is the result of the collapse as well due to conservation of angular momentum. The angular velocity $\omega = 2\pi/P$ of the neutron star, where P is its pulse period, after the collapse of the star's core with angular velocity ω_c is given by

$$\frac{\mathrm{d}}{\mathrm{d}t} R_\mathrm{c} \omega_\mathrm{c} = 0 \quad \Longrightarrow \quad \omega = \omega_\mathrm{c} \frac{R_\mathrm{c}^2}{R^2} \quad . \tag{1.9}$$

Again, if we assume a solar value for $\omega_\mathrm{c} \sim 2.9 \times 10^{-6}$ but a core radius of $R_\mathrm{c} \sim 0.01\,\mathrm{R}_\odot = 7 \times 10^8\,\mathrm{cm}$ similar to a white dwarf (Hansen & Kawaler, 1994), we derive a neutron star spin period of $2\pi/\omega = 4.5\,\mathrm{s}$, which is in good agreement with periods of observed neutron stars (see, e.g., Lyne et al., 1985).

All derived and discussed canonical values of neutron stars are summarized in Table 1.1, with instructive examples how extreme these values are.

1.2 X-ray Binaries

The fact that one member of the binary is a compact object, i.e., has reached the final state in the evolution of a star already, means the binary must have gone through different stages of evolution. If the compact object is the result of a supernova, the mass loss during the explosion must be not larger than half of the total mass of the binary. Otherwise, the binary will be disrupted, i.e., the compact object and the remaining optical star are no longer gravitationally bound. This is explained by a change of the eccentricity e of the

Table 1.1: Canonical physical properties of neutron stars (mass and diameter after Lattimer (2012, and references therein), magnetic field strength and accretion rate after Bildsten et al. (1997, and references therein), all other values are derived). Demonstrative examples based on ideas by I. Kreykenbohm.

Mass	$1.4\,M_\odot$	heavier than the Sun
Diameter	23 km	the size of a city, like Nuremberg, Germany, or Baltimore, USA
Gravitational acceleration	$10^{14}\,\mathrm{cm\,s^{-2}}$	on the neutron star's surface a car of 1000 kg would weigh as much as the Mount Everest[a]
Density	$2.7 \times 10^{14}\,\mathrm{g\,cm^{-3}}$	this is the saturation density; take the above car and squeeze it to the size of a hair
B-field strength	10^{12} G	if the Moon would have such a strong magnetic field, all credit cards on Earth would get erased[b]
Rotation period[c]	1.396 ms to 5.4 hr	For periods $\lesssim$160 s the surface speed at the equator is faster than on Earth
Accretion rate[d]	$10^{16}\,\mathrm{g\,s^{-1}}$	Lake Mead, the biggest barrier lake in the USA, would be emptied within a second
Energy output[e]	$10^{36}\,\mathrm{erg\,s^{-1}}$	all 440 nuclear power plants[d] on Earth have to run for 5 billion years (since the creation of the Solar system) to produce the same energy as an accreting neutron star does in 1 second

[a] assuming that the shape of the Mount Everest is approximately a pyramid with a height of 8844 m (Chinese Academy of Surveying and Mapping, measured in 2005), a base with an edge length of 7450 m, and made of granite with a density of $2800\,\mathrm{kg\,m^{-3}}$ (EN 1936:2006).

[b] the field strength at the position of the Earth would be around 0.4 T, which is sufficient to alter the information stored on magnetic stripes (ISO/IEC 7811-6:2014).

[c] the range is based on the fastest known neutron star (PSR J1748−2446; Hessels et al., 2006) and the slowest one (4U 1954+319; Enoto et al., 2014)

[d] values given for a neutron star in an orbit around a heavy companion (see Sect. 1.2). The accretion rate of an isolated neutron star is negligible in this context.

[e] assuming an energy output of 1 GW per nuclear power plant.

binary orbit (for a detailed discussion of binary orbits see the following Sect. 1.2.1) due to a mass loss of ΔM (Verbunt & Phinney, 1995),

$$e = \frac{\Delta M}{M_1 + M_2 - \Delta M} \quad . \tag{1.10}$$

Here, M_1 and M_2 are the masses of the stars before the supernova explosion. This equation assumes a circular binary orbit and a zero kick velocity, i.e., the velocity the binary gains due to an asymmetric explosion. For $\Delta M \geq (M_1 + M_2)/2$ the eccentricity of Eq. (1.10) is $e \geq 1$, which is an unbound orbit. Further details about the evolution of X-ray binaries are given in Sect. 1.2.2 and 1.2.3.

To investigate the mass accretion process onto the compact object the mass accretion rate, $\dot{M}$, is of particular importance. As mentioned in Sect. 1.1.1 binary systems were proposed to explain the majority of X-ray observations, where matter from an optical companion star is transferred to the compact object. Thus, the value and time evolution

of $\dot{M}$ in an X-ray binary (XRB) is mainly driven by two aspects: the type of companion star and the orbit of the binary.

To understand and model the accretion flow between the two stars the gravitational potential, in which a particle of the accretion flow is moving, has to be known. The gravitational potential depends on the individual gravitational forces of the two stars with masses M_1 and M_2 and their time dependent positions $\vec{r}_1(t)$ and $\vec{r}_2(t)$, respectively. Since both stars orbit each other these positions can be calculated for a given time t, which in general leads to a time dependency of the gravitational potential. If we assume, however, that the orbit is circular and the rotation is synchronized (i.e., both stars keep the same face towards each other) we can express the potential in the rotating reference frame, which origin is located in the center of mass of the binary. As soon as the mass m of the particle is negligible compared to the stellar masses M_1 and M_2 (with $M_1 > M_2$) the effective Roche potential is then (Roche, 1849a,b, 1851)

$$\Phi(\vec{r}) = -\frac{M_1 G}{|\vec{r} - \vec{r}_1|} - \frac{M_2 G}{|\vec{r} - \vec{r}_2|} - \frac{1}{2}(\vec{\Omega} \times \vec{r})^2 \quad . \tag{1.11}$$

Here, G is the gravitational constant, $\vec{r}$ is the position of the particle, and $\vec{r}_1$ and $\vec{r}_2$ the positions of the two stars, respectively, which are fixed in the chosen reference frame. The angular momentum $\vec{\Omega}$ is given by

$$\vec{\Omega} = \vec{n}\sqrt{\frac{GM_1}{a^3(M_1 + M_2)}} \quad , \tag{1.12}$$

where $\vec{n}$ is the normal vector to the orbital plane of the binary and a is the binary separation, i.e., the distance $|\vec{r}_2 - \vec{r}_1|$ between the two stars. It is convenient for the calculation of the Roche potential to substitute the mass ratio $q = M_1/M_2$, to normalize the distances to the binary separation, i.e., $a = 1$, and to put the origin of the reference frame in M_1, i.e., $\vec{r}_1 = \vec{0}$. In that way the Roche potential depends on the mass ratio q only.

The Roche potential for a mass ratio of $q = 0.8$ together with its five Lagrangian points, L_i, is illustrated in Fig. 1.6 (left). At these points the potential has its extrema, i.e., the force acting on a particle is zero, which is the result of a balance between the different terms in Eq. (1.11) as follows:

L_1: At the first Lagrangian point the gravitational forces of the two stars cancel. Consequently, it is located on the connection line between M_1 and M_2, but due to the centrifugal term of Eq. (1.11) its exact location has to be calculated numerically. For $0.06 < q < 1$ the position x_{L1} is approximately given by (see Appendix B)

$$x_{L1}(q) \approx 0.509 \times (q + 0.048)^{-0.182} \tag{1.13}$$

in units of the binary separation. As can be seen from Figure 1.6 (left) L_1 is a saddle point and a particle, which is at rest in this point, is stable for perturbations perpendicular to the connecting line between both stars.

L_2 and L_3: At these Lagrangian points the centrifugal force cancels the summed gravitational forces of both stars. Thus, they are located behind the stars as seen from the center of mass. The value of the potential is higher than at the position of L_1. Any perturbation destabilized a particle at rest.

L_4 and L_5: These Lagrangian points are global maxima of the Roche potential an, thus, unstable positions as well. Here, the centrifugal force is in balance with an imaginary object at the center of mass, which is the result of the sum of the position vectors and masses of both stars.

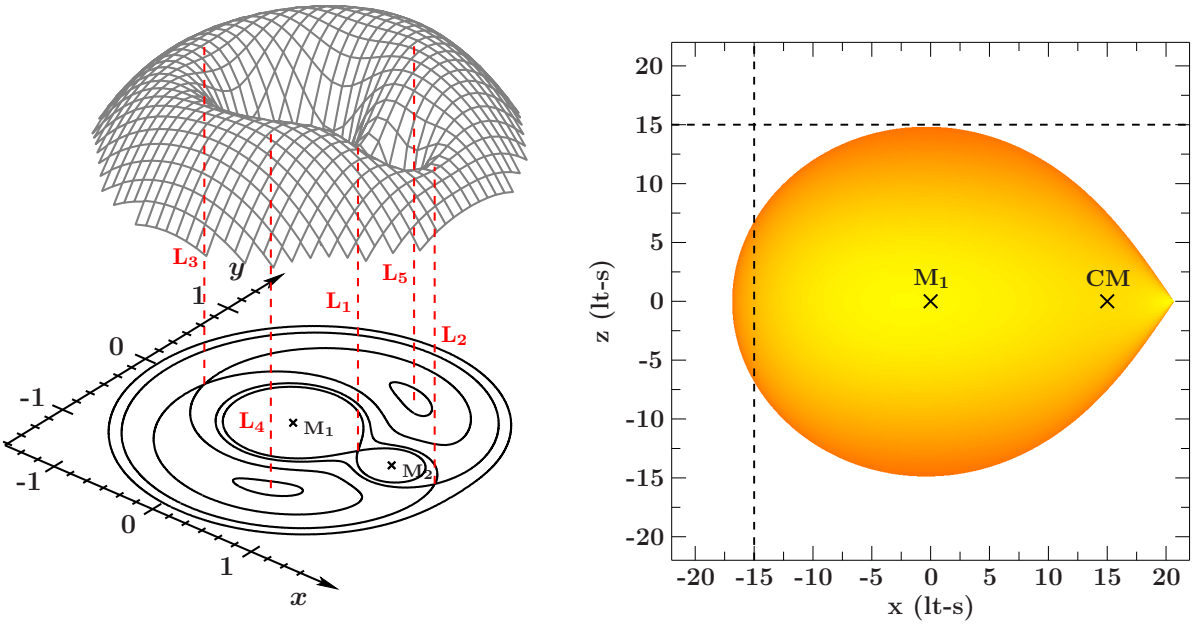

Figure 1.6: Left: the Roche-potential after Eq. (1.11) and definition of the reference frame. The orbital motion of the stars takes place in the xy-plane. The potential is calculated for a mass ratio q of 0.8 and drawn as the surface in z-direction in arbitrary units, while contour lines are drawn in the xy-plane. The red, dashed lines connect the positions of the Lagrangian points (L_1 to L_5) in the xy-plane to their potential value. **Right:** the surface of the primary star for the same mass ratio as before, assuming that it fills its Roche lobe and that it orbits the center of mass (CM) at a distance of 15 lt-s. The binary is seen from the side, i.e., in y-direction. The color represents the surface's angle to the observer from edge-on (orange) to face-on (yellow). The dashed lines are at a distance of 15 lt-s from the star's center to show its elongation relative to the z-direction, i.e., perpendicular to the orbital plane.

The most important Lagrangian point for accretion physics is L_1. The value of the potential at this points defines the critical potential, i.e., the minimum energy required, such that a particle is no longer bound by either M_1 or M_2 alone, but is still bound to the binary. The equipotential surface corresponding to the critical potential forms an "hourglass", or an "eight" in the contour representation, of the Roche potential (see Fig. 1.6, left). The volume enclosed by the critical potential around one of the two stars is called its Roche lobe. Material ejected by the optical companion, e.g., in form of a stellar wind, can be transferred via L_1 onto the compact object, which then leads to mass accretion. Once the optical star starts to evolve during its lifetime and expands, e.g., when helium is ignited in the core, or the orbit shrinks due to loss of angular momentum, the star eventually will fill its Roche lobe. Consequently, mass transfer directly from the surface of the star through L_1 onto the compact object is possible, which is called Roche lobe overflow. The star is approximately "tear-shaped" as shown in Fig. 1.6 (right). Due to the centrifugal term in Eq. (1.11) the star is elongated relative to the orbit's normal vector, which defines the z-direction in the chosen reference frame.

Which type of mass transfer occurs in an X-ray binary, e.g., directly from the companion's surface or from a stellar wind as mentioned above, depends on the parameters of the companion. In particular, the systems are classified after the mass of the companion. In a so-called low mass X-ray binary (LMXB) the companion star typically has a mass of $\lesssim 2\,M_\odot$ and for a higher mass around $\gtrsim 8$–$10\,M_\odot$ (Mészáros, 1992, and references therein), such as for an O- or B-type star, the system is classified as a high mass X-ray binary (HMXB). This basically determines the mass transfer mechanism, although a mixture of all mechanisms, which I will discuss in the next Sections, is possible. So far three mechanisms

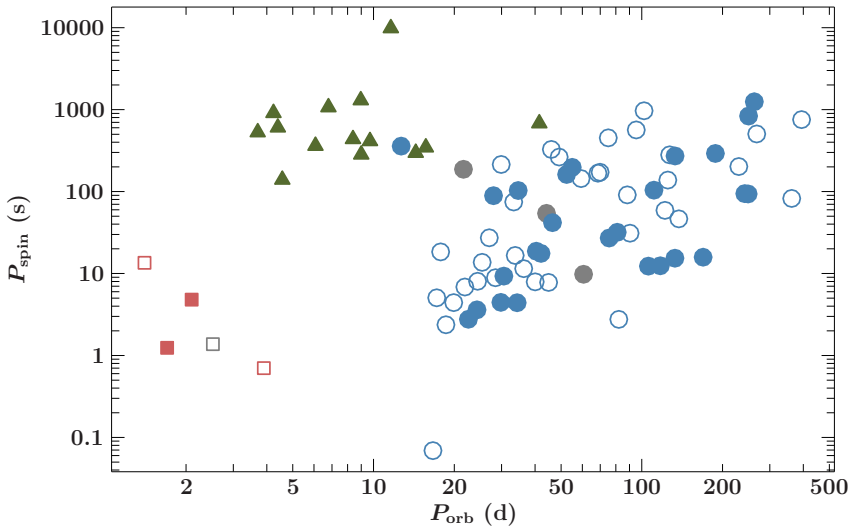

Figure 1.7: Corbet's diagram (values by R. H. D. Corbet, priv. comm.). The relation between the orbital period, $P_{\rm orb}$, and the spin period, $P_{\rm spin}$, in a neutron star X-ray binary shows three distinct regions: the blue circles mark Be X-ray binaries, the green triangles wind-fed systems, and the red squares disk-fed systems. Sources with unconfirmed mass accretion process are shown in gray. Filled symbols are sources in the Milky Way, the other ones are located in the SMC, LMC, or in case of the gray disk-fed system in M82.

are proposed, which classifies the X-ray binary further: accretion from a disk (Sect. 1.2.2), the stellar wind (1.2.3), or from the Be-disk of the optical companion (1.2.4), which is the dominant process of the majority of sources in this thesis.

In 1986, R. H. D. Corbet discovered a remarkable connection between these three accretion mechanisms and the orbital-, $P_{\rm orb}$, and spin period, $P_{\rm spin}$, of the neutron star (see Fig. 1.7). He found that X-ray binaries accreting via the same mechanism occupy distinct regions in the $P_{\rm orb}$-$P_{\rm spin}$-plane. According to Waters & van Kerkwijk (1989) this relationship for HMXBs can be explained by the equilibrium spin period (see Sect. 1.3.1 for details), whereas in the LMXB case Corbet (1986) discussed a synchronizing effect caused by torques. For systems where either the orbital period or the spin period is not known, the Corbet diagram can be used to identify the likely accretion mechanisms or to search for the optical companion (see Sect. 4.3 for an example).

1.2.1 Orbital Motion

In general, however, the orbit of many XRBs is non-circular. To calculate the Roche potential in these systems to, e.g., perform simulations of the mass transfer between both stars, their positions have to be known for any given time. The star's trajectory within the gravitational potential of a second star is an ellipse focused at the center of mass as we know from Kepler's first law (Kepler, 1609)[6]. To solve the position as a function of time we have to parameterize the ellipse, i.e., the orbit and define the following six orbital parameters[7] (see, e.g., Hilditch, 2001):

[6]In Kepler's publication of 1609 he derived similar laws for the motion of Mars. His generalized first law, which applies to all planets, and the modern version of his second law have been published 1621.

[7]Formally, a further parameter is needed to describe the orientation of the orbit in 3D, which is the angle Ω measuring the rotation of the orbit around the normal to the TP (see, e.g., Hilditch, 2001). This angle, however, can not be determined by any observation.

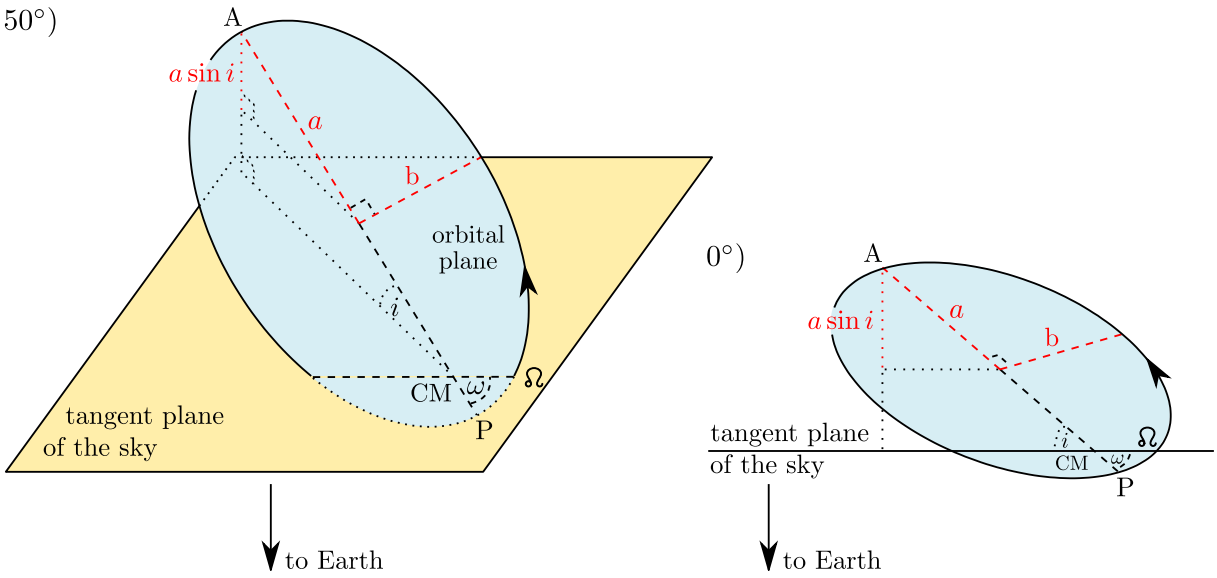

Figure 1.8: Sketch of an orbit of a neutron star around the center of mass (CM) of the binary system. The orbit is shown twice for two different viewing angles onto the tangent plane (TP; drawn in yellow) of the sky (50°, left; 0°, right). Both views have been calculated in full 3D. Dashed lines are located within the orbital plane (drawn in blue). The observer is looking from below the TP onto the binary. For the definition of the orbital parameters and further explanation see the text.

P_{orb}	orbital period, which is the time it takes for one full orbit
a	semi-major axis of the ellipse
e	eccentricity $1 - b/a$ where b is the semi-minor axis
i	inclination of the orbital plane to the tangent plane of the sky (TP)
τ	time of periastron (P) when both bodies are closest to each other
ω	longitude of periastron, i.e., the angle between the ascending node (Ω) and periastron (P)

From the above definition it is clear that the eccentricity is $0 \leq e < 1$ always. Otherwise no closed orbital trajectory exists. Figure 1.8 illustrates the orientation and definition of the orbit (in this example $i = 30°$ and $\omega = 60°$). The observer (the Earth) is located below the tangent plane, TP, of the sky, which is defined as the plane perpendicular to the line of sight and through the center of mass (CM). Furthermore, CM is equal to the focal point of the orbit close to the periastron (P) and set as the origin of the reference frame. The ascending node (Ω) is the point where the neutron star, which is moving counter clockwise, is located within the TP and is moving away from Earth. Here, its velocity projected on the direction to the observer is at maximum. The longitude of periastron, ω, is the angle between P and Ω and, thus, measured within the orbital plane (that's why the arch marking ω is a dashed line in Fig. 1.8). Consequently, ω rotates the orbit around the normal to the orbital plane and the CM. Its value is undefined for an inclination of $i = 0$ since no ascending node exists anymore (which is equivalent to that all points on the orbit are ascending nodes). Furthermore, in case of a circular orbit, i.e., $a = b$ and $e = 0$, we cannot find a value for ω as well because no periastron exists. For $\omega < 0$ the periastron is located below the TP, while the apastron (A) is above. If i is unknown for a particular system, the orbit is often shown assuming $i = 90°$ and that the observer is located in negative y-direction (the 0°-case on the right of Fig. 1.8). By analyzing, e.g., the Doppler shift of the neutron star's pulse period (see below), one cannot measure the inclination i and the semi-major axis a, but the combination of both which is the projected semi-major axis $a \sin i$ as indicated in Fig. 1.8. As a final remark on this Figure, the camera is looking

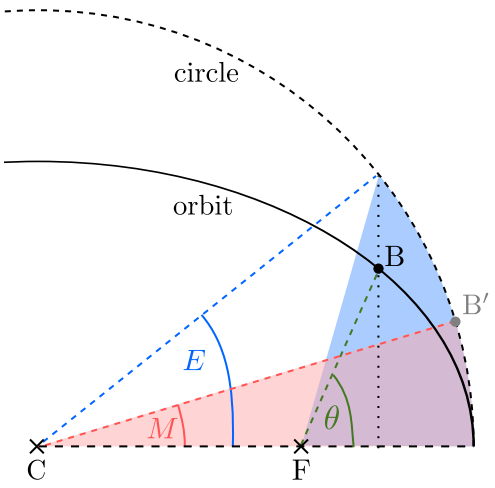

Figure 1.9: A body (B) is on an elliptical orbit around a mass located in the focus (F) of the ellipse. Its position angle with respect to the center of the circle is the eccentric anomaly E and with respect to the focus its true anomaly θ. To calculate θ the body is assumed to be on a circular orbit (B′) with the corresponding position angle M, the mean anomaly, with respect to the circle's center. The shaded regions (red and blue) are of equal area.

almost perpendicular onto the orbital plane on the left sketch (20° inclination), which means that the apparent value for ω is close to its real value of 60°. In contrast, the angles ω and i seem to be equal on the right sketch, which is, however, a projection effect of the 3D-view as one can see from the distortion of the right angle between a and b.

Kepler has realized that the equation of motion of a body on an eccentric orbit, which is an ellipse after his first law, cannot be solved algebraically. He was able, however, to derive an alternative description of the equation of motion based on his second law: the amount of time needed for the body to move between two points on the ellipse is proportional to the area swept out during the motion. That means that the ratio between the time and the area is a constant and, thus, independent of the eccentricity. In particular, this applies to a circular orbit as well, which is the idea behind his solution: *assuming* a circular orbit, calculate the position of the body and, finally, *correct* for the eccentricity of the real orbit.

Figure 1.9 illustrates this idea and defines the needed geometrical parameters. In the case of a circular orbit the position angle of the imaginary body B′ with respect to the circles center is called the mean anomaly, M, which is simply calculated by

$$M = \frac{2\pi(t-\tau)}{P_{\mathrm{orb}}} \quad , \tag{1.14}$$

where t is the time of interest. Now the real position of the body B on its orbit is constructed such that the areas swept by both bodies B and B′ in equal times are equal. This are the blue and red areas shown in Fig. 1.9. To calculate the true position angle, called the true anomaly θ, of the body B with respect to the focus of the ellipse, Kepler had to introduce the position angle E, which he named the eccentric anomaly and is measured from the center of the ellipse. The relation between E and the known M is the famous Kepler equation (1609; 1621),

$$M = E - e\sin E \quad . \tag{1.15}$$

This is a transcendental equation, i.e., it cannot be solved to E algebraically, but can be solved iteratively to any order. After having found the eccentric anomaly E one can finally calculate the true position on the ellipse in the polar coordinates θ, the true anomaly, and r, the radius,

$$\begin{aligned} \theta &= 2\arctan\left(\sqrt{\frac{1+e}{1-e}}\tan\frac{E}{2}\right) \quad , \\ r &= a(1-e\cos E) \quad . \end{aligned} \tag{1.16}$$

In the case of a circular orbit, $e = 0$, Eq. (1.15) results in $M = E$ and, consequently, $\theta = M$ after Eq. (1.16). Furthermore, for $e = 1$ no solution for the true anomaly exists,

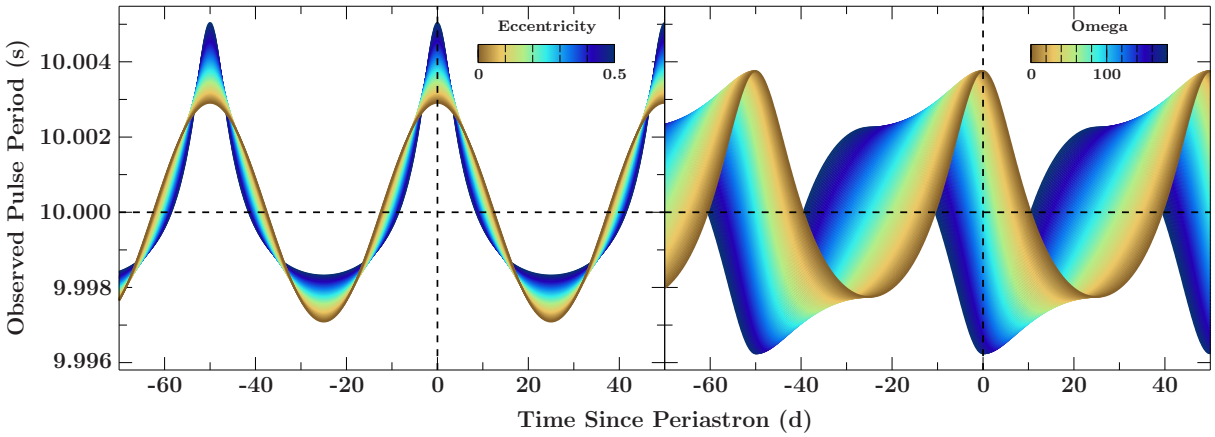

Figure 1.10: Observed pulse period as predicted by Eq. (1.17) for an artificial X-ray binary. The horizontal dashed line represents the assumed constant spin period of the neutron star, P, of 10 s. The vertical dashed lines mark the times of periastron passage. On the left the effect of different eccentricities as indicated by the color is shown, while on the right the effect of different longitudes of periastron, ω, is shown.

which corresponds to an unbound orbit. At the time of the periastron passage, $t = \tau$, we find $\theta = 0$. Finally, one notices that the longitude of periastron, ω, and inclination, i, are not needed in any of the above calculations. This is due to the fact that these parameters depend on the direction to the observer and are needed in the following.

Doppler shifted pulse period

In X-ray binaries, where the compact object is an accreting neutron star with a strong magnetic field, the apparent pulsations in the light curve can be studied to derive the orbital parameters of the binary as defined above. The pulse period, P, is modified by the motion of the neutron star along its orbit by the Doppler shift (Doppler, 1843)[8], which depends on the projected velocity, v, of the neutron star in direction to the observer. Thus, the observed pulse period, $P_{\rm obs}$, is given by (see, e.g., Hilditch, 2001)

$$P_{\rm obs}(t) = P(t)\left(1 + \frac{v(t)}{c}\right) \quad . \tag{1.17}$$

Here, it is assumed that $v(t) \ll c$ since neutron stars in X-ray binaries move non-relativistically on their orbits. For $v(t) > 0$ the neutron star is moving away from the observer. From the position vector of the neutron star on its orbit (Eqs. 1.16), calculated by solving Kepler's equation (Eq. 1.15), and projected in direction to the observer one obtains for the projected velocity (also known as the radial velocity as in, e.g., Hilditch, 2001)

$$v(t) = \frac{2\pi a \sin i}{P_{\rm orb}\sqrt{1-e^2}}\left(\cos(\theta+\omega) + e\cos\omega\right) \quad . \tag{1.18}$$

Note that for a stationary orbit the only time-dependency in this equation is the true anomaly θ.

Deriving the orbital parameters from an observed pulse period evolution is one of the main subjects of the present thesis (Chapter 4). Fitting the data to Eq. (1.17) is further complicated, however, once the intrinsic spin period, $P(t)$, is changing significantly over time (what causes these changes is given in Sect. 1.3.1). To prevent the fit-algorithm to

[8] In Doppler's subsequent works (e.g., Doppler, 1852) he referred to his publication as printed by "Prag bei Borrosch und André" in 1842.

find unphysical parameters or to zero in on a local minimum of the χ^2-landscape (see Sect. 2.1 for some details) it is, thus, important to provide good starting values for the orbital parameters. In fact, by just *looking* on the observed pulse period evolution we can already nail down possible parameter ranges.

Figure 1.10 illustrates an example of an observed pulse period evolution assuming an intrinsic constant spin period of $P = 10\,\mathrm{s}$. Here, different values for the eccentricity, e, and the longitude of periastron, ω, are indicated by another color. A periodic modulation of the observed period evolution is apparent, which represents the orbital period of $P_{\mathrm{orb}} = 50\,\mathrm{d}$. This is a consequence from the calculation of the mean anomaly (Eq. 1.14), where P_{orb} basically scales the modulation in time-direction. The amplitude of the modulation is not strongly affected by e nor ω. From Eqs. (1.17) and (1.18) we see that the projected semi-major axis, $a \sin i$, drives the strength of the amplitude ΔP (which we define here as the the difference between the maximum and minimum observed pulse period). A rule of thumb to estimate starting parameters for $a \sin i$ is (see Appendix C)

$$a \sin i \approx 7\,\mathrm{lt\text{-}s} \left(\frac{\Delta P}{0.001\,\mathrm{s}}\right) \left(\frac{P_{\mathrm{orb}}}{1\,\mathrm{d}}\right) \left(\frac{1\,\mathrm{s}}{P}\right) \quad . \tag{1.19}$$

From the Figure we get $\Delta P \sim 6\,\mathrm{ms}$ and, thus, derive $a \sin i \sim 210\,\mathrm{lt\text{-}s}$, which is very close to the assumed value of 200 lt-s. To get an estimate for the eccentricity we can compare the "width" of the visible extrema, i.e., the maximum and minimum of the pulse period evolution. With increasing eccentricity one extremum gets narrower while the other one gets wider (see Fig. 1.10, left). As a first guess the eccentricity is probably not larger than 0.2 if the extrema seem to be equal in width. Note that for the largest value of 0.5 shown here the peak of the evolution is very narrow already (less than 10 d FWHM, i.e., 20% of P_{orb}). As can be seen from Fig. 1.10 (right; $e = 0.25$ here) the extrema move by half the orbital period with changing longitude of periastron, ω. However, after Eq. (1.14) the time of periastron passage, τ, also leads to a shift of the extrema in time. Thus, a parameter degeneracy exists between both parameters, which is most tight once the orbit is nearly circular. In this case it is convenient to parametrize the orbit in a different way, which is given in the next paragraph. However, in case of an eccentric orbit, the extrema switch their shape depending on ω, i.e., the maximum is the narrow extremum for $\omega = 0°$, while its the wide one for $\omega = 180°$. From this we can we can get a hint for the range of ω. Furthermore, ω is the angle to the ascending node (compare Fig. 1.8), where the projected velocity in direction of the line of sight is at its maximum. Consequently, so does the pulse period since it is most red-shifted (see Fig. 1.10). From Eq. (1.18) we see that $\theta + \omega$ has to be zero at the position of the ascending node, from which we can get a range for the time of periastron passage. In the end, from the shape and time, t_{max}, of the observed maximum we can derive simple estimates for the longitude and time of periastron:

narrow peak	$\Rightarrow -45° < \omega < +45°$	$, -1/8 < (\tau - t_{\mathrm{max}})/P_{\mathrm{orb}} < +1/8$
wide peak	$\Rightarrow +135° < \omega < +225°\ (= -135°)$	$, +3/8 < (\tau - t_{\mathrm{max}})/P_{\mathrm{orb}} < +5/8$
right side steeper	$\Rightarrow +45° < \omega < +135°$	$, +1/8 < (\tau - t_{\mathrm{max}})/P_{\mathrm{orb}} < +3/8$
left side steeper	$\Rightarrow +225° < \omega < +315°\ (= -45°)$	$, +5/8 < (\tau - t_{\mathrm{max}})/P_{\mathrm{orb}} < +7/8$

Note that depending on the data coverage the parameter ranges might be enlarged. Furthermore, it is recommended to use a wider parameter range for τ since its estimate depends on, P_{orb} which itself is an estimate at the first place. Finally, the maximum observed radial velocity after Eq. (1.18) depends on the eccentricity as well, which introduces further systematic shifts.

Nearly circular orbits

In case of nearly circular orbits, where $e \lesssim 0.05$ (Andersen, 1983), ω and τ are statistically degenerate, i.e., correlated, since both lead to a shift of the observed maximum pulse period in time (see above). Sterne (1941) solved this problem by expanding the radial velocity as defined by Eq. (1.18) in a Fourier series due to its periodic nature. Furthermore, he chose the mean longitude,

$$l = \omega + M = \frac{2\pi(t - T_\eta)}{P_{\mathrm{orb}}} + \eta \quad , \tag{1.20}$$

as a reference for the orbit. Originally, Sterne set $\eta = 0$ such that at the time of a mean longitude of 0°, $t = T_\eta \equiv T_0$, the neutron star is at the position of the ascending node and the observed pulse period is, thus, at its maximum. In the approximation of the radial velocity below, it is, however, more convenient to set $\eta = \pi/2$, which implies that at the time of a mean longitude of 90°, $t = T_\eta \equiv T_{\pi/2}$, the neutron star is farthest away from the observer. At this time the Doppler shift of orbital motion vanishes, but this point is no longer distinct in the observed pulse period for eccentric orbits. This can be seen from Fig. 1.10, where the horizontal dashed line corresponds to the intrinsic spin period. The mean longitudes $l = \pi/2$ and $l = -\pi/2$ are at the intersections of this line with the observed pulse period. For a circular orbit (brownish curve on the left) these points are at exactly half of the apparent pulse period amplitude, which is no longer the case[9] for $e > 0$ (see brownish curve on the right).

Solving for the Fourier coefficients then leads to (see, e.g., Hilditch, 2001, and references therein)

$$v(t) = \frac{2\pi a \sin i}{P_{\mathrm{orb}}} \left(\cos l + g \sin 2l + h \cos 2l\right) \tag{1.21}$$

for the radial velocity with $g = e \sin\omega$ and $h = e \cos\omega$. To conclude, the orbital parameters e, ω, and τ have been replaced by g, h, and $T_{\pi/2}$. The time of periastron passage, τ, is no longer defined properly for nearly circular orbits.

Implications

From the known orbital parameters of an X-ray binary one can derive the so-called mass function, f, of the system (see, e.g., Hilditch, 2001)

$$f(M) = \frac{(M_{\mathrm{opt}} \sin i)^3}{(M_{\mathrm{x}} + M_{\mathrm{opt}})^2} = \frac{4\pi^2}{G} \frac{(a \sin i)^3}{P_{\mathrm{orb}}^2} = 1.0735 \times 10^{-3}\,\mathrm{M}_\odot \left(\frac{a \sin i}{1\,\mathrm{lt\text{-}s}}\right)^3 \left(\frac{1\,\mathrm{d}}{P_{\mathrm{orb}}}\right)^2 \tag{1.22}$$

Knowing the mass of the optical companion, M_{opt}, from, e.g., an analysis of its optical spectrum, one can derive the mass M_{x} of the neutron star (or an upper limit if the inclination i is unknown). This is an important measure for investigating the Equation of State of neutron stars as explained in Sect. 1.1.3. On the other hand, assuming the canonical neutron star mass of $M_{\mathrm{x}} = 1.4\,\mathrm{M}_\odot$ (see Table 1.1) and knowing the mass of the companion the orbital inclination, i, can be estimated.

[9] However, as the approximation is only valid for nearly circular orbits the time $T_{\pi/2}$ is still near the time of half the orbital amplitude.

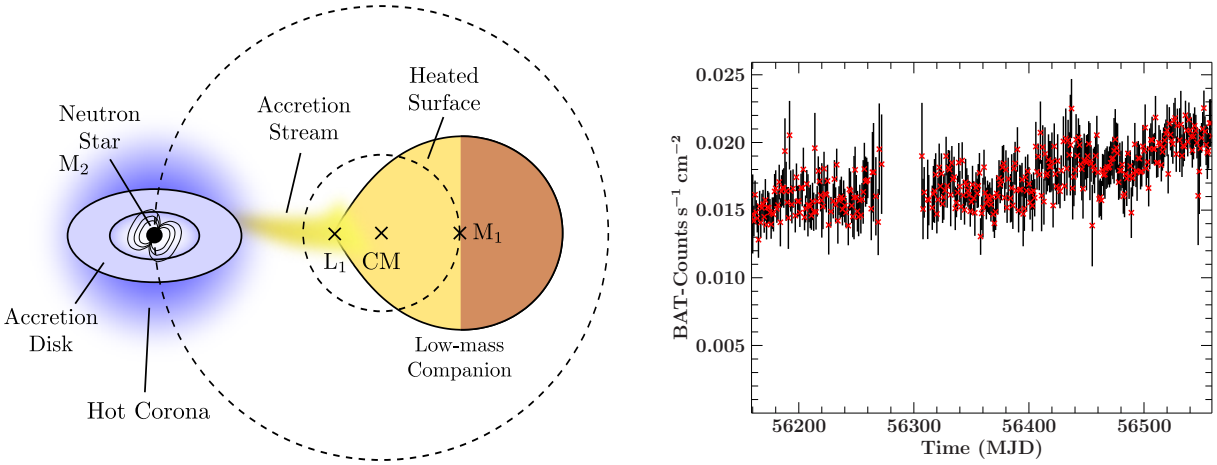

Figure 1.11: Left: schematic sketch of a low mass X-ray binary. The neutron star (M_2) and its companion (M_1) are on a circular orbit around their common center of mass (CM). The companion fills its Roche lobe, which results in an accretion stream through L_1 onto the compact object. An accretion disk forms, which is truncated near the neutron star due to its strong magnetic field. The X-rays produced by the final accretion process irradiates half of the companions surface, which heats up its atmosphere, and the accretion disk, which results in a hot corona. **Right:** in the *Swift*-BAT light curve of the LMXB Ginga 1826−238 the detected flux increases smoothly by a few 10% within a year. Around MJD 56300 the source was near the Sun as seen from the *Swift*-satellite, which results in a gap in the light curve.

1.2.2 Disk Accretion

Now that the orbits in X-ray binaries are explained we can concentrate on the consequences of different orbits and companions for the observed behavior. In most LMXBs Roche lobe overflow occurs, i.e., the optical low-mass companion star fills its Roche lobe as explained above. Thus, the orbit of the binary has to be close, which is a challenging task in binary evolution if one considers that the compact object is the product of a supernova explosion *and* the binary is still gravitationally bound. A possible evolutionary scenario, as described in Hilditch (2001), includes a common-envelope phase. The envelope of the more-massive star, a supergiant, is expanding beyond the binary separation. Thus, both stars are orbiting each other within a common envelope. Due to friction the orbital period gets much shorter and, as soon as the more massive star went supernova, a neutron star is left behind in a close orbit around a low-mass star.

Due to conservation of angular momentum of the material within the accretion stream an accretion disk forms around the neutron star. Due to viscous friction, shocks, or inelastic scattering angular momentum can be transfered within the disk, which leads to an inspiral of the matter onto the compact object as well as to a disk wind. This outflow of matter is heated by the X-ray source, which results in a hot corona in the vicinity of the accretion disk (Dove et al., 1997; Begelman & McKee, 1983). However, Miller & Stone (2000) concluded from three dimensional MHD simulations that the thermal energy needed to produce a hot corona can evolve from magnetic structures inside of a turbulent accretion disk.

The inner most stable orbit in the accretion disk is mainly driven by the properties of the neutron star, i.e., its spin period and magnetic field. The coupling of the material onto the field lines is described in Sect. 1.3.1. Furthermore, the temperature of the disk increases as the material moves inwards, leading to a strong temperature gradient compared to the outer boundary of the disk. This boundary is determined by the tidal forces of the companion star. By numerical simulations Paczyński (1977) has shown that the outer

edge of accretion disks can be up to ∼60% of the Roche radius of the compact object.

Knowing the disk-size one can estimate the so-called viscous timescale, $t_{\rm vis}$, for matter in the disk being accreted by the neutron star (Frank et al., 2002; Kato et al., 2008, see, e.g.,),

$$t_{\rm vis} = \alpha^{-1} \left(\frac{r}{H}\right)^2 \frac{1}{\Omega_{\rm K}} \quad , \tag{1.23}$$

where $\alpha \leq 1$ is the viscosity parameter by Shakura & Sunyaev (1973), which characterizes the efficiency of angular momentum transport, r is the distance to the neutron star, H the vertical height of the disk at r, and $\Omega_{\rm K} = (GM_{\rm x}/r^3)^{1/2}$ with $M_{\rm x}$ the mass of the neutron star. For typical values the viscous timescale is in the order of days to weeks (Frank et al., 2002). Since the mass transfer rate in many observed LMXBs vary on timescales much longer than $t_{\rm vis}$ the observed X-ray variability is in the order of weeks to years (compare to the light curve of Ginga 1826−238 as shown in Fig. 1.11, right).

The geometry of accretion disks around neutron stars show complex features, the most striking example is seen in Her X-1. In this system, X-ray radiation pressure or the mentioned coronal winds can induce torques on the disk, which results in a warped surface (Maloney & Begelman, 1997; Schandl & Meyer, 1994). Tidal forces of the companion's gravitation on the disk or freely precessing neutron stars can result in a precession of the disk (Ketsaris et al., 2000, and references therein). Furthermore, the accretion disk can be tilted with respect to the orbital plane due to the impact of the accretion stream onto the disk (Shakura et al., 1999).

The atmosphere of the companion is irradiated by X-rays. This reprocessing of X-rays results in an apparent increase in the optical flux of the system once the surface is seen by the observer (see, e.g., Gerend & Boynton, 1976, for an early discussion in Her X-1). Since this is a geometrical effect the observed optical flux shows a modulation with the orbital period, most prominent in systems where the orbit and stellar rotation is synchronized. In Her X-1 even optical pulsations near the ∼1.24 s pulse period of the neutron star have been discovered, which is evidence for a fast reprocessing of X-rays on the surface of the optical companion (see Kühnel, 2009, and references therein).

A summarizing sketch of a LMXB is shown in Fig. 1.11 (left).

1.2.3 Wind Accretion

In many HMXBs, the neutron star's companion is an OB-supergiant featuring a strong stellar wind with mass loss rates of in the order of 10^{-7}–$10^{-5}\,{\rm M}_\odot\,{\rm y}^{-1}$ (see Martínez-Núñez et al., 2016, for a recent review on stellar winds and wind-accreting XRBs). Since its mass is larger than $\sim 8\,{\rm M}_\odot$ (Mészáros, 1992, and references therein) it is expected to evolve rather quickly. Nevertheless, it is orbited by a neutron star, i.e., a supernova must have happened during the binary evolution: either the progenitor of the compact object was even more massive as its companion today, or the mass ratio has been inverted, i.e., a strong mass transfer between the two stars has occurred in the past. It turns out that the latter scenario is more consistent with evolutionary calculations (see, e.g., Hilditch, 2001, and references therein). Here, a massive star with more than $20\,{\rm M}_\odot$ expands and fills its Roche lobe in the red giant phase, which leads to mass transfer onto a companion star of about $\sim 10\,{\rm M}_\odot$ in mass (see Fig. 1.12). The mass transfer is very effective and transfers most of the giant's hydrogen onto the secondary, leaving a helium rich star behind. Thus, the mass ratio has been inverted and the former massive star explodes in a supernova first. The remaining neutron star starts to accrete from the stellar wind of its companion once it expands. Then the neutron star orbits its supergiant companion in a distance of a few stellar radii only, deeply embedded in its wind.

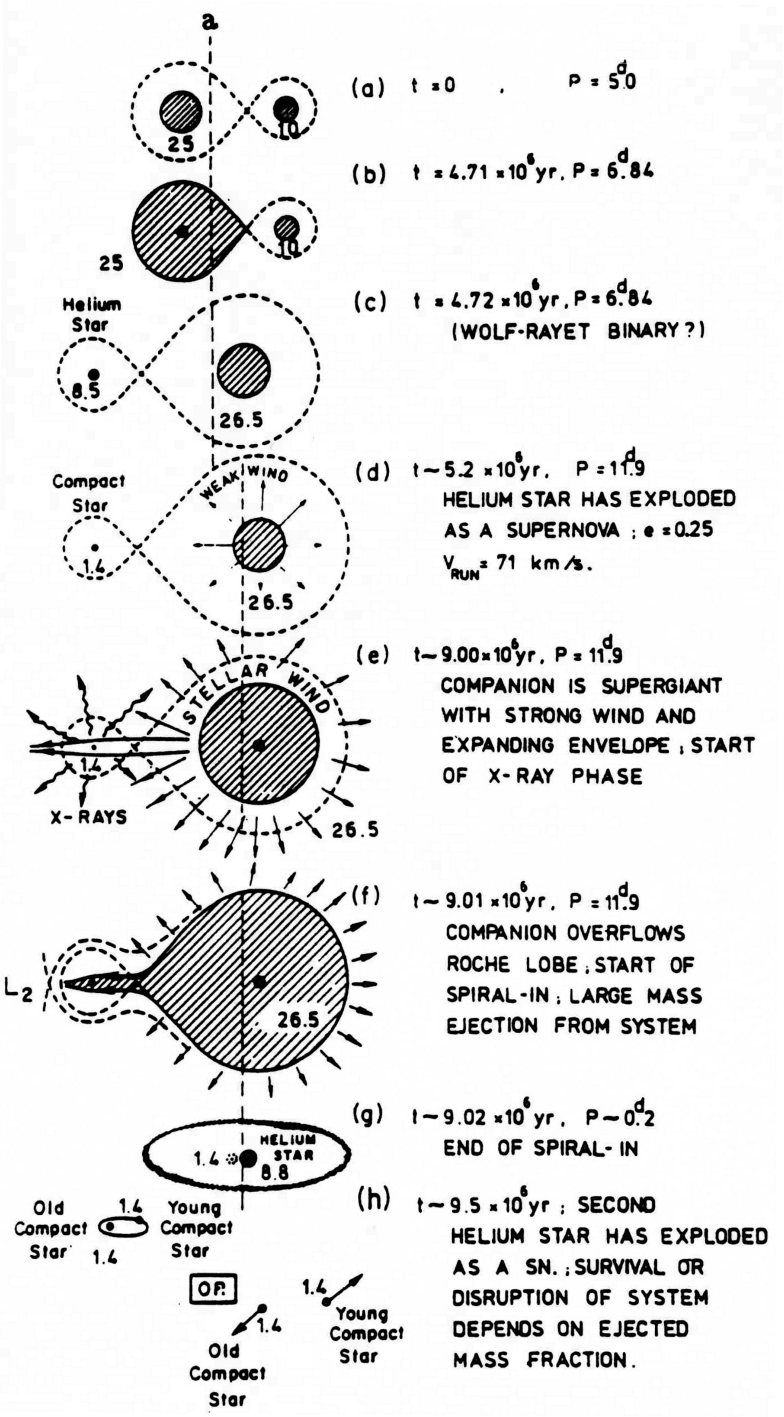

Figure 1.12: Evolutionary channel of a binary leading to a wind-accreting HMXB. The evolution is shown from the initial conditions on the top until both stars have become compact object on the bottom. A timescale as well as masses and orbital periods are provided (taken from van den Heuvel, 1983).

Due to the low angular momentum of the wind, it is unlikely that the material, which is accreted from the wind, forms an accretion disk around the neutron star (see, e.g., Petterson, 1978). As a consequence the matter distribution close to the compact object is more isotropic than in the disk-case, which leads to quasi-spherical accretion (Davidson & Ostriker, 1973). Following their approach one can calculate the so-called Bondi-Hoyle radius, $r_{\rm acc}$, to the neutron star (Bondi & Hoyle, 1944; Hoyle & Lyttleton, 1939), where the wind velocity equals the escape velocity from the compact object, i.e., material closer than $r_{\rm acc}$ gets accreted,

$$r_{\rm acc} = \frac{2GM_{\rm x}}{v_{\rm rel}^2} \quad . \tag{1.24}$$

Here, G is the gravitational constant, $M_{\rm x}$ is the neutron star's mass, and $v_{\rm rel}$ is the speed of the neutron star relative to the (homogeneous) wind given by

$$v_{\rm rel}^2 = v_{\rm x}^2(a) + v_{\rm w}^2(a,t) \quad , \tag{1.25}$$

with the wind velocity $v_{\rm w}$ and orbital velocity $v_{\rm x}$ of the neutron star, both at the binary separation a assuming a circular orbit. Usually, the orbital velocity is much smaller than the stellar wind velocity. Knowing the wind density ρ one can then derive the accretion rate $\dot{M}$ onto the neutron star,

$$\dot{M} = 4\pi\zeta\frac{(GM_{\rm x})^2}{v_{\rm rel}^3}\rho(a,t) \quad , \tag{1.26}$$

where $\zeta \lesssim 1$ is a numerical correction factor due to the finite cooling of the infalling gas and the radiation pressure. In a non-stationary case, the wind's velocity $v_{\rm w}$ and density ρ are both functions of time t. The resulting X-ray luminosity L is finally given by Eq. (1.5).

As wind-fed HMXBs usually do not feature an accretion disk the viscous time-scale (Eq. 1.23) vanishes and the accretion time scale is given by the free-fall time at $r_{\rm acc}$, which is on the order of a few hundred seconds (Frank et al., 2002). Thus, any changes in the wind velocity or density in Eq. (1.26) results in an almost immediate variation of the X-ray luminosity. This is indeed observed as in, e.g., 4U 1700−377 (see Fig. 1.13, right). In fact, the observed X-ray light curves are extremely variable such that the assumption of a homogeneous wind breaks down. Instead, it is believed that the wind is highly structured in form of "clumps", which was first proposed by Sako et al. (2003) who reviewed analyses of several wind-accreting XRBs. In particular, evidence for a clumpy wind has been seen, e.g., in Vela X-1 (Kreykenbohm et al., 2008; Fürst et al., 2010; Martínez-Núñez et al., 2014) and GX 301−2 (Fürst et al., 2011). Studying the time evolution of the X-ray flux and the X-ray spectra would, in principle, allow to derive clump masses and sizes. However, the physical processes leading to the formation of clumps is under discussion and, thus, deriving physical quantities of the wind is still uncertain (see Martínez-Núñez et al., 2016, for a discussion and references therein). Fürst et al. (2010) have measured that the photon flux of Vela X-1 as observed by *INTEGRAL* is log-normal distributed. By performing simulations they concluded that this result is nicely explained by a clumpy wind. In addition, some rare strong flares have been detected, which are expected from the distribution. As the accretion of clumps involves stochastic processes these sudden flares can occur during X-ray observation.

Clumping is not the only structure in a dense stellar-wind. As one might expect from Eq. (1.24) the wind in a region of radius $r_{\rm acc}$ around the neutron star is accreted and, thus, the wind-density decreases. However, since this radius is much smaller than the binary separation only a tiny fraction of the total wind of the companion is affected (Martínez-Núñez et al., 2016). More interestingly are structures caused by the X-ray

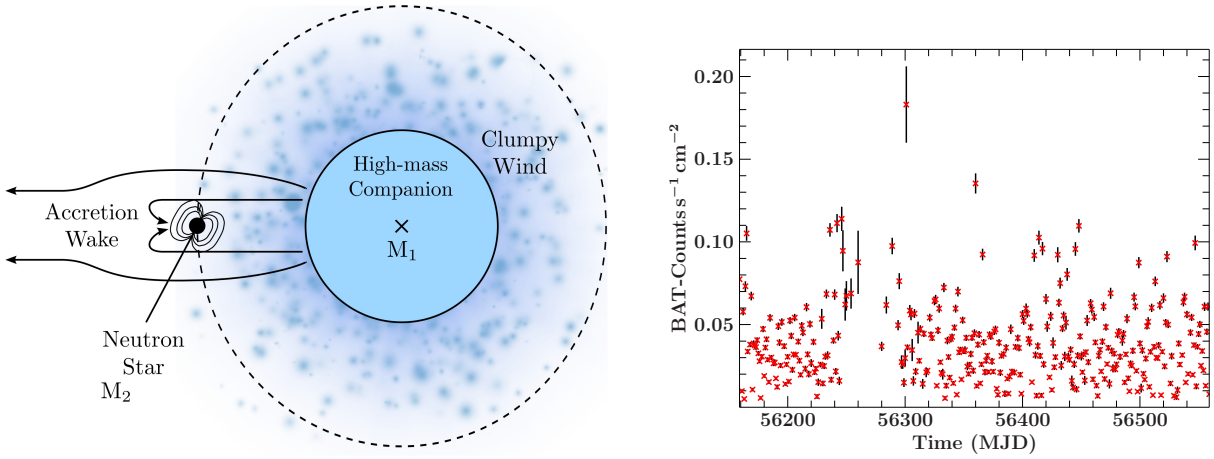

Figure 1.13: Left: schematic sketch of a high mass X-ray binary, where the neutron star (M_2) is orbiting a giant companion star (M_1), which features a strong and clumped stellar wind. The neutron star's orbit is within a few stellar radii, deeply embedded in the wind, which focuses the wind onto the compact object. This results into an accretion wake, i.e., differences in the wind's density and velocity profile in the vicinity of the neutron star. **Right:** the *Swift*-BAT light curve of the wind accreting HMXB 4U 1700−377 shows a strong variability of the X-ray flux on very short time-scales of minutes to days.

luminosity of the neutron star: if the mass accreting rate is high enough the resulting radiation is able to ionize the wind in the vicinity of the neutron star. Thus, photoelectrical absorption of optical photons on electrons bound to atoms of the wind is no longer possible. This process, however, is thought to be the main driving mechanism of the high wind velocities (see Puls et al., 2008, for a review). As a consequence, the wind slows down in a sphere of ionized material around the neutron star, which is known as the Strömgren sphere. At the boundaries of this sphere a bow shock forms where matter accumulates (see, e.g., Fransson & Fabian, 1980). In combination with the movement of the neutron star along its orbit leads to an elongated stream of enhanced density, which is known as the accretion wake (see, e.g., Blondin et al., 1990). Watanabe et al. (2006) found evidence for an accretion wake in Vela X-1 by studying Doppler shifts of X-ray emission line energies of several elements. To derive wind properties from the measurements detailed theoretical

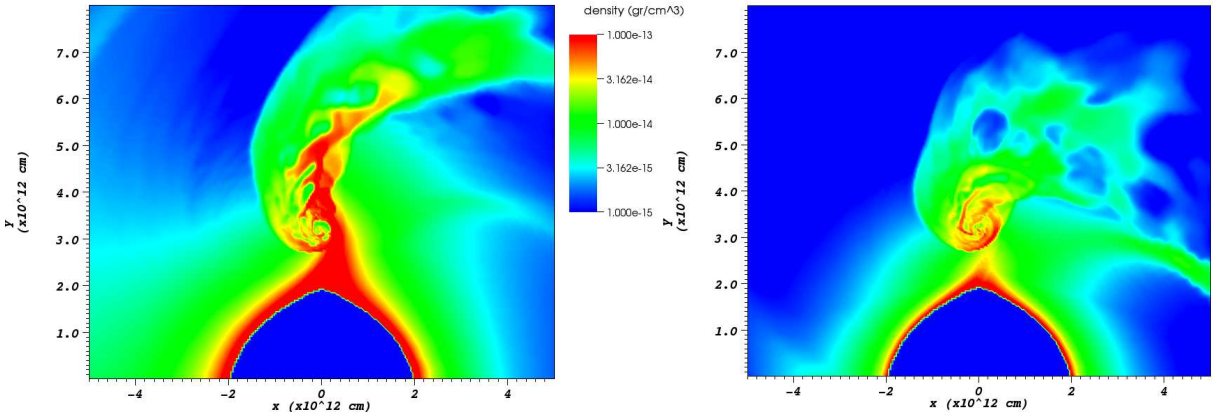

Figure 1.14: Hydrodynamic simulation of the stellar wind structure around a neutron star in a HMXB. A low mass-loss rate of the companion of $\dot{M}_\mathrm{w} \sim 2 \times 10^{-7}\,\mathrm{M}_\odot\,\mathrm{yr}^{-1}$ is assumed. **Left:** The accretion wake for a wind velocity of $500\,\mathrm{km\,s}^{-1}$ is dense and tilted **Right:** For higher velocities around $1200\,\mathrm{km\,s}^{-1}$ the accretion wake gets suppressed (both Figs. taken from Manousakis et al., 2012).

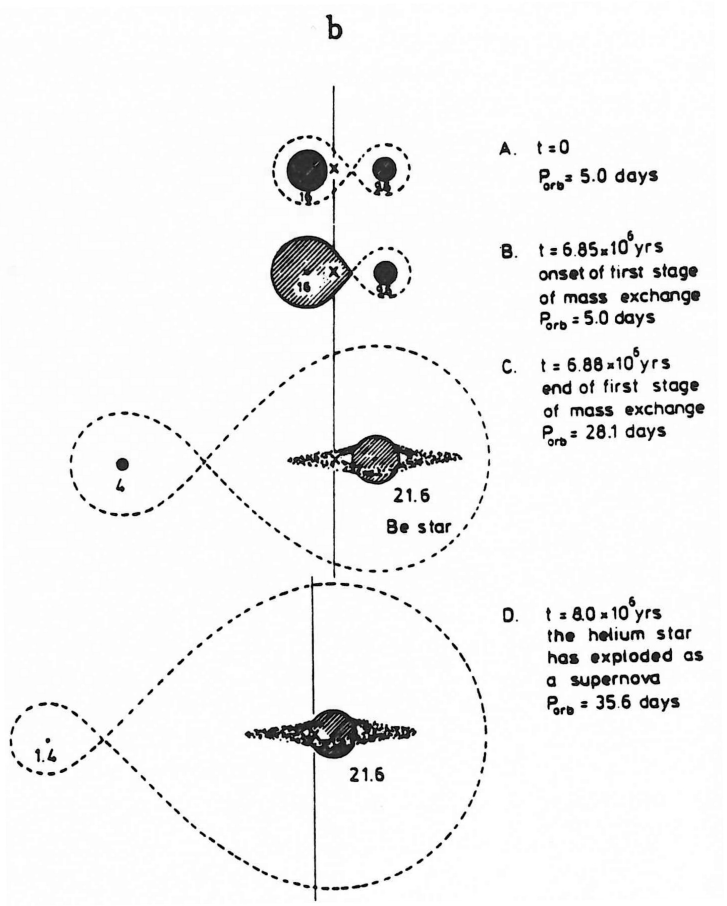

Figure 1.15: Evolutionary channel similar to Fig. 1.12 but for a BeXRB (taken from van den Heuvel, 1983).

studies are required first. Blondin et al. (1990, 1991) and recently Manousakis et al. (2012) performed complex MHD simulations of a homogeneous stellar wind interacting with the X-ray radiation within the Roche potential (Eq. 1.11) to reveal a detailed structure of the accretion wake (see Fig. 1.14 for an example).

A sketch of the above description of a HMXB is presented in Fig. 1.13 (left). As a final remark, a wider and eccentric orbit eventually leads to further structuring of the wind. As proposed by Leahy & Kostka (2008) based on observations of GX 302−1, a high-density stream originating from the companions surface might form, which follows the neutron star and, as it overtakes the compact object, results in an increase of the mass accretion rate.

1.2.4 Be phenomenon

The class of BeXRBs has been proposed in the 1970's to explain the transient nature of X-ray sources (Rappaport et al., 1978). Here, the companion star shows emission lines of hydrogen, most prominent in Hα. Since in most cases the companion is of type B, this subclass are the so-called Be X-ray binaries (BeXRBs), where the "e" indicates that emission lines are present in the optical spectrum. Their origin has to be irradiated hydrogen rich material in order to produce fluorescent emission. Furthermore, many Be stars show a double peaked emission line structure (see, e.g., Hanuschik, 1996). These observational facts can be explained by the presence of an equatorial disk around the optical companion star. What causes this disk (or torus, the "Be phenomenon" in general) is not entirely understood yet and possible explanations include (see Rivinius et al., 2013,

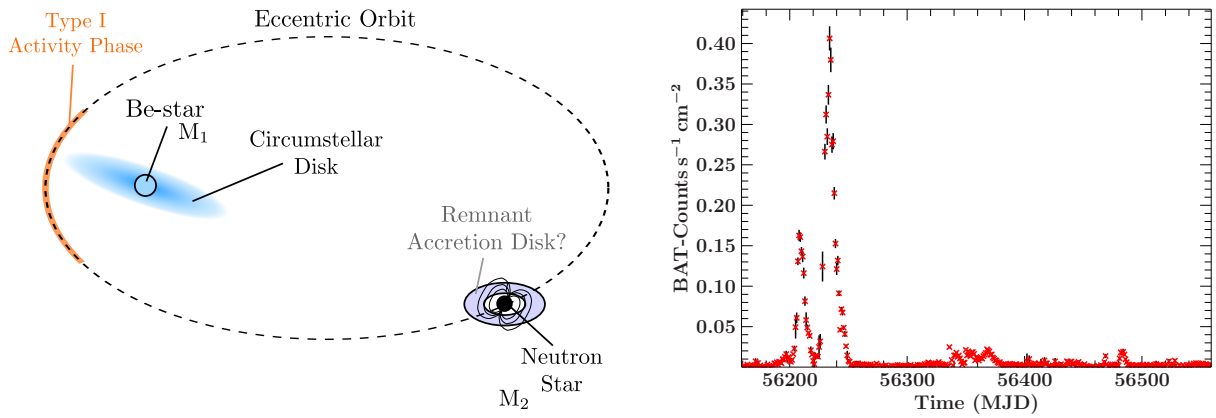

Figure 1.16: Left: schematic sketch of a Be X-ray binary. Here, the neutron star (M_2) is on an eccentric orbit around a Be-type companion (M_1), which features a circumstellar disk. The plane of the disk is probably misaligned to the orbital plane. Once the neutron star is close to the Be star, which is around the periastron, mass can be transfered from the disk onto the compact object, which leads to type I X-ray outbursts. Material which has not been accreted during the outburst might remain in a remnant accretion disk far away from the companion. **Right:** The *Swift*-BAT light curve of the BeXRB GX 304−1 shows two major outbursts between MJD 56200 and 56250. Their separation is much shorter than the orbital period of about 169 d indicated by the weak activities around MJD 56350 and 56480. Note that the peak flux is two times brighter than the Crab pulsar.

for a review and more details) a star with a rotational velocity close to its break-up leading to a viscous disk or stellar winds, which are compressed around the equator due to a higher angular momentum (compared to OB supergiants) or due to magnetic confinement.

The idea of a fast rotating star can be easily explained by mass transfer in a binary system (compare Fig. 1.15; see Pols et al., 1991, and references therein). Similar to the evolution of a classical HMXB (Sect. 1.2.3 and Fig. 1.12) the initially more massive star, but less than 20 $M_\odot$, transfers a large fraction of its mass onto a companion star (Rappaport & van den Heuvel, 1982). Thus, the mass ratio is inverted during the evolution as well. Due to angular momentum conservation the companion will spin-up and eventually reach rotational velocities sufficient for the formation of a Be disk. The former massive star, which probably became a helium star after the mass transfer, will undergo a supernova explosion leading to a binary containing a neutron and a Be star.

The stellar wind of a Be star is highly anisotropic. At its poles wind velocities are high but the density is low, while it is denser near the equator but much slower due to the presence of the disk (Poeckert & Marlborough, 1978; Lamers & Pauldrach, 1991). As a consequence, the accretion rate from the wind (Eq. 1.26) is strongly reduced compared to supergiant companions leading to low X-ray luminosities especially when the neutron star is far away from periastron. Usually, the X-ray source is below any detection limit, i.e., it is in a quiescent state. However, once the neutron star is close to periastron mass transfer from the Be disk by, e.g., Roche lobe overflow is possible. As a consequence, the mass accretion rate and, thus, the luminosity is increasing by orders of magnitude out of quiescence within days. This leads to a so-called type I X-ray outburst, which usually lasts around ∼2 weeks until the source has faded again, and resemble the transient nature of these sources.

Nearly all known BeXRBs show, however, much more complicated behavior in the X-rays than this simple picture suggests. In the majority of sources sporadic X-ray activity around the periastron is detected. Instead type II X-ray outbursts are observed, which

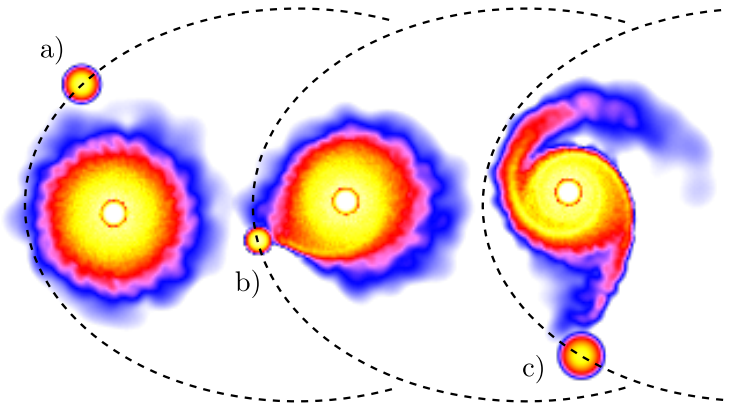

Figure 1.17: A hydrodynamical simulation of a BeXRB with a high eccentricity of 0.68 (like in GRO J1008−57, see Sect. 4.4) as performed by Okazaki et al. (2002). The particle density is shown from low (blue) to high (yellow). The white circle in the center of the Be-disk is the Be star itself. The neutron star is too small in this scale to be visible, but its accretion disk can be seen. **a:** Once the neutron star approaches periastron the Be-disk gets deformed. **b:** A tidal accretion stream forms which hits the neutron star around periastron. **c:** Density waves are excited in the disk, leading to a spiral structure after the neutron star has passed (images taken and modified from Okazaki-san's homepage[10]).

are not connected to any specific orbital phase and are usually brighter by an order of magnitude compared to type I outbursts (see, e.g., Finger & Prince, 1997). That is why these outbursts are often called "giant" outbursts. In fact, transient BeXRBs outbursts can be brighter than the Crab pulsar, making these systems the brightest X-ray sources the sky for for some time. In some systems, type II outbursts last longer than one orbital period, such as in 4U 0115+63 (see, e.g., Müller et al., 2010). Figure 1.16 shows a sketch of our (too) simple picture of BeXRBs (left) and the light curve of GX 304−1 (see Sect. 5.2) as an example of their X-ray behavior. This light curve also shows two successive outbursts, which are within one orbital period. These double peaked outbursts are extremely rare and, besides GX 304−1, have been observed in A 0535+26 as well (Caballero et al., 2013). Very recently, GRO J1008−57 has featured even three successive outbursts within one orbital period (see Sect. 5.1).

The occurence and absence of type I outbursts around the periastron have been theoretically investigated and explained by Okazaki & Negueruela (2001). These authors calculate the size of the Be disk under the influence of the neutron star's gravitational field. Depending on the orbital parameters, they conclude that the disk gets tidally truncated at specific resonance radii. If this radius is larger than the Roche radius of the companion (see Eq. 1.13) at the periastron[11] mass transfer by Roche lobe overflow occurs, which leads to a type I X-ray outburst. However, the disk radius in most systems is smaller than the Roche radius due to an effective tidal truncation by close orbits. Okazaki & Negueruela (2001) argue that regular type I outbursts should occur in systems with long orbital periods and high eccentricities only ($P_{\rm orb} \gtrsim 200\,{\rm d}$, $e \gtrsim 0.6$). As prototype examples for these systems they discuss the BeXRBs 2S 1835−024 ($P_{\rm orb} = 242.2\,{\rm d}$, $e = 0.88$; Finger et al., 1999) and GRO J1008−57 ($P_{\rm orb} = 249.48\,{\rm d}$, $e = 0.68$, see Fig. 1.17; Kühnel et al., 2013, and Sect. 4.4) and, in fact, predict regular periastron outbursts for GRO J1008−57 before they have been confirmed (Coe et al., 2007; Kühnel et al., 2013). There is, however, a third BeXRB known which shows regular outbursts, which is EXO 2030+375 but with moderate orbital parameters ($P_{\rm orb} = 46\,{\rm d}$, $e = 0.41$ Wilson et al., 2001). This behavior

[10] http://harmas.arc.hokkai-s-u.ac.jp/~okazaki/BeX/sim/index.html
[11] Note that for BeXRBs the Roche potential (Eq. 1.11) depends on time due to the eccentric orbit.

depends on further details of the system, such as the companion's spectral type or disk parameters. Furthermore, Okazaki & Negueruela (2001) argue that small differences in these parameters leads to significant different X-ray behaviors.

Explaining the occurrence of type II outbursts is much more challenging. From studying the Hα emission line in the optical spectra it is concluded that Be disks change their sizes and one-armed oscillations may form (see, e.g., Coe et al., 2007; Camero-Arranz et al., 2012). Recently, by theoretical work Okazaki et al. (2013) proposed inclined Be disks with respect to the orbital plane to be the origin of "giant" outbursts. The neutron star's gravitational field leads to a precessing of the disk similar to the accretion disk in LMXBs (compare Sect. 1.2.2). Thus, at some point the disk moves into the neutron star's orbit, which then can accrete from the disk directly, leading to strong X-ray outbursts. Following this idea, Moritani et al. (2013) found observational evidence for a precessing warped disk in A 0535+26. Whether this scenario applies to all BeXRBs, and whether it can also explain double- or multi-peaked outbursts is not clear yet. Especially, type II outbursts are yet impossible to predict.

From the simulations by Okazaki & Negueruela (2001) and Okazaki et al. (2013) one is in principle able to describe the observed outburst light curves. However, to do so the orbital parameters and, especially, the inclinations of the orbit and the Be disk have to be known. Furthermore, to connect the observed luminosity to the mass accretion rate a density of the Be disk has to be assumed. Due to the tidal truncation, however, their density is probably twice the density of isolated Be stars (Zamanov et al., 2001). The absolute disk densities or their mass distribution is, however, only marginally known[12] and on the order of $10^{11}\,\mathrm{g\,cm^{-3}}$. Another important results from theory is that the standard accretion disk scenario does not work for the observed type I outbursts. The viscous timescale (Eq. 1.23) is much longer than what is derived from the rapid rise of these outbursts (Okazaki et al., 2013). Instead, radiatively inefficient accretion flows (RIAF) are proposed with the accretion timescale

$$t_{\mathrm{acc}} \approx 2.0 \times 10^{-4} m_{1.4} c_1^{-1} \alpha_{0.1}^{-1} \hat{r}^{3/2}\,\mathrm{s} \quad . \tag{1.27}$$

Here $m_{1.4}$ is the neutron star's mass in units of $1.4\,\mathrm{M}_\odot$, $c_1 \approx 0.53$ is a numerical constant, α is the Shakura-Sunyaev's viscosity parameter (see Eq. 1.23) in units of 0.1, and $\hat{r}$ is the radius from the neutron star measured in Schwarzschild radii.

Nevertheless, the neutron star gravitationally drags material from the Be disk after the periastron passage as seen in these simulations. The Roche lobe overflow from the disk, however, has abated resulting in a low particle density and pressure. Thus, the magnetic pressure of the neutron star is able to stop the material from being accreted, which is called propeller effect and discussed in more detail in the next Sect. 1.3.1. Since the material is gravitationally bound to the neutron star it forms a disk around it, which is, however, trapped in a state of little to no accretion onto the neutron star (D'Angelo & Spruit, 2012). We might have already observed such a trapped disk in, e.g., A 0535+26 at very low flux levels (Rothschild et al., 2013). In all cases the time scales are on the order of tenth of days, causing the disk to survive a large fraction of the orbital period or even one full orbit until mass is again transfered from the Be-disk.

[12] During the concluding discussion session at the BeXRB conference in Valencia 2014, Okazaki-san asked if someone knows a value for the density of Be disks in binaries. Unfortunately, no one could give an answer.

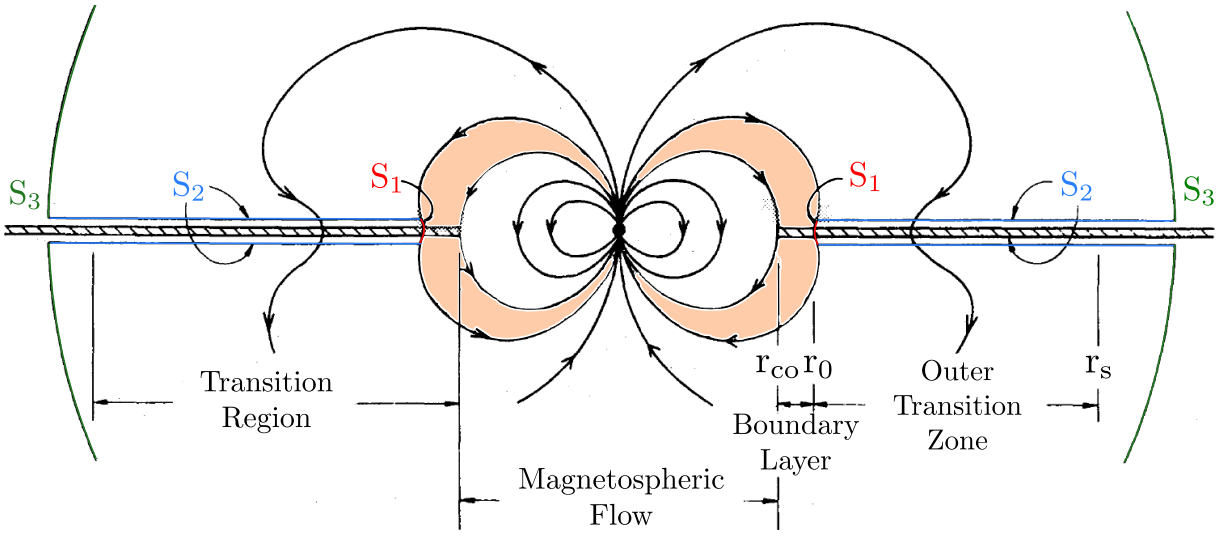

Figure 1.18: Coupling of the accretion disk to the magnetic field of a neutron star after. The accretion disk, seen from the side, is assumed to be composed of an outer transition zone, where the angular velocity is Keplerian, and a narrow boundary layer, where the plasma is coupling onto the magnetic field of the neutron star and redirected onto its poles (red region). For the definition of symbols and the surfaces S_1, S_2, and S_3 see the text (taken and modified from Ghosh & Lamb, 1979b).

1.3 Accretion Column Physics

All effects discussed in the previous Sections, like the X-ray activity, are driven by properties of the binary. The very last step in accretion by a neutron star is dominated by the compact object itself. Thus, let us "zoom" into the region where the material is forced to follow the magnetic fields lines of the neutron star: the magnetosphere.

1.3.1 Angular Momentum Transfer

Ghosh et al. (1977) and Ghosh & Lamb (1979a,b) published a series of three papers, where they investigated the "Accretion by rotating magnetic neutron stars" as their series is entitled. In particular they concentrated on the coupling of the accreted plasma onto the magnetic field of the neutron star.

At a certain radius away from the neutron star the pressure of the infalling plasma is in equilibrium with the magnetic pressure induced by the neutron star. As calculated by Elsner & Lamb (1977) this so-called Alf̌en radius, $r_{\rm A}$, depends therefore on the mass accretion rate, $\dot{M}$, the mass of the neutron star, M, and its magnetic moment, μ,

$$r_{\rm A} = 3.2 \times 10^8 \dot{M}_{17}^{-2/7} \mu_{30}^{4/7} (M/{\rm M}_\odot)^{-1/7} \,{\rm cm} \quad . \tag{1.28}$$

Here, the $\dot{M}$ is given in units of $10^{17}\,{\rm g\,s^{-1}}$, μ in $10^{30}\,{\rm G\,cm^3}$, and M in solar masses. For typical values the Alfvén radius is on the order of 1000 km away from the neutron star. Material, which is within the Alfvén radius or surface, is forced to follow the magnetic field of the neutron star.

Once the material has coupled onto the magnetic field of the neutron star, its initial angular momentum has to be conserved. Consequently, the spin of the neutron star will accelerate, leading to a spin-up. To theoretically calculate the rate of this spin up, $\dot{P}$, Ghosh & Lamb (1979b, hereafter GL79) investigated the torque, N, onto the neutron star by integrating the angular momentum flux over any closed surface, S, surrounding the

star,

$$N = \int_S \left(-\rho v_\mathrm{p} w^2 \Omega + w \frac{B_\mathrm{p} B_\phi}{4\pi} + \eta w^2 \nabla\Omega \right) \hat{n}\, \mathrm{d}S \tag{1.29}$$

Besides the surface normal, $\hat{n}$, and the radius to the magnetic axis, w, three terms contribute to the total torque:

- material-stress: this represents the material of density ρ, angular velocity Ω, and poloidal velocity v_p (i.e., in direction of the magnetic axis), which transfers its angular momentum on the neutron star (the resulting torque is negative).
- magnetic-stress: the magnetic field of the neutron star with its poloidal and azimuthal components, B_p and B_ϕ, respectively, both functions of the position on the surface, act on the material flowing in.
- viscous-stress: depending on the effective dynamic viscosity, η, angular momentum of the plasma is lost due to inward motion ($\nabla\Omega$) and transformed into heat.

To solve Eq. (1.29), GL79 chose an accretion disk scenario (see Fig. 1.18). The accretion disk itself is modeled by two surfaces. The first surface, S_1, is a cylindrical surface with height h and radius r_0, which is located at the boundary layer to the outer transition zone. After GL79, the angular velocity at r_0 is Keplerian and is approximately half the Alfvén radius (see Eq. 1.28). At smaller radii the plasma is forced to rotate with the velocity of the neutron star, which is reached down at the co-rotation radius, r_co. The thickness of the boundary layer, $r_0 - r_\mathrm{co}$, is typically $\sim 0.04 r_0$. The second surface, S_2, represents the upper and lower surface of the accretion disk itself, separated by the height h, and extends from r_0 to infinity. The screening radius, r_s, as denoted in Fig. 1.18, is the radius below which the magnetic field gets deformed by the plasma. Finally, to account for the conservation of angular momentum, the integral over the surface most be closed, which is achieved by a third surface, S_3, and consists of two hemispherical surfaces at infinity.

After having defined the above accretion geometry, Eq. (1.29) can be integrated. It turns out that the term corresponding to the material-stress is mainly determined by boundary surface S_1, while the magnetic-stress is given by the disk surface S_2 (GL79). The viscous-stress can be neglected for all surfaces in good approximation. At the end, GL79 derived two solutions for the spin-up, $\dot{P}$, of the neutron star, whether an accretion disk exists or not:

$$\text{disk-accretion:}\quad \dot{P} = -5.0 \times 10^{-5} {\mu_{30}}^{2/7} n(\omega_\mathrm{s}) S_1(M) (P {L_{37}}^{3/7})^2 \,\mathrm{s\,yr^{-1}} \tag{1.30}$$

$$\text{wind-accretion:}\quad \dot{P} = -3.8 \times 10^{-5} R_6 (M/\mathrm{M}_\odot)^{-1} {I_{45}}^{-1} (l_\mathrm{a}/10^{17}\,\mathrm{cm^2\,s^{-1}}) P^2 L_{37}\,\mathrm{s\,yr^{-1}} \tag{1.31}$$

Here, μ_{30} is the magnetic moment of the neutron star in units of $10^{30}\,\mathrm{G\,cm^3}$, L_{37} the luminosity in $10^{37}\,\mathrm{erg\,s^{-1}}$, R_6 the neutron star's radius in $10^6\,\mathrm{cm}$, I_{45} its moment of inertia in $10^{45}\,\mathrm{g\,cm^2}$, M its mass, and l_a is the specific angular momentum of the accreted plasma at the Alfvén radius (r_A, Eq. 1.28). The function $n(\omega_\mathrm{s})$ is the dimensionless accretion torque (Eq. 7 of GL79) and depends on the so-called fastness parameter ω_s, which is the angular velocity of the neutron star in units of the Keplerian velocity at r_0 (Eq. 16 of GL79). Finally, the structure function $S_1(M)$ depends on the mass, equation of state, and dynamical response of the neutron star (Eq. 18 of GL79).

In the case of accretion from a wind no accretion disk is present. Thus the surface S_2 (see Fig. 1.18) vanishes and S_1 becomes a sphere at r_A. Thus, the torque is completely dominated by the material-stress onto the magnetosphere of the neutron star. Thus, Eq. (1.31) assumes spherical symmetric accretion. Furthermore, the specific angular momentum of the plasma, l_a, depends on the orbital parameters of the binary and the wind velocity of the companion.

Both equations for $\dot{P}$ above (Eq. 1.30 and 1.31) are proportional to $P^2 {L_{37}}^\alpha$, where α depends whether the compact object accretes from a disk or from the wind. Thus, it is

convenient to simplify and combine these equations when analyzing observed pulse period evolutions (see Chapter 4),

$$\dot{P} = -bP^2 {L_{37}}^{\alpha} \tag{1.32}$$

where b is a proportional constant. GL79 noted that in the case of accretion from a wind, the angular momentum of the plasma, $l_{\rm a}$, is a function of time and depending on the conditions $1 \leq \alpha \leq 7/3$. In the disk case and if the neutron star is a slow rotator ($\omega_{\rm s} \ll 1$) the luminosity exponent $\alpha = 6/7$. Otherwise, when the spin period is small *or* the source is in a low luminosity state, $\alpha = 3/7$ and $\dot{P}$ is no longer proportional to P^2, but P instead. This is simply because the material-stress decreases, causing the boundary layer to move outwards (the magnetospheric radius increases) and, thus, the disk-stress becomes more important. Once the boundary layer crosses the screening radius, $r_{\rm s}$, the Keplerian angular velocity at this distance is slower than the neutron star's rotation. Consequently, angular momentum is transfered to the disk, causing the star to *spin-down*. While accretion after GL79 is still possible once the inner parts of the disk a sufficiently accelerated, at even lower luminosities and, thus, higher radii of the boundary layer, the transfered angular momentum on the disk may cause its material to be expelled. This is where the propeller-regime sets in and the theory by GL79 is no longer applicable.

In the so-called propeller-regime the magnetosphere at the distance of the boundary layer is rotating at a velocity similar to the free fall velocity (Davidson & Ostriker, 1973; Illarionov & Sunyaev, 1975). This is the case for accretion rates around $10^{14}\,{\rm g\,s^{-1}}$, which corresponds to a luminosity in the order of $10^{34}\,{\rm erg\,s^{-1}}$ after Eq. (1.5). "*If the rotation and magnetic-field axes are not parallel, the neutron star during this phase will work like a mill.*" (Shakura, 1975). Consequently, the material is heated up by shock-waves, which results in an hydrodynamic ouflow and accretion is, thus, no longer possible. The expected spin-down, $\dot{\nu}$, during this regime is given by (see, e.g., Illarionov & Sunyaev, 1975; Davies & Pringle, 1981)

$$\dot{\nu} \approx -\frac{4\pi\nu^2\mu^2}{GMI} \tag{1.33}$$

with the spin frequency ν of the neutron star, its magnetic moment μ, its mass M, and its moment of inertia I. The exact solution to the angular momentum transfer depends, however, on the mass accretion rate and the details of the interaction between the accretion disk, or the accreted material in general, with the magnetosphere, which depends on the geometry as well. As argued recently by D'Angelo & Spruit (2012), the matter might even stay in a trapped accretion disk rather than "propelled" out the system, which further complicates the pulse period evolution of the neutron star in this regime.

Since the work by GL79 on the spin-up at high luminosities and the early work on the propeller-regime, attempts were made to combine these theories. Especially, the transition between spin-up and -down regimes were theoretically investigated (see, e.g., Arons et al., 1984; Lovelace et al., 1995; Perna et al., 2006), since sudden torque reversals have been observed. In GX 1+4 (see, e.g., González-Galán et al., 2012) and 4U 1626−67 (see, e.g., Camero-Arranz et al., 2010; Takagi et al., 2016) a spin-down phase set in after decades of spinning up.

Applying the torque theories to transient X-ray binaries (see Sect. 1.2.4), one would expect a spin-up during outbursts, where the mass accretion rate is high, while in quiescent states or at very low luminosities the spin period evolution is probably dominated by a spin-down due to the propeller effect. Indeed, the period evolution of such BeXRBs show long-term phases of spin-up and -down (e.g., Bildsten et al., 1997). However, the observed evolutions are much more complicated than what is described above, probably due to changing parameters of the accreted material or the disk, missing orbital solutions and

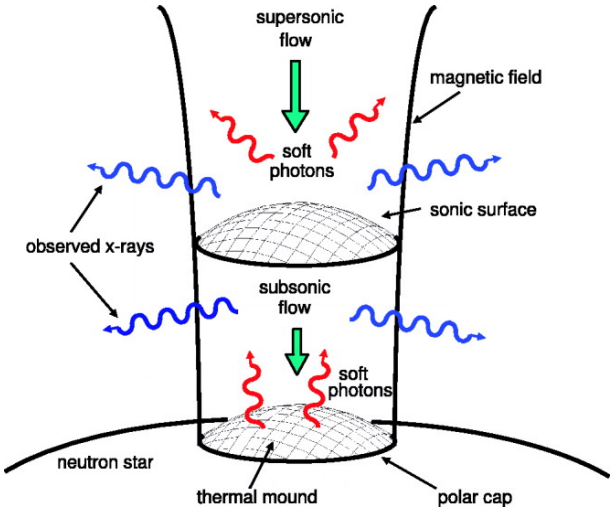

Figure 1.19: X-ray photon production in the accretion column of a neutron star. Soft seed photons (red) are produced via black body radiation on the surface and in the column by bremsstrahlung and cyclotron emission. The infalling supersonic plasma upscatters these photons to higher energies by inverse Compton effects. Here, a shock forms and the plasma sinks onto the surface with subsonic velocities (taken from Becker & Wolff, 2007).

geometries, and unknown behaviors of the Be companions, which drive the mass accretion rate.

1.3.2 Continuum Emission

To understand why accreting neutron stars emit X-rays we further zoom in on a region much smaller than the Alfvén radius: the accretion columns above the neutron star's surface. Here, the plasma falls with relativistic velocities within the magnetic field of the neutron star of the order of 10^{12} G and, finally, hits its surface. The details of the physical mechanisms, which are able to stop $10^{16}\,\mathrm{g\,s^{-1}}$ (see Table 1.1) within fractions of a second, determines the emerging X-ray spectrum. In fact, how the plasma comes to rest at the surface is one of the key aspects in theoretical investigations. Early attempts to solve the radiative transfer in strongly magnetized plasmas (Basko & Sunyaev, 1976; Mészáros & Nagel, 1985a,b; Nagel, 1981a,b) were not able to describe the observed spectra well. As already pointed out by Basko & Sunyaev (1976), the pressure in the columns are dominated by radiation and, thus, radiative shocks must be considered. The current knowledge of the formation of the X-ray spectrum of accreting pulsars is summarized in the next paragraphs, which are based on theoretical investigations by Becker & Wolff (2005a,b, 2007, hereafter BW07).

BW07 considered the accretion geometry and processes illustrated in Fig. 1.19 to solve their radiative transfer equation for the photon distribution $f(z,\epsilon)$ depending on the height z above the surface and energy ϵ:

$$\begin{aligned}\frac{\partial f}{\partial t} + v\frac{\partial f}{\partial z} = \frac{Q(z,\epsilon)}{\pi r_0^2} - \frac{f}{t_{\mathrm{esc}}} + \frac{\mathrm{d}v}{\mathrm{d}z}\frac{\epsilon}{3}\frac{\partial f}{\partial \epsilon} \\ + \frac{n_\mathrm{e}\bar{\sigma}c}{m_\mathrm{e}c^2}\frac{1}{\epsilon^2}\frac{\partial}{\partial\epsilon}\left[\epsilon^4\left(f + kT_\mathrm{e}\frac{\partial f}{\partial\epsilon}\right)\right] + \frac{\partial}{\partial z}\left(\frac{c}{3n_\mathrm{e}\sigma_\parallel}\frac{\partial f}{\partial z}\right)\end{aligned} \tag{1.34}$$

The terms on the left is the time derivative of the photon distribution, $f(z,\epsilon)$, comoving with the infalling plasma with velocity $v < 0$. The right-hand terms correspond to the following aspects (compare Fig. 1.19):

- seed photons: these soft X-ray photons (red photons in Fig. 1.19) are produced by three different mechanisms and, thus, at different heights in the accretion column of radius r_0: 1) Black body radiation at the thermal mound ($z = 0$), i.e., on the polar caps of the neutron star, where the material hits the surface. These seed photons have a energy continuum, but are restricted in space (see Eq. 123 of BW07). 2)

Cyclotron emission resulting from radiative deexcitation of electrons after collisions with protons. Due to the strong magnetic field of the neutron star the electron energy levels are quantized perpendicular the field. Consequently, the deexcitation emits photons at the cyclotron energy. In contrast to black body radiation, the cyclotron emission can be assumed to be monochromatic, but present in the whole column (Eq. 116 of BW07). 3) Bremsstrahlung radiation by the electrons deflected in the infalling thermal plasma (free-free emission). This radiation is more complicated to handle since it is distributed in energy and space (Eq. 126 of BW07).

- photon escape: at some point the photons distributed within the column, after having undergone various scattered processes, will escape through the walls of the column (blue photons in Fig. 1.19) and are, thus, no longer available (minus-sign). This happens at the characteristic escape time-scale, $t_{\rm esc}$, which depends on the column radius, r_0, and its optical thickness perpendicular to the symmetry axis (see Eq. 18 and 19 of BW07). These escaping photons are the main part of radiation seen by the observer.
- bulk Comptonization: this term can be understood as inverse Compton scattering of photons off relativistic electrons. Because this scattering depends on the deceleration of the plasma ($\mathrm{d}v/\mathrm{d}z$), Becker & Wolff (2005a) introduce a radiation-dominated shock in the accretion column, based on initial ideas by Davidson (1973). This results in a velocity profile with sufficiently strong deceleration (Eq. 29 of BW07), which amplifies itself once the photons are upscattered to higher energies ($\partial f/\partial\epsilon$, which corresponds to the nature of a radiation dominated deceleration). Note that in contrast to, e.g., a gas shock the radiation-dominated shock is a *continuous* transition.
- thermal Comptonization: inverse Compton effects with the angle averaged electron scattering cross-section $\bar{\sigma}$ take place in the plasma consisting of electrons of mass $m_{\rm e}$, density $n_{\rm e}$, and temperature $kT_{\rm e}$. The two contributions in parentheses are a result of the Kompaneets-operator (1957) and correspond to the Doppler effect ($\partial f/\partial\epsilon$) and the electron recoil (f), which transfers momentum from the photon-field to the plasma, resulting in an energy transfer from high ($\epsilon \gtrsim T_{\rm e}$) to low energy photons ($\epsilon \lesssim T_{\rm e}$).
- diffusion: similar to the escape of photons through the walls of the column, i.e., their perpendicular diffusion relative to the column, the photons can diffuse parallel as well, but against the infalling plasma with the scattering cross-section $\sigma_{\parallel}$.

In order to solve the radiative transfer equation (Eq. 1.34), BW07 assumed the steady state ($\partial f/\partial t = 0$) of a pure, fully ionized hydrogen plasma at supersonic speeds. This plasma gets decelerated by Comptonization in the region of the radiation-dominated shock to subsonic velocities (Fig. 1.19). Furthermore, they assumed cylindrical symmetry, a constant B-field and temperature along the column, used simplified equations for the electron cross-sections, i.e., they assumed photons propagating parallel or perpendicular to the column only and the cross-sections are computed using the mean photon energy.

Fig. 1.20 shows an example of the theoretical X-ray spectrum as expected by the model of BW07. It is compared with *BeppoSAX*-data of the supergiant system LMC X-4, which is, however, not an actual fit in the usual sense of data analysis, but rather example calculations to roughly match the observed *unfolded* and *unabsorbed* source flux (see Sect. 3.1 and 1.3.5, respectively). The overall spectral shape is dominated by bremsstrahlung radiation (green line) with contribution from cyclotron radiation (blue), while the black body (black) is negligible. Note that these contributions show the upscattered seed photon spectra after having solved the radiative transport equation. An iron emission line at 6.4 keV is also present in the spectra (magenta, see Sect. 1.3.5). The power-law shape below 20 keV is

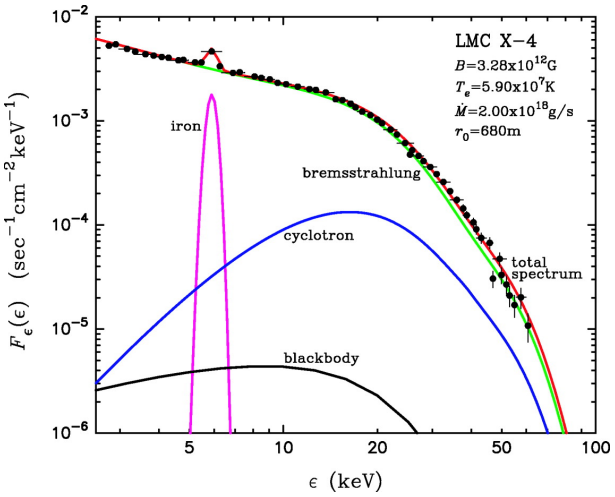

Figure 1.20: Theoretical spectrum of LMC X-4. The X-ray spectrum is dominated by bremsstrahlung emission (green), followed by cyclotron (blue) and black body (black) radiation. An iron emission line (magenta) is visible as well (see Sect. 1.3.5). The model is compared with data by La Barbera et al. (2001) (taken from Becker & Wolff, 2007).

mainly the result of the bulk Comptonization because the electron temperature, T_e, in accreting pulsars is much lower than the bulk velocity and, thus, thermal Comptonization is not important. However, also already noted by Becker & Wolff (2005a), the power-law due to pure bulk Comptonization is expected to follow $f \propto \epsilon^{-\Gamma}$ with $\Gamma > 2$, which is in contradiction to the observed, harder spectra with an exponential cut-off at energies >10 keV as seen in, e.g., LMC X-4 (Fig. 1.20). After BW07 this issues is solved by the electron recoil of thermal Comptonization, which leads to an exponential cut-off and a flattening of the spectrum at lower energies, i.e., with a power-law exponent $\Gamma \leq 2$. Very recently, Postnov et al. (2015a) theoretically investigated the spectral hardness, i.e., the flux in hard X-rays relative to the the soft X-rays, with the mass accretion rate, i.e., the luminosity. Their result is a spectral hardening, i.e., a decrease in Γ with increasing mass accretion rate due an increase of the density inside the column and, thus, the Comptonization rate, and the height of the accretion column.

Unfortunately, the solution of the radiative transfer equation after BW07 numerically takes some time on current CPUs, which is not reasonable when fitting actual data from accreting neutron stars. A first attempt in modeling these data was carried out by Ferrigno et al. (2009) on the example of the BeXRB 4U 0115+63. They have found, however, that the model is not completely able to explain the observed spectra. In particular, they needed an additional thermal Comptonization model for data below 5 keV, which they attributed to a hot halo around the neutron star, and a ∼1 keV broad Gaussian emission feature around 9 keV to get acceptable fits. Currently, improved implementations of the BW07 theory are developed (Farinelli et al., 2012, 2016, and Wolff et al., 2016, in prep.), which have been applied already to data from Cen X-3 and XTE J1946+274 by Marcu et al. (2015) with promising qualitative results. Until these models are able to describe the observed spectra well, however, phenomenological models are used to fit the spectra of accreting pulsars[13] (see Sect. 1.3.4).

1.3.3 Cyclotron Resonance Scattering Features

This Section is based on Schönherr et al. (2007) and Schwarm (2010).
As already mentioned in the previous Section the electron's movement perpendicular to the strong magnetic field of the neutron star is quantized, which results in emission of cyclotron radiation as the result of collisions with protons (BW07). In classical physics the electron moves on a circle around the field lines, where its Lamor radius depends on the magnetic field strength. Once this radius is on the order of the electron's de Broglie

[13] This would provide the answer "not yet" to specific question 5.

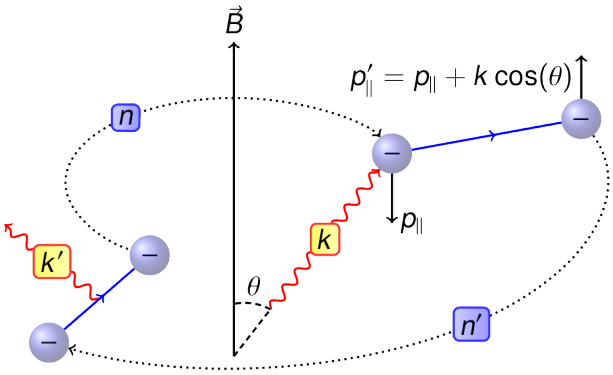

Figure 1.21: Excitation and deexcitation of an electron on a Landau level resulting in the formation of a CRSF. An incoming photon k under the angle θ to the magnetic field $\vec{B}$ excites an electron with the momentum $p_\parallel$ from the Landau Level n to n'. After the lifetime of the excited state the electron decays to the level n again and emits a photon k' in a (quasi) random direction (sketch by F.-W. Schwarm, priv. comm.).

wavelength quantum effects have to be considered, which is the case for magnetic fields near the critical field strength, $B_{\rm crit}$, of (Canuto & Ventura, 1977)

$$B_{\rm crit} = \frac{m_{\rm e}^2 c^3}{e\hbar} = 44.14 \times 10^{12}\,{\rm G} \quad , \tag{1.35}$$

with the electron's mass, $m_{\rm e}$, and charge, e, and Planck's constant, $\hbar = h/2\pi$. As a result, the electron's momentum perpendicular to the magnetic field is quantized, which leads to discrete energy levels, $E_{\rm n}$, called Landau levels (Lai, 2001, and references therein),

$$E_{\rm n} = \sqrt{c^2 p_\parallel^2 + m_{\rm e}^2 c^4 \left(1 + 2n\frac{B}{B_{\rm crit}}\right)} \quad . \tag{1.36}$$

B is the magnetic field strength at the location of the electron, $n \in \mathbb{N}$ is the Landau quantum number, and $p_\parallel$ the electron's (continuous) momentum parallel to the field. Here and throughout this discussion, the magnetic field is assumed to be a dipole. The magnetic field of most accreting pulsars is much weaker than the critical field, i.e., $B \ll B_{\rm crit}$, in which case we can compute the Taylor approximation of Eq. (1.36) and derive

$$E_{\rm n} = E_0 + m_{\rm e} c^2 n \frac{B}{B_{\rm crit}} \quad , \tag{1.37}$$

and after having used Eq. (1.35) and entering values for all constants we get the so-called 12-B-12 rule for the fundamental cyclotron energy, $E_{\rm cyc} = E_{\rm n+1} - E_{\rm n} \equiv E_0$,

$$E_{\rm cyc} = 11.6\,{\rm keV}\,B_{12} \quad . \tag{1.38}$$

Here, B_{12} denotes the magnetic field strength in units of 10^{12} G.

Excitation of an electron from the Landau level n to $n+1$ is possible by the absorption of a photon, $\vec{k}$, as well (see Fig. 1.21), which in principle results in absorption features around the cyclotron energy, $E_{\rm cyc}$, and its multiples in the observed X-ray spectra. This is a very import aspect since it allows us to *directly* measure the magnetic field strength of an accreting neutron star at the line forming region. As shown by (Latal, 1986) the lifetime of the excited electron state is on the order of 10^{-15} s and, thus, a spawned photon, k', is almost instantly emitted after the electron has been excited. That is why this effect is commonly called Cyclotron Resonant Scattering Feature (CRSF). The BeXRB 4U 0115+63 is the record holder for the number of detected CRSFs in a single source. As an example the *BeppoSAX* spectrum of an outburst in 1999 is shown in Fig. 1.22, which shows five absorption features in total: the *fundamental* CRSF around 11 keV, labeled E_0, and four *harmonics* at its multiples, labeled E_1 to E_4.

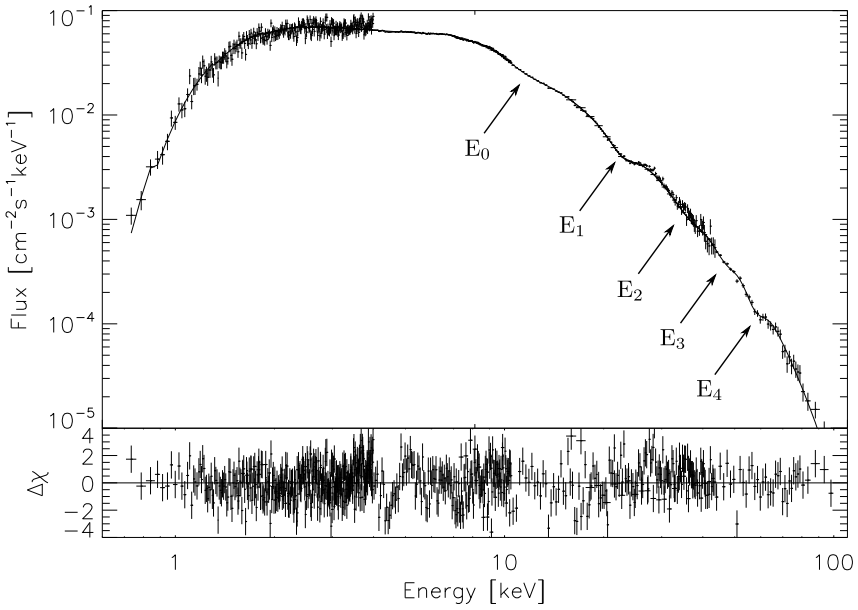

Figure 1.22: Top: X-ray spectrum of 4U 0115+63 as recorded by *BeppoSAX* in the decline of the 1999 outburst. **Bottom:** Residuals of the model, which includes five cyclotron lines (E_0 to E_4) (taken and modified from Ferrigno et al., 2009).

The observed CRSF energy, $E_{\rm cyc}^{\rm obs}$, gets, however, redshifted due to the strong gravitational potential of the neutron star,

$$E_{\rm cyc}^{\rm obs} = \frac{E_{\rm cyc}}{1+z} \quad , \tag{1.39}$$

with the redshift z

$$z = \left(1 - \frac{2GM}{r_{\rm cyc}c^2}\right)^{-1/2} - 1 \quad . \tag{1.40}$$

Here, $r_{\rm cyc}$ is the radius from the center of the neutron star to the emission region where the CRSF is formed. If we assume this region to be located near the surface of the neutron star, we can use typical values for the neutron star's radius, $r_{\rm cyc} = R = 11.5\,{\rm km}$, and its mass, $M = 1.4\,{\rm M}_\odot$, as listed in Table 1.1 and calculate a gravitational redshift of about $z \sim 0.25$. Thus, the intrinsic cyclotron energy and magnetic field strength is higher by $\sim$25% compared to the observed one.

Furthermore, the scattering process has to conserve momentum and energy. This is calculated best in the rest frame of the electron, where $p_\parallel = 0$. Here, the projection of the photon's wave vector, $\vec{k}$ (see Fig. 1.21), projected perpendicular to the field has to match the electron's perpendicular momentum, $p_\perp$, for resonant scattering. As a result, the required photon energy, $E_\nu = h\nu$, depends on on its incident angle, θ, to the magnetic field (e.g., Schönherr et al., 2007),

$$E_\nu = \frac{m_{\rm e}c^2}{\sin^2\theta}\left(\sqrt{1 + 2n\frac{B}{B_{\rm crit}}\sin^2\theta} - 1\right) \quad . \tag{1.41}$$

The different Landau levels are, therefore, no longer equally spaced in energy as in Eq. (1.37). This would be the case for $\theta = \pi/2$, i.e., for photons perpendicular to the field only. Thus, an observer looking perpendicular on the accretion column would see very narrow and equally spaced cyclotron lines, since only one specific energy matches the resonant condition. For other viewing angles, i.e., $\theta \neq \pi/2$, Eq. (1.41) has two solutions

for the required energy, i.e., two photons of different energy can match the scattering condition on the same electron.

Further effects have to be considered, which complicates the shape of CRSFs, which are the relativistic velocity of the electrons and their temperature. To account for the first the photon wave-vector has to be Lorentz boosted, which leads to both an energy shift of the observed cyclotron lines and a broadening. While the shift can be understood as a relativistic Doppler effect, the broadening is a result of the boost of the incident angle θ, which leads to even more solutions of Eq. (1.41). The temperature of the electrons, T_e, which is also considered in the continuum emission of Eq. (1.34), leads to a Maxwellian distribution distribution of the electron's parallel momenta, $p_\parallel$, which again leads to a broadening of the observed cyclotron lines (e.g., Schönherr et al., 2007).

To calculate the shape of the resulting cyclotron lines, where all the effects discussed before are taken into account, Monte Carlo simulations are necessary as first performed by Isenberg et al. (1998) and followed by Araya & Harding (1999), Araya-Góchez & Harding (2000), and (Schönherr et al., 2007). These simulations also handle photon spawning, which is the decay of Landau levels for $n > 2$. Since the decay rate for the transition from $n' \to n' - 1$ is much higher than, e.g., for $n' \to n'2$ the excited state decays in a cascade down to the ground state. As a result during each cascade step a photon of the fundamental energy, E_cyc, is emitted, i.e., spawned. This fills up the fundamental line in the spectra, causing the line to be less deep than the first harmonic. Due to inelastic scattering of the spawned photons emission wings around the fundamental line might form as well. To date theoretical models are still under development (Schwarm, 2010; Schwarm et al., 2016, in prep.) due to the complicated physics and required CPU time. Until these models have been successfully applied to observed spectra phenomenological models have to be used as presented in the next Sect. 1.3.4.

Very recently, Becker et al. (2012) have theoretically investigated the last effect discussed here, which is the dependance of the measured cyclotron line energy, $E_\mathrm{cyc}^\mathrm{obs}$, on the source's X-ray luminosity, L_x. In particular, a positive correlation of $E_\mathrm{cyc}^\mathrm{obs}$ with L_x has been observed in Her X-1 (Staubert et al., 2007; Vasco et al., 2011) and GX 304−1 (Klochkov et al., 2012), while a negative correlation was found V 0332+53 (Mowlavi et al., 2006; Tsygankov et al., 2010). Although a negative correlation was also observed for 4U 0115+63 (Nakajima et al., 2006; Tsygankov et al., 2007), Müller et al. (2013) and Boldin et al. (2013) concluded that the apparent correlation is an artifact of the phenomenological continuum model. By choosing another model the cyclotron line energy seemed to stay constant with luminosity.

In order to explain this behavior theoretically, Becker et al. (2012) proposed different mechanisms to stop the infalling plasma above the surface of the neutron star. Depending on the luminosity, i.e., on the mass accretion rate, transition between these mechanisms take place (compare Fig. 1.23). For very low luminosities the plasma is stopped near the neutron star's surface by a gas-mediated shock, which is, however, not yet clear. With increasing luminosity the emission region first stays at the surface (Fig. 1.23a) resulting in a constant CRSF energy. As the plasma piles-up above the surface the altitude of the gas shock increases and the CRSF energy decreases accordingly (b). For luminosities above the Coulomb luminosity,

$$\begin{aligned} L_\mathrm{coul} = 1.23 \times 10^{37}\,\mathrm{erg\,s^{-1}} \left(\frac{\Lambda}{0.1}\right)^{-7/12} \left(\frac{\tau_\star}{20}\right)^{7/12} \left(\frac{M_\star}{1.4\mathrm{M}_\odot}\right)^{11/8} \\ \times \left(\frac{R_\star}{10\,\mathrm{km}}\right)^{-13/24} \left(\frac{E_\star}{10\,\mathrm{keV}}\right)^{-1/3} \quad , \end{aligned} \tag{1.42}$$

the infalling plasma is stopped by Coulomb interactions, i.e., a radiation dominated shock forms and bulk Comptonization takes place (see Sect. 1.3.2 and Eq. 1.34). In this equation,

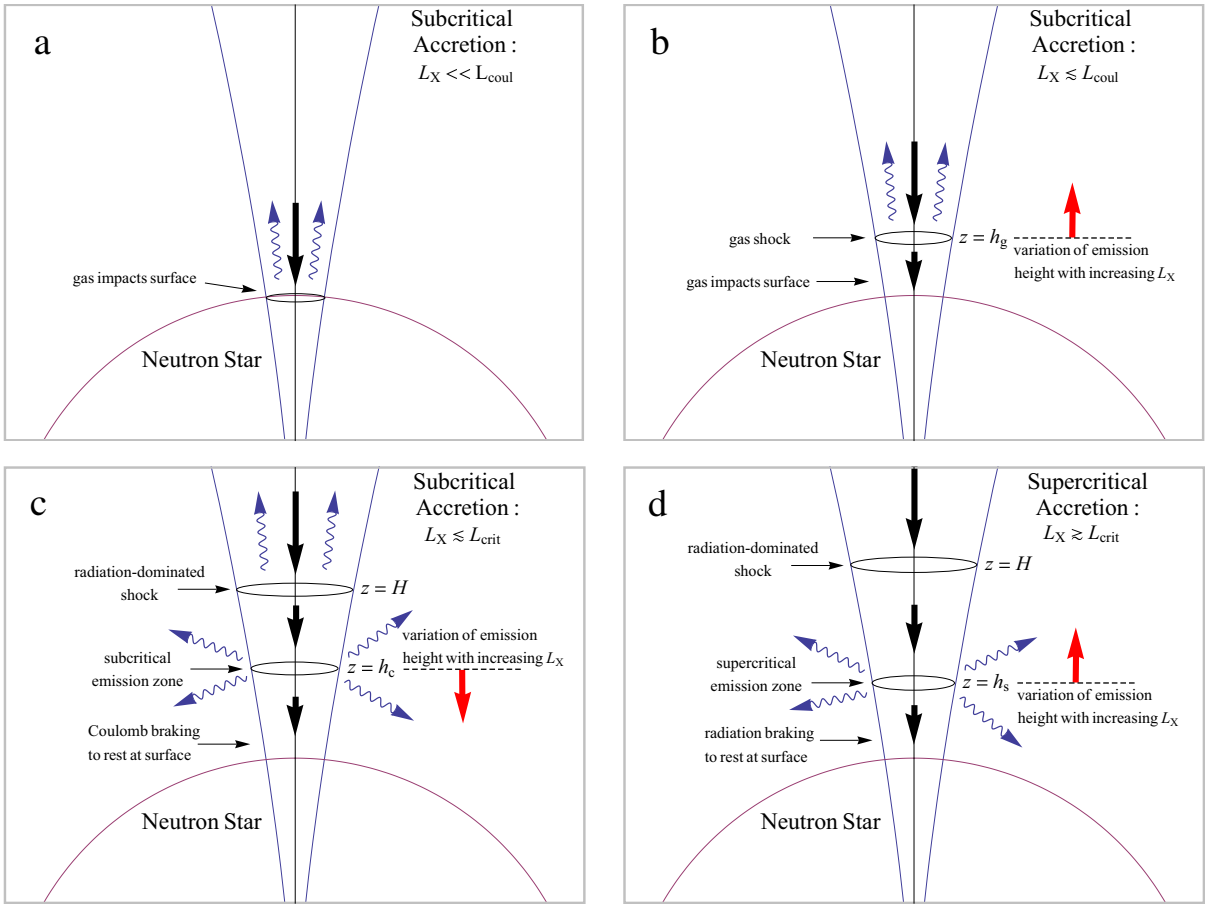

Figure 1.23: Theoretical variation of the height of the cyclotron line emission region with the luminosity and deceleration of the infalling material. **a:** At very low luminosities the gas is stopped at the surface and the emission region is settled on the surface. **b:** As soon as a the luminosity increases a gas shock evolves, which rises with the luminosity and so does the cyclotron emission region. **c:** Near the critical luminosity the radiation pressure forms a shock and the emission region goes down with luminosity, while the plasma is stopped via Coulomb interactions. **d:** For super-critical luminosities the radiation is even able to stop the infalling plasma and the emission region starts to rise again (taken from Becker et al., 2012).

$\Lambda = 1$ for spherical and $\Lambda < 1$ for disk accretion, $\tau_\star$ is the Thomson optical depth required for Coulomb stopping (Eq. 49 of Becker et al., 2012), $M_\star$ the mass, $R_\star$ the radius of the neutron star, and $E_\star$ the intrinsic energy of the CRSF. This energy increases with the luminosity as the emission zone is pushed down (c). This increase continues until a critical luminosity,

$$L_{\rm crit} = 1.28 \times 10^{37}\,{\rm erg\,s^{-1}} \left(\frac{\Lambda}{0.1}\right)^{-7/5} w^{-28/15} \left(\frac{M_\star}{1.4{\rm M}_\odot}\right)^{29/30} \times \left(\frac{R_\star}{10\,{\rm km}}\right)^{1/10} \left(\frac{E_\star}{10\,{\rm keV}}\right)^{16/15}\,, \tag{1.43}$$

where $w \sim 1$–3 depends on the shape of the spectrum inside the column, is reached where the radiation pressure dominates the dynamics of the plasma. Hence, increasing the mass accretion rate further adds more radiation pressure to the column and the emission height starts to increase again (d).

1.3.4 Phenomenological Models

As discussed in the previous Sections physical models for the continuum emission (Sect. 1.3.2) and cyclotron resonance scattering features (Sect. 1.3.3) are currently under development[14]. Until this models are available for the general public and are able to reproduce the majority of the observed spectra phenomenological models have to be used to describe the observed spectra. That one still can improve our understanding of accretion physics although these models do not have any physical related parameters is shown in Chapter 5. The following models provide the photon flux density, i.e., photons $\mathrm{s}^{-1}\,\mathrm{cm}^{-2}\,\mathrm{keV}^{-1}$ as a function of energy, E, which is later folded with the detector response (see Sect. 3.1).

As described in Sect. 1.3.2, bulk Comptonization, i.e., the upscattering of X-ray seed photons results mainly in a power-law shape of the continuum,

$$\texttt{powerlaw}(E) = NE^{-\Gamma} \tag{1.44}$$

Here, the normalization N corresponds to the flux at 1 keV. The exponent Γ is called the photon index. Note that $\Gamma > 0$ means a negative exponent and the resulting the photon flux density is monotonic decreasing with energy. After BW07 a photon index of $0 < \Gamma \leq 2$ is expected from the Comptonization process. The observed spectra of accreting neutrons stars feature, however, an exponential roll-over at energies between 5 and 25 keV (see Bildsten et al., 1997, and references therein). Therefore, a cut-off power-law is commonly used

$$\texttt{cutoffpl}(E) = \texttt{powerlaw}(E) \cdot \exp(-E/E_{\mathrm{fold}}) \tag{1.45}$$

where E_{fold} is the folding energy above which the spectrum is dominated by an exponential roll-over. Note that E_{fold} is often named the cut-off energy, which is, however, misleading since the function is continuously differentiable, i.e., there is nothing special happening at $E = E_{\mathrm{fold}}$. In contrast, the multiplicative `highecut` model,

$$\texttt{highecut}(E) = \begin{cases} \exp(-(E - E_{\mathrm{cut}})/E_{\mathrm{fold}}) & \mathrm{for} E \geq E_{\mathrm{cut}} \\ 1 & \mathrm{for} E < E_{\mathrm{cut}} \end{cases} \tag{1.46}$$

has a break in its derivative at the cut-off energy, E_{cut}. The observed exponential roll-over caused BW07 to include also thermal Comptonization in their radiative transport equation (see Eq. 1.34). Although bulk Comptonization usually dominates they could show that thermal Comptonization indeed leads to an exponential roll-over of the neutron star's X-ray spectrum. Due to this fact the folding energy, E_{fold}, is often interpreted as electron temperature, kT_{e}, which is, however, not yet proven.

In many accreting pulsars a soft X-ray excess below $\sim$5 keV is observed (see, e.g., Mihara, 1995). This excess is commonly modeled by either an additional power-law (see the `NPEX` model, Eq. 1.48) or a black-body spectrum,

$$\texttt{bbody}(E) = 8.0525\, N\, \frac{E^2}{(kT)^4\,(\exp(E/kT) - 1)} \tag{1.47}$$

The normalization N corresponds to the source's flux in units of $10^{39}\,\mathrm{erg\,s^{-1}}\,(10\,\mathrm{kpc})^{-2}$ and kT is the temperature of the black-body. Another normalization is often chosen which directly corresponds to the emission area of the black-body using the Stefan-Boltzmann

[14] During the time of writing this thesis a few people tested new implementations of the continuum model after BW07 and the Monte Carlo CRSF model after Schwarm et al. (2016, in prep.) with some success. Thus, it is likely that my thesis will be one of the last ones at the Remeis observatory still using the old-fashioned phenomenological models, which have been used for decades.

law (see Eq. 1.3). One would expect the black-body area not to exceed the area of the accretion column or the accretion mound, which is on the order a few km^2 (Lamb et al., 1973). However, as argued by BW07 and exemplarily displayed in Fig. 1.20, the intrinsic black-body on the surface contributes marginally to the total X-ray spectrum. Rather that it is likely that additional empirical soft components model the cyclotron emission.

Another way of modeling the soft excess at lower X-ray energies is the so-called `NPEX` model (Negative Positive power law EXponential, Mihara, 1995)

$$\texttt{NPEX}(E) = (N_1 E^{-\Gamma_1} + N_2 E^{+\Gamma_2}) \exp(-E/kT) \tag{1.48}$$

It consists basically of two `powerlaw`s given by Eq. (1.44) with the same exponential roll-over as in Eq. (1.45) but with $E_{\rm fold}$ replaced by kT. As already applied by Mihara (1995) the second photon index, Γ_2, is often fixed to a value of 2. In this case the `NPEX`-model is very similar to a `cutoffpl` with an additional `bbody` (compare Eq. 1.47). However, in the presence of CRSF in the X-ray spectra, this model can lead to artifacts in the cyclotron line parameters as argued by Müller et al. (2013) and Boldin et al. (2013). Nevertheless, the `NPEX`-model is quite successful in describing the spectral shape for many X-ray pulsars.

A third way to model the soft excess is to use a Gaussian calculated by

$$\texttt{gauss}(E) = \frac{A}{\sigma\sqrt{2\pi}} \exp\left(-\frac{(E-E_0)^2}{2\sigma^2}\right) \tag{1.49}$$

The normalization constant A corresponds to the total area, i.e., the flux within the Gaussian, E_0 to the centroid energy, and σ to the width such that 68% of the total flux is within the energy interval $-\sigma \leq E - E_0 \leq \sigma$. When modeling the soft excess the width might around a few keV as in, e.g., Müller et al. (2013). The Gaussian is also commonly used to model emission lines from neutral and ionized elements, which is described in the next Sect. 1.3.5.

The last empirical model presented here is a Lorentzian absorption profile to model a CRSF in the spectra (Makishima et al., 1990),

$$\texttt{cyclabs}(E) = \exp\left(-\tau \frac{(WE/E_{\rm line})^2}{(E-E_{\rm line})^2 + W^2}\right) \tag{1.50}$$

Here, $E_{\rm line}$ is the CRSF's centroid energy, W its width, and τ the optical depth. For some source, however, the shape of the cyclotron line is described better by a Gaussian absorption profile. Even in a few sources, the best example being V 0332+53 (see, e.g., Kreykenbohm et al., 2005), a combination of absorption profiles has to be added to account for the complex shape of the fundamental cyclotron line. As mentioned in Sect. 1.3.3 this might be due to photon-spawning resulting in emission wings near the cyclotron energy.

1.3.5 Photoelectric Absorption

The intrinsically emitted X-ray spectrum of the neutron star gets, however, modified on its way to the observer by passing through neutral or ionized material. This material can be either located in the vicinity of the X-ray source, i.e., within the binary or within the Milky Way as part of the ISM. The interaction of the X-ray photons with the material leads to two observed features in the spectrum. The first one is a lack of photons at energies below $\sim$10 keV, which results in a turn-over of the spectrum towards lower energies (see Fig. 1.24) and is called X-ray absorption. The second effect is the appearance of fluorescent emission lines in the spectra, which are a result of the absorption in the first place. Measuring the amount of absorption and flux within emission lines would allow us, in principle, to

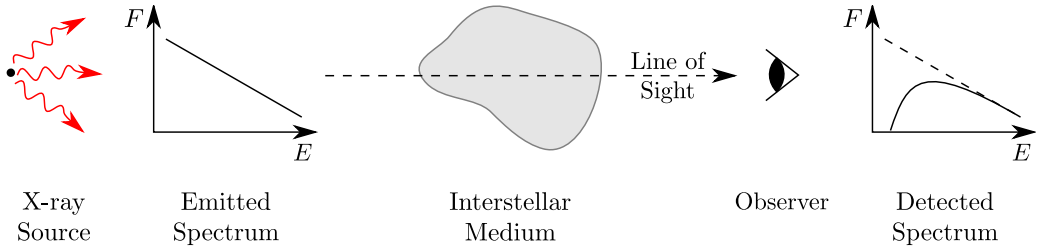

Figure 1.24: Absorption of the spectrum of an X-ray source due to the material in the line of sight to the observer, e.g., the interstellar medium. The detected spectrum (on the right) shows a lack of low-energy X-ray photons compared to the emitted spectrum of the X-ray source (on the left), which is assumed to be a power-law for simplicity.

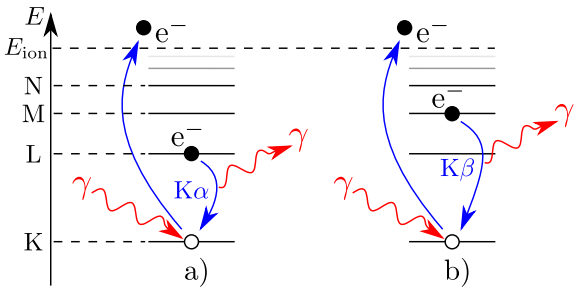

Figure 1.25: Kα and Kβ fluorescence emission. A photon (γ) ionizes one inner most electron (e^-) of an atom, leaving a hole in the K-shell. An electron from a higher energy level, e.g., the L- (a) or M-shell (b), fills this hole by emitting a photon with an energy equal to the difference between the energy levels.

derive the density and mass of the absorbing material. This is an important input for understanding, e.g., stellar winds or Be-disks.

In general, an X-ray photon gets absorbed by an electron bound in, e.g., an atom once its incident energy is above the ionization energy, $E_{\rm ion}$, for this particular electron (photo effect, see Fig. 1.25). This energy depends on the energy level of the electron, i.e., on its shell (K, L, M, N, ...), the atomic number, Z, of the element, and its ionization state. After having ionized the atom the missing electron is replaced by an electron from a higher shell. This transition emits a photon itself with an energy corresponding to the energy difference between the shells. This emission is labeled with the shell, where the photo effect occurred, and the difference in energy levels of the recombination (in Greek letters: $1 = \alpha$, $2 = \beta$, ...). In Fig. 1.25 a K-shell electron is ionized by the incident X-ray photon and gets replaced by either an L-shell-electron, resulting in Kα-emission, or an M-shell-electron, labeled Kβ. The resulting emission lines in the observed spectra are labeled the same way. The most prominent emission line in accreting pulsars in the Kα emission of neutral iron at 6.4 keV (see Palmeri et al., 2003, and references therein).

Since absorption is not possible below the required energy, $E_{\rm ion}$, so-called absorption edges, where the flux gets reduced suddenly, occur in the spectra at each edge for a given atom. The cross-section for absorption of even higher energies is approximately[15] proportional to E^{-3} (Daltabuit & Cox, 1972). The sum over all edges and atoms results in an turn-over towards lower X-ray energy. The multiplicative model describing the absorption follows an exponential of the form (e.g., Wilms et al., 2000)

$$\exp(-\sigma(E)N_{\rm H}) \tag{1.51}$$

where $N_{\rm H}$ is the density of the material measured in atoms cm^{-2} and usually normalized to the total hydrogen number density. The cross-sections, $\sigma(E)$, for the absorption of X-ray photons of energy E is a sum of three different cross-sections (Eq. 1 of Wilms et al.,

[15]The energy dependance is in general a function of atomic number Z, ionization state, and electron shell. See Table 1 of Daltabuit & Cox (1972) for an example of exponents for absorption on K-shell electrons.

2000),

$$\sigma(E) = \sigma_{\rm gas}(E) + \sigma_{\rm molecules}(E) + \sigma_{\rm grains}(E) \tag{1.52}$$

The first term, $\sigma_{\rm gas}$, describes the absorption of X-ray photons on electrons of atomic gases, which is the main contribution to the total cross-section, and proportional to

$$\sigma_{\rm gas}(E) \propto \sum_{Z,i} A_{\rm Z}\, a_{\rm Z,i}\, \sigma_{\rm bf}(Z,i,E) \tag{1.53}$$

Here, $A_{\rm Z}$ is the abundance of the element Z, $a_{\rm Z,i}$ is the ion fraction of element Z that are in the ionization state i, and $\sigma_{\rm bf}(Z,i,E)$ is the ionization cross-section depending on Z, i, and energy E. As already mentioned above this cross-section follows E^{-3} roughly.

The second cross-section in Eq. (1.52), $\sigma_{\rm molecules}$, accounts for the absorption of photons by molecules. Following Eq. (4) of Wilms et al. (2000) this is mainly driven by molecular hydrogen due to its large abundance compared to other molecules. The last contribution, $\sigma_{\rm grains}$, are absorption by dust grains, which is a complex function of the grain's chemical composition, density and geometry. Assuming spherical dust grains and a homogeneous composition Wilms et al. (2000) showed that X-rays are absorbed at the surface of the grains only. Consequently, dust grains reduce the effective column density, $N_{\rm H}$, because the material inside is invisible due to this self-shielding effect.

As one can see from Eq. (1.53) the X-ray absorption heavily depends on the assumed element abundances, $A_{\rm Z}$, and elemental cross-sections, $\sigma_{\rm bf}(Z,i,E)$. Our knowledge of these two quantities is increasing steadily. Especially, the cross-sections for high ionization states and energies, as needed to describe absorption in, e.g., wind-accreting X-ray binaries (see Sect. 1.2.3), are difficult to measure in laboratories on Earth. Furthermore, the abundances in these binaries are possibly very different to solar because of the supernova explosion having produced the compact object (see Sect. 1.1.2). The same applies for the ISM and, in a most general way, its abundances are functions of the position within the Milky Way. Unfortunately, all these aspects lead to systematic uncertainties in the derived column density, $N_{\rm H}$, in case of, for instance, an occultation of the X-ray source by the Be-disk (consider footnote 12 for its importance and see the references in Sect. 5.2 for such an event).

Table 1.2 gives an overview about the different cross-sections, abundances, and absorption models (which differ in the implementation of Eq. 1.52) as available in the analysis software solutions *ISIS* and *XSPEC* (see Chapter 2 for details about these software). To estimate the systematic uncertainties described above I have simulated spectra assuming specific configurations, but fitted with different configurations. The results will be published in Martínez-Núñez et al. (2016).

Figure 1.26 shows the results of this analysis. The widely used `phabs` absorption model, which takes atomic gas into account only, shows differences up to 5% for the derived column density, $N_{\rm H}$ compared to the more sophisticated model `tbnew` (panel a). Differences of the same order result when using different cross-sections (panel b). The strongest difference in the derived column densities of up to 30% is caused by the assumed element abundances (panel c). The choice of the cross-section and model, however, causes significant deviations around the absorption edges. Since the cross-sections are a function of energy the shape of the edges can be complicated due to, e.g., the electron's fine-structure. The cross-sections are, however, often approximated and in the worst case the edges are model by a simple step, which leads to significant issues when analyzing data with supreme energy resolution as observed with, e.g., *XMM-Newton* and *Chandra* (see Sect. 3.2.4 and 3.2.5, respectively).

Table 1.2: List of photoionization cross-sections[a] and abundances[b] as available in *ISIS*/*XSPEC* as well as absorption models. A * marks the default *XSPEC* configuration (version 12.8.2, build in July 2014). This table will be published in Martínez-Núñez et al. (2016).

Cross-sections		Comment
obcm	[1]	
bcmc*	[1]	H_2-cross-section from Yan et al. (1998)
vern	[2]	
Abundance vector		**Origin**
aneb	[3]	solar
angr*	[4]	solar
feld	[5]	solar
grsa	[6]	solar
wilm	[7]	ISM
lodd	[8]	solar
aspl	[9]	solar
Absorption model		**Contributions**
wabs		neutral, atomic, thin gas (abundances fixed to aneb)
phabs		neutral, atomic, thin gas
tbabs	[7]	neutral, atomic, thin gas + neutral H_2-molecules + spherical, chemical homogeneous dust grains (cross-sections fixed to vern)
tbnew[c]	[10]	improved version of tbabs including high resolution cross-sections at important edges
cabs		optically-thin Compton scattering
ctbabs	[11]	full Compton scattering + fluorescence line emission
warmabs		uniform, collisional ionization (warm stellar winds) based on a fixed, ionization-balanced, thin gas

Notes. [a] http://heasarc.nasa.gov/xanadu/xspec/xspec11/manual/node36.html#SECTION00669000000000000000
[b] https://heasarc.gsfc.nasa.gov/xanadu/xspec/manual/XSabund.html
[c] http://pulsar.sternwarte.uni-erlangen.de/wilms/research/tbabs
References. [1] Balucinska-Church & McCammon (1992) [2] Verner et al. (1996) [3] Anders & Ebihara (1982) [4] Anders & Grevesse (1989) [5] Feldman (1992) [6] Grevesse & Sauval (1998) [7] Wilms et al. (2000) [8] Lodders (2003) [9] Asplund et al. (2009) [10] Wilms et al. (2016, in prep.) [11] Eikmann et al. (2012, 2014)

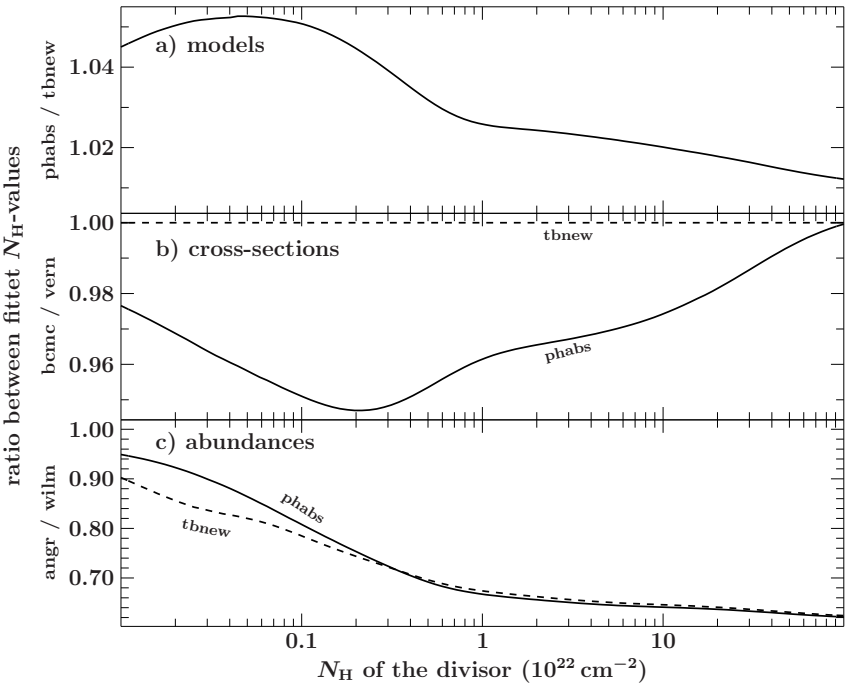

Figure 1.26: Comparison of absorption column densities, N_{H}, fitted with **a** different models, **b** cross-sections, **c** abundances. The ratio of the N_{H} values between the two configurations named by the panel's label are plotted over the assumed N_{H} value of the divisor. For the comparison between the models the cross-sections and abundances are set to vern and wilm, respectively. The solid lines shows the results for the `phabs`- and the dashed lines for the `tbnew`-absorption-model (taken from Martínez-Núñez et al., 2016).

Chapter 2

Methods for Timing and Spectral Analyses

This Chapter describes the methods I have used during my Ph.D. thesis for neutron star timing and spectral analyses. Furthermore, useful functions for the *Interactive Spectral Interpretation System*[1] (*ISIS*; Houck & Denicola, 2000), which I have developed and implemented, are presented here. These functions have been made available to the general public as part of the *ISISscripts*[2], which is a collection of functions developed at the ECAP & Dr. Karl Remeis-Sternwarte Bamberg and MIT. *ISIS* itself was originally developed to interactively analyze X-ray spectra, but can be used for nearly any kind of data. It is much more flexible and expandable than *XSPEC*[3] (Arnaud, 1996), which is also commonly used in X-ray data analysis. Many types of analyses involve, however, some kind of fitting of a model to observed data, which is described first in the following Section.

2.1 Model Fitting by χ^2-minimization

To fit any model to measured data, e.g., a spectrum of an accreting neutron star, the so-called χ^2-statistic can be used as soon as the number of data points, e.g., the number of counts in each energy bin is large enough such that the data are Gaussian distributed (see, e.g., Lampton et al., 1976, or Siemiginowska, 2011, for statistical details; see Sect. 3.1 for the technical details of the count rate spectrum measured by an X-ray detector). Once the model has been calculated for each data point, k, the χ^2 is given by

$$\chi^2 = \sum_{k=1}^{n} \frac{(\mathrm{data}_k - \mathrm{model}_k)^2}{\mathrm{error}_k^2} \quad , \tag{2.1}$$

where the difference between the data and model is normalized by the measurement uncertainty of the data, error, which have to be given on the 1σ, i.e., 68% confidence level. Investigating $\chi = (\mathrm{data}_k - \mathrm{model}_k)/\mathrm{error}_k$ as a function of k, called the residuals of a model, is the most used tool to qualitatively check the goodness of a fit. In this way missing components, like fluorescence lines (see Sect. 1.3.5), can be identified and their corresponding definitions can be added to the model (see Sect. 1.3.4).

To account for the increase of the χ^2 with the number of data points, n, the reduced χ^2 normalizes the χ^2 by the number of degrees of freedom, $n - p$, with the number of free fit-parameters p,

$$\chi^2_{\mathrm{red}} = \frac{\chi^2}{n - p} \quad . \tag{2.2}$$

For purely Gaussian distributed data $\chi^2_{\mathrm{red}} \sim 1$ is expected for a perfect fitting model.

[1] http://space.mit.edu/cxc/isis/
[2] http://www.sternwarte.uni-erlangen.de/isis/
[3] https://heasarc.gsfc.nasa.gov/xanadu/xspec/

To find the best-fit of a model to the data the global minimum of Eq. (2.1) has to be found, i.e., the χ^2 has to be minimized. Since the χ^2 is a function of the free fit-parameters, p, finding the global minimum is a p-dimensional mathematical task. Several fit-algorithms exist for this purpose, each using another method to find the minimum. For example, the Levenberg-Marquardt technique (Levenberg, 1944; Marquardt, 1963), known as `mpfit` in *ISIS*, *XSPEC*, and *IDL*, iteratively "moves" along the gradient of the χ^2-landscape, spanned by the fit-parameters, starting at an initial guess of the parameters provided by the user. If the χ^2-landscape features several minima the algorithm might not find, however, the global minimum in terms of the χ^2-value. Thus, the initial parameters should be near the best-fit already, which can be achieved by, e.g., investigating the spectra by eye and restricting the parameter values to physically allowed ranges.

Once the best-fit is found, that is the reduced χ^2 is close to unity, reliable uncertainties of a fit-parameter can be derived. One way is to investigate the χ^2 after Eq. (2.1) as a function of the parameter of interest, while all remaining parameters are fitted. The uncertainty at the chosen confidence level corresponds to a certain difference in the fit statistic, $\Delta\chi^2$, compared to the best-fit statistic, $\chi^2_{\rm best}$, i.e.,

$$\Delta\chi^2 = \chi^2(v) - \chi^2_{\rm best} \quad , \tag{2.3}$$

which has to be solved for the value, v, of the parameter of interest. This results in two solutions corresponding to the upper and lower confidence limits of the parameter. The default confidence level in *ISIS* is set to 90% ($\Delta\chi^2 = 2.71$), but 68% or 1σ confidences ($\Delta\chi^2 = 1$) are commonly found in the literature as well.

An issue when computing single parameter uncertainties after Eq. (2.3) arises, however, once parameter degeneracies are present. That is, the gradient at a certain point in the p-dimensional χ^2-landscape significantly depends on more than the parameter of interest. Descriptively speaking, a parameter degeneracy is present if two parameters result in a similar shape of the model. For example, a steeper spectral shape at higher energies using the `cutoffpl` (Eq. 1.45) can be achieved by either a larger photon index or a smaller folding energy. Depending on the uncertainties of the data it is often not possible to distinguish between both possibilities. Consequently, the $\Delta\chi^2$-values for the single parameter uncertainties above are statistically no longer justified. Instead, the $\Delta\chi^2$ for two degrees of freedom can be used, e.g., $\Delta\chi^2 = 2.30$ for the 68% confidence level. To visualize and check on parameter degeneracies the χ^2 as a function of two parameters of interest can be computed by fitting the remaining parameters. The resulting map of χ^2-values for the two parameters is known as a contour or confidence map. For some examples see Fig. 2.7, and for more details about contour map calculations see Sect. 1.3.4 of Hanke (2011).

2.2 Pulsar Timing Techniques

After an observation with an X-ray detector the data are often available as an event list. This list contains the arrival times of photons in the detector and their corresponding energies. To study the flux evolution of the X-ray source the events are usually binned into a time grid, which results in an event rate, strictly speaking in a count rate over time, called light curve (for details about X-ray detections and the definition of a count see Chapter 3).

To demonstrate how one can derive the pulse period from a light curve an artificial light curve of a pulsar is used in the following. This light curve is created using the

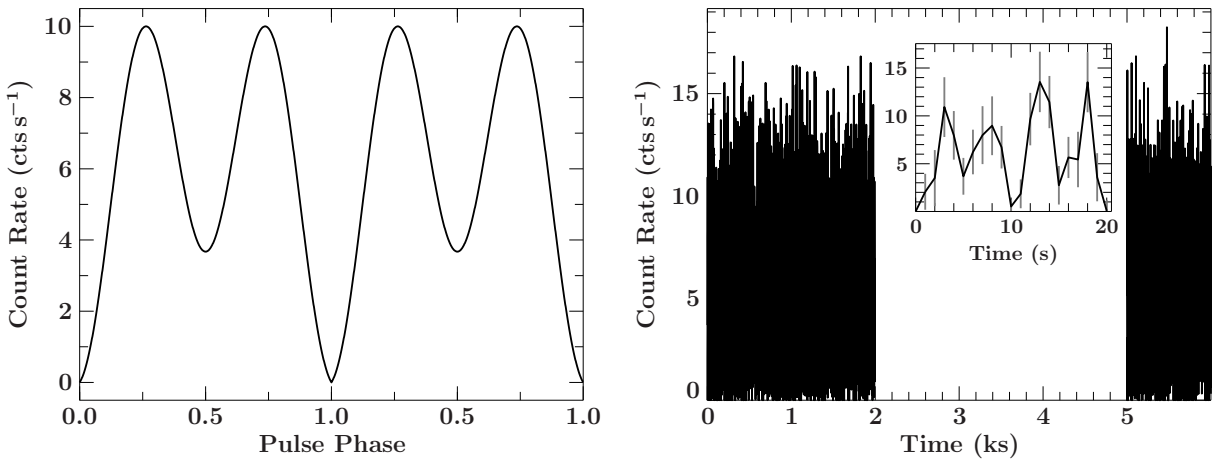

Figure 2.1: Left: The symmetric double-peaked pulse profile of 10.25 s length as used to generate the synthetic light curve. **Right:** The light curve has a gap of 3 ks in length and the full observation time spans 6 ks. The inset shows the first two pulsations in the light curve, which count rates have been randomized during the generation process.

function `fake_pulsar_lightcurve`, which has been put into the *ISISscripts*[4]. This function takes an input time grid and simulates the count rate at each time. A function called `pulseperiod2phase` is used to calculate the pulse phase, $\phi(t)$, from the given pulse period evolution, $P(t)$,

$$\frac{\mathrm{d}\varphi(t)}{\mathrm{d}t} = \frac{1}{P(t)} \quad . \tag{2.4}$$

This equation can be solved for $\phi(t)$ easily in case $P(t)$ is a Taylor series up to a specific order. Otherwise, if $P(t)$ includes orbital motion for instance, it is found numerically by integration. Then, `fake_pulsar_lightcurve` takes a synthetic pulse profile, given as count rate over pulse phase and provided by the user, and maps it onto the pulse phase grid. Finally, Gaussian noise proportional to the counts in each time bin is added to the synthetic light curve[5].

The pulse profile assumed here is shown in Fig. 2.1 (left) and follows a double-peaked shape. This kind of profile is often observed in BeXRBs, like A 0535+26 (e.g., Kendziorra et al., 1994), 4U 0115+63 (e.g., Müller et al., 2010; Ferrigno et al., 2011), or GRO J1008−57 (e.g., Kühnel et al., 2013, see Sect. 4.4). The pulse period is assumed to be $P = 10.25\,\mathrm{s}$ with a linear period change of $\dot{P} = -10^{-6}\,\mathrm{s\,s^{-1}}$ (which is rather strong compared to many observed pulsars, see Chapter 4). The light curve shown in Fig. 2.1 (right) has a total length of 6 ks with a time resolution of 1 s. For demonstration purposes a gap with no signal has been added between 2 and 5 ks.

In the following three different techniques are applied to this light curve. A quick overview about their resolution and restrictions is given in Table 2.1.

2.2.1 Fourier Transformation

To search for periodicities of any frequency the light curve can be transformed into frequency space using the Fourier transformation. This gives the amplitude of any sinusoidal signal as a function of its frequency. Due to the discretization of the light curve, x_t, as a result

[4]The source code is available at http://www.sternwarte.uni-erlangen.de/git.public/?p=isisscripts;a=blob_plain;f=src/data/pulsar/fake_pulsar_lightcurve.sl;hb=HEAD

[5]This statement is valid only if the number of counts in each bin is large enough such that the Poisson distribution can be approximated by a Gaussian distribution (see, e.g., Bevington & Robinson, 2003).

Table 2.1: Overview of the timing techniques to determine the pulse period, P, from an observed light curve of length T with N time bins of resolution Δt. The value given for the resolution of the pulse period, ΔP, is calculated for the example light curve of Fig. 2.1. For the description of each technique see the corresponding paragraph.

Technique	ΔP	(ms)	Restrictions
Fourier Transform	$P^2/(N\Delta t)$	$= 205.2$	light curve may not contain gaps; less sensitive to non-sinusoidal signals
Epoch Folding	P^2/T	$= 17.5$	computationally intense; "ghost signals" at multiples of P; used best when P is roughly known
Pulse Arrival Times	$P\Delta t/T$	$= 1.7$	pulse profile must be known and stable over the observation; requires fitting of the arrival times to derive the pulse period

from the detector's time resolution, Δt, the Fast Fourier Transformation (FFT) is usually applied (Jenkins & Watts, 1969),

$$X_\mathrm{f} = \sum_{k=1}^{2^m} x_k \exp(2\pi i f t_k) \quad \text{with} \quad f = j/T \text{ where } j = 1, 2, \ldots, 2^{m-1} \quad . \tag{2.5}$$

Here, f is the frequency of the signal and x_k is the count rate at the time bin t_k in the light curve. In general, efficient algorithms in terms of runtime exist for any number of bins, N (van der Klis, 1988). In case of an FFT the number of bins have to be, however, $N = 2^m$ such that its total length is $T = N\Delta t = 2^m \Delta t$. From the resulting Fourier transform, X_f, which is in general a complex number, the power spectral density (PSD), P_f, represents the strength of each frequency present in the light curve (Leahy et al., 1983),

$$P_\mathrm{f} = \frac{2}{N_\gamma} |X_\mathrm{f}|^2 \quad \text{with} \quad N_\gamma = \langle x_k \rangle N \Delta t \quad . \tag{2.6}$$

The PSD calculated here is normalized by the total number of photons, N_γ, where $\langle x_k \rangle$ is the mean count rate in the segments assuming that each photon results in one count. Using this normalization the expected power for a light curve of pure Poisson noise is 2 and its variance is 4 (Leahy et al., 1983; van der Klis, 1988).

Due to the finite time resolution of the light curve the highest possible frequency which can be detected, f_max, is given by the Nyquist frequency, f_c (Kurtz, 1983),

$$f_\mathrm{max} \equiv f_\mathrm{c} = \frac{1}{2\Delta t} \quad . \tag{2.7}$$

The shortest frequency, f_min, is determined by Eq. (2.5) and equal to the frequency spacing, Δf,

$$f_\mathrm{min} \equiv \Delta f = \frac{1}{T} = \frac{1}{N\Delta t} \tag{2.8}$$

We can now find the period resolution, ΔP (see Table 2.1),

$$\Delta P = \left| \frac{\partial}{\partial f} \frac{1}{f} \Delta f \right| = \frac{\Delta f}{f^2} \overset{2.8}{=} \frac{1}{N \Delta t f^2} = \frac{P^2}{N \Delta t} \quad . \tag{2.9}$$

Note that this resolution is the theoretical upper limit and does not account for, e.g., noise and background signals. If gaps are present, which need to be avoided, the light curve has to be split into segments of the same length. The final FT then is the average of the individual FTs of the segments. For the detection of sinusoidal signals, however, no averaging should be done (van der Klis, 1988).

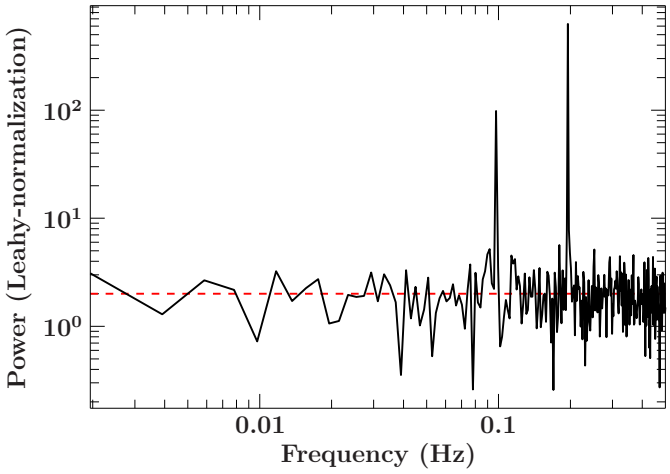

Figure 2.2: Power spectral density of the synthetic light curve of Fig. 2.1. The pulse period of 10.25 s is clearly detected at ∼0.1 Hz. The stronger peak at twice of this frequency is the second harmonic, which arises due to the double-peaked structure of the pulse profile. The red, dashed line shows the expected value of 2 for Poisson noise.

As an example, the synthetic light curve shown in Fig. 2.1 (right) is split into four segments of $N = 2^9 = 512$ bins due to using the FFT and the gap at 2–5 ks: three segments before the gap, resulting in 1536 s usable data out of 2 ks, and one segment after the gap, which covers 512 s out of 1 ks. The corresponding period resolution for $P = 10.25$ s is $\Delta P = 205.2$ ms. The final PSD is shown in Fig. 2.2 and shows a significant signal at $f = 97.6$ mHz, which is the assumed pulse period. However, an even stronger signal is seen at twice this frequency of 195 mHz. The origin of this frequency is the double-peaked structure of the pulse profile as shown in Fig. 2.1 (left). Multiple harmonics found in the PSD have to be investigated carefully to determine which frequency corresponds to the actual pulse period of the neutron star. If no complex harmonics are found, i.e., only a few multiples are detected, the shortest apparent frequency in the PSD might be interpreted as the pulse period.

2.2.2 Epoch Folding

Another method to search for periodicities in a light curve is epoch folding (Leahy et al., 1983; Schwarzenberg-Czerny, 1989). It is based on assuming a test pulse period, P_{test}, which the light curve is folded on by sorting the count rates into a pulse phase histogram,

$$H_i = \frac{P_{\text{test}}}{T_i} \sum x(i/N \leq \varphi < (i+1)/N) \quad , \tag{2.10}$$

where H_i is the mean count rate in pulse phase bin i $(= 0, \ldots, N-1)$, N is the number of phase bins within the period P_{test}, T_i is the total exposure within the pulse phase interval $i/N \leq \varphi < (i+1)/N$, with $\varphi = (t \mod P_{\text{test}})/P_{\text{test}}$, and x is the count rate in the light curve matching the pulse phase interval. The normalization factor P_{test}/T_i corresponds to the number of pulsations covered by the light curve. If the test period, P_{test}, matches an actual oscillation present in the light curve, the histogram H_i over the pulse phase bin i is equal to its pulse profile. On the other hand, the profile is averaged to a constant mean count rate if no oscillation with the assumed test period matches. Thus, H_i can be checked against a constant profile using a χ^2-test,

$$\chi^2 = \sum_{i=0}^{n-1} \frac{(H_i - \langle H \rangle)^2}{\sigma_i^2} \quad , \tag{2.11}$$

in which $\langle H \rangle$ is the averaged pulse profile, H_i, as given by Eq. (2.10) and $\sigma_i = \langle H \rangle / T_i$ a normalization factor. Since $\langle H \rangle$ is equal to the hypothesis of a constant profile, a large resulting χ^2 would cause us to refuse this hypothesis and, consequently, an oscillation with

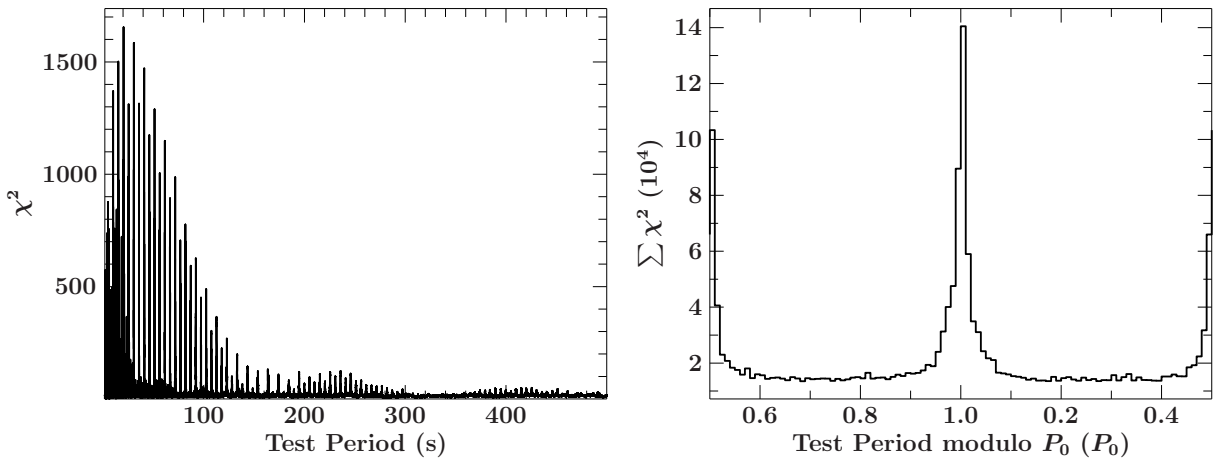

Figure 2.3: Left: Epoch folding of the full synthetic light curve shown in Fig. 2.1 over a wide range of test periods. Many significant peaks are visible, which separation is about 5 seconds. **Right:** The χ^2-landscape on the left folded on the simulated pulse period of $P_0 = 10.25\,\mathrm{s}$. The peak at 1.0 corresponds to this period, while the one at 0.5 is due to the double-peaked pulse profile. Note that the test period is given in units of P_0.

$P = P_{\mathrm{test}}$ is present. To finally search for pulsations in a light curve a range of test periods has to be checked. The resulting χ^2-distribution as a function of the test periods will have, at least, a maximum at the pulse period of the pulsar.

Other maxima, however, are present in the epoch folding result. At each multiple of the pulse period the folding of the light curve results in a periodical repeat of the actual profile. Consequently, using epoch folding to detect an unknown pulse period is not suitable compared to a Fourier analysis. Figure 2.3 (left) demonstrates this disadvantage by applying epoch folding to the synthetic light curve of Fig. 2.1 (right) in the test period range of 205.2 ms to 500 s, which is identical to the frequency range of the Fourier example shown in Fig. 2.2. The χ^2-landscape shows significant peaks at almost all multiples of $\sim$5 s, which is half of the simulated pulse period of 10.25 s. This is due to the double peaked shape of the assumed pulse profile. The χ^2-values, i.e., the significances of the detections drop with increasing pulse period due to the finite length of the light curve. The number of actual pulses folded on the test periods is decreasing, i.e., less iterations of the sum in Eq. (2.10) are performed and noise gets dominant.

The advantage of using epoch folding is that gaps are handled naturally by converting the times into pulse phase. Thus, the light curve can be used without the need for segmentation. Although a Fourier transform formally allows gaps, the resulting PSD might show complicated features, which have to be understood to allow a correct interpretation. Using the full length of the light curve leads to a high precision of the determined pulse period. Calculating the uncertainties of the period determined by epoch folding is, however, complicated due to the involved folding and χ^2-test. As a rough estimation we investigate the uncertainties of the count rate histogram, i.e., the pulse profile, of Eq. (2.10). Assuming that the relative uncertainties of the count rates in the light curve $\Delta x/x \ll 1$, the main contribution to the uncertainty of the pulse profile bin, ΔH_i, is driven by the number of iterations, n, of the sum, which is equal to the number of pulses covered by the light curve. Usually, the length of the light curve length, T, is not an exact multiple of the pulse period. Thus, n is not an integer and we can assume $\Delta n = 1$. The period uncertainty, ΔP, is then estimated to

$$P \approx \frac{T}{n} \;\Rightarrow\; \Delta P = \left| \frac{\partial}{\partial n} \frac{T}{n} \Delta n \right| = \frac{T}{n^2} = \frac{P^2}{T} \quad . \tag{2.12}$$

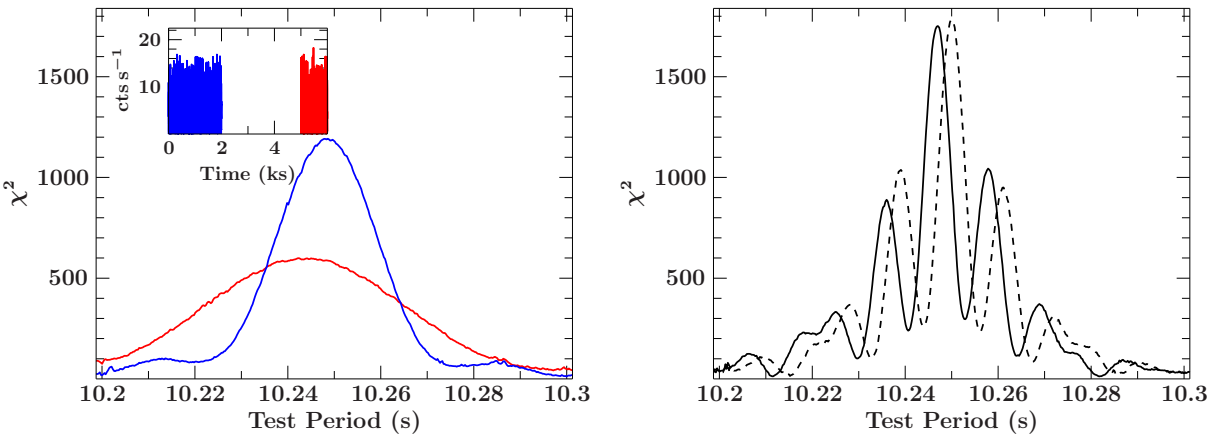

Figure 2.4: Left: Epoch folding of the first (blue) and second (red) part of the synthetic light curve as shown in the inset and Fig. 2.1. Although the maxima of the χ^2-distributions are different, pointing to a spin-up as simulated, they overlap significantly. **Right:** Epoch folding of the full light curve showing several maxima due to the gap. The dashed distribution is the result when no spin-change is simulated ($\dot{P} = 0$). Both epoch folding results are equal in shape.

This uncertainty is independent from the binning, Δt, of the light curve as compared to the theoretical uncertainty of a Fourier analysis (Eq. 2.9).

Figure 2.4 (left) shows the χ^2-landscapes of the two parts of the synthetic light curve above before (blue) and after the gap (red). The peak around 10.25 s matches the simulated pulse period in both parts. The full width at half maximum (FWHM) of the peak of the first 2 ks of the light curve is around 25 ms. The uncertainty calculated after Eq. (2.12) of $\Delta P = 52$ ms is worse. The same applies for the 1 ks part after the gap, where the FWHM and uncertainty doubled due to the shorter light curve. To derive a reliable uncertainty for real astrophysical data, Monte Carlo simulations have to be performed. Here, several synthetic light curves based on the measured pulse profile, count rate evolution, and apparent noise have to be generated by, e.g., using the `fake_pulsar_lightcurve` routine. For each generated light curve an epoch folding is performed individually. The distribution of all best-matching pulse periods usually follows a normal distribution. As the final uncertainty for the measured pulse period the standard deviation can be used. In *ISIS*, this task is performed by a function called `epferror`, which was originally implemented by J. Wilms for the *Interactive Data Language* (*IDL*).

As mentioned above one major advantage of epoch folding compared to a Fourier transformation is the handling of gaps. Gaps lead, however, to secondary maxima in the χ^2-distribution of the pulse periods, which is known as a "windowing" effect. The reason is that the true number of pulses, n, in the full light curve (including gaps) cannot be measured. If one or more pulses are "hidden" in the gap, the calculated pulse phase at the beginning and end of the gap does not change significantly. As a consequence, the folding of the light curve still results in the pulse profile and the χ^2-landscape features a peak. The peak separation can be calculated following the same idea as for the period uncertainty of Eq. (2.12) with T equal to the length of the gap. Again as illustration, Fig. 2.4 (right) shows the result of epoch folding the synthetic light curve over its full length of 6 ks (where 3 ks have no data due to the gap). Several secondary maxima are visible, the main maximum (solid line) at ∼10.253 s is narrower than those of the two parts due to the longer time base (Fig. 2.4, left). Additionally, the peak is not exactly at the simulated period of 10.25 s because of the strong spin-up, which has been included in the simulation. Compared to a light curve without spin-up (dashed line) the shape of the χ^2-landscapes are, however, equal. Thus, there is no evidence for the apparent spin-up in

the results. The separation of the peaks after having analyzed the individual light curve parts (left) might be a hint, but due to the overlapping FWHMs this difference is, at first glance, not significant. The method described in the following is able to detect and measure the spin-up. For more examples of effects produced by gaps see Kühnel (2011).

2.2.3 Pulse Arrival Times

The pulse arrival times or pulse times of arrival (ToA) are all times in the light curve, at which a pulse is detected. Once all times have been determined from the light curve they are compared with a model, in which the expected arrival times are calculated. To find the arrival time of the n^{th} pulse in a light curve, one needs to first calculate the emitting time of the pulse in the reference frame of the neutron star. The time is then transformed into the binary's reference frame. The emitting time, t_{emit}, is when the pulse phase, $\varphi(t)$, yields an integer. If we express $\varphi(t)$ as a Taylor series and use $n \equiv \varphi$, Eq. (2.4) can be solved to (see Kühnel, 2011, for details)

$$t_{\text{emit}}(n) = t_0 + P_0 n + \frac{1}{2}\dot{P}Pn^2 + \frac{1}{6}\ddot{P}P^2n^3 + \mathcal{O}(n^4)\mathcal{O}(\dot{P}^2) \quad . \tag{2.13}$$

Here, P_0 is the pulse period at the reference time t_0, $\dot{P}$ is the linear and $\ddot{P}$ the quadratic change of P over time, respectively. Finally, the Doppler shift of orbital motion adds a delay, z, to the emitting time, which then results in the observed arrival time,

$$t_{\text{obs}}(n) = t_{\text{emit}}(n) + \frac{z(t_{\text{emit}}(n))}{c} \quad . \tag{2.14}$$

The delay, z, which is often called the z-position, is equal to the position of the neutron star in the direction of the line of sight of the observer. It is calculated by solving Kepler's equation (see Eq. 1.15) and projecting the resulting position vector onto the line of sight (see, e.g., Hilditch, 2001),

$$z(t) = a \sin i \left(\sin\omega\,(\cos E(t) - e) + \cos\omega \sin E(t)\sqrt{1-e^2}\right) \quad . \tag{2.15}$$

The parameters are equal to those given in Sect. 1.2.1. For negative values of z the neutron star is in front of the tangent plane of the sky in terms of Fig. 1.8.

Determining the pulse arrival times from a light curve is, however, much more challenging than calculating the expected times. That is because a pulse pattern is needed, which is used to find matches in the light curve. For this task the pulse profile can be used. Most of the observed neutron stars have, however, a changing pulse profile with time, luminosity, or energy. While the pulse profiles of Be binaries seem to be stable during observations of a few ten ks, where the flux can be considered to be almost constant, in wind accreting binaries the variability is quite high. Furthermore, pulse profiles usually show a strong energy dependance (see, e.g., Bildsten et al., 1997), which complicates the analysis once data from multiple X-ray missions with different sensitive energy ranges are used (see Fig. 4.16 for an example). In this case the pulse profiles seen by the different detectors have to be aligned before arrival times can be determined, which introduces a systematic uncertainty.

The function `atime_det` of the *ISISscripts*-collection[6] uses one or more given pulse profiles to determine the arrival times in a light curve. Because a pulse profile is defined in pulse phase space, an initial pulse period has to be provided as well, which is used to

[6]The source code is available at http://www.sternwarte.uni-erlangen.de/git.public/?p=isisscripts;a=blob_plain;f=src/data/pulsar/arrivaltimes.sl;hb=HEAD

calculate the pulse phase for each time bin. The algorithm divides the light curve into segments of one full pulse phase in length to be able to match the pulse profile with the apparent pulse. Because the time resolution of the light curve and the pulse profile might be different the light curve segments are rebinned to match the pulse profile grid. Thus, a light curve with superior time resolution should be provided. Otherwise, interpolation might cause systematic shifts[7]. To detect the shift of the observed pulse with respect to the pulse profile their cross-correlation function is searched for the global maximum. Using the corresponding phase shift at this maximum, $\Delta\varphi$, the observed pulse arrival time of this particular pulse, $t_{\mathrm{obs},n}$, is then given by

$$t_{\mathrm{obs},n} = t_n + P_{\mathrm{obs}}(t_n)\Delta\varphi \tag{2.16}$$

with the first time bin, t_n, of the corresponding light curve segment. The measured pulse arrival times therefore depend on the actual observed pulse period evolution, $P_{\mathrm{obs}}(t)$ (see Eq. 1.17). This evolution is, however, usually not known before analyzing the data, but can be assumed to be constant as a first step. Only by iteratively fitting Eq. (2.14) to the data and determining the pulse arrival times, the final pulse period evolution, $P_{\mathrm{obs}}(t)$, including the orbital parameters can be determined.

Determining and analyzing the pulse arrival times is based on measuring the phase shifts of pulses with respect to a reference time. A simple analysis of the observed phase shifts, known as as the phase connection technique, allows to determine linear period changes ($\dot{P}$). Changes of the observed pulse period arise, however, due to the Doppler shift of orbital motion as well. Thus, interpreting the results must taken with care without taking the orbital motion (or uncertainties of the orbital parameters) into account. Defining the reference pulse phase $\varphi_0 = 0$ at the reference time t_0 the observed phase shift is equal to the evolution of the pulse phase with time after Eq. (2.4). Using $1/P(t) = f(t)$ with the frequency evolution $f(t)$, which we express as a Taylor series, the phase shift is given by (Hilditch, 2001)

$$\Delta\varphi(t) = (f_0 - f_{\mathrm{fold}})(t - t_0) + \frac{1}{2}\dot{f}(t - t_0)^2 + \mathcal{O}(t^3) \quad . \tag{2.17}$$

Here, $f_{\mathrm{fold}} = 1/P_{\mathrm{fold}}$ is the pulse period used to create the pulse profile for the pulse pattern, f_0 is the pulse frequency at t_0, and $\dot{f}$ its linear change. Again, this change can also be produced by the Doppler shift of orbital motion, since $P(t) = 1/f(t)$ is the observed pulse period evolution used in Eq. (2.16). Technically, Eq. (2.17) can be extended to any order in t, which allows to determine higher orders of the spin-change. However, the issue with the orbital motion still persists. The linear term in Eq. (2.17) is a result of the higher precision of this method compared to, e.g., epoch folding. Thus, the period used to to create the pulse profile, P_{fold}, might be inaccurate compared to the frequency, f_0, which one is able to achieve with this method. In contrast, a changing pulse period over time, i.e. $\dot{f} \neq 0$, leads to a quadratic trend in the phase shifts. The precision of the phase connection technique and, thus, the arrival times analysis is derived in the following.

The theoretical uncertainty of the pulse period determined by analyzing the pulse arrival times is given by the smallest possible phase shift, $\Delta\varphi$, which one is able to measure. Of course, a phase shift can only be detected if the analyzed pulse in the light curve segment is shifted by at least one time bin, i.e., the time resolution Δt,

$$\Delta\varphi_{\mathrm{min}} = \frac{\Delta t}{P} \quad . \tag{2.18}$$

[7]Such systematic shifts had caused a significant wrong $\dot{P}$ during the first analysis of *Suzaku*-XIS data of GRO J1008−57 (compare Sect. 4.4), where the light curve had a time resolution worse than that of the pulse profile. To avoid all problems, which might arise due to the rebinning of the light curve, the arrival times should be determined from the event files in the first place, which has not been implemented yet.

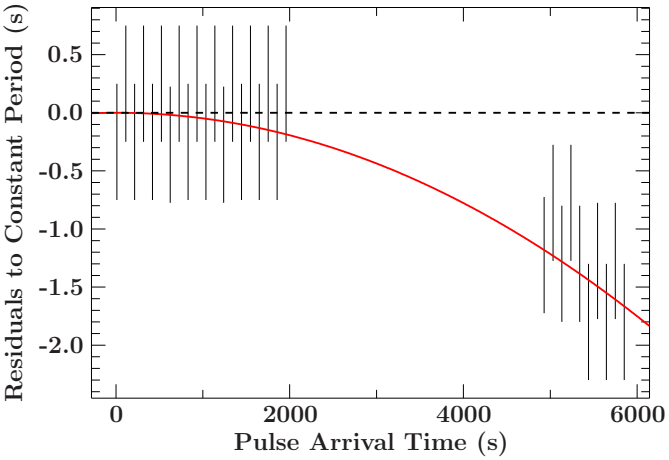

Figure 2.5: Pulse arrival times of the synthetic light curve of Fig. 2.1, averaged over 10 consecutive pulses, with respect to an assumed constant pulse period. The deviation of the arrival times of the second part of the light curve from the constant model are expected due to the spin-up as shown by the red curve.

As one can see from Eq. (2.17) the phase shift increases with time. Thus, we investigate the phase shift in the last segment of the light curve, where $t \approx T$ the light curve length. Setting $t_0 = 0$ and interpreting $f_0 - f_{\rm fold}$ as the frequency uncertainty Δf, Eq. (2.17) yields

$$\Delta\varphi = T\Delta f \;\Rightarrow\; \Delta f = \frac{\Delta t}{TP} \quad . \tag{2.19}$$

Finally, we can derive the pulse period uncertainty, ΔP, for the analysis of the pulse arrival times,

$$\Delta P = \left|\frac{\partial}{\partial f}\frac{1}{f}\Delta f\right| = \frac{\Delta f}{f^2} = \frac{P\Delta t}{T} \quad . \tag{2.20}$$

The count rates of an actual measured light curve have, however, a measurement uncertainty, which leads to an uncertainty in the determined phase shift, $\Delta\varphi$, by a cross-correlation. Thus, Eq. (2.18) is a lower limit only and the true uncertainty of the pulse period have to be determined by investigating the fit-statistics of a fit of the determined arrival times to Eq. (2.14).

Again, the synthetic light curve as shown in Fig. 2.1 (right) is used to demonstrate the pulse arrival times analysis and its derived accuracy above. The synthetic pulse profile used to create the light curve (Fig. 2.1, left) is used as the pulse pattern. Together with an assumed constant pulse period of $P = 10.25\,\mathrm{s}$ the pulse pattern is passed to the `atime_det`-function. Due to the low mean count rate of $\sim$5 cts s^{-1}, ten consecutive light curve segments have been added for the cross-correlation with the input pulse profile. Consequently, the number of determined arrival times is reduced by a factor of ten as well. Furthermore, the time elapsed between two determined arrival times is ten times the pulse period. The in this way determined pulse arrival times are shown in Fig. 2.5 relative to the assumed constant pulse period. While no apparent delay is visible for arrival times before the gap at 2–5 ks, a shift by $\sim$-1.5 ms is detected, which is in perfect agreement with the expected phase shift after Eq. (2.13) using the simulated $\dot{P} = -10^{-6}\,\mathrm{s\,s^{-1}}$. Fitting the data with the `arrivaltimes`-model as implemented in the *ISISscripts*[6] results in a pulse period of $P = 10.2518^{+0.0045}_{-0.0026}\,\mathrm{s}$ and a spin-up of $\dot{P} = -1.5^{+1.2}_{-1.6} \times 10^{-6}\,\mathrm{s\,s^{-1}}$ (uncertainties given on the 90% confidence level). The uncertainty of the determined pulse period is in very good agreement with the theoretical accuracy of $\Delta P = 10.25\,\mathrm{s} \cdot 1\,\mathrm{s}/6000\,\mathrm{s} = 1.7\,\mathrm{ms}$ after Eq. (2.20).

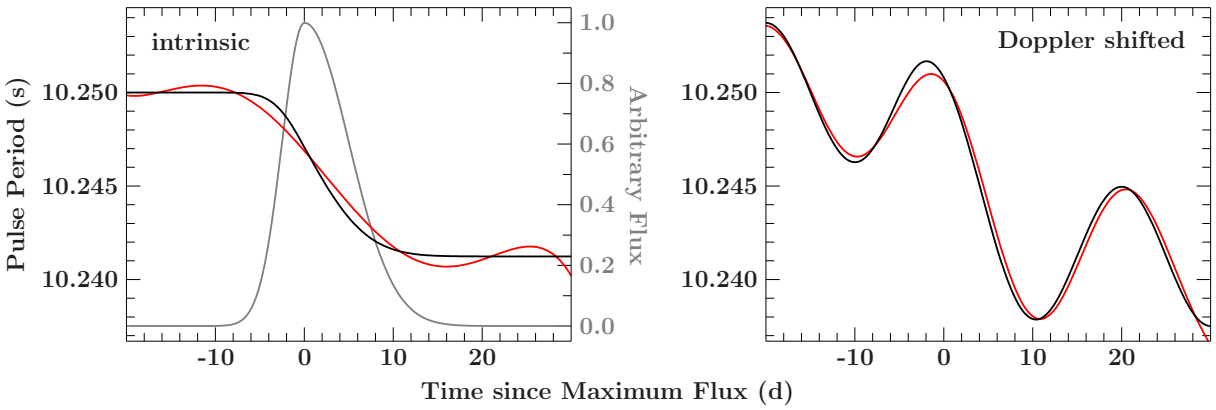

Figure 2.6: Left: Simulation (black) and polynomial fit (red) of the spin-up of a neutron star during a Be X-ray outburst. The assumed light curve of the source (gray) is used to calculate the intrinsic spin period evolution of the neutron star after the theory by GL79 (see Eq. 1.32). The spin-up is then fitted by a Taylor series up to the 5th order, which shows significant deviations from the simulated intrinsic spin-up. **Right:** These deviations complicate the fit of the actual observed pulse period, which is Doppler shifted by the binary motion. See the text for the assumed system parameters during the simulation.

2.3 Disentangling Spin-up and Orbital Motion

In order to derive the orbital parameters of accreting X-ray binaries the observed pulse period evolution, $P_{\rm obs}(t)$, of the neutron star can be studied. As described in Sect. 1.2.1, $P_{\rm obs}(t)$ is, however, a combination of the Doppler shift of orbital motion and the intrinsic spin period of the neutron star (see Eq. 1.17). Thus, a model, which can successfully fitted to the observed pulse periods, must include both of these contributions. In the literature the intrinsic spin period evolution is often described by a finite Taylor series, which leads, however, to systematic errors of the derived orbital parameters as I will show in Sect. 2.3.1. A physical motivated approach is to calculate the angular momentum transfer as caused by disk- or wind-accretion after GL79 (see Sect. 1.3.1), leading to the **Torque model**, which implementation I will describe in Sect. 2.3.2.

2.3.1 The Problem with Taylor Series

As mentioned in Sect. 2.2.3 analyzing the pulse arrival times allows to determine the observed pulse period evolution with very high precision. Most existing models calculate the intrinsic spin evolution of an accreting neutron star via a Taylor series (compare Eqs. 2.13 and 2.17),

$$P(t) = P_0 + \dot{P}_0(t - t_0) + \frac{1}{2}\ddot{P}_0(t - t_0)^2 + \mathcal{O}(t^3) \quad , \tag{2.21}$$

where P_0, $\dot{P}_0$, and $\ddot{P}_0$ are the pulse period derivatives at the reference time t_0, and apply the orbital Doppler shift after Eq. (1.17). As theoretically investigated by GL79, the spin-up caused by angular momentum transfer onto the neutron star by accretion is proportional to the source's luminosity ($\dot{P} \propto L_{37}^{\alpha}$, see Eq. 1.32). If the luminosity is changing over the time range spanned by the observations of interest, the spin-up is a non-linear function of time. Especially in BeXRBs or wind accreting binaries the luminosity is changing from days down to hours. Thus, modeling the complicated spin period evolution by a Taylor series leads to systematic uncertainties in the derived orbital parameters.

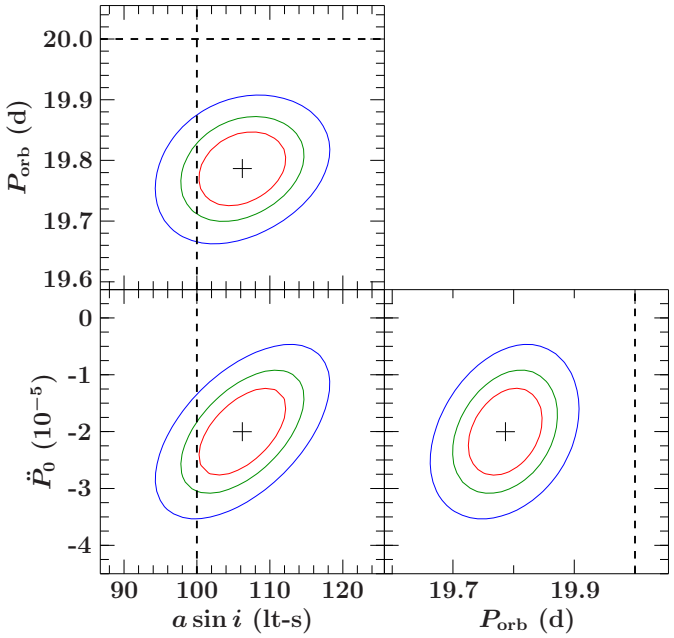

Figure 2.7: Contour maps between the semi-major axis ($a \sin i$), the orbital period ($P_{\rm orb}$), and the second derivative of the spin period evolution ($\ddot{P}_0$) for a fit of the simulated pulse period evolution of Fig. 2.6. Not only parameter degeneracies are present, visible by the tilt of the contour ellipses, but the actual assumed orbital parameters (dashed lines) do not match the fitted values also (the red contour lines represent the 68% confidence level, the green 90%, and the blue 99%.)

I demonstrate this issue by a simulation of an outburst of a BeXRB. As found in a work not presented in this thesis, the shape of an outburst light curve, $f(t)$, can be described by an asymmetric Gaussian for more than 63% of all observations (Kühnel et al., 2015a) of the form

$$f(t) = \begin{cases} f_{\rm max} \exp\left(-2\left(\frac{t-t_{\rm max}+0.5\ t_{\rm plateau}}{t_{\rm rise}}\right)^2\right), & \text{for } t < t_{\rm max} - 0.5\ t_{\rm plateau} \\ f_{\rm max}, & \text{for } -0.5\ t_{\rm plateau} \leq t - t_{\rm max} \leq 0.5\ t_{\rm plateau} \\ f_{\rm max} \exp\left(-2\left(\frac{t-t_{\rm max}-0.5\ t_{\rm plateau}}{t_{\rm decl}}\right)^2\right), & \text{for } t > t_{\rm max} + 0.5\ t_{\rm plateau} \end{cases} \tag{2.22}$$

with a plateau of $t_{\rm plateau}$ in length with the maximum flux, $f_{\rm max}$, and the middle time, $t_{\rm max}$. The rise- and decline-times, $t_{\rm rise}$ and $t_{\rm decl}$, respectively, are defined as the 2σ interval of the corresponding Gaussians. In this way, the sum of all three time intervals, $t_{\rm rise}+t_{\rm plateau}+t_{\rm decl}$, covers 95% of the integrated observed flux.

For the simulation, the outburst light curve shown in Fig. 2.6 (gray line) is assumed, which properties are similar to typical observed BeXRB outbursts (compare with the data presented in Chapter 4 and 5). Using this light curve, the intrinsic spin-up evolution of an artificial neutron star with a pulse period of 10.25 s is calculated for accretion from a disk after the theory by GL79 (see Sect. 1.3.1 and its implementation into *ISIS* described in Sect. 2.3.2). The resulting simulated spin period evolution is shown in Fig. 2.6 (left, black line) and shows a complex shape, which is linear decreasing during a short time around the maximum flux only. Finally, a Doppler shift of a circular orbit with $P_{\rm orb} = 20$ d and $a \sin i = 100$ lt-s is applied to the intrinsic spin period evolution and the resulting observable pulse period evolution is shown in Fig. 2.6 (right, black line).

The pulse period evolution simulated in this way is now fitted by a polynomial up to the fifth order for the intrinsic spin period evolution, which gets modified by the Doppler shift of orbital motion (see Eq. 1.17). For the fit, uncertainties of 1 ms are assumed for the fake period measurements. No random noise has been added to the data in order to reveal systematic shifts in the fit-parameters due to the simple model for the intrinsic spin period evolution. The fitted spin period and Doppler shifted period is shown in Fig. 2.6 (left and right, respectively, red curve).

The modeled spin period evolution does not describe the simulated evolution well. Even

around the reference time ($t = 0\,\mathrm{d}$) the apparent spin-up is systematically off. At the same time, the full model including the Doppler shift reproduces, however, the simulated data much better. Thus, it is expected that the fitted orbital parameters actually model this mismatch in the intrinsic evolution. To prove this speculation, Fig. 2.7 shows contour maps between the orbital parameters (P_{orb} and $a \sin i$) and the second order Taylor coefficient of the spin period evolution ($\ddot{P}_0$). There is a parameter degeneracy between the semi-major axis, $a \sin i$, and $\ddot{P}_0$, showing that the orbit and intrinsic spin period cannot be disentangled completely. Furthermore, the best-fit value for $a \sin i$ is at least 1σ off from the assumed input value (dashed line). The value for the orbital period, P_{orb}, is more than 4σ away from the input value. This dramatically shows that a fit assuming a Taylor series for the intrinsic spin period evolution significantly effects the fitted orbital parameters, which can be off from the true values.

2.3.2 The Torque Model

As shown in the last Section, modeling the intrinsic spin period evolution, $P(t)$, of an accreting neutron star by a Taylor series (Eq. 2.21) can result in parameter degeneracies with and significant systematic shifts in the orbital parameters. As a first solution[8], the theoretical angular momentum transfer theory after GL79 (see Sect. 1.3.1) is used here. My implementation as a model for fitting observed pulse periods is described briefly in the following. A description of how to use this model in *ISIS* is found in appendix D and applications to real data are found in Chapter 4.

The model `pulsarorbit` as implemented into the *ISISscripts*[9] solves the simplified differential equation for the angular momentum transfer (Eq. 1.32),

$$\dot{P}(t) = -bP(t)^2 L(t)^{\alpha} \quad , \tag{2.23}$$

with $\alpha = 6/7$ for disk- and $\alpha = 1$ for wind-accretion, the torque strength b, and the luminosity of the source, $L(t)$. In order to solve this equation for observational data we assume that the luminosity of the source is proportional to the source's flux, $F(t)$, as measured by a certain X-ray detector. Integrating then leads to

$$P(t) = P_0 + a(t - t_0) - b \int_{t_0}^{t} \left(\frac{P(t')}{P_0} \right)^2 \left(\frac{F(t')}{F_{\mathrm{ref}}} \right)^{\alpha} \mathrm{d}t' \quad , \tag{2.24}$$

with the spin period P_0 at the reference time t_0. The linear term $a(t - t_0)$ is a formal modification to allow for a constant spin-down due to, e.g., the propeller effect (see Eq. 1.33), with the constant a given in $\mathrm{s\,s^{-1}}$. The normalization constants P_0 and F_{ref} are used to express b in units of $\mathrm{s\,s^{-1}}$, which is the same unit as for the Taylor coefficient $\dot{P}_0$ in Eq. (2.21) usually found in the literature. Thus, b can be understood as the (stationary) spin-down at the flux F_{ref} and the spin period P_0.

Before the spin period evolution is calculated, the input time grid of the given flux, $F(t)$, is corrected for the binary motion by shifting the times by the inverse z-position (see Eq. 2.15). Then Eq. (2.24) is numerically integrated with the trapezoidal rule for each time, t, on the corrected time grid of the flux. Since the measured flux might scatter around zero the absolute value is taken to avoid complex numbers. The sign of $F(t)$ is included separately in the integration. Thus, negative flux values result in a spin-*down*.

Initially, the spin period evolution on the right side is assumed to be $P(t') = P_0$ and then iteratively set to the result of the previous integration. Usually, the spin period

[8] As a next step, recent accretion torque theories (see references in Sect. 1.3.1) will be implemented.

[9] The source code is available at http://www.sternwarte.uni-erlangen.de/git.public/?p=isisscripts;a=blob_plain;f=src/fitting/fit-functions/pulsar.sl;hb=HEAD

Table 2.2: The parameters of the torque model as implemented as the fit-function `pulsarmodel` in the *ISISscripts*. The name corresponds to the parameter in *ISIS*. The parameters of the intrinsic spin period evolution correspond to Eq. (2.24) and for the definition of the orbital parameters see Sect. 1.2.1

parameter	name	unit
P_0	p	s
t_0	t0	MJD
a	a	s/s
b	b	s/s
α	alpha	
F_{ref}	L0	same as $F(t)$
$a \sin i$	asini	lt-s
P_{orb}	porb	d
τ	tau	MJD
e	ecc	e
ω	omega	degrees

evolution converges after only a few iterations. To avoid an infinite loop, however, the number of iterations is limited to ten by default. Finally, the spin period evolution is interpolated onto the time grid of the measured periods and multiplied by the Doppler shift of orbital motion after Eq. (1.17).

2.4 Analyzing Many Datasets Simultaneously

This Section is heavily based on Kühnel et al. (2015b, 2016a) and taken partly in verbatim from there.

Many publications in X-ray astronomy either concentrate on a single observation or on comparisons between many observations. Especially for the science of cyclotron lines monitoring campaigns are needed, since the line energy shows a correlation with the X-ray luminosity (see Tsygankov et al., 2010; Staubert et al., 2014; Malacaria et al., 2015, for some examples). As found by myself, the continuum parameters of some sources show a strong dependency on the luminosity as well (Kühnel et al., 2013, see Sect. 5.1 and 5.2). In contrast to a single cyclotron line the continuum is described, however, by more parameters. Once parameter degeneracies are present, for example between the photon index and the folding energy, Γ and E_{fold}, respectively (see Eq. 1.45), it is commonly accepted to fix parameters to a reasonable value. The same holds true once a parameter cannot be constrained due to an insufficient signal to noise ratio. A third example for fixing parameters arises if a previous analysis reveals that certain parameters seem to be stable, i.e., do not change over, e.g., time or flux. Unfortunately, it is difficult to determine the true value a parameter is fixed to, especially if parameter degeneracies are present. In a worst case, fixing a parameter might lead to systematic errors in modeling the data. Solving these issues is not possible, however, using a single observation.

The solution is to fit many observations simultaneously, where the parameters of interest are not allowed to vary between the individual observations, but their values are fitted by a combination of all data. This enables further advantages, such as that stable parameters can be determined with very high precision. Furthermore, the degrees of freedom are reduced, which allows to better constrain the remaining parameters. Finally, all observations under consideration are handled the same way, which prevents potential inconsistencies during the analysis. A simultaneous fit requires, however, a lot of individual

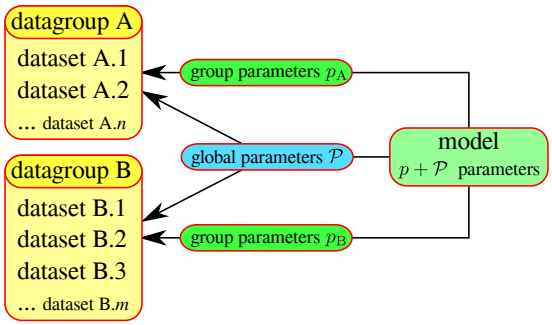

Figure 2.8: Terminology of simultaneous fits as implemented in *ISIS* (taken from Kühnel et al., 2016a). Many individual datasets define a datagroup, A and B for example. Each datagroup has its own set of group parameters, p_A and p_B. The global parameters, $\mathcal{P}$, affect all defined datagroups.

parameters for each observations, such as the flux. Quickly, the number of free parameters increases dramatically due to the potential large number of observations loaded into the fit[10]. The terminology of this kind of an analysis, called a simultaneous fit, and how to investigate its goodness is the subject of this Section. See appendix E for the corresponding implementation into *ISIS*.

2.4.1 Terminology

As mentioned above, parameters can act on individual as well as on all defined datasets. Therefor, I first define a simple terminology describing the structure of a simultaneous fit, which is illustrated in Fig. 2.8.

A dataset, e.g., a spectrum, represents a snapshot of a certain state of a physical object, e.g., a neutron star at a specific flux level. Several different detectors might have observed the object in the same state, i.e., at the same time. For instance, most X-ray satellites have more than one detector onboard (see Chapter 3), which enables to observe the source in different energy bands in most cases. The datasets representing the same physical state define a so-called datagroup. Such a group is labeled with a capital letter, e.g., A, and the different datasets are followed by a number, e.g., A.2 as in Fig. 2.8.

In principle, all datasets within a datagroup should result in the same fit-parameters. An exception might be detector calibration constants, but those can be handled differently (see below). In a simultaneous fit, each datagroup is fitted by the same parameters, called group parameters, labeled p_x with the datagroup X. Thus, a simultaneous fit of n datagroups to a model with p parameters has $n \times p$ parameters in total.

Certain model parameters can be set to be global parameters. Such a global parameter has the same value among all datagroups. Consequently, the parameter is no longer listed in the individual group parameters. Fitting a global parameter takes a long time, since all dataset have to be taken into account during the fit, in contrast to fitting group parameters. The advantage is a reduced number of degrees of freedom for each datagroup. This allows to, e.g., better constrain the group parameters. In many cases, global parameters can be the detector calibrations constants (as long as the calibration or data reduction is the same for all observations). A simultaneous fit of n datagroups with p group parameters, from which $\mathcal{P}$ are global parameters, has $n \times (p - \mathcal{P}) + \mathcal{P}$ total parameters. From now on, however, the number of group parameters, p, corresponds to the free group parameters, i.e., it is already reduced by $\mathcal{P}$ as in Fig. 2.8.

2.4.2 Goodness of a Simultaneous Fit

One issue, which might arise during a simultaneous fit of multiple observations, is that a few datagroups might not be described well by the chosen model or that the best-fit is

[10] This issue raised specific question 8.

still not found. In the commonly used χ^2-statistics this information might be hidden due to the large number of degrees of freedom. After a fit has been performed in, e.g., *ISIS*, the total number of degrees of freedom and the χ^2 and χ^2_{red} is displayed as a measure of the goodness of the fit as defined in Eqs. (2.1) and (2.2).

To demonstrate the issue of a hidden failed fit in case of a simultaneous fit, we adjust Eq. (2.2) to include the the number of datagroups, N, with the corresponding group parameters, p_i, for each datagroup, i, and the global parameters, $\mathcal{P}$,

$$\chi^2_{\mathrm{red}} = \frac{\sum_{i=1}^{N} \chi_i^2}{(\sum_{i=1}^{N} n_i - p_i) - \mathcal{P}} \quad . \tag{2.25}$$

The χ_i^2 for each datagroup is calculated after Eq. (2.1) with the corresponding number of degrees of freedom, $n_i - p_i$. If almost all datagroups are near $\chi_i^2 = 1$, but a particular datagroup, i, failed fit with, e.g., $\chi^2 = 2$, the χ^2_{red} after Eq. (2.25) will converge to unity for a large number of datagroups, N. Thus, the "classical" χ^2_{red} misleadingly indicates a successful simultaneous fit. There are three suggestions to avoid this issue and detect failed fits of particular datagroups, which are presented in the following. Examples of all suggestions can be found in Chapter 5.

Investigate the histogram of the χ^2_{red} of all datagroups
One way to check on a failed fit is to investigate the individual $\chi^2_{\mathrm{red,i}}$ of each datagroup i (compare Eqs. 2.1 and 2.2), calculated by

$$\chi^2_{\mathrm{red,i}} = \frac{\chi_i^2}{n_i - p_i} \quad . \tag{2.26}$$

To simplify this investigation the $\chi^2_{\mathrm{red,i}}$ of all datagroups are sorted into a histogram. Such a histogram has been added as a separate function, `group_stats` (see appendix E), to the simultaneous fit structure. It is called automatically after the group or global parameters have been fitted, such that a failed fit can be identified by the user at first glance.

Defining a combined reduced χ^2
The interpretation of Eq. (2.25) is that all datagroups represent the same physical state of the observed object. That is because the sum of all χ_i^2, which is equal to the total χ^2, is normalized by the total number of degrees of freedom. However, as explained above, a datagroup is defined as the datasets taken within the same context, e.g., at the same time. As a consequence, the χ^2_{red} should be calculated for each datagroup separately. Furthermore, the degrees of freedom of each datagroup has to be reduced by the number of global parameters, $\mathcal{P}$, because these parameters are determined by all datagroups simultaneously. Finally, we can define a combined reduced χ^2 which takes these aspects into account,

$$\chi^2_{\mathrm{red,comb.}} = \frac{1}{N} \sum_{i=1}^{N} \frac{\chi_i^2}{n_i - p_i - \mu_i \mathcal{P}} \quad . \tag{2.27}$$

Here, the χ_i^2 for each datagroup i is calculated after Eq. (2.1). The weighting factor μ_i accounts for the effect of each datagroup on the determination of the global parameters. It scales approximately with the relative number of degrees of freedom of a datagroup to the total number of degrees of freedom,

$$\mu_i \approx (n_i - p_i) \times \sum_{j=1}^{N} \frac{1}{n_j - p_j} \quad . \tag{2.28}$$

If some datasets are not, however, sensitive to a certain global parameter, e.g., the energy grid of a spectrum does not include the cyclotron line, Eq. (2.28) has to be modified accordingly.

Please note, however, that Eq. (2.27) is the result of an empirical study. A more sophisticated goodness would alter the underlying statistics, e.g., following a Bayesian approach instead of the χ^2-statistics. Furthermore, the combined reduced χ^2 does not affect the best-fit found by a χ^2-minimization, which is still calculated after Eq. (2.1). The advantage is, however, that in the case of a failed fit or a weak feature, which is visible in the combination of the residuals only (see below), the $\chi^2_{\mathrm{red,comb.}}$ is higher than the traditional χ^2_{red}. Usually, this triggers a further investigation of the data.

Combining the residuals of all datagroups

In some cases the number of degrees of freedom for each datagroup, i.e., $n_i - p_i = n - p$ are equal for all i, for instance once the spectra have been taken by the same detector and the same channel binning has been applied. Using Eq. (2.1) and $f = N(n - p - \mu\mathcal{P})$ the combined reduced χ^2 (Eq. 2.27) then is

$$\chi^2_{\mathrm{red,comb.}} = \frac{1}{f} \sum_{i=1}^{N} \sum_{k=1}^{n} \frac{(\mathrm{data}_{i,k} - \mathrm{model}_{i,k})^2}{\mathrm{error}^2_{i,k}} \quad . \tag{2.29}$$

The summand does not depend on i nor k explicitly. Consequently, it is allowed to switch the order of the sums. Interpreting k as spectral energy channel the final statistic is a function of k,

$$\begin{aligned} \chi^2_{\mathrm{red,comb.}}(k) &\propto \sum_{i=1}^{N} \frac{(\mathrm{data}_{i,k} - \mathrm{model}_{i,k})^2}{\mathrm{error}^2_{i,k}} \\ &\propto \sum_{i=1}^{N} \mathrm{data}^2_{i,k} \quad . \end{aligned} \tag{2.30}$$

Thus, each energy channel of all datagroups of the simultaneous fit is summed up in the calculation of the combined reduced χ^2. In the context of a spectral analysis, this is a dramatic increase of the total exposure in each energy bin k. To check on any weak features in each energy channel, the combined residuals of all datagroups, $R(k)$, as a function of k can be investigated,

$$R(k) = \sum_{i=1}^{N} \mathrm{data}_{i,k} - \mathrm{model}_{i,k} \quad . \tag{2.31}$$

In a similar way, the spectra of a simultaneous fit can be combined into a single spectrum for plotting purposes. Once all spectra are on the same energy grid, the data in each energy channel can be summed over all datasets weighted by their statistical uncertainty. The combined model to be plotted is handled in the same way and, thus, the response for each individual dataset is still taken into account (see Sect. 3.1 for details). The `plot_data`-function as available in the *ISISscripts*, written by M. A. Nowak, can be used to do these tasks.

Chapter 3

Detecting X-rays of Extraterrestrial Sources

X-rays interact much more weakly with matter than photons with longer wavelengths, such as optical light. Thus, detecting X-ray photons and measuring their arrival time and energy is a challenging task. Furthermore, Earth's atmosphere blocks X-ray radiation, which requires detectors to be assembled on satellites and launched into space. This raises further requirements on the detectors as incident cosmic rays and particles trapped in the Earth's magnetosphere interact with the satellite.

In principle, X-rays can be detected by their ionizing effect (similar to Fig. 1.25) This is the bases for the following classes of X-ray detectors (see Knoll, 1999, for details and more detection technologies).

- *Proportional Counters*
  Electrons produced by ionizing the detection material, which are light gases like Xenon in most cases, are collected by anodes. In first order, the number of measured electrons is proportional to the number of photons penetrating the detector. The main advantage of this detector type is that it can be big in size, which results in a very high sensitivity for weak sources. However, the direction of the incident photon cannot be determined unless the X-ray radiation is collimated. Furthermore, the detection materials used in proportional counters are most sensitive for soft X-rays between 1 and 10 keV only[1].
- *Scintillators*
  In order to detect hard X-rays[1] between 10 and 100 keV, heavier atoms have to be used as detector material. Such materials, e.g. iodine, are bound in crystals and, thus, anodes cannot be used to collect the produced electrons. These electrons are converted, however, into lower energy photons, e.g., UV photons through sites of doped material within the crystal. Using, e.g., photo multipliers these photons are converted into an electrical signal. Like for proportional counters, the direction of the incident X-ray radiation cannot be reconstructed in scintillators, such that collimators have to be used.
- *Charge Coupled Devices* (CCDs)
  The transition zone between two layers of specifically doped semiconductors, called a photodiode, is sensitive to incoming photons. Electrons are excited from the valence into the conduction band, where they are collected and readout by an external voltage. The semiconductor used, such as silicon, and the doping determine the minimum photon energy required to excite electrons. In X-ray astronomy the photodiodes are sensitive for photons above $\sim$0.1 keV[1]. As photodiodes are tiny in size compared to proportional counters the incoming X-ray radiation has to be focused to increase the sensitivity. A so-called Wolter telescope focuses X-rays by grazing incidence mirrors onto a chip made of a 2D-grid of photodiodes (CCD), which results in an

[1] The definition of these energy ranges differ among the literature and are often specific for each detector. Here, the definition is based on orders of magnitude.

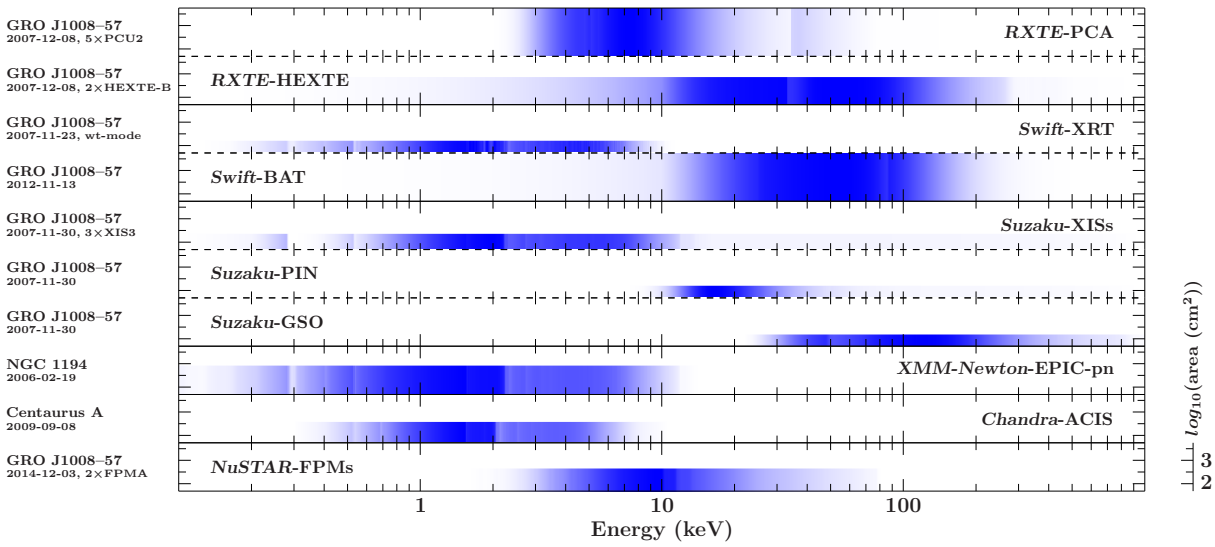

Figure 3.1: Sensitive energy ranges and effective areas ($A(E)$; ARF), of the various X-ray instruments used in this thesis (inspired by Fig 1.17 of Hanke, 2011). In each panel the effective area of an instrument relative to itself is color coded, while the height is proportional to the maximum effective area of the instrument. The observed source and date, from which the ARF is taken, is labeled on the left. The ARFs of *XMM-Newton*-EPIC-pn and *Chandra*-ACIS have been provided by E. Fink (priv. comm.) and C. Gräfe (priv. comm.), respectively. Note that instruments consisting of multiple identical detectors have been multiplied by their number as indicated.

actual image (see, e.g., Fürst, 2011, for a summary about X-ray mirrors). The focal length of these telescopes determine the highest possible photon energy, which is still focused onto the CCD, which is usually around 10 keV.

For high photon fluxes it gets probable that more than one photon hits the same pixel on the CCD during the same readout cycle. As no information about the number of photons is available, the total energy of both photons is misleadingly interpreted as the energy of a single photon. This effect, known as pile-up, leads to a distortion of the resulting X-ray spectrum as soft photons seem to be missing, while more hard energy events are detected. To avoid pile-up effects region on the CCD exposed by high photon fluxes have to be avoided during the data extraction.

3.1 Detector Response

Depending on the technology used an X-ray detector is sensitive to a certain X-ray energy range. Furthermore, the discrete electron levels of the materials involved in the detection process (e.g., the detection material itself, the collimators, or the mirrors) can result in sudden changes in the sensitivity. Thus, this sensitivity on the photon energy, E, is a complicated function, $A(E)$, which is called the *ancillary response function* (ARF). It is usually normalized to the size of a perfect detector with 100% photon sensitivity at each energy. Thus $A(E)$ is given in units of cm^2 and also known as the effective area of the detector. Figure 3.1 shows the ARFs of all instruments used in the present thesis. The effective area often depends on the angle between the optical axis of the detector and the source, such that $A(E)$ is unique for each observation.

Reconstructing the photon energy from a single signal is a complex procedure due to the nature of the detection process. First, the detectors have a finite energy resolution, which leads to a distribution of signals with the same energy over the detector's energy

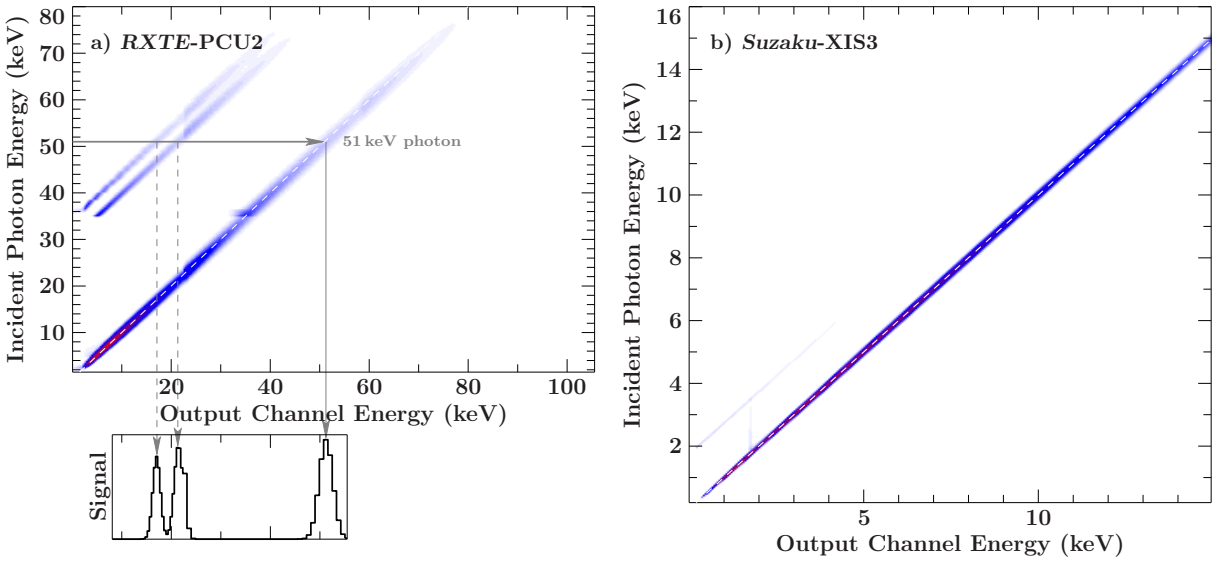

Figure 3.2: Examples for Response-Matrix-Functions (RMF). Color coded (from white via blue to red) is the probability that an incident photon with a certain energy is detected at an output channel energy. The white dashed line follows an identity matrix. **a** The RMF of *RXTE*-PCU2, which contains the effective area as well. An X-ray photon might cause further signals at lower energies, like the escape peaks in *RXTE*-PCU2 above ∼35 keV. Here, an example photon of 51 keV leads to the detection of three signals (gray lines and histogram at the bottom). **b** In CCD-detectors, such as *Suzaku*-XIS3, these escape peaks are not as prominent. Note the different sensitive energy ranges of both detectors (compare Fig. 3.1).

channels. That is, an artificial beam of monochromatic X-ray photons results in a broad peak in the measured spectrum. Secondly, a photon does not necessarily result in a single signal. For example, once the energy of a photon is sufficient to ionize an L-shell electron in the detection material, a Kα fluorescence photon is emitted. Thus, the energy of the registered signal is reduced by the energy of this photon. As the detector's cross-section at the energy of the fluorescence photon is reduced, some of these photons will leave the detector without causing a further signal. These events are visible as so-called escape peaks in the spectrum. Figure 3.2a shows an example for escape peaks in *RXTE*-PCU2 (see Sect. 3.2.1 for a brief description). In CCD detectors, such as *Suzaku*-XIS3, these escape peaks are less pronounced (see Fig. 3.2b). To account for these effects the detector's energy response is described by a matrix, $R(i, E)$, called *redistribution matrix function* (RMF). It contains the probability that an incident photon with energy E is detected in the detector channel i.

The measured X-ray spectrum of a source is contaminated by the *background spectrum*, $B(i)$, which consists of two major contributions. The first is the detector background caused by the decay of radioactive isotopes within the satellite, which were activated by, e.g., cosmic rays. The second contribution is the non X-ray background, like noise and directly detected cosmic rays. Note that the X-ray background which originates from, e.g., unresolved background sources, is not included in $B(i)$, but rather measured together with the source's spectrum.

In summary, a source spectrum, $S(E)$, as measured by an X-ray detector is given by

$$C(i) = T \int_0^\infty R(i, E) A(E) S(E) \mathrm{d}E + B(i) \quad , \tag{3.1}$$

where $C(i)$ is the number of events (called *counts*) in the detector's energy channel i. Here the source spectrum, $S(E)$, is assumed to be constant over the exposure time,

T, given in units of photons $s^{-1}\,cm^{-2}\,keV^{-1}$ (called *photon space*). The corresponding measured spectrum, $C(i)$, is given in counts and looks different to $S(E)$, even normalized to counts $s^{-1}\,keV^{-1}$ after the background has been subtracted (called *detector space*).

The detector's response is not a stable function over time since the satellite in space is constantly exposed to cosmic rays and highly energetic particles. Even micro meteorites can damage the detector and alter its response. To update the detector's response functions, RMF and ARF, regular calibration observations are required. The Crab pulsar (see Fig. 1.2) is usually used in X-ray astronomy as a standard candle, i.e., a source with a stable spectrum over time (see, e.g., Kirsch et al., 2005, and references therein). In recent years, however, it was found that the Crab is variable over time (Wilson-Hodge et al., 2011), which causes cross-calibration issues among the various X-ray missions.

3.2 X-ray Missions

In this Section a brief description of the X-ray detectors used in this thesis is given. Table 3.1 provides an overview about important properties of each detector and Fig. 3.3 illustrates the spacecrafts with the detectors onboard.

3.2.1 *RXTE*

The *Rossi X-ray Timing Explorer* (*RXTE*) was launched in 1995 December and operated until the beginning of 2012. It consisted of three instruments, the *Proportional Counter Array* (PCA; Jahoda et al., 2006), the *High Energy X-ray Timing Experiment* (HEXTE; Rothschild et al., 1998), and the *All Sky Monitor* (ASM; Levine et al., 1996; Bradt et al., 2007). For a detailed summary of the instruments see, e.g., Hanke (2011) or Fürst et al. (2011).

PCA itself was an array of five identical detectors, the *Proportional Counter Units* (PCUs, labeled 0–4). Each PCU contained a propane layer on top of four xenon layers, which detected X-rays in the 3–50 keV regime. The propane as well as the bottom xenon layers were used as veto layers to determine whether a signal was caused by a high energy photon or particle entering the detector from the side. In 2000 May 12 the PCU0 was hit by a micro meteorite, which caused the loss of propane and making this PCU unavailable for data analysis[2]. Often, data analysis is restricted to PCU2 as it is known as the best calibrated one (Jahoda et al., 2006). Furthermore, only data from the "top-layer", i.e., the first xenon layer is extracted for the same reason. The background of each PCU could not be measured directly, rather it had to be modeled.

The HEXTE consisted of two identical instruments, cluster A and B, which themselves were made of four[3] NaI/CsI scintillators, connected to photo multiplier tubes. The light pulse's decay time within the CsI crystal is different to that within the NaI crystal. Pulse shape discriminators analyzing the decay time of an event were able to identify in which crystal the event took place. An event in both crystals at the same time was considered as a background event caused by a charged particle traveling through the detector. Thus only event in the NaI crystal, which was located in front of CsI crystal, were accepted as X-ray photon events. To measure the background both HEXTE clusters were alternating every 16 s between two positions – 1.5° or 3° off source (the "+" and "-" background positions) and the on-source position. Due to a crossed movement of both cluster, the

[2]See http://heasarc.gsfc.nasa.gov/docs/xte/whatsnew/big.html

[3]Two months after launch of *RXTE* the electronics of cluster B's scintillator #3 failed partly and data could no longer be used since then.

Table 3.1: Overview of the properties of the X-ray satellites and instruments used in this work (inspired by Tab. 3.1 of Fürst et al., 2011). The given values should be understood as a guide since the actual values depend on the performed observation. Note that the instruments onboard *Fermi* are not listed here as it is designed as a gamma-ray mission (see Sect. 3.2.7 for a brief description).

Satellite/ Instrument	Description paper	FoV[a] (arcmin)	E range[b] (keV)	ΔE @E [c] (keV) (keV)	$A(E)$ @E [d] (cm^2) (keV)	T-res[e] (ms)
RXTE						
ASM	Levine et al. (1996) Bradt et al. (2007)	360×5400	1.5–12	[f]	3×30 @5	125
PCA	Jahoda et al. (2006)	60	3–50	1 @6	5×1000 @8	0.001
HEXTE	Rothschild et al. (1998)	60	15–250	10 @60	2×4×200 @60	0.0076
Swift	Gehrels et al. (2004, 2005)					
XRT	Burrows et al. (2005)	23.5	0.2–10	0.14 @5.9	120 @1.5	1.8–2500
BAT	Barthelmy et al. (2005)	1500×900	15–150	7 @122	1700 @60	200
Suzaku	Mitsuda et al. (2007)					
XRS[g]	Kelley et al. (2007)	2.9	0.3–12	0.006 @6	180 @6	∼100
XIS	Koyama et al. (2007)	18	0.2–10	0.13 @6	4×330 @1.5	8
HXD/PIN	Takahashi et al. (2007) Kokubun et al. (2007)	34	10–70	4 @40	160 @20	0.061
HXD/GSO	Takahashi et al. (2007) Kokubun et al. (2007)	270	40–600	24 @100	260 @100	0.061
XMM-Newton	Jansen et al. (2001)					
EPIC-pn	Strüder et al. (2001)	30	0.15–15	0.15 @5.9	1200 @1.3	0.007–199.2
EPIC-MOS[h]	Turner et al. (2001)	30	0.2–10	0.15 @5.9	500 @1.3	1.75–2600
RGS[h]	den Herder et al. (2001)	N/A	0.33–2.5	0.16 @2	140 @0.8	5700
Chandra						
ACIS	Garmire et al. (2003)	16	0.5–8	0.1 @3	500 @2	2.85–3200
HRC[h]	Murray et al. (2000) Kraft et al. (2000)	31	0.07–10	1 @1 [i]	250 @1	0.016
NuSTAR	Harrison et al. (2013)					
FPMA & -B	Harrison et al. (2013)	10	3–79	0.4 @10	850 @10	0.002

Notes. [a] Field of View. [b] Sensitive energy range. [c] Energy resolution at a specific energy. [d] Effective area at a specific energy. If the detector is composed of multiple identical instruments the effective area of one instrument is then given with the total number of instruments as a factor. [e] Time resolution. Different read out modes can modify the time resolution. [f] *RXTE*-ASM had the energy channels 1.5–3.0, 3–5, and 5–12 keV. [g] The *Suzaku*-XRS failed after launch and is listed for completeness. [h] Not used in this thesis but listed for completeness. [i] The HRC is optimized for use with gratings and not intended to measure energies intrinsically (see http://cxc.harvard.edu/proposer/POG/pdf/MPOG.pdf for details).

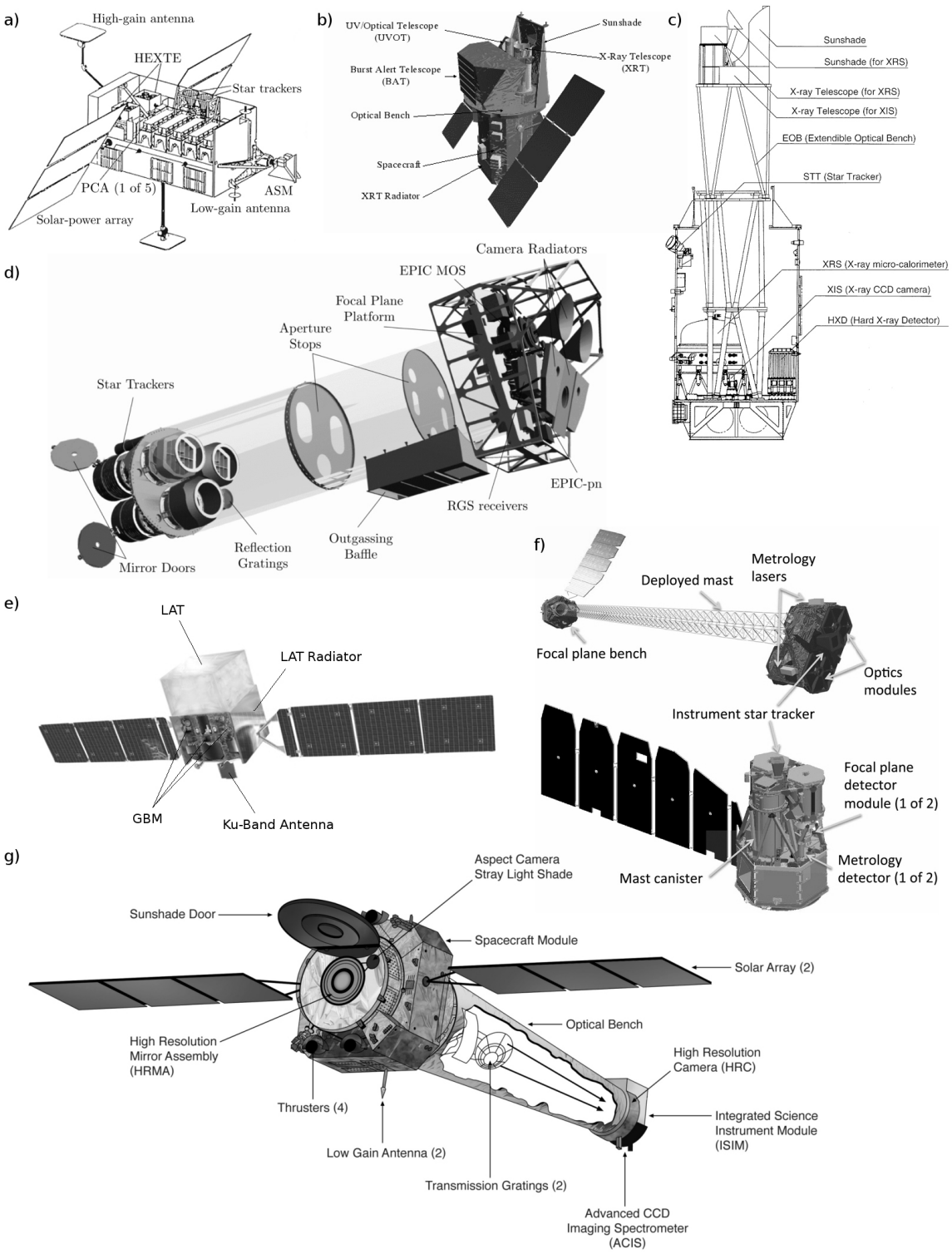

Figure 3.3: Sketches of **a:** the *Rossi X-ray Timing Explorer* (*RXTE*, image taken and modified from https://heasarc.gsfc.nasa.gov/docs/xte/xte_images.html#scraft), **b:** *Swift* (image taken and modified from from http://www.swift.ac.uk/about/instruments.php), **c:** *Suzaku* (image taken from and modified from Mitsuda et al., 2007), **d:** *XMM-Newton* (image taken and modified from http://xmm.esac.esa.int/external/xmm_user_support/documentation/technical/Spacecraft/xmm_payl.shtml, courtesy of Dornier Satellitensysteme GmbH), **e:** *Fermi* (image taken and modified from http://fermi.sonoma.edu/multimedia/gallery/index.php, courtesy of NASA E/PO, Sonoma State University, Aurore Simonnet **f:** the *Nuclear Spectroscopic Telescope Array* (*NuSTAR*, image taken and modified from Harrison et al., 2013), and **g:** *Chandra* (image taken from http://chandra.harvard.edu/resources/illustrations/craftIllustrations.html).

source and the background were continuously measured throughout an observation. This so-called "rocking" mechanisms, however, failed for cluster A on 2006 October 20, which was then fixed in the on-source position[4]. Four years later, on 2010 April 20 cluster B stopped "rocking" as well and it was fixed in the off-source position[5]. As the background for both clusters differ by 10% (Pottschmidt et al., 2006) estimating the background for cluster A from data of cluster B is barely feasible.

The ASM was built to monitor the X-ray sky and discover transient sources. In order to observe a large fraction of the sky three cameras with a large field of view were mounted on rotating axes. Each camera consisted of a position sensitive proportional counter, which uses a one-dimensional coded-mask on top to determine the source positions. Like in PCA, the proportional counters used xenon as detector material for X-rays. Due to the fast rotation of the cameras of 90 s around their axes, the ASM was able to provide continuous light curves for many known sources over 15 years in length.

3.2.2 *Swift*

The *Swift* mission, launched in 2004 November, was designed to detect gamma-ray bursts and observe their afterglow from the optical up to the X-ray band (Gehrels et al., 2004, 2005). To cope with this task the *Burst Alert Telescope* (BAT: Barthelmy et al., 2005) constantly monitors the hard X-ray sky in the energy range from 15–150 keV. Once a gamma-ray burst is detected, an on-board system triggers the satellite to point to the location of the burst and start observing with the focusing *UV/Optical Telescope* (UVOT; Roming et al., 2004) and *X-ray Telescope* (XRT; Burrows et al., 2005). See Fürst et al. (2011) for a detailed summary about *Swift*. Since UVOT is not sensitive for X-rays it is not discussed here.

X-rays in *Swift*-BAT are detected by 32768 photo diodes, which are read out individually such that loosing a pixel due to, e.g., a micro meteorite hit does not significantly reduce the instrument's performance. As no mirrors are used to focus the X-rays on the photo diodes, a two-dimensional coded mask is used to reconstruct the source positions. This coded mask is much more complicated than the one-dimensional mask of *RXTE*-ASM and with 2.7 m^2, much larger (see, e.g. Oertel, 2013, for details about the image reconstruction using coded masks).

The XRT is a Wolter telescope focusing the incident X-rays on a CCD chip. In order to observe bright sources with a count rate above[6] 0.5 counts s^{-1} the CCD can be operated in two readout modes. In the "photon counting" (PC) mode the full chip is read out resulting in a complete image of the source, which limits the time resolution to around 2.5 s. If the "windowed timing" (WT) mode is selected, then the rows of the CCD are readout all at once, which results in a collapsed one-dimensional image. Determining the source position is not possible anymore, but the time resolution is reduced to ∼1.8 ms, which effectively avoids pile-up.

3.2.3 *Suzaku*

The *Suzaku* X-ray mission (Mitsuda et al., 2007), known as Astro-E2 before its launch[7] in July 2005, covered the energies between 0.2 and 600 keV by combining three different

[4] https://heasarc.gsfc.nasa.gov/docs/xte/whatsnew/newsarchive_2006.html#_hexteA-norock

[5] https://heasarc.gsfc.nasa.gov/docs/xte/whatsnew/newsarchive_2010.html#hexteB_locked

[6] See the *Swift* data processing guide at http://www.swift.ac.uk/analysis/xrt/pileup.php

[7] The space missions of the *Japan Aerospace eXploration Agency* (JAXA) are usually named after they have been successfully deployed into their orbits

instruments. These were the *X-ray Imaging Spectrometer* (XIS; Koyama et al., 2007) and the *Hard X-ray Detector* (HXD; Takahashi et al., 2007; Kokubun et al., 2007), which itself consisted of two instruments, the PIN diodes and the gadolinium silicate (GSO) scintillators. The original fourth instrument onboard *Suzaku*, the *X-ray Spectrometer* (XRS; Mitsuda et al., 2007) had a leak in its cooling device, which required the detector to be shutdown a few weeks after launch. In 2015 May, almost ten years after launch, the XIS and HXD were shutdown due to an insufficient power supply[8]. The power supply never recovered.

Like in *Swift*-XRT, X-ray photons in the range of 0.2–10 keV entering one of the four XISs (labeled XIS0–3) were focused by a Wolter telescope (named X-ray Telescope (XRT) here; Serlemitsos et al., 2007) onto a CCD. Each XIS was assembled in the focal plane of a separate telescope. One of the CCDs (XIS1) was front-illuminated, while the other (XIS0, 2, and 3) were back-illuminated. Data from XIS2 after 2006 November 9 could no longer be used probably due to a hit by a micro meteorite[9] In order to reduce the amount of telemetry data, the pixels of the CCDs in a 3×3 or 5×5 region around each event were transfered. These so-called editing modes depended on the source flux and available bandwidth. In principle, the spectra across the editing modes should be identical and are, thus, often combined during the analysis. For bright sources, the possibility for pile-up could be reduced by combining a certain number of rows during the CCD readout process, which reduced the exposure time. The available options were full window (no rows are combined), 1/4 window (every four rows), or 1/8 window (every 8 rows). Furthermore, the burst option limited the effective exposure time by introducing an artificial dead time during the fixed exposure (8 s in the full window mode).

As mentioned above, the HXD consisted of two separated instruments in order to detect X-rays between 10 and 600 keV. At the end of collimator, which limits the field of view to 4.5°×4.5°, the photons travel through 16 silicon photodiodes (PIN), which were sensitive to energies between 10 and 70 keV. Here, each photodiode was readout separately, as their edge length of 21.5 mm was large compared to a CCD. Additionally, bronze collimators on top of each 2×2 PIN diodes reduced their field of view to 34′ for photons below 100 keV. Photons, which were not absorbed in the photodiodes, entered gadolinium silicate scintillator crystals (GSO), which could detect X-rays up to 600 keV. Furthermore, bismuth germanate crystals (BGO) below the GSO acted as anti-coincidence shields, like the CsI crystals in HEXTE. At the end of the optical axis photo multipliers were connected, which converted the scintillation photons produced in the GSO into a signal.

3.2.4 *XMM-Newton*

The ESA X-ray mission *XMM-Newton* was launched in 1999 December 10. Three Wolter type telescopes focus X-ray photons onto different instruments, which are three *European Photon Imaging Cameras* (EPIC-pn, Strüder et al., 2001; EPIC-MOS1 and MOS2, Turner et al., 2001) and two *Reflection Grating Spectrometers* (RGS; den Herder et al., 2001). Here, a brief description of the EPIC-pn is given as data from the other instruments are not used within this thesis. See Hanke (2011) or Fürst et al. (2011) for a summary of EPIC-MOS and RGS.

The EPIC-pn consists of 2×6 CCDs, which are distributed among the focal planes of all three X-ray telescopes. Since the EPIC-MOS1 and -MOS2 CCDs as well as the two RGS share two of three telescopes, EPIC-pn has the highest effective area of all instruments

[8] http://www.astro.isas.jaxa.jp/suzaku/log/operation/.
[9] https://heasarc.gsfc.nasa.gov/docs/suzaku/news/xis2.html

onboard *XMM-Newton*. A full frame of the 2×6 CCDs of the EPIC-pn is readout in ∼73.3 ms (Strüder et al., 2001). By selecting a specific "window mode" the CCDs are readout in parts only, similar to the modes of *Suzaku*-XIS. In the "timing mode" the rows of the CCDs are continuously readout, resulting in a one-dimensional image where the exposure time is reduced to 0.007 ms. Problems during an observation with EPIC-pn might arise due to incident cosmic ray particles. These particles, such as protons, are focused by the mirrors of the telescopes similar to X-rays photons. Events caused by an unpredictable particle are known as background flares in *XMM-Newton*. They are able to influence a significant portion of an observation due to their duration ranging from minutes to hours (Strüder et al., 2001).

3.2.5 *Chandra*

Chandra was launched on 1999 July 23 and its main characteristics are high resolution spectroscopy and a superior angular resolution. A Wolter type telescope, the *High Resolution Mirror Assembly* (HRMA; see Schwartz et al., 2000, and references therein), focuses incident X-rays on two instruments, the *Advanced CCD Imaging Spectrometer* (ACIS; Garmire et al., 2003) and the *High Resolution Camera* (HRC; Murray et al., 2000). These instruments themselves are not responsible for the high spectral resolution known for *Chandra* (compare the instruments listed in Table 3.1). Rather two X-ray gratings, the High or Low Energy Transmission Gratings (HETG or LETG; Canizares et al., 2005, or Brinkman et al., 1997, Predehl et al., 1997, respectively) can be moved into the optical path, which act like a prism in optical wavelengths and cast spectra on ACIS or HRC, respectively. Here, only a description of the ACIS is given as HRC and the gratings were not used. See, e.g., Hanke (2011), for a summary about these devices.

In order to use the angular resolution of the HRMA of around 0.″5, the ten CCDs of which ACIS consists are constructed such that a single pixel corresponds to the same angular resolution, which results in 1024×1024 pixels per CCD. During an observation six of the ten pixels can be operated at the same time. Four CCDs are arranged in a 2×2 grid and optimized for imaging (ACIS-I), while six CCDs are lined up in a row to measure the spectrum casted by HETG. Two modes are available to readout the CCDs. In "timed exposure" (TE) the readout is triggered after an exposure time of 3.2 s for a full frame, while the exposure can be reduced once the CCDs are readout in parts only. In the "continuous clocking" (CC) mode the rows are readout continuously, allowing for an exposure time of 2.85 ms, which results, however, in a one-dimensional image similar to the WT mode in *Swift*-XRT.

3.2.6 *NuSTAR*

In 2012 June 13, the *Nuclear Spectroscopic Telescope Array* (*NuSTAR*, Harrison et al., 2013, and references therein) was launched into space. After it reached its final orbit an extendible mast was deployed, on which two grazing incidence telescopes with a focal length of 10.14 m were mounted. They focus X-rays onto the two *Focal Plane Modules* (FPMA and -B) which are then able to measure X-ray energies between 3 and 78 keV due to the long focal length.

The mast system is not perfectly stiff. Therefore, the image of a source "wobbles" within the focal plane and, thus, on the CCDs. Star trackers mounted next to the telescopes as well as a two laser units are used to track the exact position and orientation of the optical bench, where the telescopes are mounted. The final accuracy of the tracking is around 3″.

Each FPM consists of 2×2 CCDs with 32×32 pixel each, which results in a field of view of 12′. In contrast to that used in *Swift*-XRT, *Suzaku*-XIS, or *Chandra*-ACIS, the readout of the pixels are triggered as soon as an X-ray photon hits the CCDs. Onboard electronics identify the exact pixel, in which the photon was detected, and the 3×3 pixels around this event are readout. This readout strategy basically prevents pile-up until a flux of $10^5\,\mathrm{counts\,s^{-1}\,pixel^{-1}}$. Due to a readout time of 2.5 ms per FPM, not every single photon is directly measured, however they can be reconstructed from the 3×3 pixel pattern. The derived photon fluxes are accurate within 1% up to $10^4\,\mathrm{counts\,s^{-1}}$. Around each FPM an anti-coincidence shield of CsI scintillators is placed. Events detected simultaneously in this shield and the CCDs are rejected by the onboard electronics.

3.2.7 *Fermi*

Originally, *Fermi* was designed to monitor the sky in gamma-rays. The *Gamma-ray Burst Monitor* (GBM; von Kienlin et al., 2004; Meegan et al., 2007, 2009) is, however, also sensitive to X-rays above ∼8 keV. Since no pointed observations are possible with *Fermi*, the GBM is used to provide the spin frequency evolution for neutron star X-ray binaries, which are above the detection threshold. As the light curves and spin measurements are available online through the *Fermi*-GBM pulsar project[10] (Finger et al., 2009), data reduction is not necessary. For this reason only a brief description of the GBM is given here (see the above references for details or Böck, 2012, for a summary). See Atwood et al. (2009) for a description of the main instrument on *Fermi*, the *Large Area Telescope* (LAT).

As GBM was designed to detect gamma-ray bursts in the first place, which are transient events in the gamma-rays with durations between a few and several 1000 seconds (see Atwood et al., 2009, for a brief introduction to gamma-ray bursts see Sect. 3.3 of), the instrument's field of view has to be extremely large. In fact, a permanent observation of the whole sky is performed by 12 NaI scintillators and 2 BGO detectors mounted around the spacecraft. Due to this design the instrument cannot resolve point sources. Nevertheless, in order to derive fluxes for individual sources, the Earth occultation method is applied. This method uses the fluxes of known sources and compares the change in the detector count rate once one or more of these sources are occulted by the Earth (see, e.g., Case et al., 2011, for details). The *Fermi*-GBM pulsar project uses known pulsars to search for their pulsation signals in these data.

[10] http://gammaray.nsstc.nasa.gov/gbm/science/pulsars.html

Chapter 4

X-ray Pulsar Orbit Determinations

Determining reliable orbital parameters of neutron star X-ray binaries is challenging. Accretion torques (compare Sect. 1.3.1) can result in a complex spin period evolution of the neutron star. Using a Taylor series to model the observed data might cause, however, systematics in the derived orbital parameters (see Sect. 2.3.1 for details). To model the spin period evolution correctly, an accretion torque theory, as developed by GL79, should be applied to the measured period evolution in combination with the observed luminosity of the source.

In the present chapter, the torque model I have implemented in Sect. 2.3.2 is used to derive the orbital parameters of XTE J1946+274, RX J0520.5−6932, and XTE J1859+083. Among data from X-ray missions, from which pulse periods are determined, the pulse frequency measurements provided by the *Fermi*-GBM pulsar project have been used (see Sect. 3.2.7). Furthermore, the orbits of GRO J1008−57 and 4U 2129+47 are determined, where the torque model, however, was not needed to explain the observations. In all cases, the orbital parameters found in the literature could be improved or determined for the first time at all. Unless stated otherwise, all presented uncertainties are at the 90% confidence level.

4.1 XTE J1946+274: Dominated by Spin-up

Most of the results presented in this Section have been published as part of Marcu-Cheatham et al. (2015), which is the basis of this Section. The temporal analysis of the data was performed in close collaboration with Mark H. Finger, which is why the "we"-style is used here. This collaboration has triggered the development of the torque model[1] (see Sect. 2.3.2). All Figures have been produced by myself and text from Marcu-Cheatham et al. (2015) has been paraphrased.

Since its discovery in 1998 with *RXTE* (Smith & Takeshima, 1998) the transient BeXRB XTE J1946+274 has been a mystery. Between 1998 and 2001, the source showed several outbursts separated by around 80 d, which were interpreted as the orbital period of the binary (Campana et al., 1999). However, Wilson et al. (2003) found the orbital period to be 169.2 d, based on an analysis of the Doppler shifted ∼15.8 s pulse period using data of *CGRO*-BATSE and *RXTE*-PCA. Thus, XTE J1946+274 featured two outbursts every orbital period, in disagreement with the simple picture of a BeXRB (see Sect. 1.2.4). Furthermore, the observed 13 outbursts were not connected to a specific orbital phase.

The neutron star in XTE J1946+274 is orbiting a B0–1 V–IVe stellar companion (Verrecchia et al., 2002). Constraining all orbital parameters well was not possible for Wilson et al. (2003) due to a strong intrinsic spin-up during the outbursts. They tried to model the neutron star's spin evolution using a Taylor series from the first- up to the 10^{th}-order (see Eq. 2.21) resulting in unacceptable high χ^2_{red}-values. Another approach

[1] Regarding specific question 6, a talk by Mark H. Finger at the BeXRB conference 2011 inspired me to implement the torque model as his presented fit of *Fermi*-GBM frequency measurements of XTE J1946+274 using the $\dot{P}$-L-relation was not successful due to fixed orbital parameters.

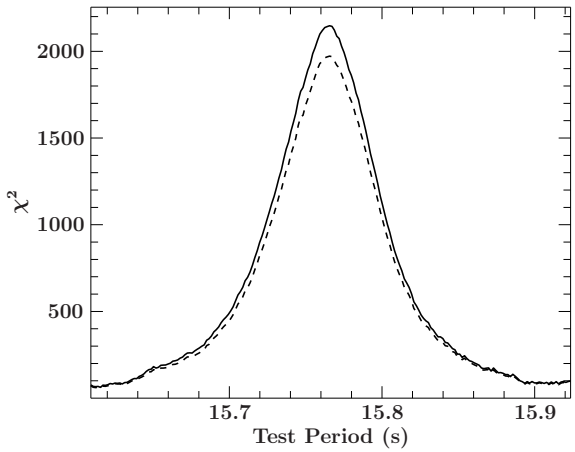

Figure 4.1: χ^2-landscape after epoch folding the light curve of the *RXTE*-PCA observation 95032-12-01-00. The dashed line shows the result when using the initial light curve while the solid line uses the flux-corrected light curve as explained in the text.

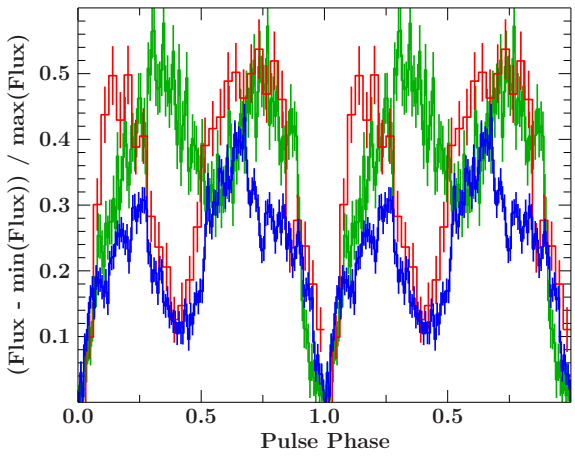

Figure 4.2: Some examples for pulse profiles of XTE J1946+274 normalized by the pulse amplitude as given in the label and aligned to match the minimum flux. The *RXTE*-PCA 2–60 keV profile is shown in blue (observation 95032-12-01-02), the *Swift*-XRT 0.3–12 keV profile in red (observation 00031888002), and the *Suzaku*-PIN 10–70 keV in green (observation 405041010).

by these authors was to use a piecewise linear model, where the period measurements of each outburst were divided into a few segments. During each segment the spin-evolution was fitted independently with a first-order polynomial, while the orbital parameters were fitted by all segments at the same time (comparable to a simultaneous fit as described in Sect. 2.4). Although this model provided the best description of the data so far, the fit quality was still not satisfying.

After the 13$^{\text{th}}$ consecutive outburst after its discovery, XTE J1946+274 has faded and the source could no longer be detected in any all-sky-monitor for the next decade. In the early days of 2010 June, the source was suddenly detected in *Swift*-BAT and *Fermi*-GBM (Finger, 2010; Krimm et al., 2010). In the following year, XTE J1946+274 featured five outbursts in a row, again separated by approximately half the orbital period (see gray light curve in Fig. 4.3; this Figure shows the observed and modeled pulse period evolution as well). With ∼140 mCrab in *Swift*-BAT the first outburst of this series was the brightest one and similar to what have been observed between 1998 and 2001. Several X-ray missions, including *RXTE*, *Swift*, and *Suzaku*, observed the source during its activity in 2010 (see Table F.1 for details).

4.1.1 Deriving pulse periods

The extraction of the *RXTE*-, *Swift*-, and *Suzaku*-data is described briefly in the following. For more details see Müller et al. (2012) and Marcu-Cheatham et al. (2015). *RXTE*-PCA light curves were extracted using the extraction pipelines based on `HEASOFT` (v6.10 and 6.11). Exclusively, data from the top layer of PCU2 have been used. As data from the GoodXenon event analyzer was available, it was possible to choose 125 ms as the time resolution of the light curves. The SAA passage was removed from the light curves with additional 10 minutes after the passage. The *Swift*-XRT was operated in windowed timing mode due to the relatively high count rate of the source. XRT light curves were extracted

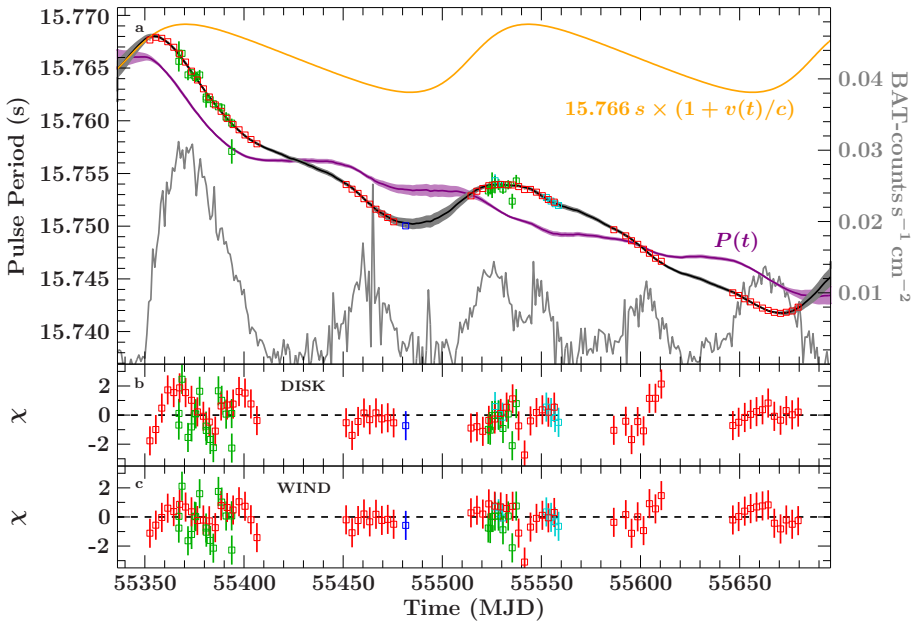

Figure 4.3: a: Pulse period evolution of XTE J1946+274 as observed by *Fermi*-GBM (red), *RXTE*-PCA (green), *Swift*-XRT (cyan), and *Suzaku*-PIN (blue). The *Swift*-BAT light curve (gray) has been used as input to calculate the intrinsic spin period evolution ($P(t)$, for the DISK case, purple). Together with the orbital motion (orange) the resulting total model (black) was able to describe the data. The width of the intrinsic and total period evolution corresponds to the model uncertainties due to the BAT data (shown in Fig. 4.5). **b:** Residuals of the DISK model and **c:** residuals of the WIND model (taken from Marcu-Cheatham et al., 2015).

from a circular region with a $\sim$0.′5 radius centered at the brightest pixel. A time resolution of 1 s for these light curves was chosen. None of the *RXTE* and *Swift* light curves were corrected for the X-ray background. The *Suzaku*-PIN event files were calibrated and screened by running the `aepipeline` tool.

Pulse periods from each of the *RXTE*- and *Swift*-observations were determined by applying the epoch folding technique to the corresponding light curves (see Sect. 2.2.2). For *Suzaku*, epoch folding was performed directly on the PIN events. Pulsations were searched around the period measured by *Fermi*-GBM near the date of the corresponding observation (see Fig. 4.3). To account for pulse-to-pulse flux changes during the observations, the corresponding light curves were rebinned on a time resolution equal to an initially determined pulse period. These light curves were then subtracted from the original light curves to remove these flux changes. The final pulse periods were found by epoch folding the resulting flux-corrected light curves. In this way the main peak in the χ^2-landscape is slightly sharpened and amplified, which allows a finer period search grid and, thus, a more accurate period estimation. An example χ^2-landscape as the result of this iterative epoch folding is given in Fig. 4.1. This approach is even more efficient for weak signals (Larsson, 1996; see Rothschild et al., 2013 for a further example). The uncertainties of the pulse periods determined by epoch folding were estimated by the `epferror` function of the *ISISscripts*, which is based on Monte Carlo simulations (see Sect. 2.2.2 for details). The resulting pulse profiles of XTE J1946+274 as measured by *RXTE*-PCA, *Swift*-XRT, and *Suzaku*-PIN are exemplarily given in Fig. 4.2. The difference in shape between the profiles is explained by the different sensitive energy range of the used instruments. Furthermore, the detector and X-ray background was not subtracted from the light curves and, thus, the pulse amplitudes (expressed as the pulsed fraction in Fig. 4.2) systematically differ.

4.1.2 Using the torque model

The pulse periods measured by the various X-ray missions, including the frequency measurements provided by the *Fermi*-GBM pulsar project, revealed their respective time evolution over the outburst series as shown in Fig. 4.3. The data from the different missions are in excellent agreement with each other. Apparently, the data covers two orbital cycles, although the source underwent five outbursts during this time. Thus, XTE J1946+274 showed more than one outburst per orbit as has been observed already between 1998 and 2001. A similar strong spin-up, which has been observed back then, was seen during the recent outburst series as well. As can be seen already by eye in Fig. 4.3, the spin-up during one orbital cycle was stronger than the actual amplitude of the orbital modulation, which is a fascinating fact. At least during type I X-ray outbursts the orbital modulation dominates the observed pulse period evolution (see Sect. 4.4, Stella et al., 1985, Müller et al., 2010, or Finger et al., 2006 for examples).

To model this strong intrinsic spin-up of the neutron star, we fitted the torque model as described in Sect. 2.3.2 to the pulse period measurements. In order to fit this model to the measured pulse period evolution, we chose the 15–50 keV *Swift*-BAT light curve as the input flux evolution, $F(t)$ (gray line in Fig. 4.3), set the reference flux $F_{\rm ref} = 1\,\mathrm{BAT\text{-}count\,s^{-1}\,cm^{-2}}$, and fixed the reference time, t_0, to MJD 55550. In order to determine the orbital parameters we multiplied the torque model by the Doppler shift of orbital motion, which results in a model for the observed pulse period evolution, $P_{\rm obs}$, after Eq. (1.17). See Table 2.2 for a list of all parameters of the Torque model.

Due to the very precise pulse period measurements and the complexity of the model, we needed to estimate good initial parameter values for the fit. Applying the rules of thumb given in Sect. 1.2.1 restricts the range of possible orbital parameters. The two apparent orbital cycles allow us to directly restrict the orbital period to $160\,\mathrm{d} < P_{\rm orb} < 180\,\mathrm{d}$ (derived from peak to peak of the orbital amplitude). From the pulse period of $\sim$15.76 s and the amplitude of the Doppler shift of $\Delta P \sim 12$ ms (from the maximum to the minimum of the second cycle) we derive $a \sin i \sim 906$ lt-s after Eq. (1.19). However, this is an upper limit due to the strong spin-up, which biases the apparent amplitude towards higher values. We can estimate its influence from the difference of $\sim$8 ms between the minima of the two orbital cycles (and thus ignoring the very strong first outburst), which leads to $a \sin i \sim 300$ lt-s, which we take as lower limit. Estimating the eccentricity by eye is difficult due to the strong spin-up. We see, however, that the minimum of the first cycle around MJD 55480 (near the *Suzaku* observation) is much closer to the maximum of the second cycle around MJD 55540 than the next minimum at the end of last observed outburst around MJD 55670. Thus, the left side of the maximum must be steeper, which is not possible for circular orbits. Consequently, we allow for an eccentricity of $e > 0$, restrict the longitude of periastron to $-135° < \omega < -45°$, and the time of periastron passage[2] to MJD 55460 $< \tau <$ MJD 55538.

In order to find initial parameters for the spin period evolution we have performed a first fit with the orbital parameter fixed to the estimates values (or to the mean of the allowed parameter range). The reference time, t_0, of the spin period evolution was fixed to MDJ 55550 and the luminosity exponent, α, to 6/7 as we expect accretion from an accretion disk (the DISK model) rather than from a stellar wind ($\alpha = 1$, the WIND model) since the Be companion does not feature such a strong wind (see Sect. 1.2.4). After having fitted the intrinsic spin period, P_0, at t_0 and the torque strength, b, the modeled period

[2]Following the rule of thumb given in Sect. 1.2.1 the time of periastron passage would be restricted to $+5/8 < (\tau - t_{\rm max})/P_{\rm prb} < +7/8$. In order to take the range of possible orbital periods into account and to define τ to be within the first observed orbital cycle, we restrict τ from $t_{\rm max} + 5/8 \cdot 160\,\mathrm{d} - 180\,\mathrm{d}$ to $t_{\rm max} + 7/8 \cdot 180\,\mathrm{d} - 160\,\mathrm{d}$.

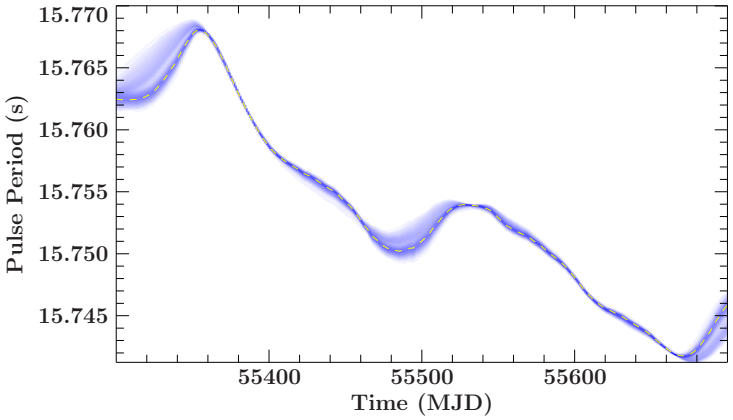

Figure 4.4: Color coded density distribution of all simulated pulse period evolutions as described in the text. The dashed line close to the most likely pulse period evolution presents the best-fit to the measured pulse periods using the DISK model (see Fig. 4.3), which took the actual BAT light curve as input.

evolution already followed the measured period roughly if compared by eye. The bad fit quality of $\chi^2_{\rm red} \gg 10$ required, however, to unfix the orbital parameters. Furthermore, there were features in the residuals during the first and last observed outburst, i.e., at times far away from the chosen reference time, t_0. To get rid of these features we have also allowed to fit a constant spin-down, i.e., $a > 0$. This fit with 8 free parameters in total (5 orbital parameters, a, b, and P_0) resulted in a perfect match of the model with the data by eye, however, the $\chi^2_{\rm red} \sim 8.9$ is not acceptable.

4.1.3 Error propagation of the BAT light curve

Due to a lack of distinct features in the residuals, i.e., only a strong scattering of the residuals is found, the reason for the bad fit quality is likely to be of statistical nature. Indeed, the statistical uncertainties of the BAT-light curve (see gray line in Fig. 4.3), which is used to actually calculate the model, are not taken into account yet. One might interpret this as an uncertainty of the model itself. There are two possible ways to derive the impact of this uncertainty: by error propagating the model (Fig. 2.24) or by performing a Monte Carlo simulation. The latter is a more robust approach since the model includes the numerical solution of a differential equation. The idea of a Monte Carlo simulation to include the statistical uncertainties of the BAT-light curve is to generate a large number of synthetic BAT-light curves and to perform a fit of the observed pulse period evolution for each of these light curves. This results in many possible modeled period evolutions. Their scattering of a predicted pulse period, $P_{\rm model}(t)$, at a specific time, t, is then considered as additional model uncertainty.

We have simulated 10000 BAT light curves, where for each time in the original light curve, t_i, a random count rate is generated from a Gaussian distribution with mean and standard deviation given by the measured BAT rate and uncertainty, respectively. As explained above, a fit of measured pulse period evolution to the torque model is performed. This results in 10000 best-fit pulse period evolutions, which are shown in Fig. 4.4 as a density distribution. The "thickness" of this distribution can be understood as a measure for the model uncertainty as a result from the uncertainties of the input BAT light curve. The standard deviation of all models, $\sigma_{M(t_i)}$, at a specific time, t_i, is added in quadrature to the uncertainties of the measured pulse periods. In that way the calculation of the χ^2 during each fit iteration includes the uncertainties of the BAT light curve.

As fits during the Monte Carlo simulation depend on the measurement uncertainties as well, fitting the pulse period evolution and deriving the additional uncertainties due to the BAT light curve is an iterative process. Usually three iterations are needed until a stable pulse period is found. The final parameters of the best-fit with a $\chi^2_{\rm red} = 1.05$ are listed in

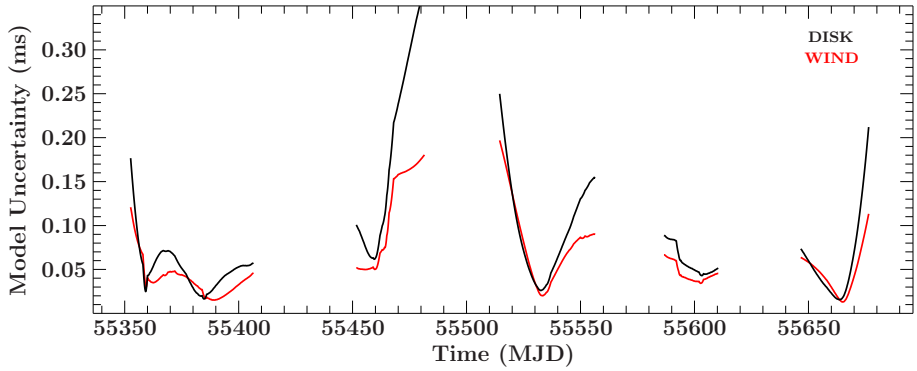

Figure 4.5: The uncertainties of the DISK (black) and WIND model (red) as derived by the standard deviation of the simulated pulse period evolutions as shown in Fig. 4.4. Times when no continuous pulse period measurements were available are not shown here (taken from Marcu-Cheatham et al., 2015).

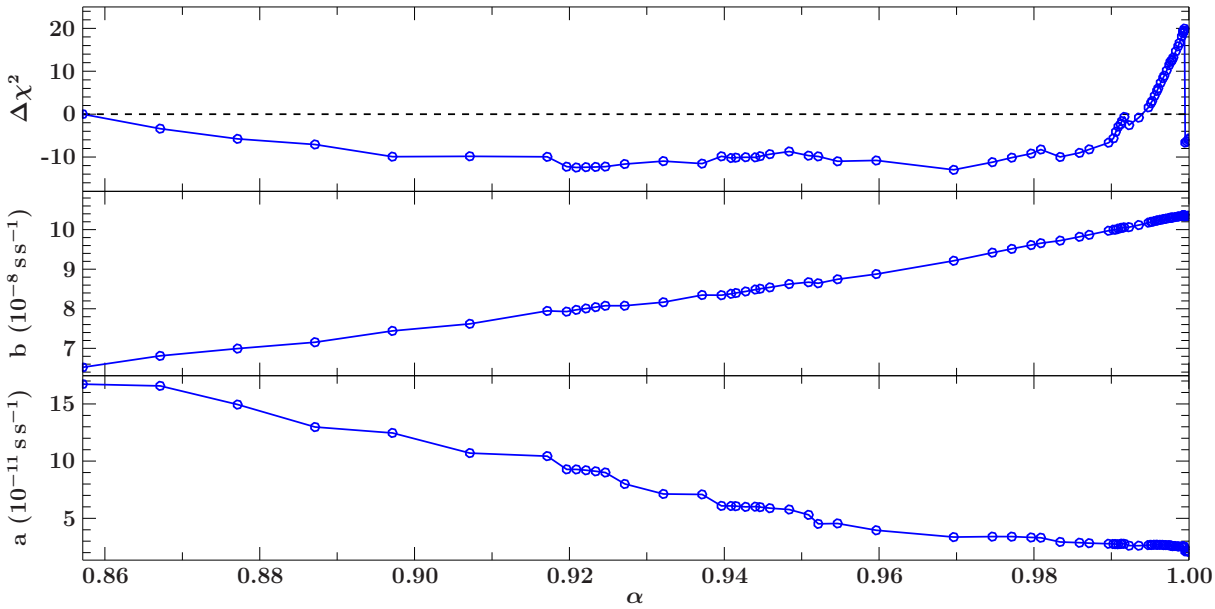

Figure 4.6: The parameter degeneracy between the spin period parameters a, b, and α. For each value of α a fit of the torque model to the pulse period evolution was performed and the resulting $\Delta\chi^2$ relative to the best-fit DISK model are shown in the top panel and the corresponding parameters a and b in the middle and bottom panel, respectively. Error bars in the parameters are not drawn because they are on the same order (for a) or smaller (for b) than a tic mark.

Table 4.1 and Fig. 4.3a shows the corresponding modeled Doppler shifted pulse period evolution (black curve). The thickness of the model curve corresponds to the estimated model uncertainties due to the measured BAT light curve, which is shown in Fig. 4.5 (black curve). These uncertainties are added to the intrinsic spin period evolution, $P(t)$, as well (purple curve in Fig. 4.3). The estimated model uncertainties are between 0.02 and 0.38 ms with a mean of 0.09 ms. Note that the individual pulse period measurements are much better determined than this model uncertainty. For example, epoch folding of the *Suzaku*-PIN events results in an uncertainty of 0.027 ms, while the modeled period at the time of the observation has an uncertainty of 0.380 ms.

4.1.4 Determining orbital parameters: DISK vs. WIND accretion

We have found that modeling the data assuming accretion from a stellar wind, i.e., fixing $\alpha = 1$ (the WIND model), leads to an equally well determined fit ($\chi^2_{\rm red} = 1.06$, see Table 4.1 and Fig. 4.3c). The WIND model uncertainties after having performed the Monte Carlo simulations with this setup are very similar to those of the DISK model[3] (compare the results shown in Fig. 4.5). Thus, it is not possible to distinguish between these two torque models due to the large uncertainties of the BAT light curve. We have tried to let the fit determine the value for α, but this turned out to be difficult because a very tight parameter degeneracy exists between all three spin period parameters (a, b, and α). Revealing this degeneracy by, e.g., calculating contour maps is impossible as for each parameter combination a new Monte Carlo estimation of the model uncertainties is required. Since the run-time for the Monte Carlo simulation for a single fit result is about one day, the total run-time for a contour map of, e.g., 32×32 parameter combinations would be almost 3 years. Nevertheless, using the computing cluster at the Remeis-observatory, we were able to reveal the dependency of the parameters a and b on α as shown in Fig. 4.6. Here, for each value of α on a grid between 6/7 (DISK) and 1 (WIND) we have performed a full fit including the model uncertainties as estimated by the Monte Carlo approach. As can be seen from Fig. 4.6 almost every value for α results in a fit quality, $\Delta\chi^2$, equal or even better than compared to the DISK model (see Table 4.1). The parameters a and b show a very strong and tight correlation with α, although their single parameter uncertainties are much smaller than the amplitude of the correlation. This is possible only if parameter degeneracies are present, i.e., computing single parameter uncertainties is not statistically justified. From the revealed parameter ranges, however, we can derive systematic uncertainties on a of $\sim 1.5 \times 10^{-10}\,\mathrm{s\,s^{-1}}$ and on b of $\sim 4 \times 10^{-8}\,\mathrm{s\,s^{-1}}$, which are on the same order as the actual values of the parameter.

The best-fit orbital parameters for the DISK and WIND model, as listed in Table 4.1, agree within their uncertainties. Thus, the determination of the orbital parameters of XTE J1946+274 is insensitive to the choice of the accretion mechanism onto the neutron star (DISK or WIND). The orbital parameters as found by Wilson et al. (2003) are listed in Table 4.1 for comparison. The orbital period, $P_{\rm orb}$, and eccentricity, e, agree best with their linear model. The semi-major axis, $a \sin i$, on the other hand is consistent with their $10^{\rm th}$-order polynomial model. For the same model, their determined time of periastron passage, τ, agrees with our findings within 2σ once extrapolated back to 1998. Finally, the longitude of periastron, ω, is consistent to their piecewise approximation within the uncertainties. The χ^2 of all three different models of Wilson et al. (2003) is, however, not acceptable because they do "not completely describe the intrinsic torques" as noticed by these authors. Using the accretion torque theory by GL79, the strong observed spin-up in XTE J1946+274 could finally be modeled successfully[4].

4.1.5 The inclination derived from the orbit

Wilson et al. (2003) also estimated the inclination angle, i, of the orbital plane to the tangent plane of the sky by investigating the mass function, $f(M)$, of the binary (see Eq. 1.22). The value of the mass function is determined either by the masses $M_{\rm opt}$ and $M_{\rm x}$ of the optical companion star and the neutron star, respectively, or by the orbital

[3] For a few times the WIND model uncertainties are smaller by a factor of 2 compared to the DISK model.

[4] This answers specific question 6.

Table 4.1: Orbital parameters of XTE J1946+274 as derived by different approaches to model the strong intrinsic spin-up performed by Wilson et al. (2003, uncertainties are given at the 68% confidence level) and this work (Marcu-Cheatham et al., 2015, uncertainties at 90% confidence). The parameters of the spin period evolution as found in this work are listed as well.

	Wilson et al. (2003)			this work (Marcu-Cheatham et al., 2015)	
	Linear	10^{th}-order	Piecewise	DISK model	WIND model
$a \sin i$ (lt-s)	972^{+118}_{-118}	474^{+14}_{-14}	640^{+120}_{-120}	$471.2^{+2.6}_{-4.3}$	$471.1^{+2.7}_{-2.8}$
P_{orb} (d)	173^{+2}_{-2}	$167.8^{+0.6}_{-0.6}$	$169.2^{+0.9}_{-0.9}$	$172.7^{+0.6}_{-0.6}$	$171.4^{+0.4}_{-0.4}$
τ (MJD)	$51524.1^{+16.9}_{-16.9}$	$51571.8^{+1.6}_{-1.6}$	$51558.2^{+4.0}_{-4.0}$	$55514.8^{+0.8}_{-1.1}$	$55515.5^{+0.8}_{-0.7}$
e	$0.19^{+0.13}_{-0.13}$	$0.35^{+0.03}_{-0.03}$	$0.33^{+0.05}_{-0.05}$	$0.246^{+0.009}_{-0.009}$	$0.266^{+0.007}_{-0.007}$
ω (°)	-153^{+37}_{-37}	-38^{+5}_{-5}	-91^{+23}_{-23}	$-87.4^{+1.5}_{-1.7}$	$-87.1^{+1.2}_{-1.0}$
t_0				55550 (fixed)	55550 (fixed)
P_0 (s)				$15.749742^{+0.000023}_{-0.000014}$	$15.749753^{+0.000013}_{-0.000013}$
a ($\text{s}\,\text{s}^{-1}$)				$1.67^{+0.16}_{-0.18} \times 10^{-10}$	$0.47^{+0.20}_{-0.10} \times 10^{-10}$
b ($\text{s}\,\text{s}^{-1}$)				$6.52^{+0.06}_{-0.08} \times 10^{-8}$	$10.76^{+0.05}_{-0.04} \times 10^{-8}$
α				6/7 (fixed)	1 (fixed)
χ^2_{red}/d.o.f.	26728/101	312/92	5.9/37	1.05/89	1.06/89

Notes. The number of degrees of freedom are abbreviated with d.o.f. from now on.

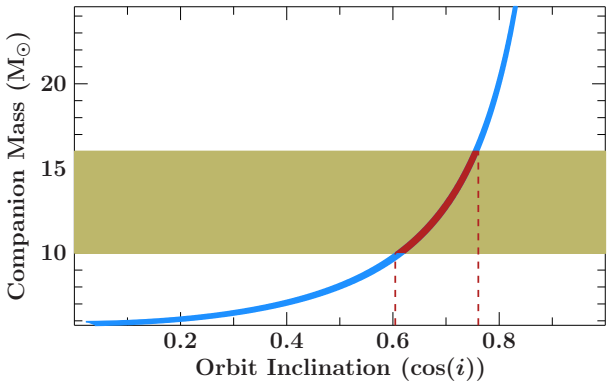

Figure 4.7: The mass function of XTE J1946+274 depending on the orbit inclination, $\cos i$, and the mass of the companion star. The allowed region after Eq. (1.22) using the orbital parameters is shown in blue. The khaki colored region corresponds to the probable mass range of a B0/B1-type companion. The inclination of the system was derived from the intersection of both regions (red).

period, P_{orb}, and projected semi-major axis, $a \sin i$. Using our fitted orbital parameters as listed in Table 4.1 we have derived $f(M) = 3.77^{+0.11}_{-0.07}\,\text{M}_\odot$ for the DISK model and $f(M) = 3.82^{+0.07}_{-0.07}\,\text{M}_\odot$ for the WIND model. Both are consistent with each other. If we now assume a neutron star mass of $M_{\text{x}} = 1.4\,\text{M}_\odot$ and a typical mass range of Be stars of $10\,\text{M}_\odot \leq M_{\text{opt}} \leq 16\ \text{M}_\odot$ as used by Wilson et al. (2003) we can derive the inclination angle, i. The numerical solution is shown in Fig. 4.7, where the intersection of the companion mass with the mass function calculated using the orbital parameters determines the orbital inclination. Taking both the DISK and WIND model into account we find an inclination angle of $41° \leq i \leq 52°$, which is in good agreement with $i \gtrsim 46°$ as found by Wilson et al. (2003).

Having determined the projected semi-major axis, $a \sin i$, the eccentricity, e, the longitude of periastron, ω, and the inclination angle, i, we can draw a sketch of the geometry of the BeXRB XTE J1946+274 as shown in Fig. 4.8. The large distance between

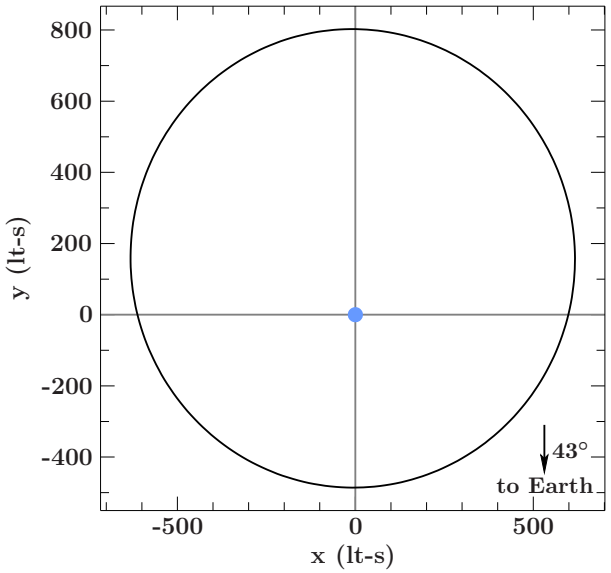

Figure 4.8: Sketch of XTE J1946+274's orbit resulting from the orbit determination. The orbit is seen from above assuming an inclination of 47°. The companion star's radius is assumed to be at least $8\,R_\odot$ (minimum radius of a B-type star; Özbey Arabacı et al., 2015). The observer is inclined by the labeled angle with respect to the orbital plane.

the periastron and the Be star of almost 500 lt-s[5] is a good argument why the source was in quiescence for a decade. Without a huge circumstellar disk around the optical companion mass accretion onto the neutron star and, thus, X-ray outbursts are not possible. Recently, Özbey Arabacı et al. (2015) observed XTE J1946+274 in optical wavebands and analyzed the Hα line profile. They concluded that still a large Be-disk is present, which is most probably tilted with respect to the orbital plane. Furthermore, they found that the disk was steadily growing. They predict a contact of the outer regions of the Be-disk with the neutron star's orbit towards the end of 2016.

4.2 RX J0520.5−6932: A BeXRB on a Circular Orbit

The orbital parameters derived in this Section have been published by Kühnel et al. (2014), which justifies the use of the "we"-style.

In order to understand the evolution of BeXRBs a large sample of these systems has to be investigated. Although the Milky Way (MW) is the home of many BeXRBs, it is widely known that their distances are not well constrained[6]. Furthermore, interstellar dust within the MW plane blocks our view on the other side of the galaxy, such that we actually can only guess how many BeXRBs are located there. A unique opportunity to study complete populations of BeXRBs with known distances is given by the Small and Large Magellanic Clouds (SMC and LMC, respectively). In the LMC, about 20 HMXBs are confirmed, from which 14 harbor neutron stars (see Vasilopoulos et al., 2014a, and references therein).

One of these HMXBs is RX J0520.5−6932, which was discovered in 1994 by Schmidtke et al. (1994) using data from *ROSAT*. Its optical counterpart of spectral type O9Ve (Coe et al., 2001) suggests the system to be a BeXRB. This was confirmed by the first detected X-ray outburst in 2013 January during a *Swift* UV survey of the LMC (Vasilopoulos et al., 2013a). A few subsequent *Swift* pointings revealed a flux evolution consistent with typical BeXRB outbursts. The source was to faint to be visible in *Swift*-BAT. However, it was suddenly detected in 2014 January during a type II outburst, where the neutron star was accreting close to the Eddington limit of $\sim 2 \times 10^{38}\,\mathrm{erg\,s^{-1}}$ (Vasilopoulos et al., 2014b).

[5]This is about the same distance as between the Earth and the Sun (= 1 Astronomical Unit, AU).

[6]The distances found in the literature, such as listed in Reig & Nespoli (2013), often do not include uncertainties as their estimation based on optical observations of the companion stars is dominated by systematics (Riquelme et al., 2012). This is not the case for sources found in nearby galaxies since they have "well known distances compared to sources in our Galaxy" (Vasilopoulos et al., 2014a).

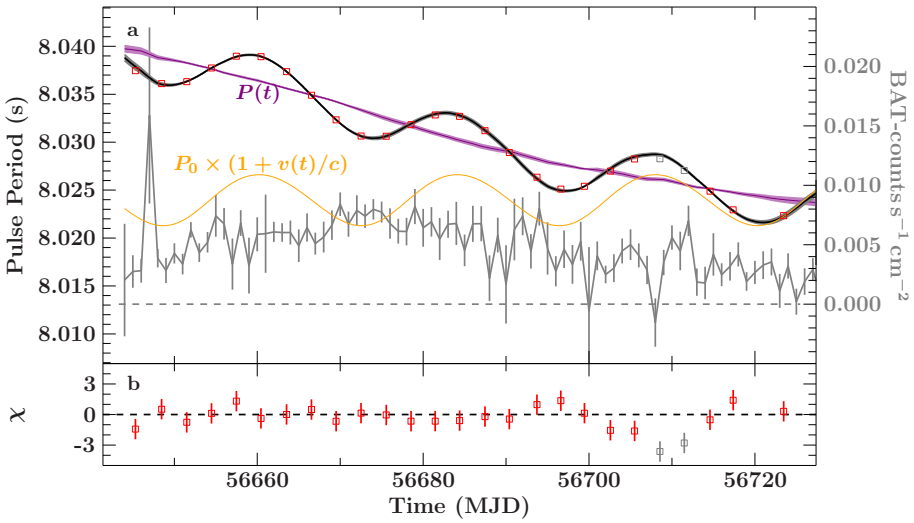

Figure 4.9: a: Pulse period evolution of RX J0520.5−6932 as observed by *Fermi*-GBM (red) together with the best-fit model (black). The purple curve is the intrinsic spin-up and the orange curve is the Doppler shifted period by orbital motion. The BAT light curve of the outburst is shown in gray. Its uncertainties affect the modeled spin-up and, thus, the total model. The resulting uncertainties of the model are represented by the thickness of the corresponding model curves (black and purple). The two data points marked in gray have been excluded from the fit due to a significant dip in the BAT count rate. **b:** Residuals of the best-fit model to the *Fermi*-GBM data.

During the onset of the outburst a pulse period of 8.03533(3) s was found in data from *Swift*-XRT (Vasilopoulos et al., 2013b). The brightness of the source during this type II outburst allowed the *Swift*-BAT and the *Fermi*-GBM pulsar project to observe its flux and pulse period evolutions, respectively, which are shown in Fig. 4.9.

4.2.1 Determining orbital parameters

The *Fermi*-GBM pulse frequencies clearly show an orbital modulation. These data are a potential candidate to be fitted with the torque model as implemented in Sect. 2.3.2. The orbital period of ∼25 d can be derived from the pulse period evolution presented in Fig. 4.9 (this Figure shows the final best-fit model and the *Swift*-BAT light curve as well). Additionally, the source was spinning down by approximately 13 ms during the three covered orbital cycles (determined from the first to the last minimum of the cycles). From the orbital amplitude of about 5 ms (9 ms from the maximum to the minimum of the first cycle and correcting for the mean spin-up) we estimated a value for the projected semi-major axis of ∼109 lt-s using the rule of thumb given in Eq. (1.19). The shape of the orbital modulation appears to be quite symmetric indicating a very low eccentricity. Thus, we calculated the Doppler shift of the orbital motion using the approximated formula for nearly circular orbits as given in Eq. (1.21). The time of mean longitude of 90°, $T_{\pi/2}$, was estimated to MJD 56666 from the time of the observed maximum of the orbital modulation with an additional quarter of the orbital period[7]. The initial values for $g = e \sin\omega$ and $h = e \cos\omega$ were set to zero.

To fit the observed pulse period evolution with the torque model we used the *Swift*-BAT light curve as a measure for the neutron star's luminosity. We fixed $\alpha = 6/7$ assuming the neutron star to accrete from a disk. Furthermore, we set the reference flux

[7]This is a simple way of estimating $T_{\pi/2}$ than guessing the time where the amplitude of orbital motion has declined to its half after the maximum (see footnote on page 20) due to the spin-up of the source.

Table 4.2: Orbital and spin period parameters of RX J0520.5−6932 resulting from fitting the *Fermi*-GBM measurements with the torque model ($\chi^2_{\rm red} = 1.00$ with 17 d.o.f.)

$a \sin i$	$= 108.8(9)$ lt-s	t_0	= MJD 56669 (fixed)
$P_{\rm orb}$	$= 23.885(25)$ d	P_0	$= 8.034365(14)$ s
$T_{\pi/2}$	= MJD 56666.388(17)	a	$= 0\,{\rm s\,s^{-1}}$ (fixed)
g	$= -0.026(7)$	b	$= 2.978(9) \times 10^{-9}\,{\rm s\,s^{-1}}$
h	$= -0.023(8)$	α	$= 6/7$ (fixed)

Notes. All parameters are slightly different to those listed in Kühnel et al. (2014) since we have fixed $a = 0\,{\rm s\,s^{-1}}$ here. The values agree, however, within their uncertainties.

$F_{\rm ref} = 0.0066\,{\rm BAT\text{-}counts\,s^{-1}\,cm^{-2}}$, which was the peak flux of the outburst in *Swift*-BAT, the reference time $t_0 =$ MJD 56669, and ignored a constant spin-down[8], i.e., fixing $a = 0$. The initial fit followed the same strategy as for XTE J1946+274 (see Sect. 4.1), that is fixing the orbital parameters to their initial values and fitting the torque strength, b, and the spin period, P_0, at t_0. Due to the roughly estimated orbital parameters further fitting was required with those parameters kept free. The uncertainties of the BAT light curve were taken into account during this fit by applying Monte Carlo simulations as described in Sect. 4.1. The resulting fit quality of $\chi^2_{\rm red} = 1.9$ with 19 d.o.f. was, however, not acceptable. Two period measurements around MJD 56710 (see Fig. 4.9) might be responsible for this bad fit. At this time the count rate in the BAT light curve suddenly dropped below zero. That the source actually switched off for one day is very unlikely, especially since the adjacent count rates show that the source was still at a high luminosity level. The negative count rate caused an erroneous spin-*down* during the model calculation, which explains the negative residuals at this time. Due to the small uncertainty of the BAT count rate, however, this residuals get significant and worsened the fit quality. Ignoring these two period measurements reduced the $\chi^2_{\rm red}$ to 1.06 with 16 d.o.f., which is our final best-fit. The resulting orbital and spin period parameters are listed in Table 4.2.

4.2.2 Discussion

The orbital period of $P_{\rm orb} = 23.885$ d as found by our analysis of the pulse period evolution is slightly shorter than the 24.4302(26) d found by Vasilopoulos et al. (2014b), who analyzed the light curve of the optical companion using data from the *Optical Gravitational Lensing Experiment* (OGLE) and confirmed earlier period estimates by Coe et al. (2001). Shorter orbital periods determined by X-ray data in comparison to optical data have been reported for a few sources in the SMC (Townsend et al., 2011). The reason for this discrepancy might be an interplay between the orbital period and the rotation of the Be-disk, which modifies the optical light curve (Vasilopoulos et al., 2014b).

Our derived orbital parameters of RX J0520.5−6932 have been used by Tendulkar et al. (2014) to perform a detailed pulse phase resolved spectroscopy of two *NuSTAR*-observations during the same type II outburst. They found the spectral parameters to vary with the pulse phase. Furthermore, a cyclotron resonance scattering feature around 31.5 keV was detected in the spectra. Using the mass function of the system under the assumption of an companion mass between 17 and 23 $\rm M_\odot$, Tendulkar et al. (2014) concluded that

[8] In Kühnel et al. (2014) we had allowed for a constant spin-down, but did not add its value of $a = 0.00^{+0.26}_{-2.38} \times 10^{-10}\,{\rm s\,s^{-1}}$ to the list of fit parameters, unfortunately. The value is, however, consistent with zero, which is why we fixed it here.

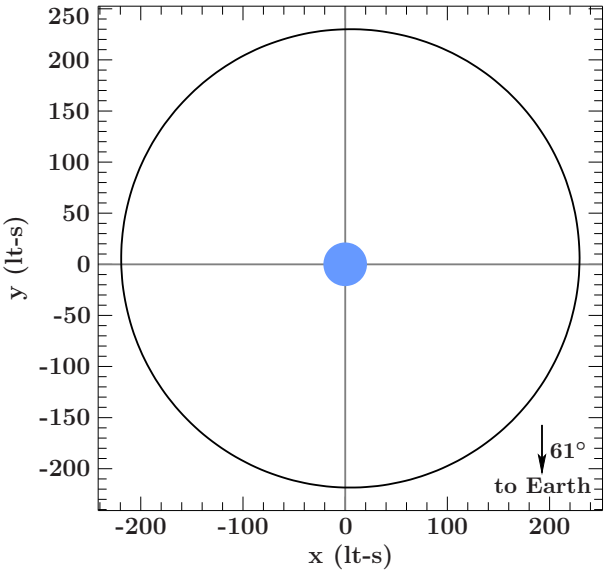

Figure 4.10: Sketch of RX J0520.5−6932's orbit resulting from the orbit determination. The orbit is seen from above assuming an inclination of 29°, which was found by Tendulkar et al. (2014) and Vasilopoulos et al. (2014b). The companion star's radius is set to 8.8 $R_\odot$ using stellar parameter tables by Vacca et al. (1996) with the spectral classification of O9Ve by Coe et al. (2001). The observer is inclined by the labeled angle with respect to the orbital plane.

the inclination, i, of the binary ranges between 27° and 31°, which was confirmed by Vasilopoulos et al. (2014b). Having estimated the inclination of RX J0520.5−6932 allows to draw the geometry of the system as shown in Fig. 4.10. The extremely small eccentricity of the binary compared to other BeXRBs is remarkable as well as the small distance of ∼200 lt-s at which the neutron star orbits its O9Ve companion[9]. As noted by Vasilopoulos et al. (2014b), this low eccentricity is expected in systems with short spin periods (Knigge et al., 2011), where the neutron star was born through an electron-capture supernova of a white dwarf.

Finally, the orbital and pulse period of RX J0520.5−6932 are very similar to those of the BeXRB 4U 0115+63 in the Milky Way ($P_{\rm orb} = 24.3161$ d and $P = 3.614$ s, Müller et al., 2010). In addition, both systems feature only rare outbursts separated by several years in quiescence. In the case of 4U 0115+63, Okazaki et al. (2013) proposed a misaligned Be-disk with respect to the orbital plane. They argued that for a precessing disk its distance to the periastron of the neutron star's orbit depends on the precession phase. This would result in weak or even absent X-ray activity during most of the periastron passages. Once the Be-disk rotates into the orbit of the neutron star, however, a sudden transfer of a large amount of matter would be possible. This might explain the outburst behavior of RX J0520.5−6932 despite its circular orbit.

4.3 XTE J1859+083: Detection of a Superorbital Period

In this Section I derive preliminary orbital parameters for the X-ray binary XTE J1859+083. A similar analysis was performed by Mark H. Finger and Peter A. Jenke, whose results are listed on the website of the *Fermi*-GBM pulsar project[10]. All results, including a spectral analysis of the recent *NuSTAR*-data performed by Jakob Stierhof, will be published in a forthcoming paper.

In August 1999, a new X-ray source was detected by *RXTE*-PCA during slews in the direction of the constellation Aquila (Marshall et al., 1999). A subsequent pointed observation by *RXTE* at the estimated source position revealed pulsations with a period of 9.801(2) s, which confirmed a neutron star as the compact object. Further observations

[9] Mercury orbits the Sun on an eccentric orbit at a distance between 153 and 234 lt-s (JPL's HORIZONS system, ssd.jpl.nasa.gov/horizons.cgi, queried on 2016/02/07).

[10] http://gammaray.nsstc.nasa.gov/gbm/science/pulsars/lightcurves/xtej1859.html

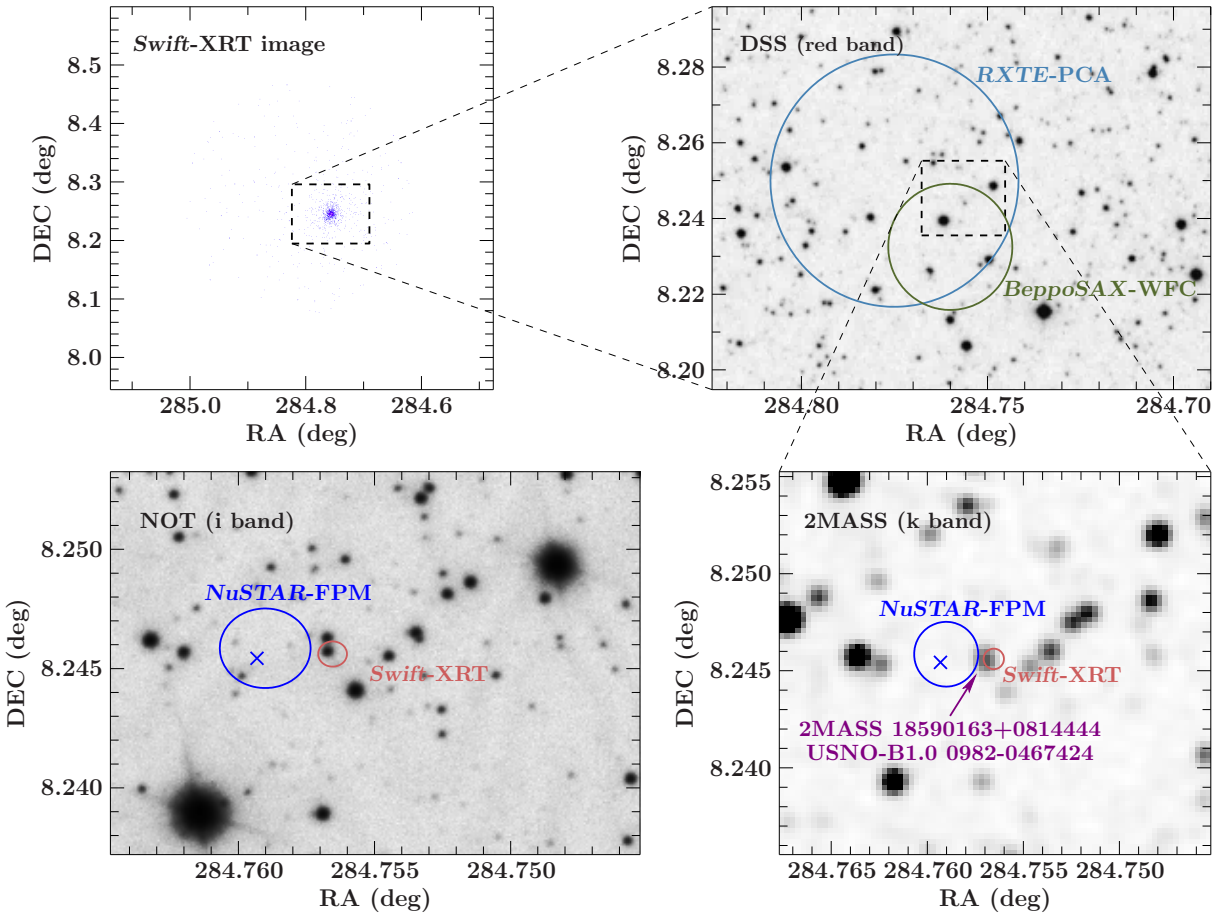

Figure 4.11: *Swift*-XRT-, DSS- (red optical band), 2MASS- (K band), and NOT-image (I band; P. Blay, priv. comm.) around the position of XTE J1859+083. The error circles in the DSS image show the X-ray positions as measured by *RXTE* (light blue; Marshall et al., 1999) and *BeppoSAX* (green; Corbet et al., 2009). An infrared source (purple labels) can be identified in the 2MASS-image within the error circle of *Swift* (red; Li & Kong, 2015). The positions derived by both *NuSTAR*-FPMs as described in the text are marked in the infrared images as well (dark blue). The crosses indicate the tendency towards the mean position as seen in *NuSTAR*. All error circles are on the 90% confidence level (except *NuSTAR*-FPM, see text for details).

distributed over 38 days produced data, which were analyzed and published by Corbet et al. (2009). These authors found a steadily decreasing flux by a factor of >30 within a month, which resembles a typical BeXRB outburst (see, e.g., Kühnel et al., 2015a).

In a subsequent ASM analysis, Corbet et al. (2009) were able to detect source activity preceding the discovery. In particular, XTE J1859+083 probably had featured a long type II outburst[11] during late 1996, which was followed by a few weak outbursts. These outbursts were separated by approximately 60.6 d, which was interpreted by Corbet et al. (2009) as the orbital period of the binary. In combination with a pulse period of 9.8 s they concluded XTE J1859+083 to be a BeXRB based on its position in Corbet's diagram (see Fig. 1.7).

However, the supposed Be star has not been identified yet by an actual optical observation, due to the large error circle of 2′ for the position of XTE J1859+083 as determined by *RXTE*-PCA (Marshall et al., 1999). Within this uncertainty a large number of stars can be seen in the images of the *Digitized Sky Survey* (DSS; see Fig. 4.11). Even when combined with the 1′ accurate position derived from images of the *Wide Field Camera*

[11] Due to a maximum flux of ∼1 ASM-count s^{-1} this outbursts happened undetected by any all-sky-monitor.

(WFC) onboard *BeppoSAX*, a single star cannot be associated with XTE J1859+083 (see Fig. 4.11 and Fig. 5 of Corbet et al., 2009).

In February 2015, the MAXI instrument and *Swift*-BAT detected a sudden increase of the X-ray flux at the position of XTE J1859+083 (Negoro et al., 2015; Krimm et al., 2015, respectively). The full BAT light curve of the source clearly showed an X-ray outburst similar to other BeXRBs (see gray curve in Fig. 4.12). Its peak flux in the 2–10 keV range of ∼25 mCrab in MAXI[12] was comparable to the type II outburst in 1996, which reached ∼13 mCrab in *RXTE*-ASM (Corbet et al., 2009). A pointed *Swift* observation was performed on 13 February 2015, which was used by Li & Kong (2015) to determine a more precise position of XTE J1859+083. Their best-fit coordinates derived from the *Swift*-XRT-image,

$$\alpha_{\mathrm{J2000}} = 18\mathrm{h}59\mathrm{m}01.57\mathrm{s} \quad \text{and} \quad \delta_{\mathrm{J2000}} = +08°14'44.2'',$$

are consistent with those determined with *RXTE*-PCA and *BeppoSAX*-WFC. Within the 1.9″ error circle one source was found in the *Two Micron All Sky Survey* (2MASS) and the *United States Naval Observatory* (USNO) infrared catalogs (Li & Kong, 2015). The XRT-observation was, however, affected by pile-up, which might add a systematic uncertainty to the error circle.

4.3.1 Determining orbital parameters

Due to the brightness of XTE J1859+083 during its outburst in early 2015, the *Fermi*-GBM pulsar project was able to measure the observed pulse period evolution (see the red data points in Fig. 4.12). An orbital signature is clearly visible in the data, spanning about three orbital cycles. Furthermore, the neutron star was spinning up during the outburst. Thus, this outburst is another ideal candidate to be fitted with the torque model (see Sect. 2.3.2).

In advance, starting values for the orbital parameters after the rules of thumb given in Sect. 1.2.1 were estimated. From the apparent periodic modulation of the observed pulse period (see Fig. 4.12) the binary's orbital period of approximately 37 d was derived (half the time range between the maxima of the first and the third cycle). The amplitude of the modulation, i.e., the period from the maximum to the minimum of the second cycle spanned 13 ms (here the source's flux did not change as much as during the first cycle, i.e., the spin-up should be almost constant). If a spin-up of 4 ms is subtracted (∼7 ms within 37 d, which is ∼4 ms within the 22 d from which the amplitude was determined) a semi-major axis of ∼240 lt-s after Eq. (1.19) was calculated using the 9.8 s pulse period. Due to the steeper left side of the maximum of the orbital modulation, the orbit must be eccentric. Consequently, the longitude of periastron is probably between $-135° < \omega < -45°$ and the time of periastron passage was between MJD 57073 $< \tau <$ MJD 57084 (from the observed maximum at MJD 57050).

After having set the orbital parameters to the estimated values above, the fit strategy was equal to the orbit determinations of XTE J1946+274 and RX J0520.5−6932 as presented in Sect. 4.1 and 4.2, respectively. The luminosity exponent, α, was fixed to 6/7, the reference time for the spin period evolution was set to $t_0 =$ MJD 57100 and a constant spin-down was neglected in the model, i.e., $a = 0$ was fixed. To calculate the torque onto the neutron star the *Swift*-BAT light curve was taken as a measure for the luminosity. The reference flux, F_{ref}, was set to 0.022 BAT-counts $\mathrm{s}^{-1}\,\mathrm{cm}^{-2}$, which was the maximum count

[12] The 2–20 keV peak count rate in the MAXI light curve was about 0.12 counts $\mathrm{s}^{-1}\,\mathrm{cm}^{-2}$ and its 10–20 keV rate was 0.03 counts $\mathrm{s}^{-1}\,\mathrm{cm}^{-2}$. With a mean count rate of 3.6 counts $\mathrm{s}^{-1}\,\mathrm{cm}^{-2}$ for the Crab pulsar, XTE J1859+083 reached a 2–10 keV flux of about $(0.12 - 0.03)/3.6 = 25$ mCrab. The light curves can be found at http://maxi.riken.jp/top/index.php?cid=1&jname=J1859+082

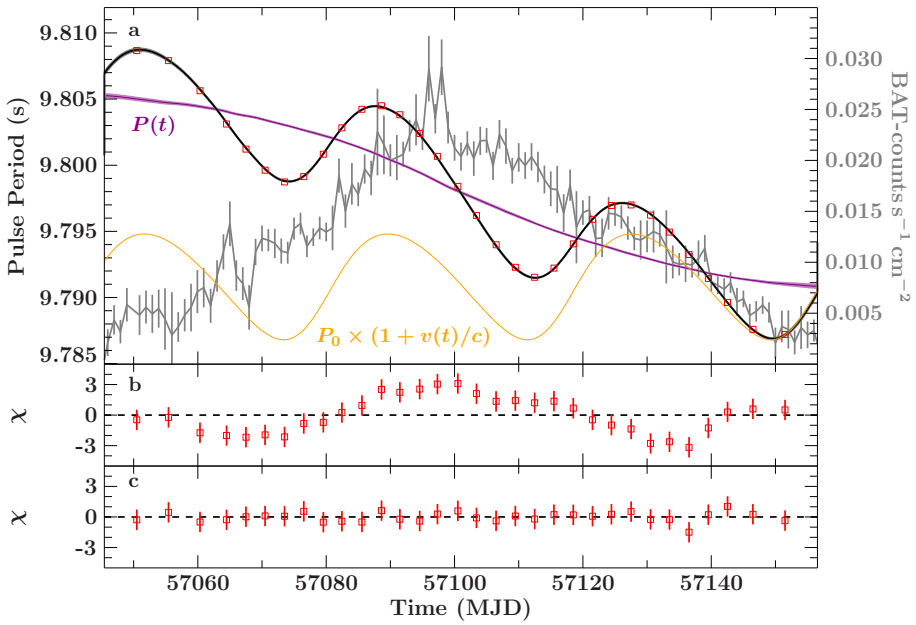

Figure 4.12: a: The pulse period evolution of XTE J1859+083 as observed by *Fermi*-GBM (red) together with the best-fit model (black). The purple curve is the intrinsic spin-up and the orange curve is the Doppler shifted period by orbital motion. The BAT light curve of the outburst is shown in gray, which uncertainties affect the spin-up and the total model. The resulting uncertainties of the model are represented by the thickness of the corresponding model curves (black and purple). **b:** Residuals of the torque model and **c:** residuals after adding a sinusoidal component to the model.

rate the outburst reached in *Swift*-BAT. The measurement uncertainties of the *Swift*-BAT light curve were taken into account by Monte Carlo simulations as described in Sect. 4.1.

This fit resulted in a reduced χ^2 of 3.94 with 25 d.o.f., although the model seemed to follow the measured pulse period evolution well. The reason was a second weak modulation, which was visible in the residuals only (see Fig. 4.12b). Nevertheless, to get reasonable uncertainties for the orbital parameters resulting from this bad fit, relative systematic uncertainties of 7×10^{-6} were added to the measured pulse periods to achieve a χ^2_{red} near unity. The resulting best-fit parameters are listed in Table 4.3.

4.3.2 Detection of a superorbital period

As mentioned above, the residuals of a fit to the torque model showed a prominent modulation with a period of around 65 d over the full range of period measurements (see Fig. 4.12b). To improve the fit without adding systematic uncertainties a relative, sinusoidal modulation was added to the model of the form

$$P^*_{\mathrm{obs}}(t) = P_{\mathrm{obs}}(t) \times (1 + A_{\mathrm{sine}} \sin(2\pi(t - t_{\mathrm{sine}})/P_{\mathrm{sine}})) \quad , \tag{4.1}$$

where $P_{\mathrm{obs}}(t)$ is the torque model including the binary orbit (see Eq. 1.17), A_{sine} is the relative amplitude of the sine, t_{sine} its reference time, and P_{sine} its period. This extension of the model led to $\chi^2_{\mathrm{red}} = 0.89$ with 22 d.o.f. after error propagating the BAT uncertainties by the Monte Carlo approach. The final best-fit parameters are listed in Table 4.3 and the residuals are shown in Fig. 4.12c. The orbital and spin period parameters were consistent with the first fit, where systematic uncertainties have been added to the data. Thus, the derived orbital solution is robust against this feature. The resulting geometry of the binary is visualized in Fig. 4.13, where an inclination of 90° is assumed, i.e., all distances are lower limits.

Table 4.3: Best-fit orbital and spin period parameters of XTE J1859+083 as derived by fitting the *Fermi*-GBM data with the torque model. For the first fit (sys. unc.) systematic uncertainties have been added to the observed period, while for the second fit (add. sine) an additional sinusoidal modulation has been included in the model as described in the text.

	sys. unc.	add. sine
$a \sin i$ (lt-s)	$211.4^{+1.9}_{-1.7}$	$211.4^{+0.5}_{-0.5}$
$P_{\rm orb}$ (d)	$37.97^{+0.08}_{-0.09}$	$37.95^{+0.04}_{-0.03}$
τ (MJD)	$57078.7^{+0.5}_{-0.4}$	$57078.64^{+0.14}_{-0.11}$
e	$0.127^{+0.008}_{-0.009}$	$0.1279^{+0.0024}_{-0.0022}$
ω (°)	$-117.0^{+1.0}_{-0.8}$	$-117.9^{+0.6}_{-0.9}$
t_0 (MJD)	57100 (fixed)	
P_0 (s)	$9.798145^{+0.000026}_{-0.000024}$	$9.798167^{+0.000008}_{-0.000007}$
a ($\mathrm{s\,s^{-1}}$)	0 (fixed)	
b ($10^{-9}\,\mathrm{s\,s^{-1}}$)	$2.463^{+0.012}_{-0.017}$	$2.456^{+0.006}_{-0.005}$
α	6/7 (fixed)	
$P_{\rm sine}$ (d)		$66.0^{+3.0}_{-3.1}$
$A_{\rm sine}$		$1.05^{+0.10}_{-0.10} \times 10^{-5}$
$t_{\rm sine}$ (MJD)		$57082.0^{+1.9}_{-1.5}$
$\chi^2_{\rm red}$/d.o.f.	1.03/25	0.89/22

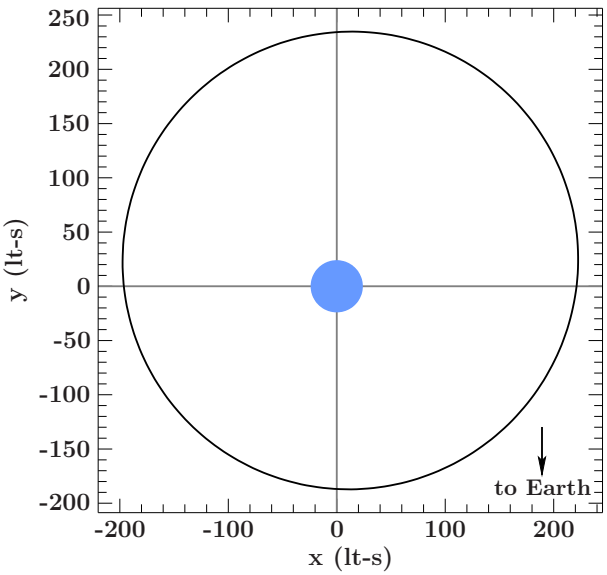

Figure 4.13: Sketch of XTE J1859+083's orbit resulting from the orbit determination. The orbit is seen from above assuming an inclination of 90°, thus the distances are lower limits because no inclination has yet been determined. The companion star's radius is set to $10\,\mathrm{R}_\odot$, although its real radius is unknown.

The ∼65 d period of the modulation detected in the residuals of the pulse period evolution of XTE J1859+083 is very close to the 60.65(8) d period found by Corbet et al. (2009) in the *RXTE*-ASM light curve. It is questionable that both observations have the same physical origin, because the authors found a modulation of the X-ray luminosity while in this work a modulation of the pulse period is detected. Assuming that their common origin is a modulation of the mass accretion rate, the theory by GL79 (see Sect. 1.3.1) can be used to derive the flux amplitude, F, from the apparent amplitude, A_{sine}, of the additional sinusoidal component found in the pulse period evolution. From the torque model given in Eq. (2.24) the needed amplitude in flux is

$$\frac{\Delta P}{\Delta t} = b\left(\frac{F}{F_{\mathrm{ref}}}\right)^{\alpha} \;\Rightarrow\; \frac{4P_0 A_{\mathrm{sin}}}{P_{\mathrm{sin}}} = b\left(\frac{F}{F_{\mathrm{ref}}}\right)^{\alpha} \;\Rightarrow\; F = F_{\mathrm{ref}}\left(\frac{4P_0 A_{\mathrm{sin}}}{bP_{\mathrm{sin}}}\right)^{1/\alpha} \quad .$$

The resulting flux amplitude is $F = 0.00036\,\mathrm{BAT\text{-}counts\,s^{-1}\,cm^{-2}}$ for the best-fit values listed in Table 4.3, which is much smaller than the uncertainties of the *Swift*-BAT light curve of XTE J1859+083 as can be seen from Fig. 4.12.

In many X-ray pulsars additional modulations apart from the orbital signature, so-called 'superorbital' modulations, have been observed (see, e.g., Priedhorsky & Holt, 1987; Kotze & Charles, 2012; Corbet & Krimm, 2013). Their periods are in the range of a few days to several months. The most prominent example is the LMXB Hercules X-1, where the modulation is thought to be caused by a precessing accretion disk (see, e.g., Staubert et al., 2009, and references therein). Superorbital modulations are also found in BeXRBs of the SMC as reported by Rajoelimanana et al. (2011). They found very long superorbital periods in the order of hundred days or more in the optical light curves of the Be companions. A possible explanation might be the propagation of global one-armed oscillations in the Be-disk as theoretically investigated by, e.g., Okazaki (1991). In case of XTE J1859+083 the super orbital period of ∼65 d is, however, much smaller than expected for such one-armed oscillations. Both scenarios are speculation only and need further investigations, which are beyond the scope of this Section.

4.3.3 Estimating companion mass, distance, and magnitude

It is particularly important to identify the spectral type of the optical counterpart of XTE J1859+083 to rule out either the accretion disk or Be-disk as origin of the superorbital period. Furthermore, if no Hα emission line is found in the optical spectrum, then the binary might not a BeXRB[13]. To select possible candidates in the crowded field around the position of XTE J1859+083, some properties of the optical companion star were derived in the following based on the orbital parameters and X-ray observations.

From the derived orbital parameters as listed in Table 4.3 the minimum mass of the optical companion star was estimated. The mass function of the binary calculated after Eq. (1.22) resulted in $f(M) = 7.04^{+0.05}_{-0.06}\,\mathrm{M_\odot}$. Solving for the companion mass and assuming a neutron star mass of $M_{\mathrm{x}} = 1.4\,\mathrm{M_\odot}$ resulted in $M_{\mathrm{opt}} \gtrsim 9.3\,\mathrm{M_\odot}$, which is consistent with a HMXB nature.

To investigate the existence of an Hα emission line in the spectra of the optical counterpart of XTE J1859+083, which would unambiguously confirm its BeXRB nature, the expected apparent magnitude is an important information to propose for an optical observation. From the X-ray flux of $2.5\times10^{-9}\,\mathrm{erg\,s^{-1}\,cm^{-2}}$ within 5 and 70 keV as measured with *NuSTAR* (J. Stierhof, priv. comm.) the distance to the source was estimated. The

[13] It is known that Be star may loose their circumstellar disk (see Wisniewski et al., 2010, and references therein). Although these disk loss phases are rare, the absence of Hα emission does not necessarily exclude a Be star as a companion.

properties of the 2015 outburst of XTE J1859+083, especially its duration of almost 100 d, is evidence for a type II outburst with a typical luminosity around $10^{37}\,\mathrm{erg\,s^{-1}}$. If isotropic emission of the neutron star is assumed, its distance would then be $d \approx 5.8\,\mathrm{kpc}$. The majority of transient BeXRBs in the Milky Way, which feature type II outbursts, consist of a B-type companion of luminosity class V (matching the sources listed in Kühnel et al., 2015a with the catalog of HMXBs by Liu et al., 2006). The absolute visual magnitude of such a star is $M_\mathrm{v} = -4.2\,\mathrm{mag}$ (Vacca et al., 1996). Using the distance modulus,

$$m_\mathrm{v} - M_\mathrm{v} = 5\log_{10}(d/10\,\mathrm{pc}) \quad , \tag{4.2}$$

an apparent visual magnitude of $m_\mathrm{v} = 9.6\,\mathrm{mag}$ was derived for the distance, d, estimated above. Interstellar extinction caused by neutral material needs to be taken into account since it increases the apparent magnitude, i.e., the star appears dimmer. Nowak et al. (2012) modified the relationship between the decrease in the visual magnitude, A_V, and the hydrogen column density, N_H, as found by Predehl & Schmitt (1995) to account for the absorption model by Wilms et al. (2000),

$$A_\mathrm{v} = 1\,\mathrm{mag} \times N_\mathrm{H}/2.7 \times 10^{21}\,\mathrm{cm^{-2}} \quad . \tag{4.3}$$

For an absorption column density of $N_\mathrm{H}{\sim}9 \times 10^{21}\,\mathrm{cm^{-2}}$ in the direction of XTE J1859+083 as found by the 21 cm surveys (LAB Survey of Galactic HI, Kalberla et al., 2005) the visual magnitude of the star would be increased to $m_\mathrm{v}{\sim}12.9\,\mathrm{mag}$. Using the absorption column density of $20 - 27 \times 10^{21}\,\mathrm{cm^{-2}}$ as found by an analysis of the X-ray spectrum (J. Stierhof, priv. comm.) resulted, however, in a visual magnitude of $m_\mathrm{v}{\sim}17.0 - 19.6\,\mathrm{mag}$. This discrepancy can be explained by either variability of the interstellar extinction on angular scales smaller than the resolution of the 21 cm surveys or by an additional source intrinsic absorption. Consequently, the final apparent visual magnitude of a B0V star as the companion of XTE J1859+083 was expected to be $m_\mathrm{v} = 16.3 \pm 3.4\,\mathrm{mag}$[14]. Repeating the above estimation for a very luminous type II outburst of $10^{38}\,\mathrm{erg\,s^{-1}}$, which GRO J1008−57 almost reached in 2012 November (see Sect. 5.1 and Kühnel et al., 2016b, in prep.), resulted in a distance of 18.3 kpc and an apparent magnitude of 22.1 mag, which would be the upper limits for these quantities. The two stars within the *Swift*-XRT error circle with magnitudes around 21 mag (P. Blay, priv. comm.) are, therefore, good candidates for the optical counterpart. However, the stars within the *NuSTAR* error circle are even fainter than the estimated apparent magnitude, which would point to a later spectral type. If this holds true, then XTE J1859+083 is probably no BeXRB, which is in contradiction to the observed X-ray outburst behavior and its location in Corbet's diagram. Without an identified optical companion star the source's type remains unclear.

4.4 GRO J1008−57: Predictable Type I Outbursts

The orbital parameters in this Section are the main result of my Master's thesis (Kühnel, 2011). The analysis is briefly presented here again due to some slight changes and more conclusions compared to my previous thesis. The results have been published in Kühnel et al. (2013), which is why this Section uses the "we"-style. Parts from this publication have been paraphrased here.

[14] As a consistency check, this apparent magnitude is in very good agreement with 15.27 mag for the B0e optical companion of GRO J1008−57 (Coe et al., 1994), which distance was estimated to be 5.8 kpc as well (Riquelme et al., 2012) and a similar interstellar absorption was found in the direction of this source (Kühnel et al., 2013).

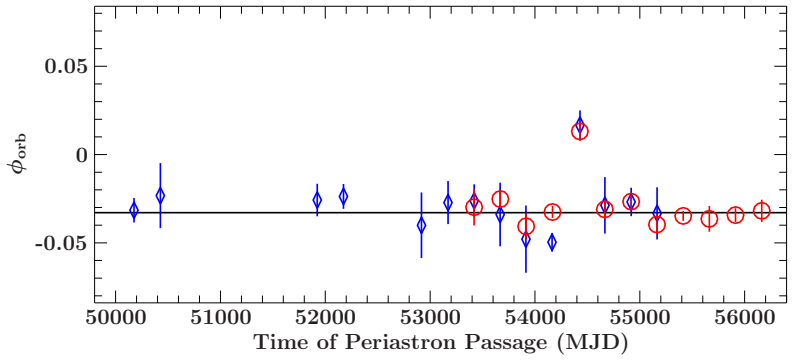

Figure 4.14: Orbital phases of the observed outburst maxima of GRO J1008−57 observed in *RXTE*-ASM (blue) and *Swift*-BAT (red). With the exception of the outburst in 2007 December all outburst times are consistent with the same orbital phase (black line) (taken from Kühnel et al., 2013).

The *Compton Gamma Ray Observatory* (CGRO) discovered the transient BeXRB GRO J1008−57 during a luminous outburst in 1993 July (Wilson et al., 1994; Stollberg et al., 1993). Its optical counterpart was identified as a B0e type star (Coe et al., 1994) at a distance of 5.8(5) kpc (Riquelme et al., 2012). By analyzing the light curve from *RXTE*-ASM, Levine & Corbet (2006, see also Levine et al., 2011) found the outbursts of GRO J1008−57 to be separated by 248.9(5) d[15] and interpreted this as the orbital period of the binary. This period is in good agreement with 247.8(4) d[15] as determined by Coe et al. (2007) by a Doppler shift analysis of the ∼93.6 s pulse period of the neutron star (Stollberg et al., 1993). Furthermore, the eccentricity of the system was found to be $e = 0.68(2)$, which is among the highest eccentricities known for a BeXRB[16] (see Townsend et al., 2011, for a recent list). See Sect. 5.1 for a description of GRO J1008−57's X-ray spectrum.

4.4.1 Predictable Type I Outbursts

GRO J1008−57 featured further regular outbursts since its discovery (Coe et al., 2007; Kühnel et al., 2013). In particular, two strong outbursts of the source occurred in 2005 February and 2007 December, the latter one reached a peak flux of around 84 mCrab, which was the highest flux observed within the lifetime of *RXTE*-ASM. The regularity of outbursts was confirmed very well with data from *Swift*-BAT, in which the source was detected during all periastron passages of the source since the launch of the satellite in 2004 November (see Fig. G.1).

We determined the times of GRO J1008−57's maximum flux during each of its detected outbursts in *RXTE*-ASM and *Swift*-BAT until 2012 July. The corresponding light curves were inspected for the time bin with the highest count rate. In order to detect weak outbursts the *RXTE*-ASM light curve was rebinned on 5 d intervals. Using the orbital parameters presented in this work (see Table 4.4) we calculated the orbital phase of maximum flux for all outbursts. As can be seen from the results presented in Fig. 4.14 all detected outbursts of GRO J1008−57 are consistent with a specific orbital phase of $\phi_{\mathrm{orb}} = -0.0323(17)$. This value was determined by a joint analysis of the pulse arrival times as presented below. Thus, the outbursts of GRO J1008−57 reach their maximum luminosity ∼7.5 d before the actual periastron passage of the neutron star, which allows us to predict the type I outbursts times,

$$T_{\mathrm{outburst}} = \mathrm{MJD}\ 54416.65 + n \times 249.48\,\mathrm{d} \quad , \tag{4.4}$$

[15]This uncertainty is on the one sigma confidence level.

[16]To my knowledge, there is only one BeXRB known with an even larger eccentricity, which is 2S 1845−024 ($e = 0.8792(54)$, Finger et al., 1999). There are, however, a few fast spinning pulsars known ($P < 1$ s) with similar eccentricities (compare to Table 7 of Townsend et al., 2011).

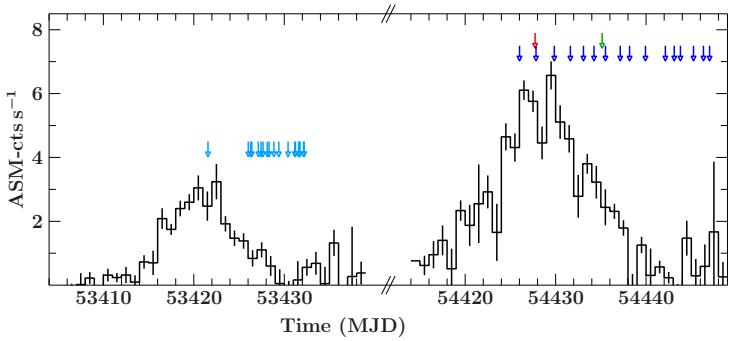

Figure 4.15: *RXTE*-ASM light curve of the 2005 February and 2007 December outbursts of GRO J1008−57. The outbursts were monitored with several pointings during their decays by *RXTE* (light and dark blue), *Swift* (red), and *Suzaku* (green).

where n is the outburst number since 2007 December. From the scattering of the actual observed outburst maxima (compare Fig. 4.14) we estimated an uncertainty of 3 d for the predicted dates.

As can be seen from Fig. 4.14, the strong type I outburst of GRO J1008−57 in 2007 December was delayed by ∼11 d compared to the predicted date. Consequently, we have ignored this outburst during the above analysis of the outburst time. Due to the typical outburst duration of about 14 d (compare Fig. G.1) the 2007 outburst is, however, still connected to the periastron passage of the neutron star.

The question is why the outbursts of GRO J1008−57 occur regularly every orbital period. A regular outburst behavior around the periastron passage was theoretically predicted already by Okazaki & Negueruela (2001). These authors concluded that Be-disks in BeXRBs should be truncated at specific resonances due to the disk's tidal interaction with the neutron star. This would result in smaller but denser Be-disks compared to isolated stars. The resonance radius particularly depends on the eccentricity and the orbital period of the binary. The more time the neutron star spends far away from its companion, which would be the case for long orbitals period and high eccentricities ($e \gtrsim 0.6$), the larger the Be-disk can grow uninterruptedly. In case of GRO J1008−57 Okazaki & Negueruela (2001) concluded that the Be-disk should be truncated at the 7:1 or 8:1 resonance, which would result in a disk size slightly beyond the critical Roche radius at the periastron. Consequently, type I X-ray outbursts would occur at each periastron passage[17] (assuming that the disk size is maintained steadily). The observed outbursts are located, however, slightly *before* periastron. A misaligned Be-disk with respect to the orbital plane might explain this observational fact[18] as proposed by Okazaki et al. (2013). These authors also discussed this misalignment as origin for the type II "giant" outbursts. Another source with regular type I outbursts is 2S 1845−024 ($e = 0.8792(54)$, $P_{\rm orb} = 242.180(12)$ d, Finger et al., 1999), however, here the outbursts were observed slightly after periastron.

4.4.2 Measuring Pulse Arrival Times

The decays of the 2005 February and 2007 January outbursts of GRO J1008−57 have been monitored intensively with pointed *RXTE* observations. Additionally, *Swift* observed the 2007 outburst during maximum luminosity while a *Suzaku* observation was performed during its decay (see Fig. 4.15 and Table F.2 for details). We used the light curves of all these observations to determine the orbital parameters of GRO J1008−57 (see Kühnel et al., 2013, for more details about the data extraction described briefly in the following). Due to the low count rates at the end of the outbursts only *RXTE* data from the top layer of PCU2 were used. The light curves with a resolution of 1 s were extracted from the

[17] This answers specific question 1.
[18] This answers specific question 3.

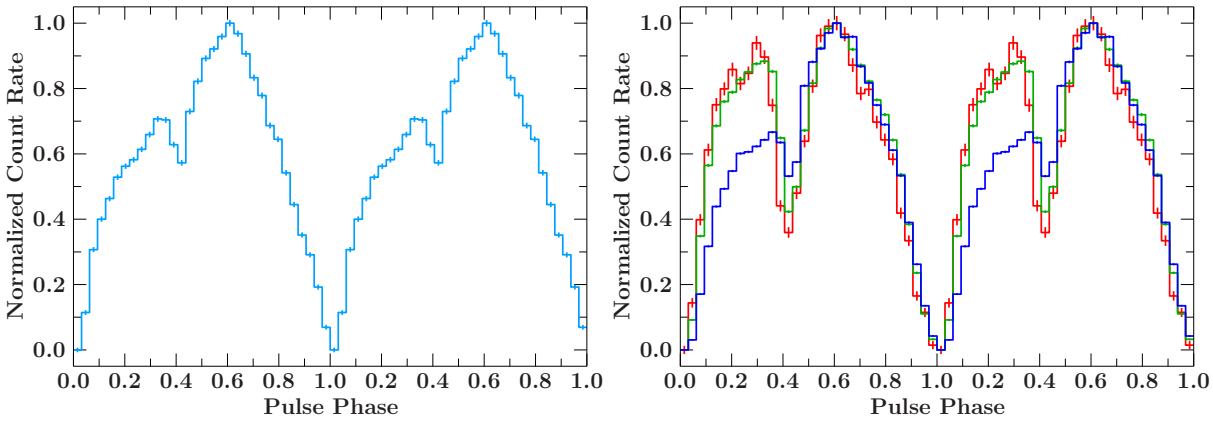

Figure 4.16: Pulse profiles of GRO J1008−57 as seen in **Left:** *RXTE*-PCA during the 2005 February outburst (light blue) and **Right:** *RXTE*-PCA (dark blue), *Swift*-XRT (red), and *Suzaku*-XIS3 (green) during the 2007 December outburst. The profiles are normalized to their count rate range and shown twice for clarity. They were used to determine the pulse arrival times in the light curves measured by the corresponding instrument.

GoodXenon data using `HEASOFT` v6.11. and the standard reduction pipelines developed by Wilms et al. (2006). The *Swift*-XRT was operated in WT mode during the observation due to a high source count rate. Its 1 s light curve was extracted with `xselect` from a circular region centered on the source with a 1′ radius. After the attitude of *Suzaku* had been corrected by `aeattcor2` (Nowak et al., 2011), the source events measured with XIS3 were extracted from a 90″ circular region. Areas within this circle with more than 4% pile-up, calculated using `pileest` (Nowak et al., 2011), were excluded. The final source region was applied with `xselect` to extract the XIS3 light curve of GRO J1008−57 with a 2 s time resolution[19].

To determine the pulse arrival times from the extracted light curves a pulse profile template is needed in order to find the matches with the observed pulses (see Sect. 2.2.3) for each outburst and detector. In order to produce pulse profile templates for *RXTE*, we used the observations 90089-03-02-00 and 93032-03-02-02 for the outbursts in 2005 February and 2007 December, respectively. Initially, the corresponding light curves were folded into 32 phase bins with a local period found by epoch folding (see Sect. 2.2.2). The resulting pulse profiles measured with *Swift* and *Suzaku* in 2007 were aligned in shape with the corresponding *RXTE* profile. Since determining and fitting the arrival times is an iterative process (see Sect. 2.2.3) the final pulse profile templates presented in Fig. 4.16 were corrected for binary motion and spin-up using the parameters listed in Table 4.4. The profiles in *Swift*-XRT and *Suzaku*-XIS3 are similar in shape due to comparable energy ranges of the detectors (compare Fig. 3.1). Although taken at different flux levels of the source the profiles between 2005 and 2007 as measured with *RXTE* are almost identical.

Having created the pulse profile templates, we searched the light curves of GRO J1008−57 for individual pulses by cross-correlation (see Sect. 2.2.3). We set the reference times needed to determine the phase shifts to MJD 53427.6609 for the 2005 data (the first time bin of *RXTE* observation 90089-03-02-00) and to MJD 54434.4819 for the 2007 data (the first time bin of the *Suzaku* observation). For observations with an insufficient S/R to detect individual pulses we accumulated 3–5 consecutive pulses. At the end of each outburst it was even necessary to use the full light curves to accumulate a single pulse sufficiently for the cross-correlation. We then used Eq. (2.16) and the local period of the

[19]For the analysis presented in Kühnel (2011) a resolution of 5 s was chosen, which was coarser than the bin size of the pulse profile pattern. This choice caused an artificial shift of the determined arrival times introduced by an interpolation of the input light curve.

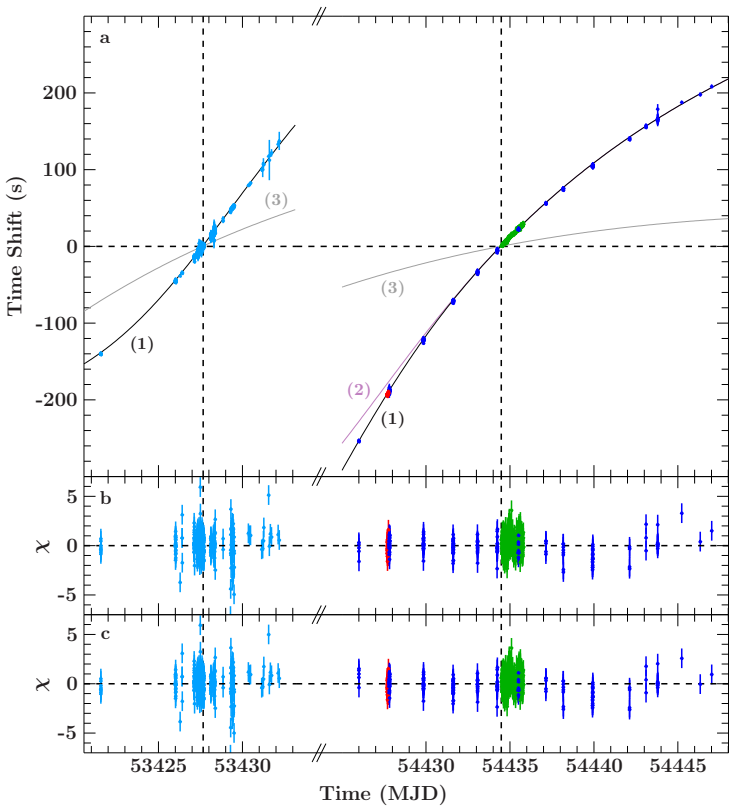

Figure 4.17: **a:** Pulse arrival times of GRO J1008−57 with respect to a constant observed pulse period, i.e., without spin-up and orbital effects as measured by *RXTE* (blue), *Suzaku* (green), and *Swift* (red). The observed delays in the arrival times cannot be explained by the orbital parameters initially found by Coe et al. (2007; 3, gray model). Updating $P_{\rm orb}$ and τ leads to a better description of the data (2, purple model) and the final best-fit includes a slight spin-up during the 2007 outburst as well (1, black model). **b:** Residuals of the best-fit model and **c:** Residuals after a fit including the times of the outburst maxima (see Fig. 4.14) (taken from Kühnel et al., 2013).

template profiles found by epoch folding to derive the pulse arrival times.

4.4.3 Determining orbital parameters

Figure 4.17a shows the pulse arrival times of GRO J1008−57 during its 2005 and 2007 outburst relative to a constant pulse period, i.e., without taking the Doppler shift by orbital motion into account. The delay of ∼450 s between the expected arrival times and the observed ones indicate a strong change of the apparent pulse period over the full duration of the 2007 data. For the 2005 data the total delay is around 300 s. For a first investigation we included the orbital motion of the neutron star using the parameters found by Coe et al. (2007, see also Table 4.4). The resulting expected arrival times (Fig. 4.17, gray model 3) could not explain the observations. Allowing for an additional intrinsic spin-up of the neutron star resulted in a spin-up on the order of $10^{-8}\,\mathrm{s\,s^{-1}}$, which is, however, much larger than expected for this source (Coe et al., 2007) and for BeXRBs in general (compare Tables 4.1, 4.2, and 4.3). Consequently, the mismatch between the expected and observed pulse arrival times is probably caused by an uncertainty in the orbital parameters after Coe et al. (2007). This is strengthened by the fact that the accumulated uncertainty in the time of periastron passage extrapolated to the 2007 outburst is about 8.5 d. After examining the influence of the orbital parameters on the expected arrival times carefully (Kühnel, 2011), the only parameters which can cause the mismatch between the data and the gray model in Fig. 4.17 are the time of periastron passage, τ, and the orbital period, $P_{\rm orb}$. Fitting these parameters in addition to the intrinsic spin period resulted in a good description of the observed pulse arrival times (purple model in Fig. 4.17). The only remaining mismatch of ∼15 s was observed during the maximum of the 2007 December outburst (the first dark blue data point in Fig. 4.17). Adding a spin-up to the 2007 data modeled by $\dot{P} \neq 0$ and $\ddot{P} \neq 0$ for times between MJD 54426 and MJD 54434 improved the description of the pulse arrival times ($\chi^2_{\rm red} = 1.01$ for 1001 d.o.f.; black curve in Fig. 4.17). The resulting fit parameters are listed in Table 4.4.

Table 4.4: Orbital and spin period parameters of GRO J1008−57 as derived by fitting the pulse arrival times iteratively and together with the observed outburst times of Fig. 4.14 (joined). The eccentricity, e, longitude of periastron passage, ω, and projected semi-major axis, $a \sin i$, have been fixed to the values found by Coe et al. (2007), whose results are listed for comparison.

		this work (Kühnel et al., 2013)	
	Coe et al. (2007)	arrival times	joined
$a \sin i$ (lt-s)	530^{+60}_{-60}	530 (fixed)	
$P_{\rm orb}$ (d)	247.8^{+4}_{-4}	$249.60^{+0.06}_{-0.06}$	$249.48^{+0.04}_{-0.04}$
τ (MJD)	$49189.8^{+0.5}_{-0.5}$	$54425.16^{+0.20}_{-0.21}$	$54424.71^{+0.20}_{-0.16}$
e	$0.68^{+0.02}_{-0.02}$	0.68 (fixed)	
ω (°)	-26^{+8}_{-8}	-26 (fixed)	
P_{2005} (s)		$93.67926^{+0.00008}_{-0.00011}$	$93.67928^{+0.00010}_{-0.00009}$
P_{2007} (s)		$93.71284^{+0.00019}_{-0.00018}$	$93.71336^{+0.00017}_{-0.00022}$
$\dot{P}_{2007}$ (10^{-9} s s^{-1})[a]		$-0.82^{+0.18}_{-0.29}$	$-0.61^{+0.24}_{-0.22}$
$\ddot{P}_{2007}$ (10^{-14} s s^{-2})[a]		$3.38^{+0.16}_{-0.10}$	$3.38^{+0.07}_{-0.16}$
$\chi^2_{\rm red}$/d.o.f.	- [b]	1.01/1001	1.04/1024

Notes. [a] The spin-up during the 2007 December outburst is applied to times earlier than MJD 54434.4819 only. The same date is used as reference time, t_0, for the spin period evolution with $P(t_0) = P_{2007}$. [b] The fit quality is not listed in Coe et al. (2007).

Using the orbital parameters we calculated the orbital phases of GRO J1008−57's outbursts as observed in *RXTE*-ASM and *Swift*-BAT (see Fig. 4.14). We found the times of the maximum flux during the outbursts to be consistent with a single orbital phase (see last paragraph for the details). In order to enhance the precision of the orbital parameters these outburst times (excluding the 2007 December outburst) were fitted together with the pulse arrival times. This resulted in a similar fit quality compared to fitting the arrival times alone (compare the residuals in Fig. 4.17b and c), but a slightly different orbital period. This can be explained by the mentioned degeneracy between $P_{\rm orb}$ and τ, which is reduced due to the joint fit. Although the 90% single parameter uncertainties ($\Delta\chi^2 = 2.71$) between both parameters do not overlap, the 68% two parameter uncertainties ($\Delta\chi^2 = 2.30$) do overlap as can be seen from the contour maps shown in Fig. 4.18. Our best-fit parameters for the orbit are listed in Table 4.4 and the resulting geometry of GRO J1008−57 is shown in Fig. 4.19.

4.4.4 Estimating the magnetic field

As GRO J1008−57's orbital period of ∼250 d is very long compared to a typical outburst duration of 14 days, the source spends most of the time at very low accretion rates. Thus, if we assume a maximum spin-up of 10^{-9} s s^{-1} during an outburst as measured during the 2007 outburst then the total period change would be $\Delta P_{\rm up}$<1 ms. During low accretion rates far away from periastron, however, one would expect the source to spin-down due to the propeller effect. Assuming the neutron star's moment of inertia to be $I = \frac{2}{5}MR^2$ and a dipole magnetic field with the moment $\mu = \frac{1}{2}BR^3$, the spin-down after Eq. (1.33) for 220 d in the propeller regime accumulates to a spin change of $\Delta P_{\rm down}$∼1 ms using standard neutron star parameters as listed in Table 1.1. As $\Delta P_{\rm up}$ is an upper limit we would expect the source to spin down over the decades although the spin up is on the same order as $\Delta P_{\rm down}$. This is indeed what is observed for GRO J1008−57 as shown in Fig. 4.20, where

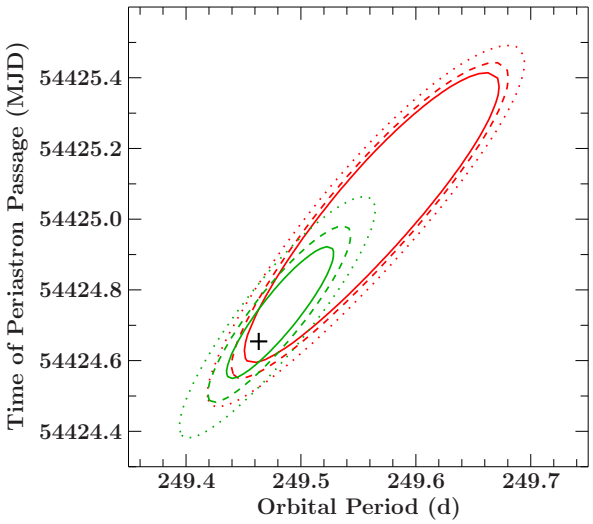

Figure 4.18: Contour maps between the orbital period and time of periastron passage resulting from the arrival times fit (red) and the joined fit together with outburst times (green). The solid lines represent the 68%, the dashed lines the 90%, and the dotted lines the 99% confidence levels for contours for two degrees of freedom.

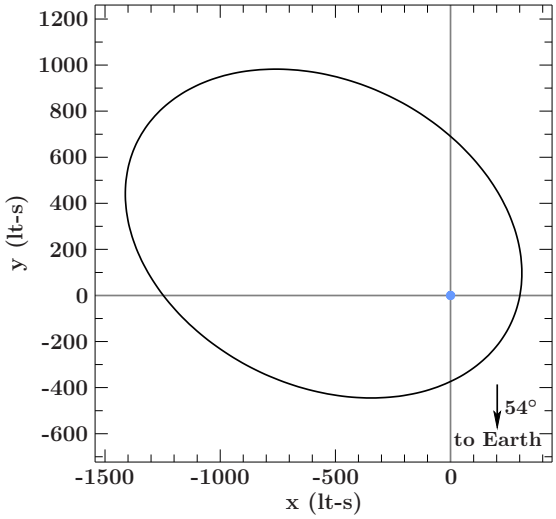

Figure 4.19: Sketch of GRO J1008−57's orbit resulting from the orbit determination. The orbit is seen from above assuming an inclination of 36° (Coe et al., 2007). The companion star's radius is set to $7\,R_\odot$ (Coe et al., 2007). The observer is inclined by the labeled angle with respect to the orbital plane.

we corrected the historic measurements by Shrader et al. (1999), Stollberg et al. (1993), and Coe et al. (2007) for the Doppler shift by binary motion (black crosses). A long-term spin down of the neutron star in the order of $\dot{P} = 2 \times 10^{-10}\,\mathrm{s\,s^{-1}}$ is visible. This would imply a surface magnetic field of $B{\sim}2.6 \times 10^{12}\,\mathrm{G}$ after Eq. (1.33). As we have neglected the spin-up periods during the outbursts in this calculation the spin-down could be even larger. Consequently, we consider the derived magnetic field strength to be a lower limit. A possible cyclotron line would then be located at energies above $E_{\mathrm{cyc}}{>}30\,\mathrm{keV}$ (see Eq. 1.38). In the X-ray spectrum of GRO J1008−57 taken during its discovery outburst in 1993 a cyclotron line was claimed at 88 keV (Shrader et al., 1999), which is consistent with our estimation (see Sect. 5.1 for details about GRO J1008−57's CRSF).

4.5 4U 2129+47: A Hierarchic Triple Candidate

This Section is using the "we"-style as it presents an analysis in collaboration with Michael A. Nowak. Since the final best-fit is not found yet, the presented results are preliminary and should be considered with caution. Once the remaining issues are solved the results will be published in a forthcoming paper. The work has been already discussed in parts in Nowak et al. (2014).

The X-ray source 4U 2129+47 is different to the other binaries discussed in this Chapter. In fact, there is evidence from spectroscopic observations of the optical companion that the neutron star binary is orbited by a third star on a wider orbit, making this system a hierarchic triple candidate (Garcia et al., 1989; Bothwell et al., 2008). After the source was discovered by Forman et al. (1978) with the *UHURU*-satellite a 5.2 hr modulation of the optical companion was found. Thorstensen et al. (1979, 1980) suggested that this modulation is caused by the heating of the companion's atmosphere by the X-ray radiation of the neutron star. These authors determined the stellar type of the companion, V1727 Cygni, to an early K- or M-star, which classifies 4U 2129+47 as a LMXB. Later optical

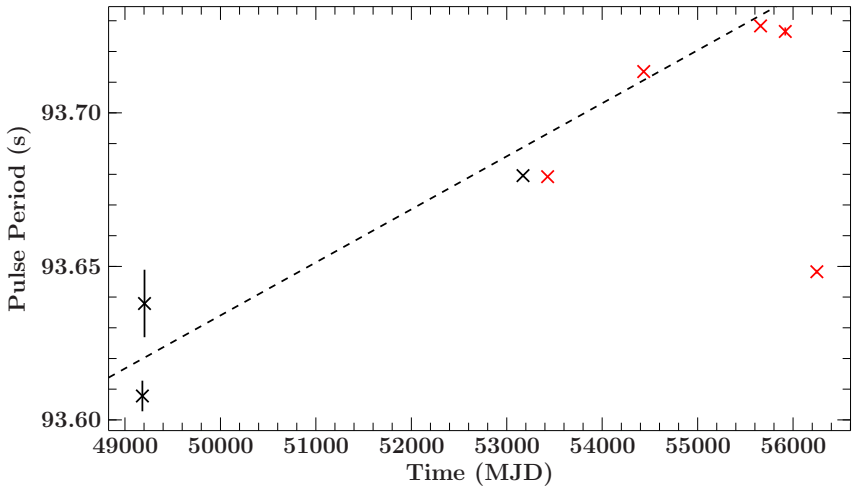

Figure 4.20: Pulse period evolution of GRO J1008−57 over the decades. The black measurements represent historic pulse period determinations by Stollberg et al. (1993), Shrader et al. (1999), and Coe et al. (2007). The red periods are results of this thesis with the last measurement during the type II "giant" outburst of the source (see Sect. 5.1 for details about this outburst). The dashed line represents a constant spin-down of $2 \times 10^{-10}\,\mathrm{s\,s^{-1}}$ to guide the eye (taken from Kühnel et al., 2013).

observations during an absence of X-ray activity determined the companion to be, however, an F-star (Garcia et al., 1989; Chevalier et al., 1989). Surprisingly, the 5.2 hr optical modulation was not detected anymore. These observations led to the speculation that 4U 2129+47 might be a triple system (see, e.g., Garcia et al., 1989). Although no X-ray pulsations have been detected yet, the compact object was identified as a neutron star due to the observation of a type I X-ray burst (Garcia & Grindlay, 1987). The lack of pulsations are consistent with a neutron star in an old system, where the magnetic field is too weak to redirect the accreted matter from the Roche lobe of the companion onto the poles of the neutron star. The X-ray light curve of 4U 2129+47 shows eclipses, which are separated by the 5.2 hr orbital period of the inner binary (Ulmer et al., 1980; McClintock et al., 1982). A timing analysis of the eclipse midpoint times performed by Bozzo et al. (2007) showed a strong non-linear evolution. This evolution could be described by an increase of the 5.2 hr orbital period, which is contrary to the usual orbital decay of close binaries due to gravitational wave losses. As a solution, Bozzo et al. (2007) argued that the proposed outer F-star could be responsible for the non-linear evolution of the eclipse midpoint times. In this Section, we present a timing analysis of this evolution using the most recent *XMM-Newton*- and *Chandra*-data.

4.5.1 Detecting eclipses using Bayesian blocks

4U 2129+47 was observed 11 times by *XMM-Newton* and *Chandra* between 2000 and 2015 (see Table F.3 for the details). To determine the ingress and egress times in all observations with the highest statistically possible accuracy, we calculated the Bayesian block representation of the measured photon arrival times after Scargle et al. (2013). The Bayesian blocks are constructed such that the detections of all photon events within a block are consistent with originating from the same event rate distribution. Compared to a classical light curve, where the events are sorted into an equidistant time-grid, the Bayesian block representation of the event data can be understood as a light curve with time bins of variable width. This time-grid is constructed according to the most likely structure in the event rate over time. The code for calculating the Bayesian block representation of

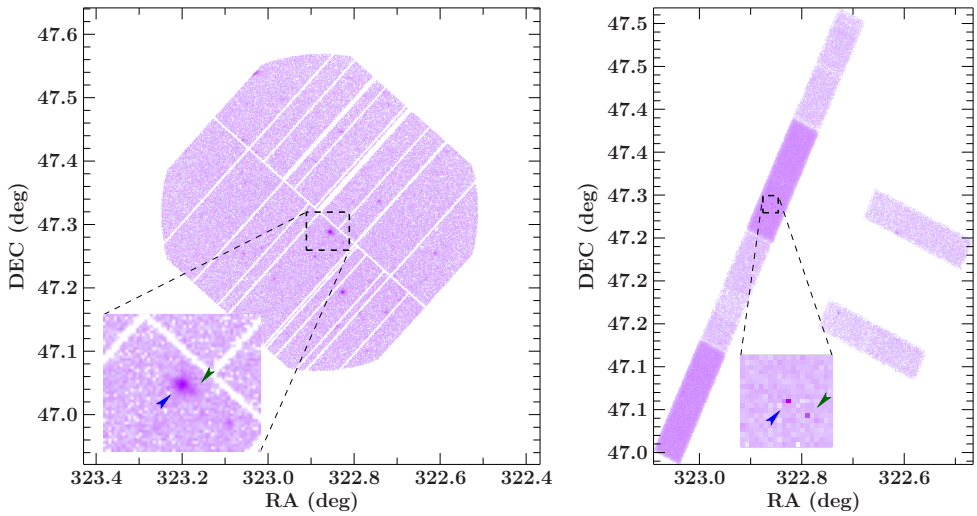

Figure 4.21: Left: *XMM-Newton*-EPIC-pn- (ObsID 0502460201) and **Right:** *Chandra*-ACIS-image (ObsID 1925) around the position of 4U 2129+47 (blue arrow). Apart from many point sources in the field of view, 4U 2129+47 can be resolved best in *Chandra*, while *XMM-Newton* might be contaminated by the nearby source S3-β (green arrow, Nowak et al., 2002).

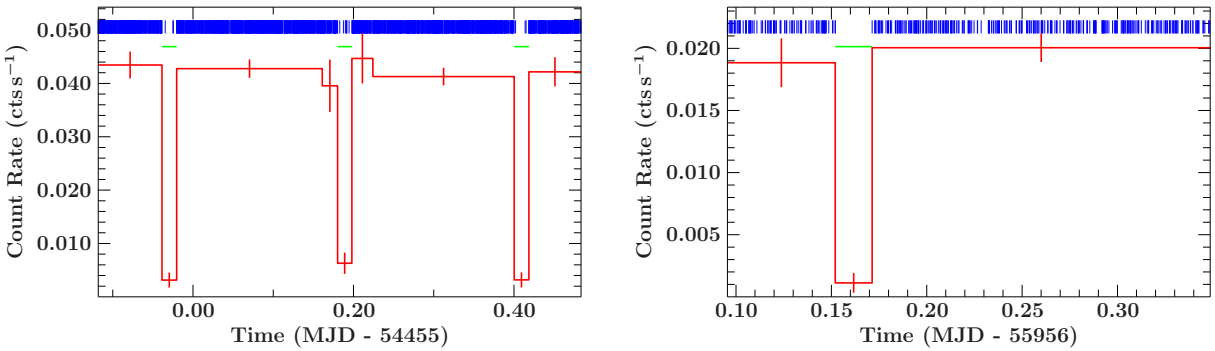

Figure 4.22: Light curve of 4U 2129+47 represented by Bayesian blocks (red) as derived from the photon arrival times (each blue line on top marks a single event) in *XMM-Newton*-EPIC-pn (left; ObsID 0502460201) and *Chandra*-ACIS (right; ObsID 13681). The eclipses of the neutron star by its companion are clearly detected (green marks). Note that during the eclipse observed in *Chandra* no background events were detected. However, since the Bayesian block has to contain at least one event, the corresponding count rate is non-zero.

various types of data is provided in Scargle et al. (2013), which "implements the spirit of Reproducible Research, a publication protocol initiated by John Claerbout [Claerbout 1990]". The code has been developed using the MATLAB[20] programming language and has been ported into *ISIS* for this analysis. It is part of the *ISISscripts* as a function called `bayesian_blocks`.

For each of the *XMM-Newton*- and *Chandra*-observations listed in Table F.3 the Bayesian block representation of the measured event list was calculated. Figure 4.22 exemplarily shows the Bayesian block light curves from events measured by *XMM-Newton* (ObsID 0502460201; left) and *Chandra* (ObsID 13681; right). During the *XMM-Newton*-observation three eclipses separated by ∼5 hours are clearly detected. The flux of the source outside of the eclipses was fairly constant. The same behavior was observed during the *Chandra*-observation, although only one eclipse with a duration of ∼28 min. was detected. The count rate within the eclipse, which is equal to the detector background, was extremely low. In fact, *no* photon was detected, but since the construction of the

[20] www.mathworks.com/products/matlab/

Bayesian blocks are assumed to contain at least one event the corresponding count rate is non-zero. Thus, the background in *Chandra* was <5% of the source count rate, while it was 10–15% in *XMM-Newton*.

As mentioned in the beginning, a detailed investigation of the evolution of the midpoint times of the eclipses of 4U 2129+47 over the years showed that the eclipses were not just separated by the orbital period of the binary. The *XMM-Newton*- and recent *Chandra*-data are important to clarify the physical reason for the non-linear evolution of the eclipse midpoint times. Formally, each Bayesian block representing an eclipse in these data can be used to derive the eclipse's midpoint time. From the two change points (CP) in the Bayesian block representation defining the eclipse, which are the start- and stop-times of the block, $t_{\rm start}$ and $t_{\rm stop}$, respectively, the observed eclipse midpoint time, $t_{\rm mid,obs}$, is simply given by

$$t_{\rm mid,obs} = \frac{t_{\rm start} + t_{\rm stop}}{2} \quad . \tag{4.5}$$

The uncertainty of the midpoint time is calculated after error propagation of the uncertainties of the block's start- and stop-time. Their uncertainties can be estimated by, e.g., following Scargle et al. (2013), who based their estimations on the underlying Bayesian statistics.

4.5.2 Change point probability distributions

The constant eclipse length can be used to further increase the accuracy of the observed eclipse midpoint times. The goal of the following analysis was to determine the probability distribution of the midpoint time for each observed eclipse under the condition of a global eclipse length among all eclipses.

To estimate the probability distribution for the observed data, we performed Monte Carlo simulations of event lists, which were analyzed afterwards on the change points of their Bayesian block representation. The arrival time, t_i, of the i$^{\rm th}$ photon in an event list was simulated assuming a Poisson distribution (see, e.g., Deák, 1990; Gould et al., 2006),

$$t_i = t_{\rm i-1} - \frac{\log u}{r} \quad , \tag{4.6}$$

with a constant event rate, r, the time of the former event, t_{i-1}, and a uniformly distributed random number, $0 \leq u \leq 1$. For $i = 1$ we have defined $t_0 = 0$. First, we generated a source event list of a 5 ks long observation. The event rate was assumed to be $r = r_{\rm out} - r_{\rm in}$, where $r_{\rm out}$ is the mean observed event rate in the two adjacent blocks of the eclipse and $r_{\rm in}$ the event rate within the eclipse, which we interpreted as detector background. If no events have been detected within the eclipse, as is the case for almost all *Chandra*-observations, we assumed at least one event in the simulated background. Then, all events within an arbitrary defined eclipse of 2 ks in length and centered at the middle of the 5 ks observation were removed from the source event list. Finally, we added background events to the list after Eq. (4.6) with $r = r_{\rm in}$ over the full time range.

For each detected eclipse, n, in the *XMM-Newton*- and *Chandra*-observations, we simulated 1 000 000 event lists using the method described above. The Bayesian block representations were calculated for all of these lists and the change point locations of the eclipse, i.e., the ingress and egress times were sorted into a histogram, $P^n_{\rm ingress}(\Delta t)$ and $P^n_{\rm egress}(\Delta t)$, respectively. Here, Δt is the time since the actual ingress or egress occurred. The resolution of the histogram's time-grid were set to the readout time[21] of the used

[21] Given by the `TIMEDEL` keyword in the FITS-header of the observed event file.

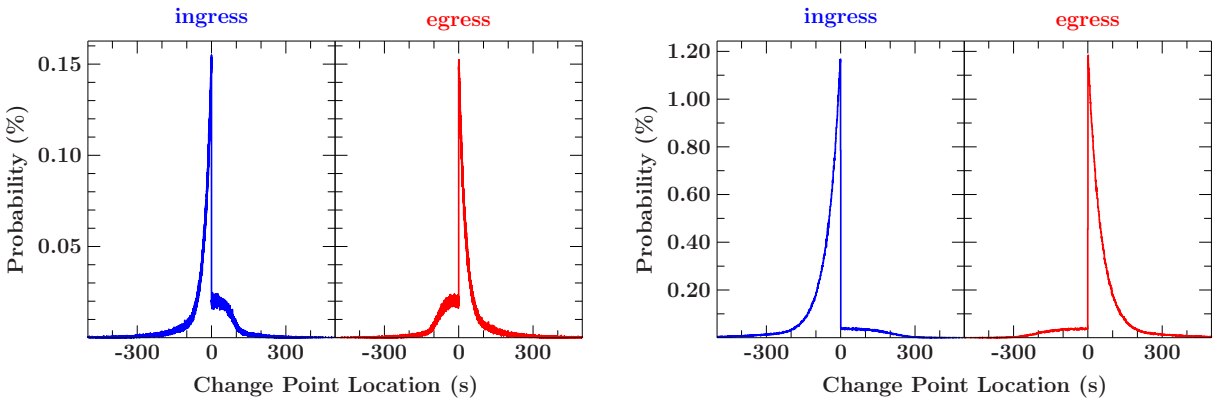

Figure 4.23: Simulated probability distributions of the change point locations of the eclipse's ingress ($P^n_{\rm ingress}(\Delta t)$, blue), and egress ($P^n_{\rm egress}(\Delta t)$, red). The left plot shows the result for the *XMM-Newton*-observation 0502460201 and the right one for the *Chandra*-observation 13681. The change point locations are given relative to the simulated ingress and egress times, respectively.

CCD-detector (EPIC-pn on *XMM-Newton*, ACIS on *Chandra*). The histograms were normalized such that

$$\sum_k P^n_{\rm ingress}(\Delta t_k) = 1 \quad \text{and} \quad \sum_k P^n_{\rm egress}(\Delta t_k) = 1 \quad , \tag{4.7}$$

with the time-bin k. These histograms represent the probability distributions that the change points of the eclipse have been observed at the time Δt since the actual ingress and egress, respectively. For an infinite high source count rate and no background counts within the eclipse the distributions are expected to be a δ-function at $\Delta t = 0$.

Figure 4.23 shows examples of the resulting probability distributions, whereas Fig. 4.22 displays the respective Bayesian block light curves. The peaks of the distributions have a very sharp edge in direction of the actual eclipse, while it has a certain width towards the ingress or away from the egress. This width anti-correlates with the observed count rate of the source. Since the source count rate of the *XMM-Newton*-observation (Fig. 4.23, left) was higher than of the *Chandra*-observation (right), its peaks are narrower. The wings of the distribution into the eclipse are, however, much more prominent for the *XMM-Newton*-observation. This is due to the higher background count rate, which can move the change point location inside the eclipse, although with a low probability.

4.5.3 Deriving a global eclipse length

The next step towards our goal deriving the probability distribution for the midpoint times was to calculate the probability, $P^n_{\rm eclipse}(t_{\rm mid}, T)$, that an eclipse of length T centered at a midpoint time, $t_{\rm mid}$, was consistent with the observed change point locations, $t_{\rm start}$ and $t_{\rm stop}$. Using the above simulated distributions of the change point locations, $P^n_{\rm ingress}(\Delta t)$ and $P^n_{\rm egress}(\Delta t)$, we found

$$P^n_{\rm eclipse}(t_{\rm mid}, T) = P^n_{\rm ingress}(t_{\rm start} - t_{\rm mid} + T/2) \times P^n_{\rm egress}(t_{\rm stop} - t_{\rm mid} - T/2) \quad . \tag{4.8}$$

The probabilities for a grid of possible midpoint times, $t_{\rm mid}$, and eclipse lengths, T, resulted in maps similar to those shown in Fig. 4.24. A cross-shaped structure is visible in the probability distributions, whose center is located at the midpoint and length of the determined Bayesian block from the observed event list. This cross structure divides the probability map into four tiles. Each tile, labeled A–D in Fig. 4.24, represents a different interplay between the properties of the Bayesian block and the actual (unknown) eclipse parameters:

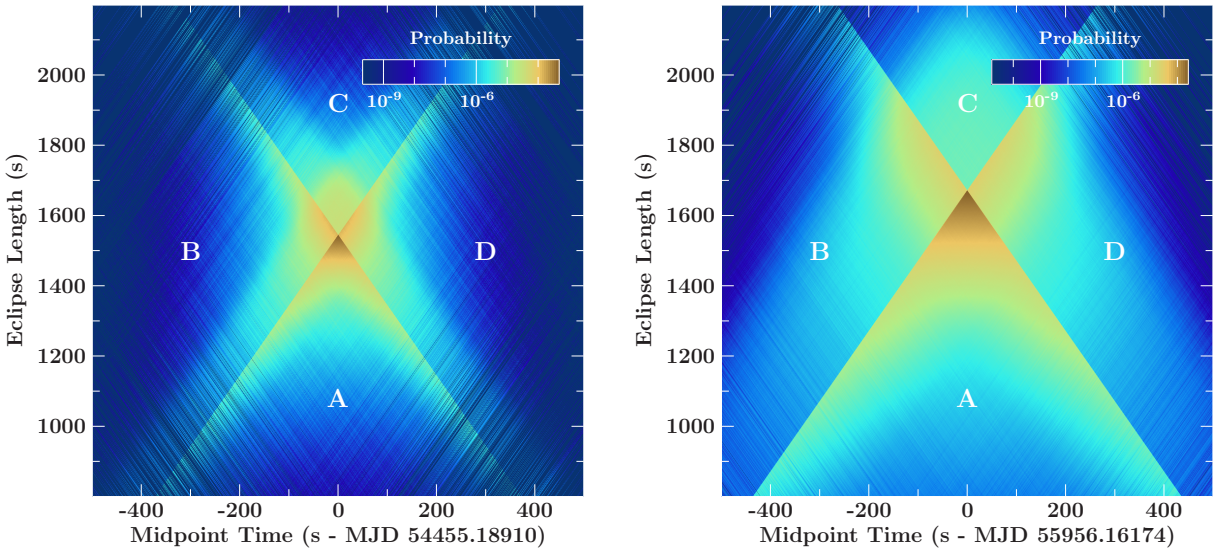

Figure 4.24: Color coded probability maps, $P^n_{\text{eclipse}}(t_{\text{mid}}, T)$, after Eq. (4.8) for the same observations as in Fig. 4.23 (left and right). The probabilities were calculated for the combinations of the given eclipse lengths (y-axis) and midpoint times (x-axis). The latter are given relative to the midpoint of the Bayesian block representing the eclipse.

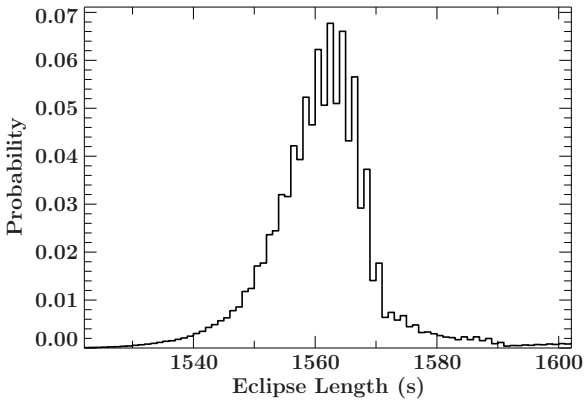

Figure 4.25: The probability distribution for the eclipse length, $P_{\text{eclipse}}(T)$. This is the result of the combination of all probability maps, exemplarily shown in Fig. 4.24, after Eq. (4.10).

A) the actual eclipse is shorter than the length of the Bayesian block. This is very likely since, in this case, the observed change points would be located within the rising and falling edge of the change point probability distribution before and after the eclipse, respectively (compare Fig. 4.23).

B) here the center of the Bayesian block is located at earlier times than the actual midpoint time of the eclipse, which moves the change point of the egress into the eclipse, where its probability is very low (see Fig. 4.23). By increasing the eclipse length, however, this change point would be located in the falling edge again, where the probability is higher. This is the reason why the probability in this area of the map increases towards longer eclipses.

C) within this area of the map the eclipse is longer than the Bayesian block. The change points would be located inside of the eclipse, where their probabilities, $P^n_{\text{ingress}}(\Delta t)$ and $P^n_{\text{egress}}(\Delta t)$, are, however, very low and depend on the background count rate. In the best-case of an almost negligible background, as for *Chandra*, this area is very homogeneous (compare the area C of the right with that of the left map in Fig. 4.24).

D) the same as in B, but the Bayesian block is observed later than the actual eclipse.

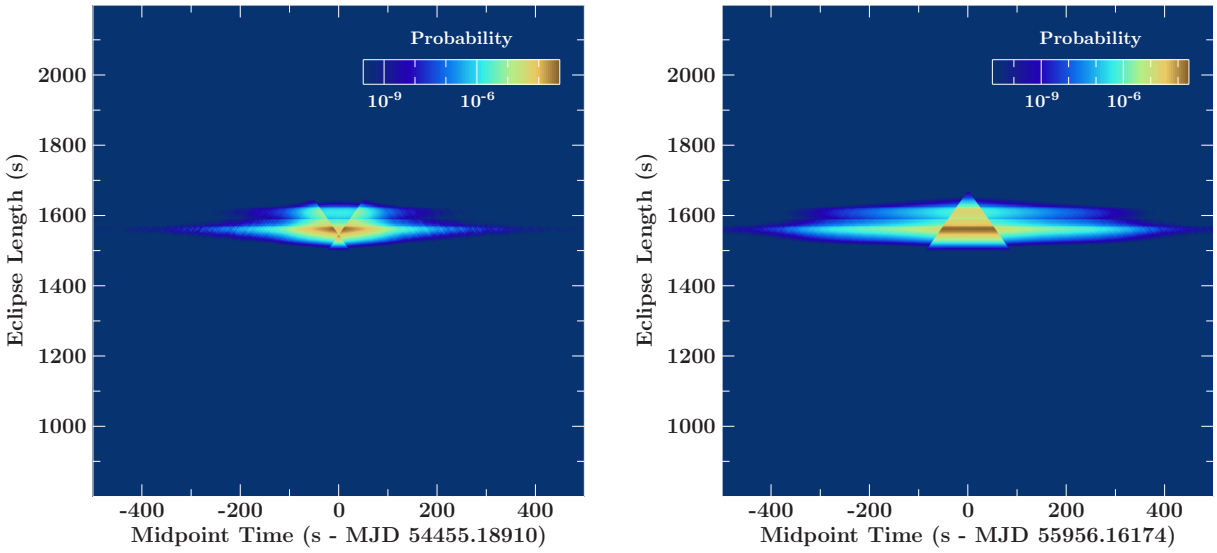

Figure 4.26: The same probability maps as in Fig. 4.24, but folded with the probability distribution for the eclipse length as shown in Fig. 4.25.

Summing up the probability map as defined in Eq. (4.8) in direction of the midpoint time, i.e., in column direction, results in the probability distribution, $P^n_{\text{length}}(T)$, of the eclipse length,

$$P^n_{\text{length}}(T) = \sum_{t_{\text{mid}}} P^n_{\text{eclipse}}(t_{\text{mid}}, T) \quad , \tag{4.9}$$

as determined by a particular observation, n. The total probability distribution for the eclipse length, $P_{\text{length}}(T)$, is now given by the product of $P^n_{\text{length}}(T)$ over all observations,

$$P_{\text{length}}(T) = \prod_n P^n_{\text{length}}(T) \quad . \tag{4.10}$$

Furthermore, we normalized the result to

$$\sum_T P_{\text{length}}(T) = 1 \quad . \tag{4.11}$$

This probability distribution shown in Fig. 4.25 features a sharp peak at $T = 1562^{+6}_{-8}\,\text{s}$ (uncertainties are given at the 68% confidence level), which is our final result for the actual eclipse length. Although further analysis is required, the uncertainties are small enough to provide evidence against a changing magnetic field of the M-dwarf companion, which would cause changes of $\lesssim$20 s in the eclipse length (Lin et al., 2009, and references therein). This scenario has been proposed to explain the variable eclipse length in the LMXB EXO 0748−676 (Wolff et al., 2009).

4.5.4 Determining the eclipse midpoint times

The probability map, $P^n_{\text{eclipse}}(t_{\text{mid}}, T)$, as calculated by Eq. (4.8) were folded with the probability distribution of the eclipse length, $P_{\text{eclipse}}(T)$ (Eq. 4.10), after

$$P^n_{\text{eclipse,fold}}(t_{\text{mid}}, T) = P^n_{\text{eclipse}}(t_{\text{mid}}, T) \times P_{\text{length}}(T) \quad . \tag{4.12}$$

This effectively weights the map for a certain observation with the eclipse length distribution derived by all observations. Figure 4.26 shows this effect on the example of the maps of

Fig. 4.24. Finally, summing up the folded map similar to Eq. (4.9), but in direction of the eclipse length, i.e., in row direction resulted in the probability distribution, $P_{\mathrm{midpoint}}(t_{\mathrm{mid}})$, of the eclipse midpoint time,

$$P^n_{\mathrm{midpoint}}(t_{\mathrm{mid}}) = \sum_T P^n_{\mathrm{eclipse,fold}}(t_{\mathrm{mid}}, T) \quad . \tag{4.13}$$

In this way we have derived the possible midpoint times for each observation under the condition of a global, i.e., constant eclipse length over time. The resulting midpoint probability distributions for all observation (Table F.3) are shown in Fig. 4.27.

Comparing any model with the derived midpoint probability distributions of Eq. (4.13) requires further investigation. Using a standard χ^2-minimization is not possible because the underlying data do not follow a Gaussian distribution. Once a model has calculated a midpoint time, $t^{\mathrm{model}}_{\mathrm{mid}}(n)$ for a particular observation n, we can directly look up the observable probability for this midpoint time by Eq. (4.13). Thus, fitting a model to the probability distributions can be achieved by maximizing the total probability,

$$P_{\mathrm{fit}} = \prod_n \sqrt[n]{P^n_{\mathrm{midpoint}}(t^{\mathrm{model}}_{\mathrm{mid}}(n))} \quad , \tag{4.14}$$

where the P^n_{midpoint} for each observation, n, has been normalized to $\sum_{t_{\mathrm{mid}}} P^n_{\mathrm{midpoint}}(t_{\mathrm{mid}}) = 1$.

4.5.5 Fitting the midpoint times

In first order, the midpoint times of eclipses in a binary are expected to occur at

$$t_{\mathrm{mid}}(k) = t_0 + kP_{\mathrm{binary}} \quad . \tag{4.15}$$

with the orbital period, P_{binary}, and the orbit number k since a reference time t_0. Fitting this model to the midpoint probability distribution derived from the observations, however, failed. This is expected since earlier attempts to model the eclipse times already revealed their non-linear time evolution as mentioned in the beginning. We therefore followed the idea of a third body orbiting the inner neutron star binary. We assumed a hierarchic system, in which the orbit of the third body does not influence the inner binary and vise versa. Consequently, the eclipse midpoint times after Eq. (4.15) are modified by the Doppler shift of the inner binary,

$$t'_{\mathrm{mid}}(k) = t_{\mathrm{mid}}(k) + z(t_{\mathrm{mid}}(k)) \quad , \tag{4.16}$$

where the z-position of the binary center is calculated after Eq. (2.15). The z-position itself depends on the orbital parameters of the inner binary around the common center of mass of the hierarchic triple system, which are the orbital period, P_{orb}, the time of periastron passage, τ, the semi-major axis, $a_{\mathrm{binary}} \sin i$, the eccentricity, e, and the longitude of periastron, ω (see Sect. 1.2.1).

Fitting Eq. (4.16) to the probability distributions derived from the observations was performed by maximizing the total probability (Eq. 4.14). A first attempt to model the data led to a good match with an eccentricity consistent with a nearly circular orbit. In order to reduce the number of fit parameters compared to the low number of observations, we forced the orbit to be circular, i.e., fixing $e = 0$ and $\omega = 0$. Consequently, the time of periastron passage is undefined and we fitted the time of the mean longitude, $T_{\pi/2}$, instead (compare Eq. 1.20). The formal total probability of the final fit after Eq. (4.14) was $P_{\mathrm{fit}} = 4.05 \times 10^{-3}$ with 8 d.o.f. (13 included eclipses and 5 free fit parameters). The

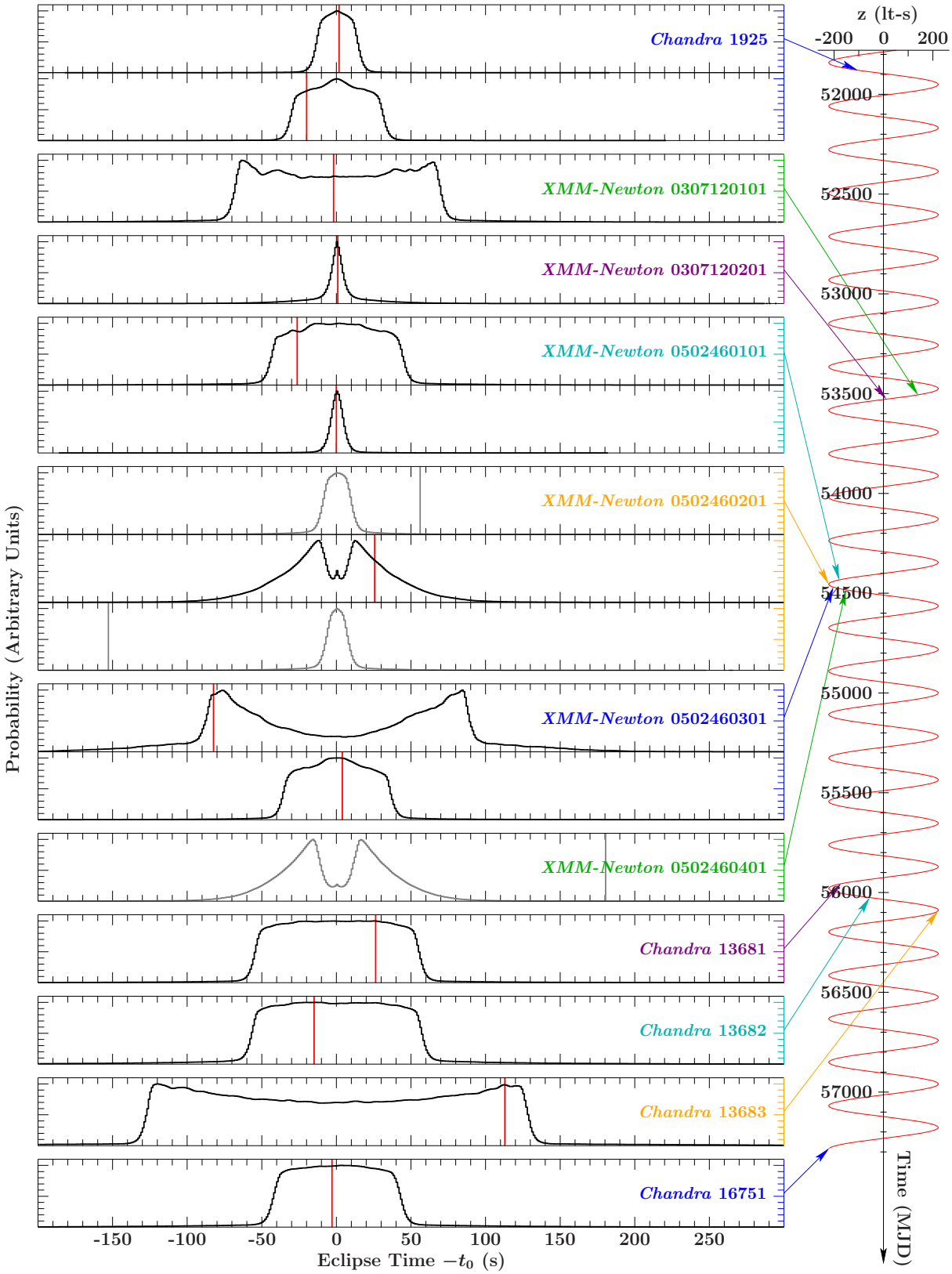

Figure 4.27: Probability distributions for the midpoint times together with the best-fit model. Each row is the distribution for an observed eclipse, grouped by the corresponding observation (the respective row ends are colored for clarity). The vertical red lines mark the midpoint times after the best-fit model. The Doppler delay by the third body after the model is shown on the right timeline, where the date of the observations are indicated by arrows. Distributions in gray have been excluded from the fit. The eclipse times are given relative to the midpoint, t_0, of the corresponding Bayesian block.

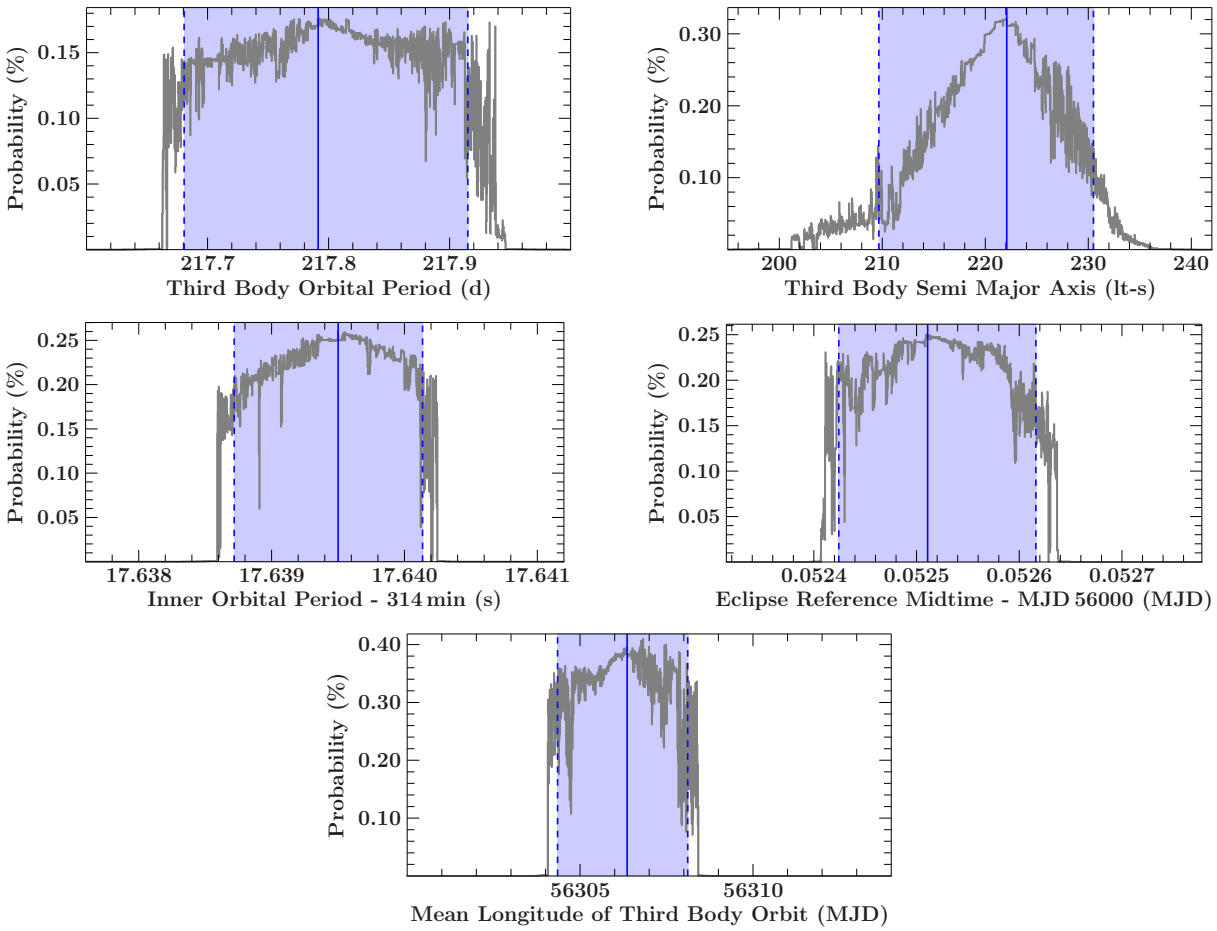

Figure 4.28: Final probability distribution of the fit parameters. The blue vertical lines are the best-fit values and the bluish areas correspond to the 90%-confidence levels. The distributions result from the Monte Carlo shooting method. The thickness of each bin represents the minimum and maximum derived probability within this bin

midpoint times after the model compared to the corresponding probability distributions are shown in Fig. 4.27 and the best-fit parameters are listed in Table 4.5. The uncertainties of the fit parameters were estimated as described below.

Three of the 16 observed eclipses had to be, however, excluded from the fit since the eclipse midtimes after the model were off by up to ∼180 s. As the probability distributions were zero at these times, the total probability of the model was zero as well and the fit was not successful. A possible reason for this mismatch could be that the fit-algorithm did not found the global best-fit. Another issue could be systematic uncertainties in the observed ingress and egress times due to background flares in *XMM-Newton*. Evidence for this issue is the high variability of the count rate around the second eclipse during observation 0502460201 (see Fig. 4.22, left). Additionally, the background rate within this eclipse was higher than during the other observed eclipses. If this is true, then a systematically shorter eclipse length would be observed and, consequently, a mismatch between the data and the model would emerge. A further explanation could be pollution by the nearby source S3-β as seen in the images of *XMM-Newton* and *Chandra* (Fig. 4.21). Until this mismatch is resolved we assumed to have found the global best-fit.

To estimate the statistical uncertainty for each parameter we investigated the total probability after Eq. (4.14) depending on the value of the parameter. In order to sample the resulting probability distribution efficiently we used a Monte Carlo shooting method. The parameter value was fixed to a random value drawn from a uniform parameter range,

Table 4.5: System parameters of 4U 2129+47 for the close inner binary and the outer third body. The distance to the system is listed in the parameters of the F-star, since it was determined by optical observations while this star was dominating the spectrum. For parameters, which have been derived, see the text for more details.

Inner binary (neutron star + M-dwarf)		
Neutron Star Mass, $M_{\rm x}$	1.3–2.2 $M_\odot$	Garcia & Grindlay (1987)
Semi-major axis, $a_{\rm x}$	0.5–1.3 lt-s	this work, derived
M-dwarf mass, $M_{\rm dwarf}$	0.25–0.50 $M_\odot$	Nowak et al. (2002)
M-dwarf radius, $R_{\rm dwarf}$	0.45–0.70 $R_\odot$	Nowak et al. (2002)
Semi-major axis, $a_{\rm dwarf}$	2.4–5.8 lt-s	this work, derived
Orbital period, $P_{\rm binary}$	$18857.6395^{+0.0007}_{-0.0008}$ s	this work, fitted
Eclipse reference time, t_0	MJD $56000.25251^{+0.00011}_{-0.00009}$	this work, fitted
Eclipse length, T	1562^{+6}_{-8} s	this work, derived
Orbital Inclination, i	$\geq 75°$	Nowak et al. (2002)
Hierarchic triple (inner binary + F-star)		
Projected semi-major axis, $a_{\rm binary} \sin i$	222^{+9}_{-13} lt-s	this work, fitted
Mean longitude, $T_{\pi/2}$	MJD $56306.4^{+1.8}_{-2.1}$	this work, fitted
F-star Mass, $M_{\rm star}$	1.0 $M_\odot$	Garcia & Grindlay (1987)
Orbital period, $P_{\rm orb}$	$217.79^{+0.09}_{-0.07}$ d	this work, fitted
Semi-major axis, $a_{\rm star}$	324–646 lt-s	this work, derived
Distance, d	∼6.3 kpc	Cowley & Schmidtke (1990)

while the remaining parameters were fitted. After 100 000 Monte Carlo runs the confidence interval around the best-fit value was determined, for which the integrated probability was at least at 90% of the total integrated probability over all runs. Fig. 4.28 shows the probability distributions and confidence intervals for each fit parameter. Because of the high number of Monte Carlo runs the probabilities were sorted into parameter histograms for display purposes. The thickness of a histogram bin (drawn in gray in Fig. 4.28) represents the minimum and maximum probability found in this bin.

4.5.6 The geometry of the triple system

We derived the full geometry of 4U 2129+47 using the fitted orbital parameters of the inner binary and the hierarchic triple (Table 4.5). The mass function, f, of a binary as defined in Eq. (1.22) is derived from Kepler's third law,

$$\frac{P^2 M}{a^3} = \frac{4\pi^2}{G} = \text{constant} \quad , \tag{4.17}$$

with the orbital period, P, the total mass, $M = M_1 + M_2$, and the total semi-major axis, $a = a_1 + a_2$. The subscripts in M and a correspond to the two stars forming the binary. From the conservation of angular momentum, the ratio of the two semi-major axes has to be inverse proportional to the ratio of the masses of the stars,

$$\frac{a_1}{a_2} = \frac{M_2}{M_1} \quad . \tag{4.18}$$

Using the estimated mass ranges of the neutron star, $M_{\rm x}$ =1.3–2.2$M_\odot$ (Garcia & Grindlay, 1987), and its M-dwarf companion, $M_{\rm dwarf}$ =0.25–0.50$M_\odot$ (Nowak et al., 2002), we derived the semi-major axes, a_x and $a_{\rm dwarf}$, of the stars after

$$a_x = \sqrt[3]{\frac{G}{4\pi^2}\frac{P_{\rm binary}^2 M_{\rm dwarf}^3}{(M_x + M_{\rm dwarf})^2}} = 0.5\text{–}1.3\,\text{lt-s} \quad \text{and} \quad a_{\rm dwarf} = \sqrt[3]{\frac{G}{4\pi^2}\frac{P_{\rm binary}^2 M_{\rm x}^3}{(M_x + M_{\rm dwarf})^2}} = 2.4\text{–}5.8\,\text{lt-s} \quad .$$

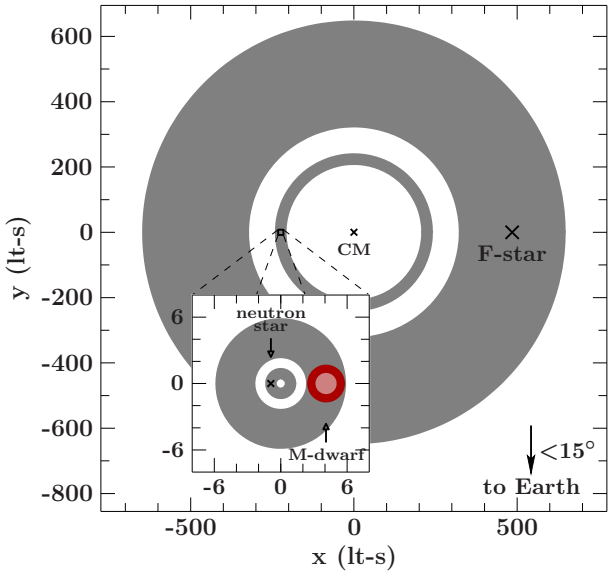

Figure 4.29: Geometry of the triple system candidate 4U 2129+47 derived from eclipse timing. The orbital planes are assumed to align and are seen from above. The outer F-star and the inner binary, consisting of a neutron star and a M-dwarf, are orbiting their common center of mass (CM). The gray width of the orbits correspond to the uncertainties in the semi-major axes. The minimum size of the M-dwarf is drawn in light red and its maximum size in dark red. The observer is inclined at a maximum of 15° with respect to the orbital plane.

From the fitted projected semi-major axis of the inner binary with respect to the center of mass of the triple system, $a_{\mathrm{binary}} \sin i$, we derived the semi-major axis of the F-star, a_{star}. Using Eq. (4.18), assuming a mass of $M_{\mathrm{star}} = 1\,\mathrm{M}_{\odot}$ for the outer F-star (Garcia & Grindlay, 1987), and an inclination of $i \geq 75°$ (Nowak et al., 2002), we got

$$a_{\mathrm{star}} = \frac{M_x + M_{\mathrm{dwarf}}}{M_{\mathrm{star}}} \frac{a_{\mathrm{binary}} \sin i}{\sin i} = 324\text{–}646\,\mathrm{lt\text{-}s} \quad .$$

A sketch of the geometry of 4U 2129+47 based on these calculations is presented in Fig. 4.29. The estimation of the semi-major axis of the F-star assumed that its orbital plane is aligned with the inner binary's one. In the case of a very high inclination, i.e., $i \sim 90°$ we would expect to detect eclipses of the neutron star by the F-star as well. These have been not observed yet. Once the issue with the fit of the eclipse times as explained above is solved, we will be able, however, to predict the times of such possible eclipses. Their lack or detection will help constraining the inclination of the outer F-star's orbit.

The large uncertainties of the derived geometrical parameters were mainly caused by the poorly known masses of the three components and the orbital inclinations. With a detailed series of frequent observations of the eclipsing times of 4U 2129+47 we should be able to constrain these parameters. This would require, however, a numerical solution of the full three body problem. The model which we applied to the data (see Eq. 4.16) assumed Keplerian orbits, which is an approximation only as it neglects the gravitational interactions between all three components of 4U 2129+47. In recent work, Ransom et al. (2014) analyzed the pulse period evolution of the very prominent hierarchical triple system PSR J0337+171, which consists of a radio pulsar and two white dwarfs. These authors were able to precisely measure the mass of the neutron star by fitting the data using a model, which solves the three body problem numerically. Thus, triple systems containing neutron stars are unique laboratories to measure neutron star masses, which are in general very difficult to determine (see Sect. 1.1.3).

Chapter 5
Spectral Investigations

This chapter presents a detailed spectral analysis of GRO J1008−57 and a brief summary of preliminary results for GX 304−1. Using several observations for each source the evolution of the spectral parameters with flux or time are revealed. The results are important aspects for the physics inside the accretion columns as recent theories investigate their properties as a function of the mass accretion rate (see Sect. 1.3.2 and 1.3.3). Due to the large number of observations analyzed here the spectra of a source are fitted using the simultaneous fit functions developed for *ISIS* (see Sect. 2.4). Unless stated otherwise, the cross-sections used to calculate the X-ray absorption (see Eqs. 1.51 and 1.53) are set to `vern` (Verner et al., 1996) and abundances are set to `wilm` (Wilms et al., 2000).

5.1 GRO J1008−57: It All Depends on Luminosity

The following spectral analysis and results have been paraphrased from Kühnel et al. (2013, 2014). The analysis of the spectra taken after 2012 November will be published in Kühnel et al. (2016b, in prep.) and the results presented here are preliminary. The *NuSTAR* observations are analyzed in close collaboration with Felix Fürst, which justifies the use of the "we"-style. See Sect. 4.4 for a summary of the discovery and timing properties of the source.

The X-ray spectrum of GRO J1008−57 above 20 keV was found to follow a power-law with exponential cut-off as measured with *CGRO*-BATSE and -OSSE (Grove et al., 1995; Shrader et al., 1999) and *INTEGRAL* (Coe et al., 2007). The earlier data hint at a cyclotron line around 88 keV, which was later claimed to be detected in spectra from *Suzaku* and *NuSTAR* as well (Yamamoto et al., 2013; Bellm et al., 2014). However, during other observations by *INTEGRAL*, *Suzaku*, and *RXTE* the claimed CRSF could not be detected (Coe et al., 2007; Naik et al., 2011; Kühnel et al., 2013). If this high energy CRSF would be confirmed unambiguously, then the neutron star in GRO J1008−57 would have one of the strongest magnetic fields known for an accreting pulsar in a BeXRB. The soft energy spectrum below 20 keV measured with *Suzaku* was first analyzed in detail by Naik et al. (2011), who revealed a complex spectrum with a fluorescent emission line of iron.

Spectra taken during several outbursts of GRO J1008−57 between 2005 and 2015 were analyzed in this Section and were grouped into data epochs as defined in Fig. 5.1 (see Table F.2 for an observation log). In 2005 February (epoch 1) and 2007 December (epoch 2) *RXTE* monitored the source during the decays of its type I outbursts. *Swift* and *Suzaku* each performed a single pointing during the latter outburst's maximum and decay, respectively. Furthermore, we triggered[1] *RXTE* observations during the onset of the 2011 April type I outburst (epoch 3) as predicted by the orbital and outburst analysis (see Sect. 4.4). In 1996/1997, *RXTE* pointings were performed over almost one full orbital cycle of the source, where the neutron star was, however, inactive since we could not detect any pulsations in these data. After a type I outburst in 2012 August, the source did not

[1]This observation was proposed to compare the spectra between the decline and rise of an outburst of GRO J1008−57, which corresponds to specific question 2.

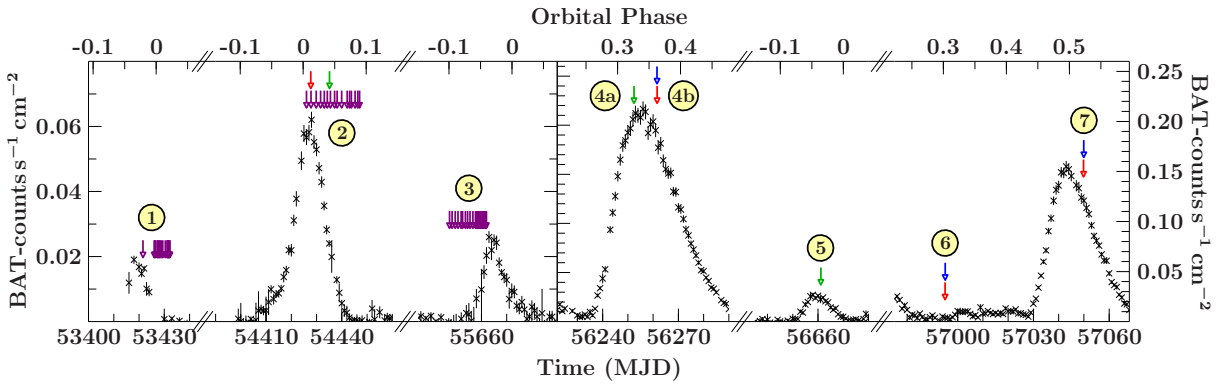

Figure 5.1: *Swift*-BAT 15–50 keV light curve of GRO J1008−57 during several type I and type II outbursts between 2005 and 2015. The arrows on top mark observations by *RXTE* (purple), *Swift* (red), *Suzaku* (green), and *NuSTAR* (blue). The encircled numbers define the data epochs. Note the different flux ranges between the left and right side. The first two outbursts are also shown in Fig. 4.15 as observed with *RXTE*-ASM. See Fig. G.1 for a full outburst history with *RXTE*-ASM and *Swift*-BAT.

fade into quiescence as expected. Rather GRO J1008−57 featured its first detected type II outburst at an orbital phase of around 0.3 after a few weeks of flaring activity (see Fig. 5.1; Kühnel et al., 2013, and references therein). The peak of this outburst, which almost reached ∼1 Crab, was observed with *Suzaku* (epoch 4a) and *NuSTAR* simultaneously with *Swift* (epoch 4b). Although these data have been analyzed already by Bellm et al. (2014) and Yamamoto et al. (2013), their choice of the phenomenological continuum model is different to what we have used so far. In order to compare these observations with our previous findings for the source, we included the corresponding spectra in the present analysis. Furthermore, our achieved $\chi^2_{\rm red}$ for epoch 4a is close to unity, while the fit performed by Bellm et al. (2014) resulted in a $\chi^2_{\rm red}$ of 3.15 (see their Table 2). The reasons are the various calibration uncertainties we have discovered in the XISs-, PIN-, and GSO-data, which are not surprising given the high source flux of around 1 Crab (see the data extraction below and Kühnel et al., 2016b, in prep., for details). After the 2012 "giant" outburst the source behaved predictably, i.e., type I outbursts slightly before the next two periastron passages were observed. We triggered a *Suzaku* observation during the second one in 2014 January (epoch 5) to analyze the X-ray spectrum of GRO J1008−57 regarding any changes since its "giant" outburst. After the next type I outburst in 2014 September the source's flux started to rise again. At orbital phase 0.2 in 2014 November it underwent a second outburst, which is a rare event known as a "double-peaked" outburst. For instance, such outbursts have been observed in A 0535+262 (see, e.g. Caballero et al., 2013, and references therein) and GX 304−1 (Nakajima et al., 2012; Postnov et al., 2015b). A few days after the outburst decayed simultaneous observations by *NuSTAR* and *Swift* were performed (epoch 6). The source remained detected, however, in *Swift*-BAT (see Fig. 5.1) and after a few weak flares evolved into a third outburst within a single orbit. The maximum flux of ∼700 mCrab and its preceding flaring morphology was comparable to the 2012 "giant" outburst. To our knowledge, this "triple-peaked" outburst behavior has not been detected in any other BeXRB so far. Shortly after the source started to decline *NuSTAR* and *Swift* again performed a simultaneous observation (epoch 7).

5.1.1 Data extraction

Details about the spectral data reduction of the epochs 1–3 and 4–7 are presented in Kühnel et al. (2013) and Kühnel et al. (2016b, in prep.), respectively.

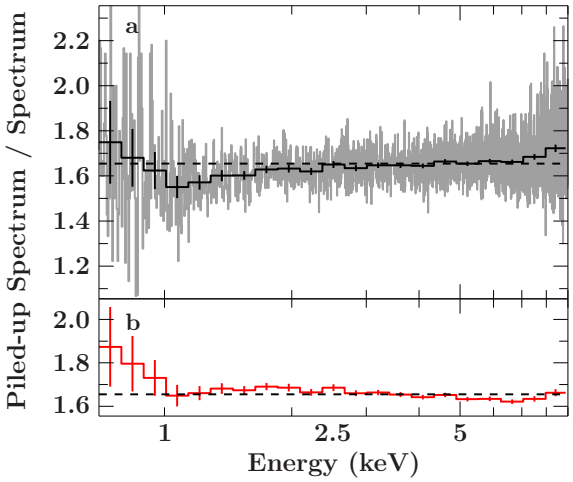

Figure 5.2: Pile-up in *Suzaku*-XIS3. The GRO J1008−57-spectrum has been extracted with and without taking pile-up into account. **a:** Ratio between these two spectra (gray) and a rebinned ratio (black). As can be seen the slope is different for energies above 1 keV. **b:** A soft excess below 1 keV emerges once the slope is fitted by a different photon index of the power-law model.

The *RXTE*-PCA and -HEXTE spectra were calibrated using `HEASOFT` v6.11 and were accumulated using the standard data reduction pipelines by Wilms et al. (2006). Source spectra from the top layer of PCU2 were used only since this PCU was the best-calibrated one (Jahoda et al., 2006). These spectra were fitted in the 4.5–50 keV range to avoid calibration problems around the Xenon L-edge at energies below 4 keV. We applied a binning factor of 2, 4, 6, and 8 for the energy channels 10–20 keV, 20–30 keV, 30–40 keV and >40 keV, respectively. Furthermore, we added 0.5% systematic uncertainties to the data (Jahoda et al., 2006). As the PCA background is estimated, we accounted for its uncertainty by a multiplicative background factor during the spectral analysis. The PCA spectra taken during the campaign in 1996/1997 were extracted from the top layer of all available PCUs and fitted in the 3.5–10 keV range. For epoch 1 data from the HEXTE clusters A and B are available. As cluster A was fixed in on-source position in 2006 October (see Sect. 3.2.1) only data from cluster B was extracted for epoch 2. No HEXTE data was used for epoch 3 since cluster B was fixed as well in 2010. For spectral analysis HEXTE data in the 20–100 keV range were fitted with a rebinning factor of 2, 3, 4, and 10 in the ranges 20–30 keV, 30–45 keV, 45–60 keV, and >60 keV, respectively.

After calibrating the *Swift*-XRT data, `xselect` was used to extract the corresponding spectra. Observations performed in WT mode were accumulated from a circular region of 60″ (epoch 2) and 47″ in radius (epochs 4b, and 7) centered on the source position. The observation in PC mode (epoch 6) had to be investigated on pile-up since the source's flux was higher than 0.5 counts s^{-1} in *Swift*-XRT[2]. After comparing the count rate profile with the expected PSF and checking the results with the `pileest` tool we extracted the source's spectrum from an annulus with an outer radius of 47″ and an inner radius of 22″. The background spectra in WT mode were extracted from regions at the edges of the chip with radii of 1′. For epoch 3 the background region was an annulus with an outer radius of 550″ and an inner radius of 250″ centered at the position of GRO J1008−57.

The *Suzaku*-spectra of epoch 2, 4a, and 5 were extracted using `HEASOFT` v6.11, v6.15.1, and v6.15.1, respectively. After calibrating the events with `aepipeline` we corrected *Suzaku*'s attitude using `aeattcor2` (Nowak et al., 2011) and a preliminary source region. The XISs were operated in 1/4 window mode due to the high count rate of the source. During the observation of the "giant" outburst (epoch 4a) the burst clock mode was enabled, which reduces the exposure time per frame in order to suppress pile-up. Circular source regions were chosen with a radius of 80″ for XIS0 and XIS3 during epoch 5 and with a radius 90″ otherwise. In order to avoid pile-up in the resulting XIS spectra we calculated the pile-up fraction in each pixel using the `pileest` tool (Nowak et al., 2011). Areas within the source region with more than 4% (epochs 2 and 5) and 2% pile-up (epochs 4a)

[2]See the *Swift* data processing guide at http://www.swift.ac.uk/analysis/xrt/pileup.php

were excluded. If pile-up is not avoided the final source spectra get distorted, which might result in additional soft components required to describe the data. Exemplarily, Fig. 5.2 shows the piled-up XIS3 spectrum from epoch 2 relative to the corrected spectrum. An emission like feature below 1 keV is visible, which was erroneously interpreted by Naik et al. (2011) as source intrinsic black body emission (compare Figs. 4 and 5 in Naik et al., 2011). Additionally, the overall shape is slightly different affecting the photon index of the power-law as shown in Fig. 5.2.

We have added the spectra of the different editing modes ('3×3" and '5×5") for each XIS during the spectral analysis. The XIS background spectra were extracted from a circular region at areas outside of the PSF with $90''$ radius. The energy ranges of the XIS were restricted to 0.8–10 keV during epoch 4a and 5 and to 1–9 keV during epoch 2. Several calibration features such as uncertainties around the Si and Au edges complicate the analysis, especially during the bright epoch 4a. The details about these features and their handling is described in Kühnel et al. (2013, 2016b). Energy channels were rebinned to achieve a combined S/R of 40 and 8 during epoch 2 and epoch 4a and 5, respectively. Furthermore, for epochs 4a and 5 we chose a minimum number of channels per energy bin close to the half-width half-maximum of the spectral resolution following the approach of Nowak et al. (2011). The spectra of the PIN and GSO were extracted using `hxdpinxbpi` and `hxdgsoxbpi`, respectively. Their energy range of PIN were restricted to 12–50 keV during epoch 2, 20–70 keV during epoch 4a, and 15–70 keV during epoch 5. The data were rebinned to achieve a S/R of 20 (epoch 2) and 15 (epochs 4a and 5). We selected the energy of 60–100 keV for GSO and grouped the channels until a minimum S/R of 5 was achieved during epochs 4a and 5. During epoch 2 we applied a binning factor of 2 for energies between 60 keV and 80 keV and of 4 for higher energies.

As distributed by `HEASOFT` v6.16 the standard `nustardas` pipeline (v1.4.1) was used to extract the spectra from *NuSTAR*-FPMA and -FPMB. The source regions were selected as circle with $60''$ in radius centered at the coordinates of GRO J1008−57. The spectral background regions of the same size were chosen outside of the PSF's wings to avoid any contamination by source photons. We have accumulated data from mode 01 (SCIENCE) and 06 (SCIENCE_SL) to increase the total exposure time for each observation. During the latter mode the star tracker on the optical bench is occulted, which can result in an insufficient reconstruction of the sky image. However, the effective area can still be calculated. After checking the spectra of both modes on consistency we combined them for the spectral analysis using `addascaspec`. The energy ranges for fitting were set to 4–78 keV. We did not use data between 3 and 4 keV due to a mismatch to *Swift*-XRT, which was already noticed by Bellm et al. (2014) for the data of epoch 4b. The combined spectra of FPMA and FPMB were rebinned to achieve a S/R of 18 in the 4–45 keV range and of 6 above 45 keV.

5.1.2 Galactic ridge X-ray emission

First investigations of the *RXTE* spectra during the 2007 outburst (epoch 2) revealed a tight correlation of the iron line flux with the source's flux. However, at low flux levels at the end of the outburst the iron line flux as expected from the found correlation is much lower than what is actually measured (see Fig. 5.3b). A likely explanation is a contribution from galactic ridge X-ray emission (GRXE) to the *RXTE*-PCA spectra. The GXRE is a diffuse X-ray emission found most prominent in the Milky Way plane and GRO J1008−57's is with a galactic latitude of $b = -1.827°$ almost within this plane. Its physical origin is the accumulated flux of many unresolved and weak point sources (Revnivtsev et al., 2009). Due to the PCA's large field of view of 1° the GRXE starts

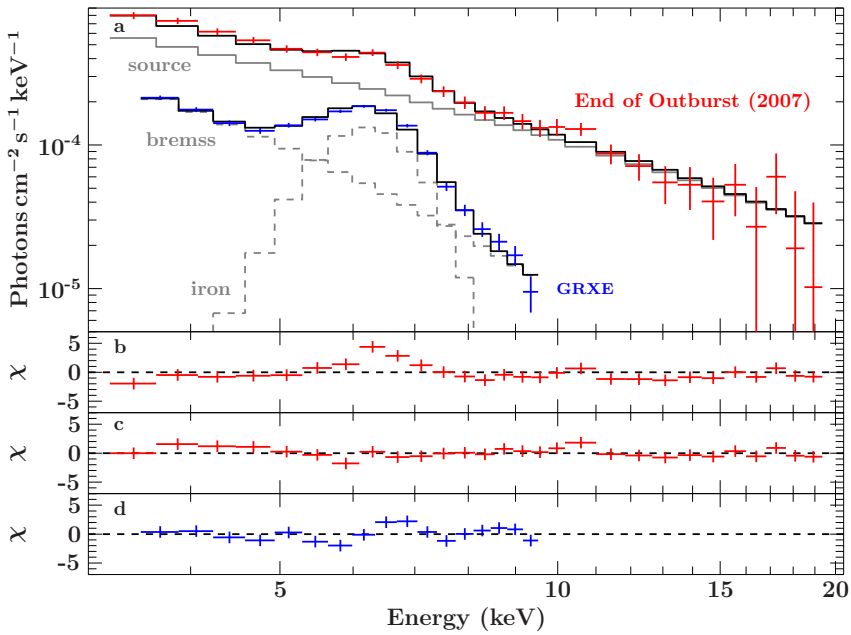

Figure 5.3: a: Galactic ridge X-ray emission (GRXE) in the direction of GRO J1008−57 as measured by *RXTE*-PCA. At the end of the 2007 December outburst the measured spectrum (red) was brighter than expected (gray). The summed spectra during the observation campaign in 1996/1997 (blue) features iron emission on top of a bremsstrahlung continuum as expected from GRXE (gray dashed lines). **b:** Residuals from a fit to the spectrum at the end of the 2007 outburst assuming an iron flux as expected from previous observations. **c:** The same fit but with taking the GRXE emission into account after **d:** fitting the GRXE as measured using the summed spectrum during the 1996/1997 campaign.

to contribute once the flux of the targeted source drops below a certain threshold (see, e.g., Müller et al., 2012). Furthermore, the background of PCA cannot be measured for any observation but is modeled instead (see Sect. 3.2.1). As the properties of the GRXE depend on the galactic longitude and latitude (Ebisawa et al., 2007; Yamauchi et al., 2009) it is not included in the background model. However, an observation campaign of GRO J1008−57 was performed with *RXTE* in 1996/1997, where the source was not detected in the light curves, i.e., no pulsations were detected. Consequently, the only contribution in these spectra are from the GRXE. We have combined all observations of the campaign to achieve a single high quality spectrum for the GRXE. This spectrum with 181 ks of exposure features a prominent iron emission on top of a nearly power-law shaped continuum (see Fig. 5.3a). Earlier observations of the GRXE emission used an empirical model consisting of a bremsstrahlung continuum and three emission lines from neutron, He-like, and H-like iron (Ebisawa et al., 2007; Yamauchi et al., 2009). As the energy resolution is not sufficient to resolve these emission lines we have fitted the iron emission by a single Gaussian with a free centroid energy and width. The final model we fitted to the combined PCA spectrum to describe the GRXE in direction of GRO J1008−57 is

$$\texttt{GRXE} = \texttt{bremss} + \texttt{gauss}_{\texttt{iron}} \quad . \tag{5.1}$$

Here, `bremss` is the corresponding *XSPEC* model for a bremsstrahlung continuum and $\texttt{gauss}_{\texttt{iron}}$ (see Eq. 1.49) the Gaussian representing the blend of the three iron emission lines. The best-fit parameters of the GRXE are determined by a simultaneous fit as described below (see Table 5.2 for values and Fig. 5.3d for the residuals of the fit to the combined spectrum). Including the GRXE in the PCA data results in consistent iron line fluxes for the low flux spectra of GRO J1008−57 (see Fig. 5.3c). Due to the particularly soft spectrum of the GRXE its contribution to the HEXTE data is negligible.

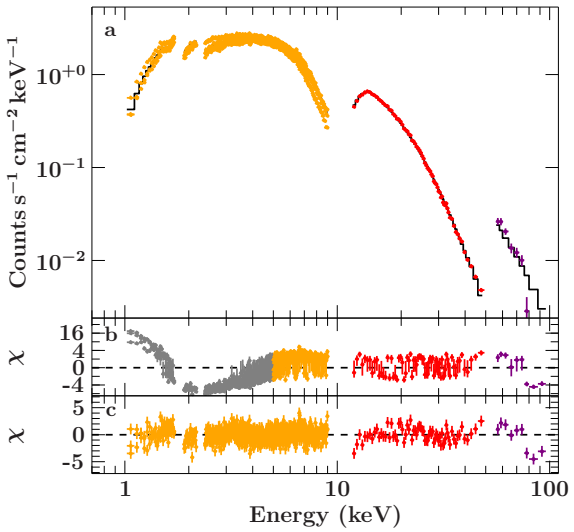

Figure 5.4: **a:** *Suzaku*-spectrum during the decay of the 2007 December outburst of GRO J1008−57. The measured *Suzaku*-XIS0, 1, and 3 spectra (orange), the -PIN-spectrum (red), and the -GSO-spectrum (purple) are shown together with the best-fit model (black line). **b:** Residuals of a fit to energies >5 keV using a simple cutoff power-law to compare with *INTEGRAL*-data (Coe et al., 2007). Lower energies are drawn in gray. **c:** Residual of our best-fit model (taken and modified from Kühnel et al., 2013).

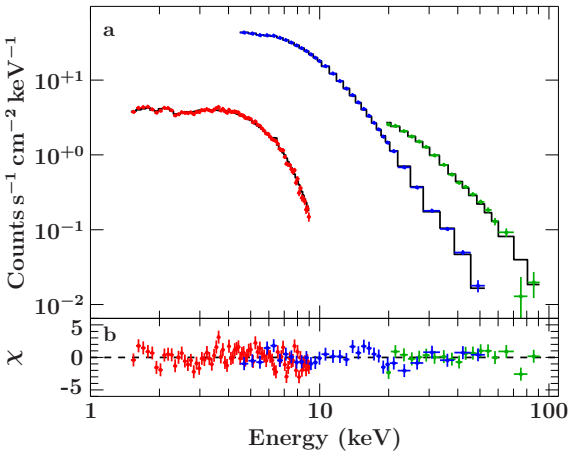

Figure 5.5: **a:** *Swift*-XRT- (red) and quasi simultaneous *RXTE*-PCA (blue) and HEXTE (green) spectrum during the peak of the 2007 December outburst of GRO J1008−57. The fit to the data uses the same model as for the *Suzaku*-data (see Fig. 5.4). **b:** Residuals of the best-fit model (taken and modified from Kühnel et al., 2013).

5.1.3 GRO J1008−57's spectral continuum model

In order to find a working broad-band X-ray continuum model for GRO J1008−57 we investigated data from epoch 2, where *Suzaku* (ObsID 902003010) and *RXTE* (ObsID 93032-03-03-01) had observed the source simultaneously and the *Swift* observation was performed quasi-simultaneously with *RXTE* (ObsID 93032-03-02-00, which started a few ks after the *Swift* observation (ObsID 00031030001) was completed, see Table F.2 for details).

As found by, e.g., Coe et al. (2007) the spectrum measured with *INTEGRAL* was described successfully by a power-law with an exponential cut-off. Thus, we applied the `cutoffpl` model (see Eq. 1.45) to the 2007 *Suzaku* data of the source (epoch 2). The residuals of the fit (see Figure 5.4b) show a good description of the spectra above 5 keV. At lower energies, however, strong differences to the data are detected. Once an additional black body is included (see Eq. 1.47) as well as interstellar absorption is taken into account (see Eq. 1.51) the model describes the observed *Suzaku* spectrum almost well. Note that the additional black body with a temperature of $kT \sim 1.85$ keV is different to the soft components caused by pile-up (see Fig. 5.2). Finally, a narrow emission line at 6.4 keV remains in the residuals, which we account to fluorescence $K\alpha$ emission from neutral iron and model with a Gaussian fixing the width to $\sigma = 10^{-6}$ keV and the energy to $E_0 = 6.4$ keV (see Eq. 1.49). We have included another Gaussian to account for the $K\beta$ emission of neutral iron at 7.056 keV and fixed its flux to 13% of the Kα flux. In summary, we find the X-ray continuum model, M_{1008}, of GRO J1008−57 to be

$$M_{1008} = \texttt{tbnew} \times (\texttt{cutoffpl} + \texttt{bbody} + \texttt{gauss}_{\mathrm{FeK}\alpha} + \texttt{gauss}_{\mathrm{FeK}\beta}) \quad , \tag{5.2}$$

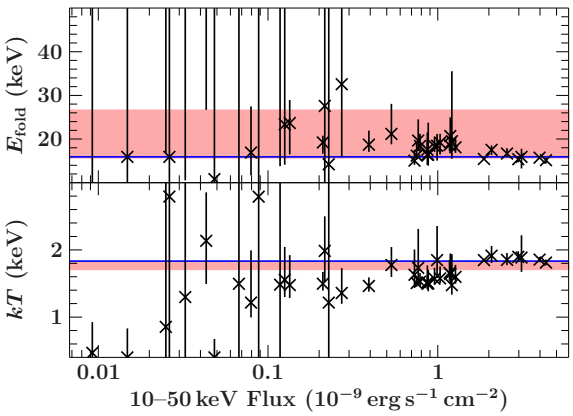

Figure 5.6: Evolution of the folding energy, $E_{\rm fold}$, and black body temperature, kT, with the 10–50 keV flux. The red region marks the weighted mean of the parameters, using both the upper and lower 90% confidence uncertainties. The values determined by the simultaneous fit are shown as blue line.

with 7 spectral parameters: the photon index, Γ, the folding energy, $E_{\rm fold}$, the 15–50 keV power-law flux, $F_{\rm PL}$, the black body temperature, kT, its bolometric flux, $F_{\rm BB}$, the absorption column density, $N_{\rm H}$, and the iron line equivalent width, W. Here, `tbnew` is an updated version[3] of the absorption model by Wilms et al. (2000, see Eq. 1.52). Note that we also included flux calibration constants, $c_{\rm X}$, which scales the flux of the instrument X, e.g., XIS1 with respect to a reference instrument, for which we chose *RXTE*-PCA. This model results in a good description of the *Suzaku* data with a $\chi^2_{\rm red} = 1.14$ for 1896 d.o.f. (compare Fig. 5.4c). Slight deviations from the continuum model are left in GSO at energies $\gtrsim$75 keV. This might be a hint to the claimed CRSF at 88 keV (Shrader et al., 1999). Due to the low signal at these high energies, however, we could not constrain any line parameters. Consequently, we have ignored the possible CRSF in GRO J1008−57's spectral model. Adding the simultaneous *RXTE*-PCA and -HEXTE spectra to the fit of the *Suzaku* data and accounting for the GRXE in PCA (see Eq. 5.1) does not change the spectral parameters. The model defined in Eq. (5.2) is also able to described the quasi-simultaneous *Swift* and *RXTE* data well ($\chi^2_{\rm red} = 1.15$, see Fig. 5.5). The best-fit parameters of both fits are listed in Table 5.1.

The absorption column density of $N_{\rm H}\sim 1.52 \times 10^{22}\,{\rm cm}^{-2}$ determined by both fits is consistent with the foreground absorption in direction of GRO J1008−57 as found by the 21 cm surveys ($N_{\rm H} = 1.35^{+0.21}_{-0.09} \times 10^{22}\,{\rm cm}^{-2}$, Kalberla et al., 2005, and $N_{\rm H} = 1.51^{+0.38}_{-0.02} \times 10^{22}\,{\rm cm}^{-2}$, Dickey & Lockman, 1990). Furthermore, converting the interstellar reddening of $E^{\rm is}(B-V) = 1.79(5)$ mag towards GRO J1008−57 as determined by Riquelme et al. (2012) into a hydrogen column density ($N_{\rm H} = 1.49 \times 10^{22}\,{\rm cm}^{-2}$ following Nowak et al., 2012) matches our X-ray result. Therefore, we conclude that there is no source intrinsic (neutral) material located in the line of sight during GRO J1008−57's 2007 December outburst. The detection of a neutral iron fluorescence line is, however, evidence for the presence of material in the vicinity of the neutron star.

5.1.4 Epochs 1–3 - a simultaneous fit of all spectra

Applying the continuum model defined in Eq. (5.2) to all *RXTE* observations during the 2007 outburst (epoch 2) gave acceptable fit qualities with $\chi^2_{\rm red}$ near unity. The same holds true for fitting the 2005 and 2011 *RXTE* observations (epochs 1 and 3). Apart from the flux parameters, i.e., $F_{\rm PL}$ and $F_{\rm BB}$ we found several parameters which seem to be consistent among all observations. As can be seen from Fig. 5.6, the folding energy, $E_{\rm fold}$, and the black-body temperature, kT, show only little to no variation with the 15–50 keV power-law flux, $F_{\rm PL}$. In fact, their mean values are consistent with the broad-band analysis using the simultaneous *Suzaku* and *RXTE* and quasi-simultaneous *Swift*-XRT and *RXTE* spectra

[3] http://pulsar.sternwarte.uni-erlangen.de/wilms/research/tbabs

Table 5.1: Best-fit continuum parameters from the simultaneous *Suzaku* and *RXTE* data and the quasi-simultaneous *Swift*-XRT and *RXTE* data of GRO J1008−57 during its 2007 December outburst (epoch 2). The GRXE is included in the fit of the *RXTE*-PCA spectrum (see Table 5.2 for its parameters).

		Suzaku +*RXTE*	*Swift* +*RXTE*
`tbnew`	$N_{\rm H}$ ($10^{22}\,{\rm cm}^{-2}$)	$1.523^{+0.029}_{-0.029}$	$1.56^{+0.17}_{-0.17}$
`cutoffpl`[a]	Γ	$0.522^{+0.024}_{-0.024}$	$0.57^{+0.07}_{-0.07}$
	$E_{\rm fold}$ (keV)	$15.6^{+0.5}_{-0.4}$	$16.1^{+0.8}_{-0.8}$
	$F_{\rm PL}$ ($10^{-9}\,{\rm erg\,s^{-1}\,cm^{-2}}$)	$1.982^{+0.029}_{-0.029}$	$3.97^{+0.08}_{-0.08}$
`bbody`[a]	kT (keV)	$1.854^{+0.025}_{-0.025}$	$1.86^{+0.06}_{-0.05}$
	$F_{\rm BB}$ ($10^{-9}\,{\rm erg\,s^{-1}\,cm^{-2}}$)	$0.501^{+0.016}_{-0.016}$	$0.77^{+0.08}_{-0.08}$
iron line	E (keV)	6.4 (fix)	
	σ (keV)	10^{-6} (fix)	
	W (eV)	$23.5^{+2.5}_{-2.5}$	41^{+10}_{-10}
constants[b]	$c_{\rm HEXTE}$	$0.84^{+0.04}_{-0.04}$	$0.853^{+0.019}_{-0.019}$
	$c_{\rm XRT}$	-	$0.809^{+0.010}_{-0.010}$
	$c_{\rm XIS0}$	$0.804^{+0.007}_{-0.006}$	-
	$c_{\rm XIS1}$	$0.845^{+0.007}_{-0.007}$	-
	$c_{\rm XIS3}$	$0.801^{+0.006}_{-0.006}$	-
	$c_{\rm PIN}$	$0.929^{+0.012}_{-0.010}$	-
	$c_{\rm GSO}$	$1.15^{+0.10}_{-0.10}$	-
	$b_{\rm PCA}$	$0.93^{+0.05}_{-0.05}$	$0.96^{+0.04}_{-0.04}$
$\chi^2_{\rm red}$/d.o.f.		1.15/1935	1.15/160

Notes. [a] $F_{\rm PL}$ is the unabsorbed power-law flux in the 15–50 keV range and $F_{\rm BB}$ the unabsorbed bolometric flux of the black-body. [b] The detector flux calibration constants, $c_{\rm X}$, are given relative to the *RXTE*-PCA; the constant $b_{\rm PCA}$ scales the PCA background.

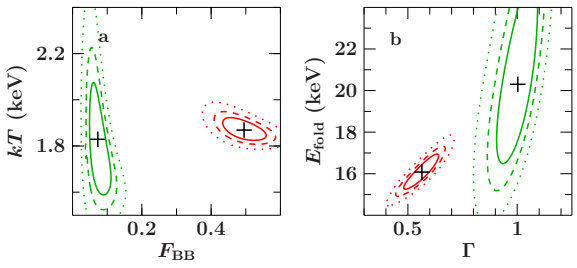

Figure 5.7: Contour maps between **a:** F_{BB} and kT and **b:** Γ and E_{fold} during the maximum (red; *RXTE* ObsID 93032-03-02-00) and the end (green; *RXTE* ObsID 93032-03-03-04) of the 2007 outburst are shown. Solid lines represent 1σ, dashed lines 90%, and dotted lines 99% confidence levels (taken and modified from Kühnel et al., 2013).

(compare Table 5.1). A closer inspection of the χ^2-contours between the black-body flux, F_{BB}, and its temperature, kT, reveals a slight degeneracy between these parameters at high flux levels of the source (see red contours in Fig. 5.7a). Consequently, calculating the uncertainty for each measured black-body temperature assuming single parameter confidence levels (see Fig. 5.6) results in an underestimation of the actual uncertainty. This supports the hint of a unique value for the black-body temperature, kT, among the spectra. The same arguments apply to the folding energy, E_{fold}, which shows an even stronger parameter degeneracy with the power-law photon index, Γ (see Fig. 5.7b).

In order to determine precise values for the black-body temperature, kT, and the folding energy, E_{fold}, among all observations in epochs 1–3, we performed a simultaneous fit of these data using the *ISIS* implementation presented in Sect. 2.4.
The following observations are grouped into a single data-group each:

- the *RXTE*-PCA and -HEXTE spectra of an observation in epoch 1 and 2
- the *Suzaku*-XISs, -PIN, and -GSO spectra during epoch 2 in addition to the simultaneous *RXTE*-PCA and -HEXTE spectra (ObsID 93032-03-03-01)
- the *Swift*-XRT spectrum during epoch 2 in addition to the quasi simultaneous *RXTE*-PCA and -HEXTE spectra (ObsID 93032-03-03-01)
- the *RXTE*-PCA spectrum of an observation in epoch 3 (here no HEXTE background was measured)
- the GRXE spectrum as measured in the combined *RXTE*-PCA data of the 1996/1997 campaign

This results in a total of 43 data-groups. The group parameters for each data-group (except the GRXE spectrum) are the power-law photon index, Γ, the power-law 15–50 keV flux, F_{PL}, the black-body flux, F_{BB}, and the PCA background scaling factor, b_{PCA}. The global parameters, whose values are determined by all data-groups simultaneously, are

- the absorption column density, N_{H}. Since its value of $\sim 1.52 \times 10^{22}\,\mathrm{cm}^{-2}$ (found by the *Suzaku* and *Swift* observations, see Table 5.1) is consistent with foreground absorption. Thus, we do not expect the value to vary with orbital phase or flux of GRO J1008−57. Additionally, as *RXTE*-PCA is not sensitive to such a low N_{H}, fitting a value for each data-group would introduce further parameter degeneracies.
- the folding energy, E_{fold}, as it seems to stay constant with the source's flux (see Fig. 5.6) and influences the photon index, Γ (see Fig. 5.7).
- the black-body temperature, kT, which seems to be independent of the source's flux (see Figs. 5.6 and 5.7).
- the cross-calibration constant, c_{HEXTE}, between *RXTE*-HEXTE and -PCA.

Since all data-groups contain a spectrum taken by *RXTE*-PCA, the parameters of the GRXE's components are added to the list of global parameters, that is

- the temperature, kT, and flux $F_{3\text{-}10\,\mathrm{keV}}$, between 3 and 10 keV of the bremsstrahlung component.
- the energy, E, width, σ, and flux, F, of the Gaussian representing the blend of iron emission lines from different ionization states.

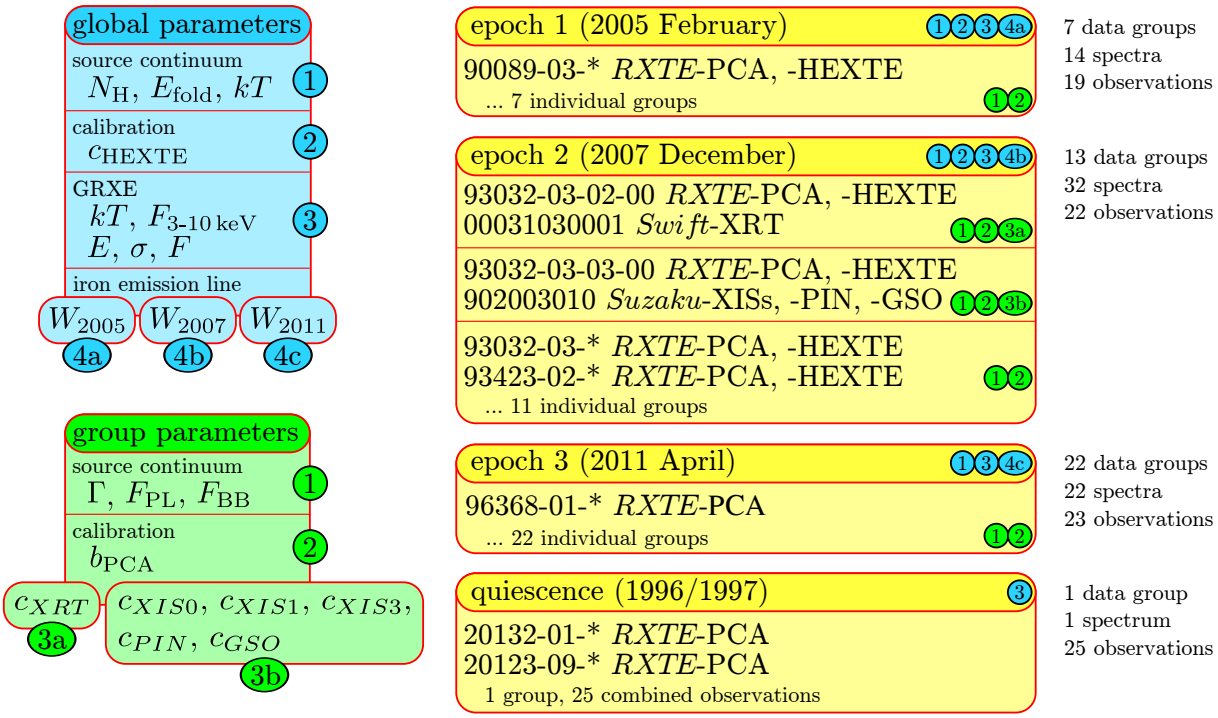

Figure 5.8: Structure of the simultaneous fit using all observations during GRO J1008−57's 2006, 2007, and 2011 outburst as well as the campaign in 1996/1997. These observation define the data-groups (yellow), where some spectra have been combined to increase the S/R (see Table F.2 for details). Specific sets of group parameters (green) are assigned to each data-group, while sets of global parameters (blue) are determined by all data-groups or those during specific data epochs. The star (*) is meant as placeholder to match all observations IDs of this pattern.

An inspection of the iron line's equivalent width, W, during epochs 1–3 showed that it stays quite constant over an epoch, i.e., an outburst. However, its value differs between the individual outbursts. Thus, we have introduced three global parameters corresponding to the equivalent widths, W_{2005}, W_{2007}, and W_{2011} during each outburst. Finally, the cross-calibration constants for *Swift* and *Suzaku* were applied to the corresponding data-groups only. Fig. 5.8 illustrates and summarizes the definition of the data-groups and both parameter types (group and global).

Performing this simultaneous fit to the 43 data-groups (containing 69 spectra) results in $\chi^2_{red} = 1.10$ with 3639 d.o.f. (191 free fit parameters). In order to check the goodness of the simultaneous fit, we calculated a combined goodness using Eq. (2.27) and found $\chi^2_{red,comb.} = 1.68$ (assuming[4] $p_i = 4, \mathcal{P} = 12$, and $\mu_i = 1/43$). The reason for this worse goodness is found in the combined residuals of all *RXTE*-PCA and -HEXTE spectra after Eq. (2.31) (excluding the GRXE spectrum). As seen in Fig. 5.9b several features are left in the residuals, which can be attributed to calibration uncertainties at the Xenon L-edges (below 7 keV), the Be/CU collimator (at 10 keV), and the Xenon K-edge (at 30 keV). These calibration features are not detected in the PCA spectrum with the highest S/R (Fig. 5.9c) and, thus, do not influence the individual group parameters. These features were detected also in a combined *RXTE* analysis of the Crab pulsar by García et al. (2014).

The successful simultaneous fit[5] of all *RXTE*-observations of GRO J1008−57 in combination with the various global parameters reduces the uncertainties in all fit-parameters significantly. Fig. 5.10 compares the relative uncertainties of the power-law's photon

[4] $p_i = 5$ for the data-group containing the GRXE spectrum and $p_i = 5$ or $p_i = 9$ for the observations where *Swift*- or *Suzaku*-data are available, respectively.

[5] This answers specific question 8.

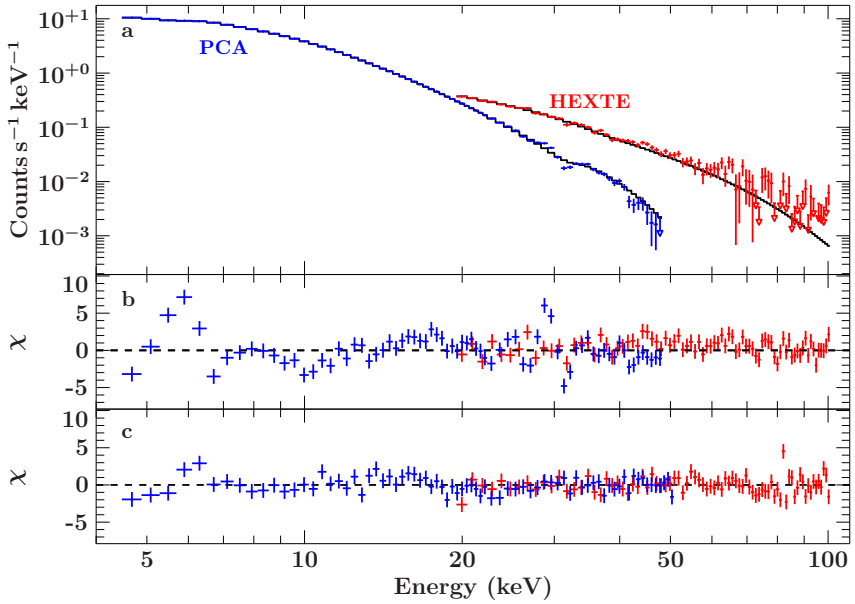

Figure 5.9: a: Averaged *RXTE*-PCA- (blue) and -HEXTE-spectrum (red) and model (black line) of the simultaneous fit of all 42 *RXTE* observations of GRO J1008−57. **b:** Combined residuals of the averaged model. Unmodeled detector features at the Xenon L-edges (around 6 keV), the Be/Cu collimator (10 keV), and Xenon K-edge (at 30 keV) are visible in PCA. These features are undetected in **c:** the residuals of the PCA spectrum with the highest S/R (taken from Kühnel et al., 2016a).

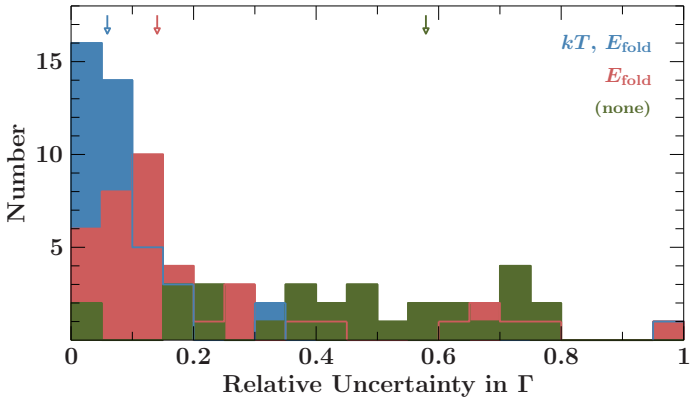

Figure 5.10: Distribution of the relative uncertainties of all photon indices. The green histogram is for the absence of a global continuum parameter, the red one for treating kT, and the blue one for treating $E_{\rm fold}$ and kT as global parameters. The arrows on top mark the median of the corresponding relative uncertainties (taken and modified from Kühnel et al., 2016a).

index, Γ, for different numbers of global parameters. The absence of a global continuum parameter results in a median uncertainty of more than 50%, which decreases to almost 5% once the folding energy and black-body temperature are set as global parameters. Thus, the relationships of the remaining group-parameters, Γ, $F_{\rm BB}$, and $F_{\rm PL}$ can be revealed with a ∼10× higher precision than by performing single fits to the observations. These relationships are shown in Fig. 5.16 and discussed in a subsequent paragraph following the analyses of recent observations by *NuSTAR* and *Suzaku*.

Estimating the uncertainties of the individual group parameters can be performed in the same way as for a single observation. That is, ignoring all data-groups except the one of interest and fixing all but its four corresponding group parameters (Γ, $F_{\rm BB}$, $F_{\rm PL}$, $b_{\rm PCA}$) and any additional flux calibration constants (in case of *Swift* and *Suzaku* observation). The uncertainties of these parameters are found by investigating their χ^2-landscape and determining the 90%-confidence parameter range ($\Delta\chi^2 = 2.71$). Since a global parameter depends on all data-groups, however, ignoring data groups and fixing parameters is not

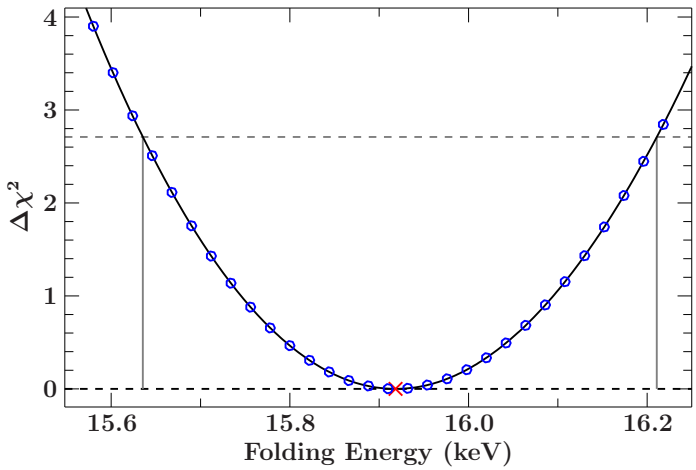

Figure 5.11: χ^2-landscape of the global folding energy, $E_{\rm fold}$. The landscape is revealed on a coarse grid by individual simultaneous fits (blue points) and interpolated afterwards (black line). The intersection of the interpolation with a $\Delta\chi^2 = 2.71$ (gray dashed line) results in the 90% confidence interval of the parameter (gray vertical lines). The red cross marks the best-fit value.

statistically correct. Such a simultaneous fit using the standard χ^2-minimization routines required about a week of calculation time[6]. It is therefore necessary to follow a different approach in calculating the parameter uncertainty. Instead of finding the $\Delta\chi^2$ by iteratively performing single fits, which would require a week of calculation time in each step, we stepped the χ^2 as a function of the global parameter of interest on a coarser grid. Although the calculation of each grid point lasts a week as well, the χ^2-landscape can be resolved within this time using a single CPU for each grid point and global parameter. After a total of 16,320 CPUh (on 100 cores) the χ^2-landscapes of all global parameters were resolved except the $N_{\rm H}$, whose uncertainty was determined by a simultaneous fit of the data-groups containing the *Swift*- and *Suzaku*-data. Fig. 5.11 shows the resulting χ^2-landscape for the folding energy, $E_{\rm fold}$, as an example. Interpolating the landscapes using a $4^{\rm th}$-order polynomial to find $\Delta\chi^2 = 2.71$ then results in the global parameter uncertainties. Table 5.2 lists the final global parameters[7], detector calibration constants, and parameters of the GRXE.

5.1.5 Epochs 4–7 - post 2012 data

GRO J1008−57 underwent one type II "giant" outbursts in 2012 November and a "triple-peaked" outburst in 2014/2015 (see Figs. 5.1 and G.1). The source reached luminosities ∼4× higher than what has been observed with *RXTE* during the type I outbursts between 2005 and 2011. The bright outbursts have been observed with *NuSTAR* and *Suzaku* (epochs 4a, 4b, and 7) and analyzing the corresponding spectra therefore extends the luminosities covered with *RXTE* alone. Furthermore, we can verify GRO J1008−57's spectral model using the two observations by *Suzaku* and *NuSTAR* between 2012 and 2015 at lower source luminosities (epochs 5 and 6). Thus, we applied the spectral model defined in Eq. (5.2) to all these observations[8].

As we discussed above the folding energy, $E_{\rm fold}$, and black-body temperature, kT, were

[6]Due to the long runtime of a simultaneous fit, simplified fitting routines as described in appendix E have been implemented. However, they cannot be used for calculating the uncertainty of a global parameter since the achieved χ^2 using these functions is worse than after a proper χ^2-minimization.

[7]The uncertainties listed here are slightly larger than in Kühnel et al. (2013) as they were accidentally calculated on a smaller confidence level.

[8]The results will be published in Kühnel et al. (2016b, in prep.). The *Suzaku* observation during the 2012 November outburst (epoch 4a) has been analyzed partly in Kühnel et al. (2013) already, but are repeated here due to an insufficient calibration of the XIS near real time data and missing HXD backgrounds.

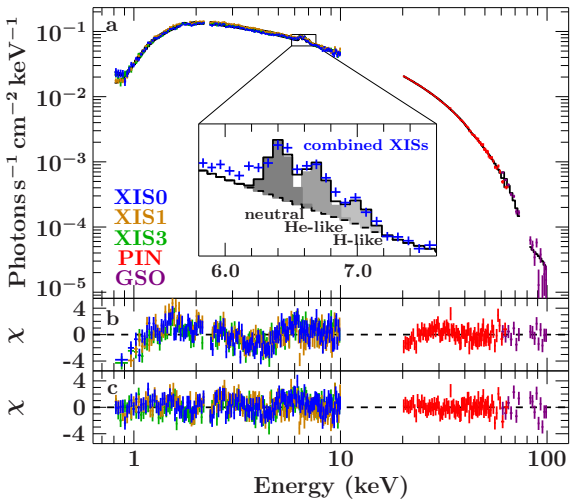

Figure 5.12: **a:** *Suzaku*-spectrum during the "giant" November 2012 outburst of GRO J1008−57 (epoch 4a). The inset shows a close-up on the iron line region. **b:** Residuals of the model used for the *RXTE*-spectra (see Eq. 5.2) including the CRSF around 76 keV and **c:** after adding a second black-body component.

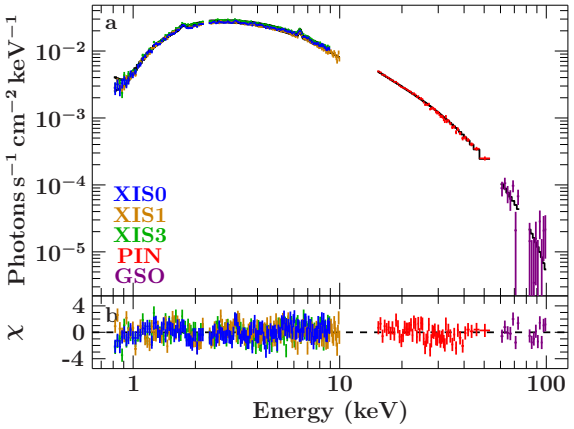

Figure 5.13: **a:** *Suzaku*-spectrum during the predicted type I outburst of GRO J1008−57 in 2014 January (epoch 5). **b:** Residuals of the model used for the *RXTE*-spectra (see Eq. 5.2).

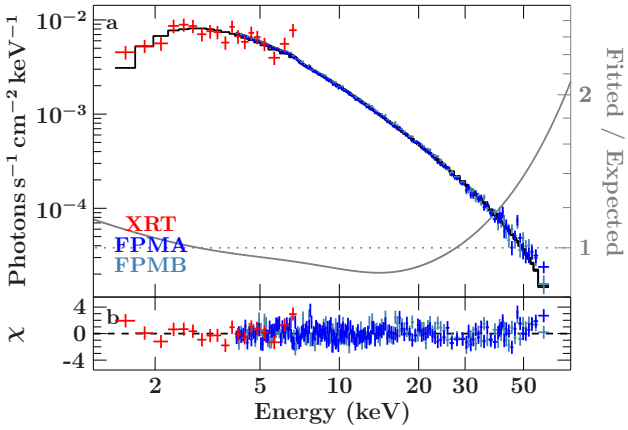

Figure 5.14: **a:** Simultaneous *NuSTAR* and *Swift*-XRT spectra between the second and third outburst of GRO J1008−57's "triple-peaked" activity in 2014/2015 (epoch 6). The gray line shows the ratio between the actual best-fit model and the model expected from the source's spectral evolution (see Sect. 5.1.8). **b:** Residuals of the best-fit model.

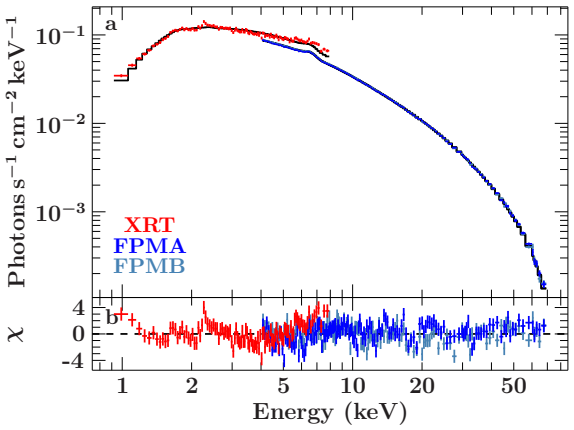

Figure 5.15: **a:** Simultaneous *NuSTAR* and *Swift*-XRT spectra after the peak of the third outburst of GRO J1008−57 during its 2014/2015 "triple-peaked" activity (epoch 7). **b:** Residuals of the best-fit model including a secondary black-body component (compare Fig. 5.12).

Table 5.2: Flux independent continuum parameters including the iron line equivalent widths during epochs 1–3, the GRXE parameters, and the flux calibration constants as found by the simultaneous fit to all *RXTE* observations of GRO J1008−57.

continuum	`tbnew`	$N_{\rm H}$	$1.547^{+0.019}_{-0.023}$	$10^{22}\,{\rm cm}^{-2}$
	`cutoffpl`	$E_{\rm fold}$	$15.92^{+0.29}_{-0.30}$	keV
	`bbody`	kT	$1.833^{+0.019}_{-0.019}$	keV
iron line	`gauss`	W_{2005}	65^{+10}_{-10}	eV
		W_{2007}	$27.9^{+2.4}_{-2.3}$	eV
		W_{2011}	83^{+5}_{-5}	eV
GRXE	`bremss`	kT	$3.4^{+0.5}_{-0.5}$	keV
		$F_{3\text{-}10\,{\rm keV}}$	$4.25^{+0.23}_{-0.23}$	$10^{-12}\,{\rm erg\,s^{-1}\,cm^{-2}}$
	`gauss`	E	$6.349^{+0.031}_{-0.031}$	keV
		σ	$0.53^{+0.06}_{-0.06}$	keV
		F	$2.39^{+0.17}_{-0.18}$	$10^{-4}\,{\rm photons\,s^{-1}\,cm^{-2}}$
constants[a]		$c_{\rm HEXTE}$	$0.859^{+0.009}_{-0.009}$	
		$c_{\rm XRT}$	$0.806^{+0.009}_{-0.009}$	
		$c_{\rm XIS0}$	$0.889^{+0.007}_{-0.007}$	
		$c_{\rm XIS1}$	$0.936^{+0.007}_{-0.007}$	
		$c_{\rm XIS3}$	$0.887^{+0.007}_{-0.007}$	
		$c_{\rm PIN}$	$1.000^{+0.010}_{-0.010}$	
		$c_{\rm GSO}$	$1.17^{+0.09}_{-0.09}$	

Notes. [a] The detector flux calibration constants, $c_{\rm X}$, are given relative to the *RXTE*-PCA. Apart from $c_{\rm HEXTE}$ all other constants were determined by a single data-group (see Fig. 5.8).

independent of the source's flux and consistent among the outbursts. Thus, we fixed these parameters for the *Suzaku* epochs 4a and 5 to the values found by the previous simultaneous fit of epochs 1–3 (see Table 5.2). In order to check whether our conclusions are valid for the *NuSTAR*-data (epochs 4b, 6, and 7), we did not fix these parameters during their spectral analysis. *Swift* observed GRO J1008−57 simultaneous with *NuSTAR*, such that the low energy part (1–5 keV) was covered. Thus, there was no need to fix the absorption column density, $N_{\rm H}$, as we did during the *RXTE* analysis. Furthermore, the GRXE is negligible in *Swift*, *Suzaku*, and *NuSTAR* due to their smaller field of view compared to *RXTE* and the possibility to measure the X-ray background (extracted from a region on the chip). As the source regions differ among the *Suzaku* observations of epoch 2, 4a, and 5 due to pile-up, the corresponding flux calibration constants were kept free and normalized to XIS3. The calibration constants during the *NuSTAR*- and *Swift*-analysis were fitted relative to *NuSTAR*-FPMA. This fitting strategy resulted, however, in unacceptable fits among all epochs except epoch 5.

Epoch 4a: the *Suzaku* spectrum during the 2012 "giant" outburst (epoch 4a) showed strong residuals in the iron line region, although a Kα emission line was included in the model. A close inspection revealed additional narrow fluorescence lines of He- and H-like iron at $E_{\rm Fe\ XXIV} = 6.69\,{\rm keV}$ and $E_{\rm Fe\ XXV} = 7.00\,{\rm keV}$ (see inset of Fig. 5.12a). The flux within the 7 keV line of $\sim$42% ± 13% relative to Kα was significantly higher than expected from neutral Kβ emission alone. Furthermore, a wave like structure below 6 keV remained

in the XISs (see Fig. 5.12b), which cannot be explained by a change in the absorption column density, N_{H}. Instead, we added a second black body component to the model, which then resulted in acceptable residuals within this energy range. The black body temperature is around $kT_2 = 0.45\,\mathrm{keV}$. Its flux was about half of the primary black body at $kT = 1.83\,\mathrm{keV}$. Finally, residuals above 60 keV in PIN and GSO were left, which we attribute to the CRSF around $E_{\mathrm{cyc}} = 76\,\mathrm{keV}$ claimed in these data (Bellm et al., 2014; Yamamoto et al., 2013). Adding the Lorentzian absorption model `cyclabs` (see Eq. 1.50) to the continuum with a fixed width of $W_{\mathrm{cyc}} = 10\,\mathrm{keV}$ finally resulted in flat residuals (see Fig. 5.12c).

Epoch 4b: Similar residuals at these high energies were detected in the *NuSTAR*-spectrum during the same outburst. Therefore, we added a CRSF to the model as we did for the *Suzaku*-observation. The iron line complex could be fitted well with a single narrow Gaussian although ionization lines were detected in the *Suzaku*-XIS spectra. They could not be resolved, however, neither in *NuSTAR* nor *Swift*-XRT due to their worse energy resolution compared to the *Suzaku*-XISs. Consequently, adding further narrow Gaussians to the model would introduce parameter degeneracies. Instead, we allowed for a free position and width of the Gaussian representing the neutral iron line. Fitting then resulted in a higher position than for neutral iron at $E_{\mathrm{Fe\,Kalpha}} = 6.4\,\mathrm{keV}$, which was expected as ionized emission lines at higher energies are present. This was confirmed by the width, $\sigma_{\mathrm{Fe\,K}\alpha}$, of a few 100 eV. See Fig. 3 of Bellm et al. (2014) for a plot of the *NuSTAR*- and *Swift*-spectra.

Epoch 5: As mentioned above applying the initial fitting strategy to the *Suzaku* data of the 2014 January outburst immediately resulted in an acceptable fit (see Fig. 5.13). This was caused by the absence of residuals at the cyclotron line energy as found during epochs 4a and 4b. A weak iron Kβ at 7.00 keV was detected, its flux of $25\% \pm 9\%$ compared to Kα was in very good agreement with the expected flux ratio from atomic transition rates (Kortright & Thompson, 2009).

Epoch 6: GRO J1008−57 did not fade into quiescence after the second outburst of its "triple-peaked" activity, but rather stayed at a level of ∼30 mCrab (compare Fig. 5.1) before it underwent its third outburst within a single orbit. During the episode of constant flux *NuSTAR* and *Swift* observed the source simultaneously (Fig. 5.14 shows the *NuSTAR*- and *Swift*-XRT spectra together with the best-fit model). A broad residual structure among *NuSTAR*'s full energy range was visible after applying the initial model. A significantly higher folding energy of $E_{\mathrm{fold}} \sim 23\,\mathrm{keV}$ is the only way to fit this feature. Furthermore, the absorption column density was about 2–3 times higher than the foreground absorption (see Table 5.2). At the time of the observation the neutron star was basically behind its companion star as seen from Earth (compare Fig. 4.19). Thus, the line of sight had crossed source intrinsic material which led to an increase of the absorption column density.

Epoch 7: The third outburst of GRO J1008−57's "triple-peaked" outburst observed with *NuSTAR* and *Swift* was almost as bright as its "giant" 2012 outburst. Interestingly, E_{fold} was no longer as high as a month before, when the source was in a flaring state (epoch 6), and is consistent to what has been found previously. The CRSF close to the end of *NuSTAR*'s spectral sensitivity was also detected and, thus, included in the model. A hint for this CRSF was also found by Sguera et al. (2014) in *INTEGRAL*-data as the source was in the field of view of the IBIS/ISGRI instrument during this outburst. The fit statistics were further improved by adding a secondary black body component to the model similar to that found in the *Suzaku*-spectrum of the 2012 "giant" outburst (epoch 4a). The fitted temperature of $kT_2 = 0.30\,\mathrm{keV}$ was close to those observed before. Finally, we had to free the iron line's position and width as similar residuals to epoch 4b were present, which were caused by a blend of iron lines in different ionization states. The final best-fit

and the spectra taken by *NuSTAR* and *Swift* are shown in Fig. 5.15.

Several fit parameters of the *NuSTAR* and *Swift* observations (epochs 4b, 6, and 7) were consistent among the epochs within their uncertainties. In particular, the black body temperature, kT, and the iron line energy, $E_{\mathrm{Fe\,K}\alpha}$, and its width, $\sigma_{\mathrm{Fe\,K}\alpha}$, seemed to be the same. During epochs 4b and 7, where the CRSF was included in the model, its energy, E_{cyc}, and its depth, τ_{cyc}, were very similar. During these epochs the folding energy, E_{fold}, were close to the flux-independent value we had found in our *RXTE* analysis (see Table 5.2). Consequently, we performed a simultaneous fit of all *NuSTAR* and *Swift* epochs (4b, 6, and 7) similar to the methods described in Sect. 2.4. The parameters, kT, E_{cyc}, W_{cyc}, τ_{tau}, $E_{\mathrm{Fe\,K}\alpha}$, and $\sigma_{\mathrm{Fe\,K}\alpha}$ were set as global parameters. The folding energies, E_{fold}, were tied together for epochs 4a and 7 (the luminous outbursts) as it was significantly different during epoch 6. This simultaneous fit resulted in a very good description of all 3 data-groups (with 3 spectra each). The final group-, global parameters, and all parameters of the *Suzaku* epochs are listed in Table 5.3.

We can confirm that including a cyclotron line between 70 and 80 keV improves the fit of epochs 4a and 4b as found by Bellm et al. (2014) and Yamamoto et al. (2013). The CRSF was also detected in epoch 7, where the source reached 700 mCrab, but was not necessary in epochs 5 and 6. However, the CRSF was still taken into account in the latter observation by the simultaneous fit of the *NuSTAR* data. Our final CRSF energy of $E_{\mathrm{cyc}} = 70.2^{+1.3}_{-1.1}$ keV is in agreement with earlier detections by Bellm et al. (2014), Yamamoto et al. (2013), and Sguera et al. (2014).

5.1.6 The continuum as a function of luminosity

Applying our spectral model of GRO J1008−57 (see Eq. 5.2) to the recent *Suzaku*-, *NuSTAR*-, and *Swift*-spectra confirmed that the folding energy, E_{fold}, and black body temperature, kT, are independent of the source's flux and time, as we had found previously in epochs 1–3. The best-fit parameter values listed in Table 5.3 are within 1σ of our previous simultaneous fit results (compare Table 5.2). The only exception was epoch 6, where the folding energy was significantly higher. Investigating this anomaly requires, however, further analysis and its discussion is presented in a subsequent Section (Sect. 5.1.8).

The only remaining free continuum parameters per observations were the photon index, Γ, the black body flux, F_{BB}, and the source's unabsorbed 15–50 keV flux, F_{PL}. As can be seen from Fig. 5.16a and d, Γ and F_{BB} were tightly correlated with F_{PL} throughout all outbursts. In particular, no hysteresis effects were seen between the rise and decline of an outburst[9] (the *RXTE* data covers the rise of the 2011 outburst, epoch 3, and the declines of the 2005 and 2007 outbursts, epoch 1 and 2, respectively). This implies that the accretion onto the neutron star is only driven by the mass accretion rate. The only clear outlier was the photon index, Γ, during epoch 6 as found with data from *NuSTAR* and *Swift*, which resembles the anomaly in the folding energy, E_{fold}, during this epoch. Thus, we ignored the data from epoch 6 in the following analysis. The two data points including *Suzaku*-data (green triangles; epochs 1 and 5) were in good agreement with each other since the source was at a similar flux level during these observations. Furthermore, the parameters during the 2012 "giant" outburst (epochs 4a and 4b) were consistent although a second black body component was included in the model of the *Suzaku*-spectrum to achieve an acceptable fit. The flux of this component was added to the corresponding F_{BB} value. The parameters during the recent *NuSTAR* observation in 2015 January (epoch 7), when GRO J1008−57 was 300 mCrab less luminous as during its "giant" 2012 outburst, are very similar to those of the latter outburst.

[9] This answers specific question 2.

Table 5.3: Continuum, emission lines, CRSF, and cross calibration constants of the spectral fits to X-ray data from GRO J1008−57 during epochs 4 to 7. Parameters in bold face have been determined simultaneously among the *NuSTAR* epochs 4b, 6, and 7.

	epoch 4a	epoch 4b	epoch 5	epoch 6	epoch 7
$F_{\rm PL}$ (10^{-9} erg s^{-1}cm^{-2})[a]	$11.76^{+0.27}_{-0.26}$	$10.331^{+0.023}_{-0.023}$	$1.50^{+0.06}_{-0.06}$	$0.3071^{+0.0030}_{-0.0030}$	$7.154^{+0.017}_{-0.017}$
Γ	$0.45^{+0.04}_{-0.04}$	$0.550^{+0.020}_{-0.022}$	$0.596^{+0.011}_{-0.011}$	$1.28^{+0.04}_{-0.05}$	$0.584^{+0.017}_{-0.018}$
$E_{\rm fold}$ (keV)	15.920[b]	$\mathbf{15.66^{+0.20}_{-0.22}}$	15.920[b]	$22.9^{+1.1}_{-1.1}$	$\mathbf{15.66^{+0.20}_{-0.22}}$
$F_{\rm BB}$ (10^{-9} erg s^{-1}cm^{-2})	$1.09^{+0.29}_{-0.29}$	$0.72^{+0.08}_{-0.08}$	$0.498^{+0.022}_{-0.022}$	$0.050^{+0.007}_{-0.007}$	$1.56^{+0.20}_{-0.17}$
kT (keV)	1.83[b]	$\mathbf{1.850^{+0.026}_{-0.026}}$	1.83[b]	$\mathbf{1.850^{+0.026}_{-0.026}}$	$\mathbf{1.850^{+0.026}_{-0.026}}$
kT_2 (keV)	$0.445^{+0.023}_{-0.026}$	-	-	-	$0.304^{+0.018}_{-0.016}$
bb_2/bb_1[c]	$0.50^{+0.19}_{-0.09}$	-	-	-	$0.67^{+0.19}_{-0.16}$
$N_{\rm H}$ (10^{22} cm^{-2})	$1.51^{+0.04}_{-0.04}$	$1.55^{+0.05}_{-0.06}$	$1.577^{+0.025}_{-0.025}$	$4.3^{+0.7}_{-0.7}$	$2.57^{+0.16}_{-0.16}$
$E_{\rm Fe\,K\alpha}$ (keV)	$6.405^{+0.022}_{-0.008}$	$\mathbf{6.540^{+0.010}_{-0.010}}$	$6.433^{+0.010}_{-0.014}$	$\mathbf{6.540^{+0.010}_{-0.010}}$	$\mathbf{6.540^{+0.010}_{-0.010}}$
$\sigma_{\rm Fe\,K\alpha}$ (keV)	0[d]	$\mathbf{0.294^{+0.015}_{-0.014}}$	0[d]	$\mathbf{0.294^{+0.015}_{-0.014}}$	$\mathbf{0.294^{+0.015}_{-0.014}}$
$F_{\rm Fe\,K\alpha}$ (10^{-4} ph s−1 cm^{-2})	$29.1^{+2.9}_{-2.9}$	73^{+4}_{-4}	$8.8^{+0.7}_{-0.7}$	$1.9^{+0.5}_{-0.5}$	$49.0^{+2.3}_{-2.3}$
$EW_{\rm Fe\,K\alpha}$ (eV)	39^{+4}_{-4}	102^{+5}_{-5}	52^{+5}_{-5}	32^{+7}_{-7}	90^{+5}_{-5}
$E_{\rm Fe\,K\beta}$ (keV)[e]	$7.000^{+0.023}_{-0.042}$	-	$7.00^{+0.09}_{-0.10}$	-	-
$F_{\rm Fe\,K\beta}$ (10^{-4} ph s−1 cm^{-2})[e]	$12.2^{+2.9}_{-2.9}$	-	$2.0^{+0.7}_{-0.7}$	-	-
$EW_{\rm Fe\,K\beta}$ (eV)[e]	18^{+5}_{-5}	-	13^{+5}_{-5}	-	-
$E_{\rm Fe\,XXIV}$ (keV)	$6.689^{+0.018}_{-0.022}$	-	-	-	-
$F_{\rm Fe\,XXIV}$ (10^{-4} ph s−1 cm^{-2})	$24.6^{+2.9}_{-2.9}$	-	-	-	-
$EW_{\rm Fe\,XXIV}$ (eV)	35^{+5}_{-5}	-	-	-	-
$E_{\rm cyc}$ (keV)	$75.7^{+1.3}_{-1.1}$	$\mathbf{70.2^{+1.3}_{-1.1}}$	-	$\mathbf{70.2^{+1.3}_{-1.1}}$	$\mathbf{70.2^{+1.3}_{-1.1}}$
$W_{\rm cyc}$ (keV)	10 (fix)	10 (fix)	-	10 (fix)	10 (fix)
$\tau_{\rm cyc}$	$2.17^{+0.29}_{-0.27}$	$\mathbf{1.06^{+0.14}_{-0.11}}$	-	$\mathbf{1.06^{+0.14}_{-0.11}}$	$\mathbf{1.06^{+0.14}_{-0.11}}$
$c_{\rm XIS0}$[f]	$0.975^{+0.005}_{-0.005}$	-	$0.958^{+0.005}_{-0.005}$	-	-
$c_{\rm XIS1}$[f]	$1.042^{+0.005}_{-0.005}$	-	$0.938^{+0.013}_{-0.013}$	-	-
$c_{\rm PIN}$[f]	$1.297^{+0.028}_{-0.027}$	-	$1.33^{+0.05}_{-0.05}$	-	-
$c_{\rm GSO}$[f]	$1.30^{+0.11}_{-0.10}$	-	$1.15^{+0.21}_{-0.21}$	-	-
$c_{\rm FPMB}$[g]	-	$1.0269^{+0.0015}_{-0.0015}$	-	$1.034^{+0.005}_{-0.005}$	$1.0147^{+0.0015}_{-0.0015}$
$c_{\rm XRT}$[g]	-	$1.182^{+0.010}_{-0.009}$	-	$0.99^{+0.08}_{-0.08}$	$1.234^{+0.011}_{-0.011}$
$\chi^2_{\rm red}$/d.o.f.	1.23 / 581	1.24 / 1811	1.19 / 527	1.00 / 579	1.17 / 1799

Notes. [a] The flux $F_{\rm PL}$ is given in the 15–50 keV energy band. [b] The value of this parameter has been fixed to its global values during epochs 1–3 (see Table 5.2). [c] This is the ratio between the normalizations of the second to the first black body. [d] The width of the emission line is fixed to 10^{-6} eV. [e] In case of epoch 4a these parameters represent a blend of the Fe Kβ and Fe XXV (H-like) emission lines. [f] The detector flux calibration constants are given relative to the *Suzaku*-XIS3 and to [g] the *NuSTAR*-FPMA.

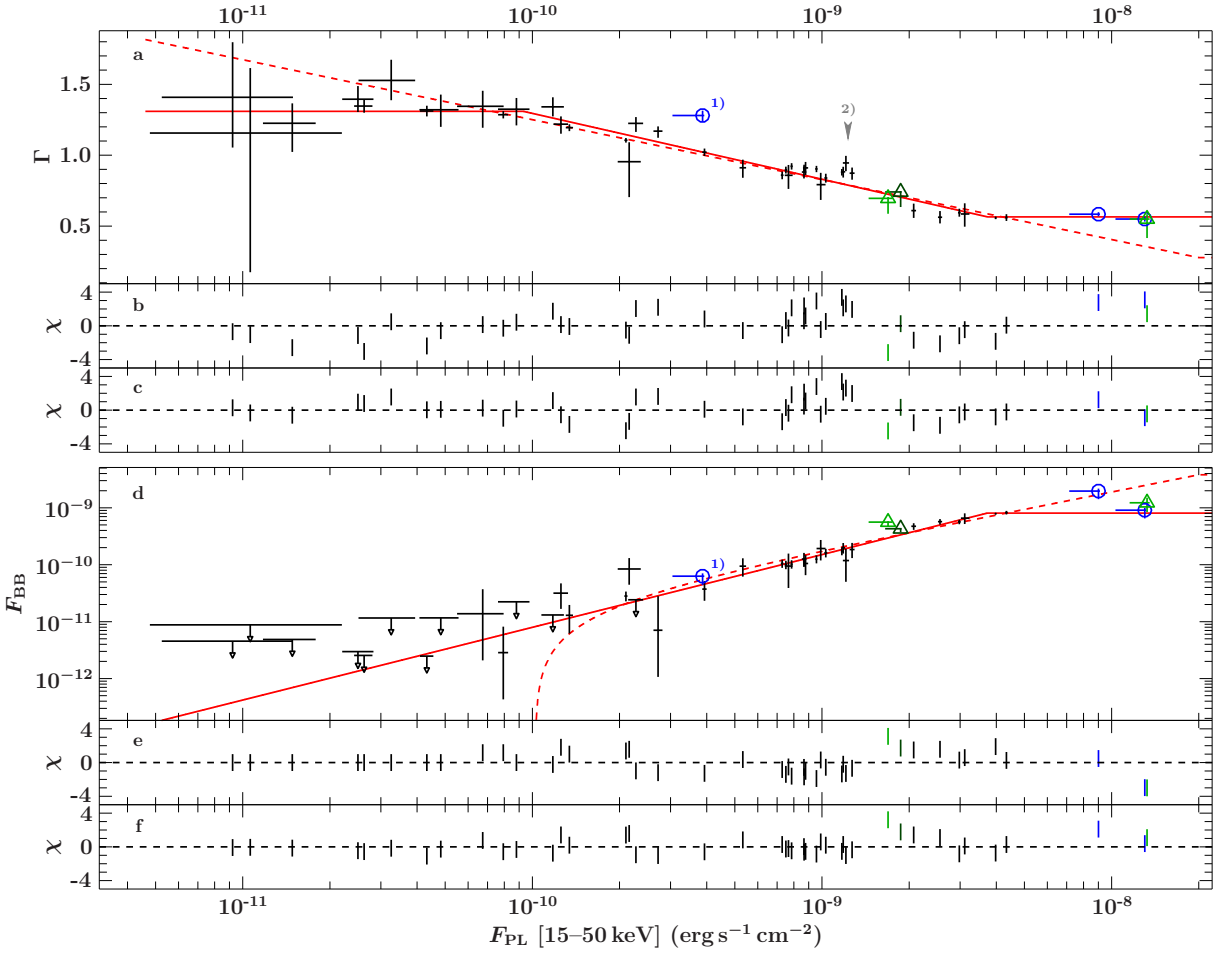

Figure 5.16: **a:** The photon indices, Γ, over the source's flux, F_{PL}, resulting from spectral fits of epochs 1–7. Parameters derived from *RXTE* are shown in black, from *Suzaku* as green triangles, and from *NuSTAR* and *Swift* as blue circles. The simultaneous *RXTE* and *Suzaku* observation in 2007 (epoch 2) is the dark green triangle. The uncertainties of the parameters include the computed 68% confidence level with two degrees of freedom ($\delta\chi^2 = 2.30$) and further systematics as explained in the text. The outlier from the correlation marked with 1) is the result of epoch 6. The *RXTE* data points responsible for the high χ^2 when fitting the dependency of Γ are marked with 2). The emerging correlations between the parameters are fitted by two empirical models (1 - dashed red line; 2 - solid red line) as defined in the text. **b:** Residuals of model 1 and **c:** of model 2. **d:** The best-fit black body fluxes, F_{BB} (in erg s^{-1} cm^{-2}), over the sources flux. The colors of the data points, marks, a red lines are the same as in panel a. **e:** Residuals of model 1 and **f:** of model 2 fitted to the observed black body flues.

In order to further analyze the spectral evolution with flux, we applied phenomenological models to the apparent parameter correlations, $\Gamma(F_{\rm PL})$ and $F_{\rm BB}(F_{\rm PL})$, of Fig. 5.16a and d, respectively. Performing a χ^2-minimization requires the parameters uncertainties to be on the 68% confidence level, i.e., 1σ uncertainties. As the data consist of parameter pairs resulting from the same spectral investigations, the 68% confidence levels for two degrees of freedom have to be calculated ($\Delta\chi^2 = 2.30$). Because the uncertainty calculation of the *RXTE* data lasted about one week we extrapolated the previous single parameter uncertainties ($\Delta\chi^2 = 2.71$) to two degrees of freedom assuming a linear relation, which is satisfied as the $\Delta\chi^2$ are close to each other.

Calculating the χ^2 as defined in Eq. (2.1) was not applicable here since each data point consists of a parameter pair $(D_{\rm x}, D_{\rm y})$ with their respective uncertainties, which are asymmetric in most cases $(\Delta D^{\pm}_{\rm x}, \Delta D^{\pm}_{\rm y})$. In order to fit a two dimensional model of the form $(M_{\rm x}, M_{\rm y})$ to the data points using a χ^2-minimization, we calculated the χ^2 after

$$\chi^2 = \sum_{k=1}^{n} \frac{(M_x - D_{{\rm x},k})^2}{S(M_x - D_{{\rm x},k}, \Delta D^{+}_{{\rm x},k}, \Delta D^{-}_{{\rm x},k})^2} + \frac{(M_y - D_{{\rm y},k})^2}{S(M_y - D_{{\rm y},k}, \Delta D^{+}_{{\rm y},k}, \Delta D^{-}_{{\rm y},k})^2} \quad , \tag{5.3}$$

where $S(r, \Delta^+, \Delta^-)$ returns Δ^+ for $r > 0$ and Δ^- otherwise. The χ^2 defined in Eq. (5.3) is therefore the sum over all distances of the datapoints $(D_{\rm x}, D_{\rm y})$ to the model curve normalized by their uncertainties. It is clear that the model $(M_{\rm x}, M_{\rm y})$ has to be calculated on a very fine grid in order to calculate proper distances. The logarithmic grid in $M_{\rm x}$, i.e., in source flux, $F_{\rm PL}$, was constructed with a bin-size finer by one order of magnitude than the smallest measurement uncertainty. This corresponds to a similar resolution in $M_{\rm y}$, i.e., in photon index, Γ, or black body flux, $F_{\rm BB}$.

A first investigation of the observed correlations $\Gamma(F_{\rm PL})$ and $F_{\rm BB}(F_{\rm PL})$ revealed significant discrepancies between the fitted models and the parameters derived from *Suzaku*- and *NuSTAR-Swift*-data. The reason were calibration differences between these missions and *RXTE*, which got significant due to the well determined fluxes and continuum parameters using *Suzaku* and *NuSTAR*. Since the majority of the results were obtained using *RXTE*-data, we converted the measurements of *NuSTAR* and *Suzaku* according to cross-calibration differences to *RXTE* as described in the following. In case of the *Suzaku* data during epochs 2, 4a and 5 the source and black body fluxes, $F_{\rm PL}$ and $F_{\rm BB}$, respectively, were multiplied by 1.127(9), which is the inverse of detector calibration constant $c_{\rm XIS3}$ as determined by the simultaneous *Suzaku* and *RXTE* observation in epoch 2 (see Table 5.2). To scale the fluxes determined by *NuSTAR*, we used the scaling constant between XIS0 and *NuSTAR*-FPMA of 1.081(5) by Tomsick et al. (2014), the mean constant $c_{\rm XIS0} = 0.967(9)$ between XIS0 and XIS3 as we found for epochs 4a and 5, and $c_{\rm XIS3}$ from epoch 2. Finally, the *NuSTAR* fluxes were scaled by 1.260(16) to match the *RXTE*-PCA fluxes. While the upper 68% uncertainty of the scaled fluxes resulted from error propagation of the former uncertainty and the calibration constants, we kept the lower confidence values to account for possible variability in the detector cross-calibrations. This resulted in asymmetric uncertainties in $F_{\rm PL}$ and $F_{\rm BB}$ determined by *Suzaku* and *NuSTAR*. The photon indices, Γ, derived from data of different instruments may not be consistent due to differences in their energy calibration (see, e.g., Kirsch et al., 2005; Tsujimoto et al., 2011). In fact, the photon indices measured by *Suzaku* during epochs 2 and 5 were $\sim$0.1 lower than what our initial fits predicted, which is consistent with energy cross-calibration issues. Therefore, we added a +0.1 shift to all photon indices, Γ, measured with *Suzaku* during epochs 2, 4a, and 5. Again, the lower confidence values remain unchanged, leading to asymmetric uncertainties in Γ.

Table 5.4: Parameter and fit statistics of two empirical models fitted to the observed parameter correlations $\Gamma(F_{\rm PL})$ and $F_{\rm BB}(F_{\rm PL})$ as shown in Fig. 5.16.

	$\Gamma(F_{\rm PL})$	$F_{\rm BB}(F_{\rm PL})$
Model 1	`log`	`lin`
a_X	$0.828^{+0.008}_{-0.008}$	$0.10^{+0.05}_{-0.04}$
b_X	$-0.423^{+0.014}_{-0.014}$	$0.192^{+0.009}_{-0.009}$
$\chi^2_{\rm red}$ / dof	3.04 / 43	1.70 / 43
Model 2	`dbl-brkn log`	`high-brkn pow`
a_X	$0.829^{+0.013}_{-0.009}$	$0.147^{+0.017}_{-0.009}$
b_X	$-0.470^{+0.034}_{-0.020}$	$1.34^{+0.05}_{-0.16}$
$F_{\rm brk,lo}$ ($10^{-9}\,{\rm erg\,s^{-1}\,cm^{-2}}$)	$0.095^{+0.021}_{-0.034}$	-
$F_{\rm brk,hi}$ ($10^{-9}\,{\rm erg\,s^{-1}\,cm^{-2}}$)	$3.60^{+0.66}_{-0.18}$	
$\chi^2_{\rm red}$ / dof	2.09 / 41.5	0.95 / 42.5

We used several phenomenological models,

$$\texttt{log}(F_{\rm PL}) = a_X + b_X \log(F_{\rm PL}/10^{-9}\,{\rm erg\,s^{-1}\,cm^{-2}}) \quad , \tag{5.4}$$

$$\texttt{lin}(F_{\rm PL}) = b_X(F_{\rm PL}/10^{-9}\,{\rm erg\,s^{-1}\,cm^{-2}} - a_X) \quad , \tag{5.5}$$

$$\texttt{pow}(F_{\rm PL}) = a_X(F_{\rm PL}/10^{-9}\,{\rm erg\,s^{-1}\,cm^{-2}})^{b_X} \quad , \tag{5.6}$$

to investigate the observed parameter evolutions, $\Gamma(F_{\rm PL})$ and $F_{\rm BB}(F_{\rm PL})$. Here, X is either the photon index, Γ, or black body flux, $F_{\rm BB}$, and a_X and b_X are model parameters. Furthermore, we assumed the black body to be in emission only, i.e., we assured $F_{\rm BB}(F_{\rm PL}) > 0$ for all source fluxes, $F_{\rm PL}$. From the apparent evolution of Γ and $F_{\rm BB}$ with the source's flux as shown in Fig. 5.16a and d, respectively, we applied

$$\text{model 1: } \Gamma(F_{\rm PL}) = \texttt{log}(F_{\rm PL}) \quad \text{and} \quad F_{\rm BB}(F_{\rm PL}) = \texttt{lin}(F_{\rm PL})$$

during a first fit of the data. Minimizing the χ^2 after Eq. (5.3) revealed, however, that this model did not describe the data well (see Table 5.4 for the χ^2-values and Fig. 5.16b and e for the residuals). Below a certain source flux of around $10^{-10}\,{\rm erg\,s^{-1}\,cm^{-2}}$ almost all residuals in Γ were negative, indicating actual lower value for Γ as predicted by the `log` function[10]. Furthermore, the observed values for Γ and $F_{\rm BB}$ at very high source fluxes around $10^{-8}\,{\rm erg\,s^{-1}\,cm^{-2}}$ (epochs 4a, 4b, and 7) were inconsistent with the `log` and `lin` functions, respectively. Using other functions in the definition of model 1 did not result in a better description of the data. To improve the fits, we allowed for an additional flattening of the above models below or above a certain flux level, $F_{\rm brk,lo}$ or $F_{\rm brk,hi}$, respectively,

$$\texttt{low-brkn}(X, F_{\rm PL}) = \begin{cases} X(F_{\rm brk,lo}), & \text{for } F_{\rm PL} < F_{\rm brk,lo} \\ X(F_{\rm PL}), & \text{for } F_{\rm PL} \geq F_{\rm brk,lo} \end{cases} \tag{5.7}$$

$$\texttt{high-brk}(X, F_{\rm PL}) = \begin{cases} X(F_{\rm PL}), & \text{for } F_{\rm PL} \leq F_{\rm brk,hi} \\ X(F_{\rm brk,hi}), & \text{for } F_{\rm PL} > F_{\rm brk,hi} \end{cases} \tag{5.8}$$

where X is one of the functions defined in Eqs. (5.4–5.6). We found that a model of the form

$$\text{model 2: } \Gamma(F_{\rm PL}) = \texttt{dbl-brkn}(\texttt{log}, F_{\rm PL}) \quad \text{and} \quad F_{\rm BB}(F_{\rm PL}) = \texttt{high-brkn}(\texttt{pow}F_{\rm PL}) \quad ,$$

[10] This discovery triggered specific question 4.

where `dbl-brkn` is a combination of `low-brkn` and high-brkn, is able to improve the fit significantly. Interestingly, the breaks at higher fluxes, $F_{\mathrm{brk,hi}}$, in the evolutions of Γ and F_{BB} are with $\sim 4 \times 10^{-9}\,\mathrm{erg\,s^{-1}\,cm^{-2}}$ at a similar flux value. Consequently, we have tied the fluxes $F_{\mathrm{brk,hi}}$ in both evolutions together during a simultaneous fit. We note that the linear dependency (`lin`) in the description of $F_{\mathrm{BB}}(F_{\mathrm{PL}})$ was replaced by a power-law behavior (`pow`) as it resulted in slightly lower χ^2-values. Our final best-fit parameters for model 2 are listed in Table 5.4 and the residuals are shown in Figs. 5.16c and f.

The final χ^2_{red} of 2.09 for the fit to the evolution of the photon index, $\Gamma(F_{\mathrm{PL}})$, still indicates a bad description of the data. We found, however, no other functions or combination of functions which results in an acceptable fit. Investigating the residuals in Fig. 5.16c shows higher photon indices for a few *RXTE* measurements around $10^{-9}\,\mathrm{erg\,s^{-1}\,cm^{-2}}$. Ignoring these data reduces the χ^2_{red} to 1.52, which is acceptable. Thus, we conclude that a systematic uncertainty in this group of *RXTE* observations might be present.

5.1.7 Accretion regimes in GRO J1008−57

In Section 5.1.4 we have shown that the phenomenological model for the broad-band X-ray spectrum of GRO J1008−57 shows flux and time independent parameters, which are the folding energy, E_{fold}, and black body temperature, kT. The remaining parameters show tight correlations with each other. In particular, Sect. 5.1.6 shows that the dependencies of the black body flux, F_{BB}, and the photon index, Γ, on the overall source flux, F_{PL}, can be described well with empirical functions. Thus, the X-ray spectrum of GRO J1008−57 at almost any given flux level is determined by only one parameter, which is the source's flux itself. This is a remarkable result which has not been seen in a BeXRB binary before[11].

Furthermore, there was a hint in the evolution of Γ with flux for changes at particular flux levels (see Fig. 5.16). Below $F_{\mathrm{PL}} \sim 10^{-10}\,\mathrm{erg\,s^{-1}\,cm^{-2}}$ the data was consistent with a constant photon index, while it started decreasing for higher fluxes, i.e., the spectrum got harder. Interestingly, if the black body dependency on the source's flux is described by a linear function (`lin`) then it starts contributing to the spectrum above $10^{-10}\,\mathrm{erg\,s^{-1}\,cm^{-2}}$ as well (see Table 5.4). At fluxes above $F_{\mathrm{PL}} \sim 3.6 \times 10^{-10}\,\mathrm{erg\,s^{-1}\,cm^{-2}}$ both the photon index, Γ, and black body flux, F_{BB}, did not seem to decrease and increase further with the source's flux, respectively.

The fact that we observed two flux levels where the spectral evolution of GRO J1008−57 with its flux changes, is in line with theoretical expectations by Becker et al. (2012, see Sect. 1.3.2). Above the so-called Coulomb breaking luminosity, L_{coul} (see Eq. 1.42), the infalling matter passes through a radiation dominated shock inside the column, but gets stopped by Coulomb interactions before it hits the neutron star's surface. At higher mass accretion rates around the critical luminosity, L_{crit} (see Eq. 1.43), the radiation pressure is able to decelerate the accreted matter to rest without the need of further deceleration mechanisms.

In order to check whether the observed flux levels, F, in GRO J1008−57 can be associated with L_{coul} and L_{crit}, we needed to convert the measured fluxes within a certain energy range into their corresponding bolometric luminosities, L. However, the commonly used equation $L = 4\pi d^2 F$ (Eq. 1.2) with the distance d to the source is only a rough approximation in case of an accreting neutron star. A more sophisticated estimate of the

[11] At the time of the corresponding publication, the authors of Kühnel et al. (2013) were not aware of any other publication claiming the same conclusion for another BeXRB. Currently, an analysis of GX 304−1 is ongoing, which preliminary results as presented in Sect. 5.2 indicate the same behavior.

luminosity is

$$L = d^2 \int_{-\infty}^{+\infty} g(E) M(E) \, \mathrm{d}(E(z+1)) \quad , \tag{5.9}$$

where

a) the observed continuum model, $M(E)$, is integrated over the full electromagnetic spectrum
b) while the energy is corrected for the gravitational redshift, z (see Eq. 1.40),
c) $0 \leq g(E) \leq 2\pi$ is a factor describing the accretion column's emission geometry[12],
d) and d is the distance to the source.

Each of these steps introduces further systematic and statistical uncertainties. In case of GRO J1008−57's continuum model as defined in Eq. (5.2), we found a 16% lower integrated flux within 3–60 keV than compared to the 0.01–100 keV range, which was nearly independent of the assumed source flux. We interpreted this difference as systematic uncertainty of the model extrapolation in a). The main part in this uncertainty was caused by the unknown spectrum below 3 keV (knowing the 1–3 keV range as observed with *Suzaku* does not change this result significantly). For standard neutron star parameters as listed in Table 1.1 the gravitational redshift on the surface of the neutron star, where we assumed the radiation to escape from, is $z + 1 = 1.250$ after Eq. (1.40). The uncertainty in z is probably around 0.1 corresponding to uncertainties in the mass and radius of $0.5\,\mathrm{M}_\odot$ and 4 km, respectively (compare Fig. 1.5), which translates to a statistical uncertainty of ∼8% in the derived luminosity. In principle, the factor $g(E)$ describing the emission geometry in c) can be derived by fitting the energy-dependent pulse profiles of a source with a geometrical model of the accretion column taking light-bending into account. As these models are currently under development (Falkner et al., 2016, in prep.) the accretion geometry of GRO J1008−57 is not known yet. Using a preliminary implementation Martínez-Núñez et al. (2016) have estimated that if most radiation leaves the accretion column sideways (fan beam) then the true luminosity of both poles combined can be off by −40% to +75% compared to assuming $g(E) = 4\pi$, i.e., isotropic emission. This effect mainly depends on the inclination angle of the observer to the rotational axis of the neutron star. Furthermore, the inclination angle between the magnetic and rotational axis has an effect on the $g(E)$. As GRO J1008−57 is not an under-luminous X-ray source the uncertainty in the emission geometry is probably in the range of ±40%. Finally, the measurement uncertainty in the distance to GRO J1008−57 of $d = 5.8(5)$ kpc (Riquelme et al., 2012) error propagates to a statistical uncertainty in L of ±18% in d). Summing up all statistical uncertainties in quadrature and adding the systematic ones leads to a total relative uncertainty of -45% and +61% in the derived luminosity, L, after Eq. (5.9).

To calculate L_coul and L_crit after Eqs. (1.42) and (1.43) several neutron star parameters, such as its mass and radius, have to be known. The magnetic field strength is inferred from the detected CRSF in the *NuSTAR* spectra (epochs 4b, 6, and 7) of $E_\mathrm{cyc} = 70.2$ keV, which needs to be corrected for the gravitational redshift following Eq. (1.39). The remaining parameters are unknown for GRO J1008−57 and, thus, we assumed canonical values (see Table 1.1). The derived luminosities after Eq. (5.9) at the breaks in the spectral evolution, $L_\mathrm{brk,lo}$ and $L_\mathrm{brk,hi}$ (compare Table 5.4), and the theoretical luminosities after Becker et al. (2012) are

$$\begin{aligned} L_\mathrm{brk,lo} &= 1.0^{+0.8}_{-0.9} \times 10^{36}\,\mathrm{erg\,s^{-1}\,cm^{-2}} \quad , \quad L_\mathrm{coul} &= 5.99^{+0.21}_{-0.19} \times 10^{36}\,\mathrm{erg\,s^{-1}\,cm^{-2}} \quad , \\ L_\mathrm{brk,hi} &= 2.1^{+1.6}_{-1.1} \times 10^{37}\,\mathrm{erg\,s^{-1}\,cm^{-2}} \quad , \quad L_\mathrm{crit} &= 12.8^{+1.4}_{-1.4} \times 10^{37}\,\mathrm{erg\,s^{-1}\,cm^{-2}} \quad , \end{aligned}$$

[12]The luminosities calculated in Becker et al. (2012) apply to a single accretion column only. In case of two columns (one at each magnetic pole) the factor would be $0 \leq g(E) \leq 4\pi$.

Note that the uncertainties in $L_{\mathrm{brk,lo}}$ and $L_{\mathrm{brk,hi}}$ include the additional uncertainties due to the conversion from the flux. The actual measurement uncertainties in the fluxes are a factor ∼5 smaller. The uncertainties in L_{coul} and L_{crit} are due to the uncertainties in E_{cyc} and z. Although the uncertainties in the derived luminosities at the breaks in the spectral evolution were quite large, they do not match the theoretical luminosities calculated after Becker et al. (2012). In fact, both seemed to be shifted towards higher luminosities compared to the observed ones. The difference between $L_{\mathrm{brk,lo}}$ and L_{coul} was about a factor of 6, corresponding to 4.6σ, and between $L_{\mathrm{brk,hi}}$ and L_{crit} a factor of 6 as well, which are 3.5σ. If the magnetic field strength of GRO J1008−57 would be half of the detected CRSF, i.e., we observed the first harmonic, worsens the difference to L_{coul}, but decreases the critical luminosity, L_{crit}, down to 1.3σ. There are, however, no indications for a CRSF around 40 keV in any of the spectra. The smallest value for L_{coul} by changing the canonical neutron star parameter is $4 \times 10^{36}\,\mathrm{erg\,s^{-1}\,cm^{-2}}$ for a mass of $1\,\mathrm{M_\odot}$, which is still a 3σ difference. The critical luminosity, L_{crit}, depends even less on these parameters and therefore does not lead to an acceptable match with $L_{\mathrm{brk,hi}}$. However, if the spectrum inside the column is a mixture between Bremsstrahlung-radiation and Planck spectrum, which is set by $1 < w < 3$ in Eq. (1.43), then L_{crit} would be consistent with the observed high luminosity break in the spectral evolution.

To conclude, the observed changes in the spectral evolution of GRO J1008−57 at $L_{\mathrm{brk,lo}}$ and $L_{\mathrm{brk,hi}}$ are unlikely associated with L_{coul} and L_{crit} after the theory by Becker et al. (2012). Although, changing w or E_{cyc} in Eq. (1.43) leads to a consistency of L_{crit} with $L_{\mathrm{brk,hi}}$, the required CRSF energy is inconsistent with the observations.

It is expected by theoretical investigations by Postnov et al. (2015a) that the X-ray spectrum starts to harden once a radiative shock is present in the accretion column, i.e., it gets optically thick. Interestingly, we observed this behavior in the spectral evolution of GRO J1008−57 above $L_{\mathrm{brk,lo}}$. This would imply that at $L_{\mathrm{brk,lo}}$ a radiative shock emerges[13] and enters the sub-critical accretion regime between $L_{\mathrm{coul}} < L < L_{\mathrm{crit}}$. If this was true then further theoretical investigations are needed to explain the strong inconsistency between L_{coul} after Becker et al. (2012) and $L_{\mathrm{brk,lo}}$ as observed in the present work.

5.1.8 Spectral anomaly of epoch 6

An advantage in knowing the spectral evolution of GRO J1008−57 with its flux over orders of magnitude is to predict a spectrum for a given source flux, which can then be compared to an observed spectrum. Using the spectral model defined in Eq. (5.2), the values for the flux independent E_{fold} and kT (see Table 5.2), and model B for the evolution of Γ and F_{BB} (see Table 5.4), we constructed a new fit model particularly for the analysis of GRO J1008−57. This model has only one free parameter, which is the source's flux, F_{PL}.

We used this model to further analyze the spectral anomaly we have found for the *NuSTAR* observation between the second and third outburst during GRO J1008−57's "triple-peaked" activity (epoch 6). The gray curve in Fig. 5.14 shows the ratio between the best-fit model and the predicted spectral shape using the new model defined above. There is a soft excess below 10 keV visible, which contributes by 20%–40% in flux. Furthermore, for energies above ∼30 keV a very hard component appeared, which was almost as bright as expected from the new model for the source at 60 keV.

In order to discuss possible physical origins of the spectral anomaly we have created the *NuSTAR*-FPMA pulse profile during epoch 6 using a pulse period of 93.44522 s, found by epoch folding the corresponding binary corrected light curve. During the February 2005 outburst (epoch 1) *RXTE* observed the source at a similar flux level than *NuSTAR* during

[13] This answers specific question 4.

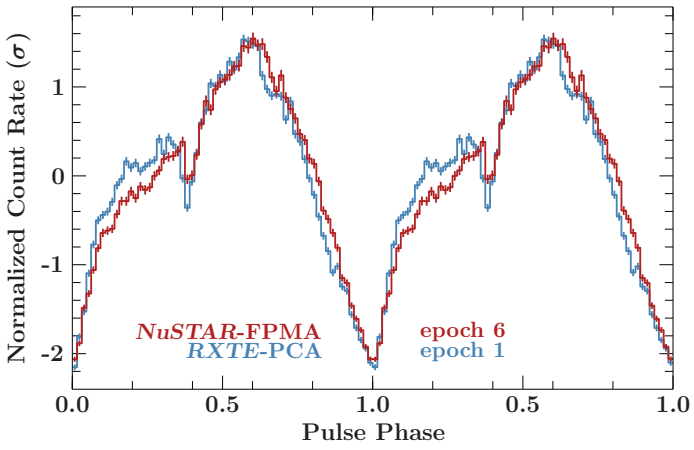

Figure 5.17: Pulse profiles of GRO J1008−57 during epoch 6 as measured with *NuSTAR*-FPMA (3–79 keV; red) and during epoch 1 with *RXTE*-PCA (3–50 keV; blue). Both observations were performed at a similar flux level of the source. The count rates are normalized using Eq. (5.10).

epoch 6 (*RXTE* ObsID 90089-03-02-01). We folded the binary corrected *RXTE*-PCA light curve with the mean period during 2005 of 93.67928 s. To compare both pulse profiles we normalized the count rates, $C_{\mathrm{norm},i}$, in each phase bin, i, following Ferrigno et al. (2011),

$$C_{\mathrm{norm},i} = \frac{C_i - \langle C \rangle}{\sigma\{C\}} \quad . \tag{5.10}$$

Here, $\langle C \rangle$ is the mean of the original count rate profile, C_i, and $\sigma\{C\}$ is its standard deviation. In this way the mean of the normalized pulse profile is zero, while its standard deviation is unity. The normalized and phase aligned *NuSTAR*-FPMA and *RXTE*-PCA profiles are shown in Fig. 5.17 in units of the original standard deviation, $\sigma\{C\}$. Both profiles match almost perfectly.

Since the pulse profile during epoch 6 showed no difference compared to an earlier observation at the same flux level means that the accretion column geometry did not change. Thus, the accretion column is very likely not responsible for the spectral anomaly discovered in epoch 6. What causes the strong difference to the expected spectral shape of GRO J1008−57 is beyond the scope of the present thesis and requires further investigation. Without knowing the spectral evolution of the source with its flux this anomaly would have been, however, unnoticed.

5.2 GX 304−1: Same Behavior as GRO J1008−57?

This Section briefly presents an ongoing analysis of the BeXRB GX 304−1 in collaboration with Richard E. Rothschild. This project was initially started by Sebastian Müller, who published the first results in his Ph.D. thesis (2013). The background of *RXTE*-HEXTE could not be measured for the observations he had analyzed, since HEXTE's "rocking" mechanism failed in March 2010 (see Sect. 3.2.1), right before GX 304−1 showed activity. Consequently, analyzing the CRSF around 54 keV in detail was not possible as *RXTE*-PCA covers the data between 3 and 50 keV only. Furthermore, the presence of the CRSF influenced the determination of the continuum shape, which led to strong parameter degeneracies. It was necessary to fix several parameters during his analysis, such as the folding energy and the width and centroid energy of the CRSF, during the first analysis. Now it is possible to provide working HEXTE background spectra. Thus, we can reveal the spectral evolution of GX 304−1 including the CRSF parameters, which is the focus of this Section. This results will be published soon in Rothschild et al. (2016, in prep.). Note that the detected enhancement of the absorption column density, N_{H}, during the 2011 May outburst as found by Müller (2013) is not part of this Section. Please see his Ph.D. thesis for details or the upcoming publication Kühnel et al. (2016c, in prep.).

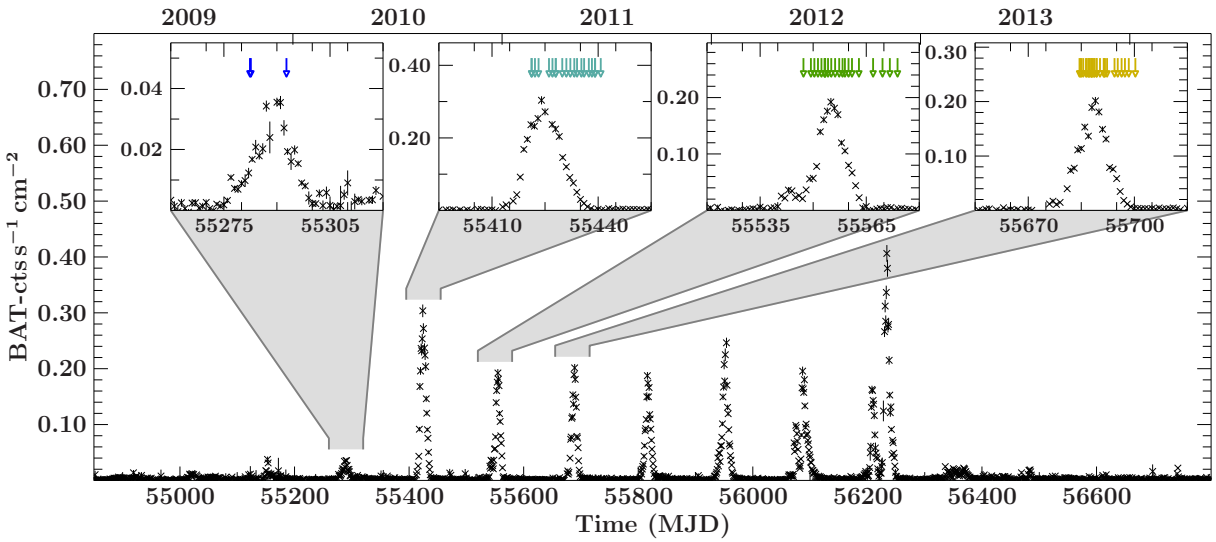

Figure 5.18: *Swift*-BAT light curve of GX 304−1 between 2009 and 2014. The insets show a zoom onto the first four outbursts of the shown series, which were monitored by *RXTE*. The arrows on top mark the times of the observations.

A new variable X-ray source, Cen XR-2, was discovered with NaI(Tl) scintillation detectors during a balloon flight in 1967 (Lewin et al., 1968b,a). This source was later confirmed and named GX 304−1 by McClintock et al. (1971) and also detected by the *UHURU*-satellite (3U 1258−61; Giacconi et al., 1972). Due to the discovery of a Be companion star of spectral type B6–9 (Mason et al., 1978), it is classified as BeXRB at a distance of 2.4(5) kpc (Parkes et al., 1980). The outburst spacing of 132.5(4) d found by Priedhorsky & Terrell (1983) is likely the orbital period of the binary. Due to the ∼272 s pulsations of the neutron star (McClintock et al., 1977), Sugizaki et al. (2015b) were able to derive the orbital parameters of the system using data from *Fermi*-GBM, *RXTE*-PCA, and MAXI-GSC, which confirmed the orbital period. Recently, Yamamoto et al. (2011) discovered a CRSF around 54 keV in the spectrum of GX 304−1, which Klochkov et al. (2012) found to correlate positively with the source's flux between 48 and 55 keV.

5.2.1 Data extraction and spectral continuum models

After nearly 30 years of quiescence GX 304−1 became active in 2008 as detected with *INTEGRAL*-IBIS (Manousakis et al., 2008). The source then underwent several type I outbursts until 2012 October, the first one revealed in 2009 March, which were separated by the orbital period (see Fig. 5.18). The last two outbursts were rare "double-peaked" outbursts. The first four outbursts of this series were monitored with *RXTE*, for most parts of the outburst decays.

We have extracted spectra from all 72 *RXTE* observations of GX 304−1 (see Table F.4 for a list). The following Section briefly summarizes the data extraction from PCA- and HEXTE, which can be found in detail in Rothschild et al. (2016, in prep.). The PCA- and HEXTE spectra were extracted using `HEASOFT` v6.16 and the reduction pipelines by Wilms et al. (2006). Here, data from the top layer of PCU2 was used. Due to the peak flux of $\gtrsim 1$ Crab during three of the four observed outbursts (see Fig. 5.18), the electron ratio threshold had to be increased to 0.5 for the GTI creation as the PCU count rates were $> 1000\,\mathrm{cts\,s^{-1}}$. As the electron ratio is usually a veto for incoming background electrons, we checked its time evolution and did not find any features apart from modulations by the source, i.e., the pulse profile. No channel grouping was applied to the extracted

spectra, which were analyzed in the 3–60 keV energy range. For a few observations (see Table F.4) we have added 0.5% systematics to data below 15 keV and 1% for higher energies. Furthermore, a narrow negative Gaussian fixed at 3.88 keV was added to the spectral model to account for calibration uncertainties at the Xenon L-edge. HEXTE on-source data from cluster A was used in combination with the background measured 1.5° off-source by cluster B. Since the actual X-ray backgrounds of both clusters are slightly different, the `HEXTEBACKEST` tool was used to estimate the background for cluster A from cluster B (Pottschmidt et al., 2006). Additionally, four narrow Gaussian shaped lines caused by detector background were found during a first investigation of the data. These lines fixed at 30.17, 39.04, 52.00, and 66.64 keV were added to the spectral model. The HEXTE spectra were restricted to energies between 20 and 100 keV during the spectral analysis.

We have applied three different continuum models to 69 of the 72 *RXTE* observations (avoiding exposure times shorter than the pulse period), which are defined as

$$M_{304,\mathrm{cutoffpl}} = \mathtt{tbnew} \times (\mathtt{cutoffpl} + \mathtt{bbody} + \mathtt{iron}) \times \mathtt{cyclabs} \quad , \tag{5.11}$$

$$M_{304,\mathrm{highecut}} = \mathtt{tbnew} \times (\mathtt{powerlaw} \times \mathtt{highecut} + \mathtt{iron}) \times \mathtt{cyclabs} \quad , \tag{5.12}$$

$$M_{304,\mathrm{npex}} = \mathtt{tbnew} \times (\mathtt{npex} + \mathtt{iron}) \times \mathtt{cyclabs} \quad , \tag{5.13}$$

where $\mathtt{iron} = \mathtt{gauss}_{\mathrm{FeK}\alpha} + \mathtt{gauss}_{\mathrm{FeK}\beta}$ accounts for the Kα and Kβ fluorescent emission lines of neutral iron. The line widths were fixed to 10 eV and their centroid energies to 6.4 and 7.056 keV, respectively. Furthermore, the flux of the FeKβ is set to 13% of the Kα flux. See Sect. 1.3.4 for the definition of the phenomenological models. During initial fits using the `highecut` model a narrow absorption feature around 10 keV was necessary for some observations. We interpreted this as the so-called "10 keV feature" typically found when using the `highecut` model (see, e.g., Coburn et al., 2002). It is fitted by a Gaussian with a fixed width of 10 eV and centroid energy of 10.5 keV. In the residuals for a few fits to the `cutoffpl` model a similar feature is present. Thus, we added this feature to all three models defined above for comparison reasons. In case of the `npex` continuum model the positive photon index was fixed to $\Gamma_2 = 2$. All models defined in Eqs. (5.11–5.13) include the CRSF around 54 keV described by the `cyclabs` model (see Eq. 1.50. Note that these models describe the source spectrum only, while further background and calibration features were taken into account during the fits. These were the Gaussians for the Xe L-edge, the four HEXTE background lines, two factors, b_{PCA} and b_{HEXTE}, allowing a slight scaling of the backgrounds of PCA and HEXTE, respectively, and a flux calibration constant, c_{HEXTE}, scaling the overall model for HEXTE with respect to PCA.

The number of free broad-band continuum parameters are 5 for the `cutoffpl`+`bbody` (Γ, E_{fold}, F_{PL}, kT, F_{BB}), 4 for the `highecut` (Γ, E_{fold}, E_{cut}, F_{PL}), and 4 for the `npex` model ($\Gamma_1 \equiv \Gamma$, E_{fold}, $F_{\mathrm{PL},1}$, $F_{\mathrm{PL},2}$). Further parameters are the absorption column density, N_{H}, the CRSF parameters E_{cyc}, W_{cyc}, and τ_{cyc}, the iron line flux $F_{\mathrm{Fe\,K}\alpha}$, the 10 keV feature's flux, the four fluxes for the HEXTE background lines, the flux within the Xe L-edge, the cross-calibration constant, c_{HEXTE}, and the background scaling factors, b_{PCA} and b_{HEXTE}. Thus, the total number of free parameters are 19, 18, and 18 for the models defined in Eq. (5.11), (5.12), and (5.13), respectively. In order to reduce the degrees of freedom and to avoid strong parameter degeneracies, we applied the following fit strategy to the 69 *RXTE*-spectra:

- first, we performed a fit of the full model except for the 10 keV feature
- then repeated the fit with the 10 keV feature included
- and finally removed this feature again if the improvement in χ^2 was smaller than 10, removed the CRSF if its depth, τ, was consistent with zero on the 90% confidence

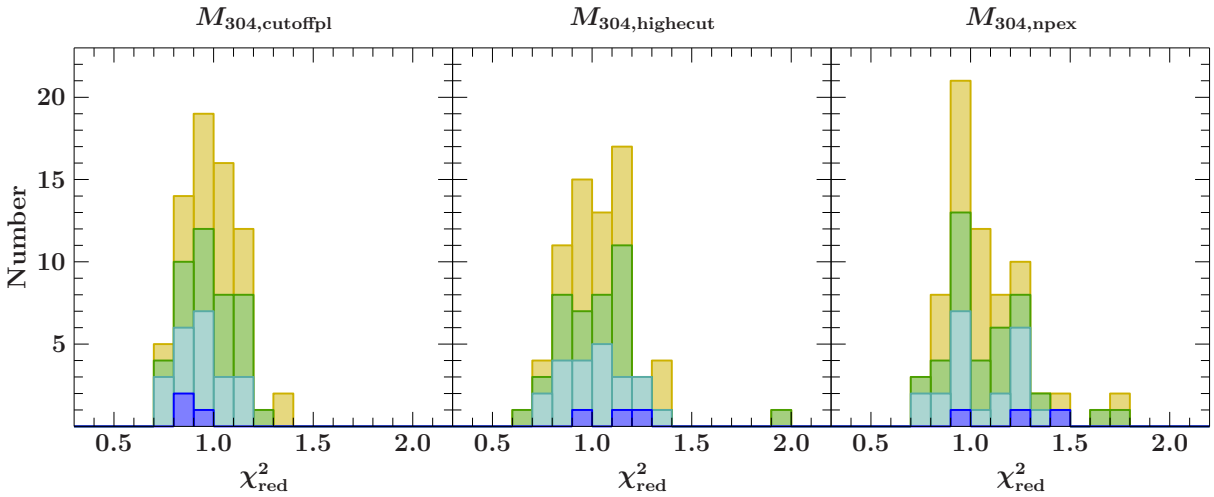

Figure 5.19: Histogram of all 69 χ^2_{red}-values for each model defined in Eqs. (5.11–5.13). The contribution to the histogram from the observations during the outburst in 2010 March is shown in dark blue, in August 2010 in light blue, in 2010 December in green, and in 2011 April in yellow (see also Fig. 5.18).

level, and removed the negative Gaussian modeling the Xe L-edge if its flux was consistent with zero as well

Figure 5.19 shows the χ^2_{red}-histogram of the best-fits for each model. We find that the median χ^2_{red} for all models is close to unity. The distribution for the `cutoffpl+bbody` continuum model ($M_{304,\mathrm{cutoffpl}}$) is the sharpest one compared to the other models, which we attribute to the higher number of continuum parameters compared to the other models. The `npex` model ($M_{304,\mathrm{npex}}$) results in the broadest distribution with a few $\chi^2_{\mathrm{red}} > 1.5$. There is one outlier with a $\chi^2_{\mathrm{red}} \sim 2$ using the `highecut` model ($M_{304,\mathrm{highecut}}$).

5.2.2 The continuum as a function of luminosity

Investigating the final best-fit parameters shows that the continuum, the CRSF, and the iron line are strongly correlated with the source's overall flux. In particular, there is no apparent difference between the four outbursts[14] covered and no hysteresis effects. This is very similar to our findings in GRO J1008−57, its spectral shape depends on the source's flux only. Due to the high number of free parameters the uncertainties for the parameters of GX 304−1 are very large especially at lower source fluxes. As the parameter seems to depend only on flux, we binned the parameters into flux histograms, H_i, with the flux bin i. The value, H_i, and uncertainty, ΔH_i, in each bin is calculated by the mean of all parameters, p_i, for which corresponding observations fall into this flux bin, weighted by the parameter uncertainties, Δp_i, after (Bevington & Robinson, 2003)

$$H_i = \frac{\sum p_i w_i}{\sum w_i} \quad \text{and} \quad \Delta H_i = \sqrt{\frac{1}{\sum w_i}} \quad , \tag{5.14}$$

with the weights $w_i = 1/\Delta p_i^2$. Figure 5.20 shows the resulting histograms for the continuum parameters except the flux of the black body, F_{BB}, for the `cutoffpl+bbody` model and the flux of the positive power-law, $F_{\mathrm{PL},2}$, in case of the `npex` model. As can be seen, all parameters nicely correlated with the overall unabsorbed flux of the source. The photon index, Γ, and the folding energy, E_{fold}, are systematically shifted between the different

[14] With the exception of the absorption column density, N_{H}, which shows a ∼3 d long excess in the 2011 May outburst. See Müller (2013) or Kühnel et al. (2016c, in prep.) for details.

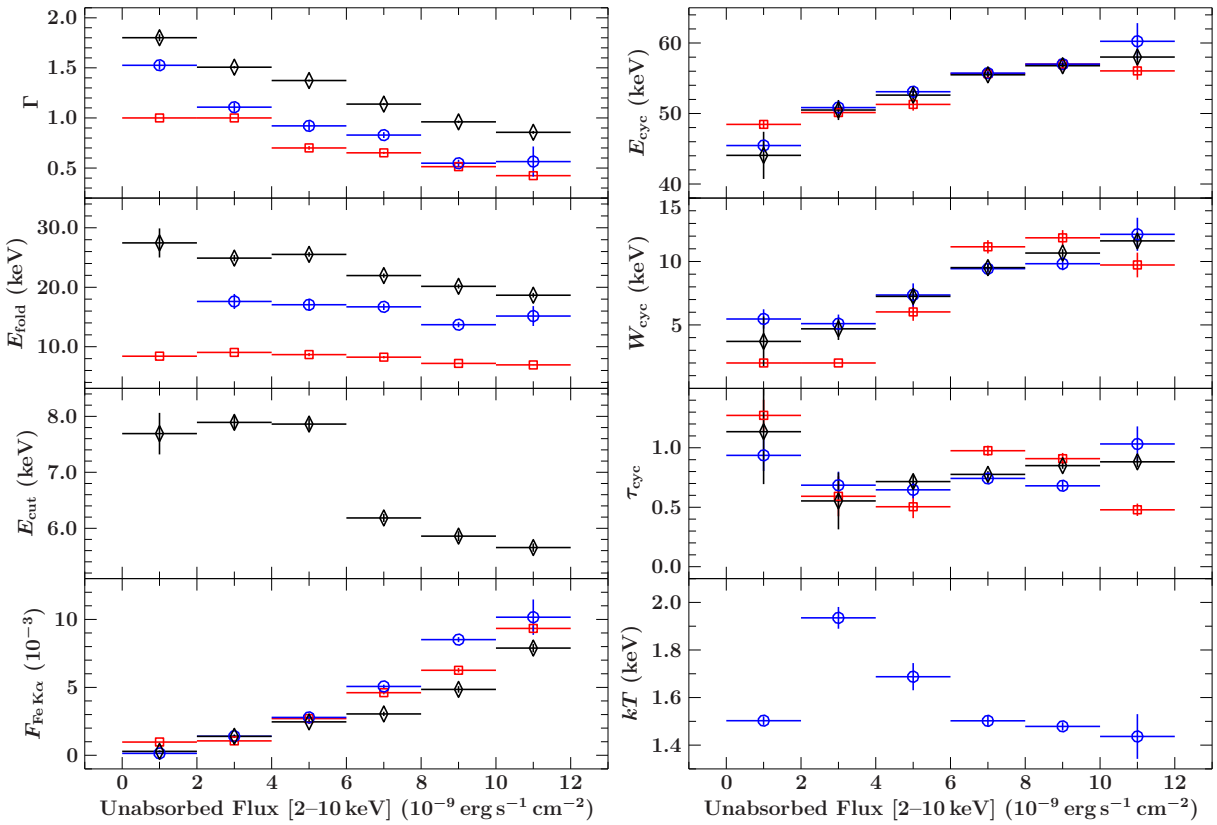

Figure 5.20: Evolution of some spectral parameters with the 2–10 keV unabsorbed flux of GX 304−1. The results are shown for the $M_{304,\rm cutoffpl}$- (blue circles; Eq. 5.11), $M_{304,\rm highecut}$- (black diamonds; Eq. 5.12), and $M_{304,\rm npex}$-model (red squares; Eq. 5.13). The parameters of the 69 analyzed observations have been sorted into a weighted flux histogram as described in the text. The iron line flux, $F_{\rm Fe\,K\alpha}$, is given in 10^{-3} photons s^{-1} cm^{-2}.

continuum models. For all models Γ decreased with increasing flux, i.e., the spectrum got harder. This has been detected in GRO J1008−57 as well (see Fig. 5.16). While the folding energy, $E_{\rm fold}$, decreased with flux in case of the `highecut` model, it stayed almost constant for the other models, which is consistent with GRO J1008−57 as well. Interestingly, the cut-off energy, $E_{\rm cut}$, changed abruptly from ∼8 down to ∼6 keV above a flux of 6×10^{-9} erg s^{-1} cm^{-2} in the `highecut` model. Neither the `cutoffpl`+bbody nor the `npex` model showed changes in their parameters at this flux level. While the iron line flux scaled perfectly with the source's flux and the values agreed between the `cutoffpl`+bbody and `npex` continuum, the fluxes were systematically lower using the `highecut` model again above 6×10^{-9} erg s^{-1} cm^{-2}. Whether there is a connection to the change in $E_{\rm cut}$ requires further investigation. The black body temperature, kT, showed an interesting evolution with the flux. While it stayed constant at $kT = 1.5$ for almost all fluxes, it was significantly higher at fluxes 2–6×10^{-9} erg s^{-1} cm^{-2}. The energy of the CRSF, $E_{\rm cyc}$, was positively correlated with the source's flux, ranging from 44 keV up to 59 keV in case of the `highecut` model. The energies derived using the other models agreed very well within the uncertainties. This confirms the result by Klochkov et al. (2012). Furthermore, the width, $W_{\rm cyc}$, of the CRSF increased with flux as well. Here, the `npex` continuum showed significant differences to the other two continuum models, which agree with each other. The same applies to the evolution of the CRSF's depth, $\tau_{\rm cyc}$, which showed only little evolution with flux around a mean value of $\tau_{\rm cyc}$∼0.9. That the `npex` continuum model can affect the parameters of the cyclotron line has been noticed by Müller et al. (2013), who analyzed *RXTE* observations of 4U 0115+63. The authors found

no correlation of the fundamental CRSF at 11 keV with flux, while Nakajima et al. (2006) found a strong anti-correlation using the `npex` continuum on the same data. This different behavior in the CRSF evolution for 4U 0115+63 on the choice of the phenomenological continuum model was confirmed by Boldin et al. (2013).

In conclusion, the preliminary results from an analysis of all GX 304−1's *RXTE* observations suggest a tight correlation of the source's spectral parameters with its flux. This applies to the evolution of the cyclotron line parameters as well. After Becker et al. (2012) the observed positive correlation with flux indicates that the source is accreting sub-critically. Apart from the evolution of E_{cut} in the `highecut` model, there is no sudden flux related change detected in the spectral evolution as we found evidence for in GRO J1008−57 (see Sect. 5.1.7). In order to check on the existence of such a change at very low fluxes further analyses are required. In particular, due to the high number of free fit parameters degeneracies might be present. Reducing the number of degrees of freedom by, e.g., performing a simultaneous fit of all spectra using global parameters during a forthcoming analysis might improve the accuracy and reliability of the GX 304−1's spectral evolution.

Chapter 6

Conclusions & Outlook

6.1 Shedding Light on Accretion Physics

6.1.1 Accretion Torques

In the present Ph.D. thesis, the orbits of several BeXRBs are derived based on the Doppler measurements of the neutron star's pulse periods (see Chapter 4). As the observed pulse period evolution is a combination of the Doppler shift by orbital motion and the intrinsic spin period evolution driven by angular momentum transfer (see Sect. 1.2.1 and 1.3.1, respectively), I have implemented the so-called torque model in Sect. 2.3.2. This model uses the angular momentum transfer theory by GL79 to calculate the intrinsic spin period evolution. Using the light curves from modern X-ray all-sky-monitors, such as *Swift*-BAT, as input allows us to disentangle the observed pulse period and to derive reliable orbital parameters.

The torque model was able to successfully explain the observed pulse period evolution of XTE J1946+274 (Sect. 4.1), RX J0520.5−6932 (Sect. 4.2), and XTE J1859+083 (Sect. 4.3). Thus, the angular momentum theory by **Ghosh & Lamb (1979a) is applicable for these sources**, which answers the general question 1 I raised in the beginning. Recently, Sugizaki et al. (2015b) and Takagi et al. (2016) applied a similar implementation of the theory by GL79 to GX 304−1 and 4U 1626−67, respectively, which confirms this conclusion. Furthermore, Sugizaki et al. (2015a) applied their implementation to a few sources with moderate success due to fixed orbital parameters. That means the intrinsic spin period evolution of a couple of sources is dominated by **angular momentum transfer, which is connected directly to the mass accretion rate** and, thus, to the observed source fluxes. However, distinguishing whether the neutron stars are accreting from a disk ($\alpha = 6/7$ in Eq. 1.32) or a stellar wind ($\alpha = 1$) was not possible for the sources analyzed here due to a degeneracy between these parameters.

The implementation of the angular momentum theory presented in Sect. 2.3.2 uses a coupling constant, b, called torque strength for the connection between the spin period derivative, $\dot{P}$, and the flux, F, of a source. Using this coupling constant and the distance to a source the spin-up at a certain luminosity can be calculated. As discussed in Sect. 5.1.7 calculating the true luminosity from an observed flux is rather complicated. Nevertheless, in order to compare the spin-ups of the sources analyzed here quantitatively, the torque strengths listed in Tables 4.1, 4.2, and 4.3 and the spin-period derivative of GRO J1008−57 in Table 4.4 are calculated for a luminosity of $L = 10^{37}\,\mathrm{erg\,s^{-1}}$. Therefor, the reference flux, F_{ref}, measured in *Swift*-BAT is converted into a physical flux (within 0.01 and 100 keV) assuming a `cutoffpl` model with typical parameters observed for accreting neutron stars ($\Gamma = 1$, $E_{\mathrm{fold}} = 15\,\mathrm{keV}$; see Chapter 5) and the response matrix of BAT as available in the calibration database (CALDB; swbresponse20041006v001.rsp). Having calculated the luminosity, L_{ref}, from the physical reference flux assuming isotropic emission and the

Table 6.1: The spin-up rates, $\dot{P}_{37}$, at a bolometric luminosity of $L = 10^{37}\,\mathrm{erg\,s^{-1}}$ for the sources analyzed in the present thesis. The uncertainties include the distance uncertainties.

source	distance	$\dot{P}_{37}$ at $L = 10^{37}\,\mathrm{erg\,s^{-1}}$
XTE J1946+274	$9(1)\,\mathrm{kpc}^a$	$-8.0^{+1.4}_{-1.8} \times 10^{-10}\,\mathrm{s\,s^{-1}}$
RX J0520.5−6932	$51.5(1.2)\,\mathrm{kpc}^b$	$-1.36^{+0.06}_{-0.06} \times 10^{-10}\,\mathrm{s\,s^{-1}}$
XTE J1859+083	5.8–$18.3\,\mathrm{kpc}^c$	$-4.8^{+2.5}_{-12.1} \times 10^{-10}\,\mathrm{s\,s^{-1}}$
GRO J1008−57	$5.8(5)\,\mathrm{kpc}^d$	$-189^{+25}_{-32} \times 10^{-10}\,\mathrm{s\,s^{-1}}$

Notes. [a] Verrecchia et al. (2002) [b] Inno et al. (2013) [c] as estimated in Sect. 4.3.3 [d] Riquelme et al. (2012)

distance to the source, the spin-up rate, $\dot{P}_{37}$, at $L = 10^{37}\,\mathrm{erg\,s^{-1}}$ is found using Eq. (1.32),

$$\dot{P}_{37} = b \left(\frac{10^{37}\,\mathrm{erg\,s^{-1}}}{L_{\mathrm{ref}}} \right)^{\alpha} \quad , \tag{6.1}$$

with $\alpha = 6/7$ for disk-accretion. Table 6.1 lists the results for the four sources analyzed here. The derived spin-up rates range from $-10^{10}\,\mathrm{s\,s^{-1}}$ for RX J0520.5−6932 up to $-2 \times 10^{-8}\,\mathrm{s\,s^{-1}}$ for GRO J1008−57.

As these values correspond to a fixed luminosity and, thus, mass accretion rate, the difference has to be caused by the parameters of the neutron star or accretion geometry. The dependencies of the spin-up rate, $\dot{P}$, on the neutron star parameters can be seen from Eq. (1.30) for disk accretion. Apart from the luminosity, L_{37}, and the spin period, P, the spin-up depends on the magnetic moment, μ_{30}, the dimensionless accretion torque, $n(\omega_{\mathrm{s}})$ with the fastness parameter ω_{s}, and the structure function, $S_1(M)$. If a dipole magnetic field is assumed then $\mu_{30} = \frac{1}{2} B R^3 / 10^{30}\,\mathrm{G\,cm^3}$. After Eq. (10) of GL79 the accretion torque can be approximated within 5% to

$$n(\omega_{\mathrm{s}}) \approx 1.39(1 - \omega_{\mathrm{s}}(4.03(1 - \omega_{\mathrm{s}})^{0.173} - 0.878))(1 - \omega_{\mathrm{s}})^{-1} \quad , \tag{6.2}$$

for a fastness of $0 \leq \omega_{\mathrm{s}} \leq 0.9$. This can be calculated after Eq. (16) of GL79 as

$$\omega_{\mathrm{s}} = 1.35 {\mu_{30}}^{6/7} S_2(M) (P {L_{37}}^{3/7})^{-1} \quad , \tag{6.3}$$

with a second structure function (Eq. 18 in GL79)

$$S_2(M) = {R_6}^{-3/7} (M/\mathrm{M}_{\odot})^{-2/7} \quad . \tag{6.4}$$

Finally, the first structure function is given by Eq. (17) in GL79

$$S_1(M) = {R_6}^{6/7} (M/\mathrm{M}_{\odot})^{-3/7} {I_{45}}^{-1} \quad , \tag{6.5}$$

with the moment of inertia, I_{45}, of the neutron star. If the neutron star can be approximated as a sphere then $I_{45} = \frac{2}{5} M R^2 / 10^{45}\,\mathrm{g\,cm^2}$. In summary the spin-up rate, $\dot{P}$, for disk-accretion depends on 4 basic properties of the neutron star: mass, M, radius, R, magnetic field strength, B, and spin period, P. It further depends on its luminosity, L_{37}, which is connected to the observed flux and distance, d, to the source.

Fig. 6.1 shows the derived spin-up rates, $\dot{P}_{37}$, for a luminosity of $L = 10^{36}\,\mathrm{erg\,s^{-1}}$ versus the measured spin-periods, P, for the four sources listed in Table 6.1. To compare the data with the theory by (Ghosh & Lamb, 1979a), the theoretical dependency of $\dot{P}_{37}$ on P in case of accretion from a disk is included as calculated by Eq 1.30 and Eqs. (6.2–6.5). For standard neutron star parameters as listed in Table 1.1 the spin-up rates for all sources

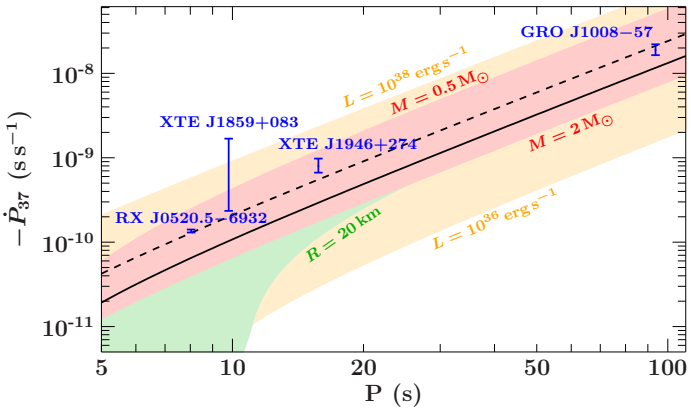

Figure 6.1: Derived spin-up rates, $\dot{P}$, at $L = 10^{37}\,\mathrm{erg\,s^{-1}}$ over the observed spin-periods, P, for the four sources analyzed in this thesis. The black curve is the theoretical prediction for disk-accretion after Ghosh & Lamb (1979a) using canonical neutron star parameters. The colored regions show the dependencies of this prediction on these parameters.

are systematically shifted to higher values compared to the theoretical prediction (black curve in Fig. 6.1). However, the data seem to follow the slope of the prediction. Reducing the mass, M (red region), or increasing the actual luminosity, L (yellow region) would result in consistency with the theory. The latter means that the pulsar's luminosity is underestimated which is possible as isotropic emission is assumed, but this is not the case for an accreting neutron star. The luminosity was calculated here assuming the same arbitrary spectral shape for each source, which leads to further shifts in the actual luminosity. Indeed, the data matches very well once the luminosity is increased by a factor of 2 (dashed line in Fig. 6.1). Interestingly, the spin-up rate of XTE J1859+083 is consistent with the apparent dependency on the spin period for a distance of 18.3 kpc (the lower confidence level of the corresponding datapoint). This would support the idea of a luminous type II outburst with a luminosity close to $10^{38}\,\mathrm{erg\,s^{-1}}$ as argued in Sect. 4.3.3.

As presented in this thesis, the spin period evolution of several BeXRBs follows the relationship between the spin-up rate and the luminosity of the source after the theory by GL79. However, a more sophisticated calculation of the expected spin-up using the canonical neutron star parameters leads to a systematic shift in the data as shown in Fig. 6.1. Thus, the observed spin-up rates are not in perfect agreement with the theoretically calculated values. Further investigation is required to answer whether the reason is an insufficient accretion torque theory or different neutron star parameters, such as the mass or luminosity, for the sources analyzed here.

6.1.2 The Accretion Column

In Sections 5.1 and 5.2 all *RXTE* observations of the BeXRBs GRO J1008−57 and GX 304−1 were analyzed, respectively. In order to investigate their spectral evolution with flux the same model has to be applied to all datasets. Furthermore, parameter degeneracies introduced due to the large number of fit parameters of the phenomenological models need to be taken into account. Using functions to handle this large amount of data and, in particular, performing simultaneous fits, which have been implemented into *ISIS* (see Sect. 2.4), I was able to reveal the spectral evolution of the sources over large orders of magnitude in flux with high precision.

For GRO J1008−57 and GX 304−1 it was found that their spectral parameters show tight correlations with the overall X-ray flux. In particular, the dependencies of the parameters on the flux do not change between the outbursts. This implies that the **spectral shape is determined only by the mass accretion rate** for an individual source, which is a remarkable result and answers general question 2. In GRO J1008−57, we were even able to determine flux independent parameters of the used phenomenological

model and provide functions for the flux dependent parameters (see Sect. 5.1.6).

In GRO J1008−57 only two spectral parameters are functions of the mass accretion rate, which are the photon index, Γ, and the flux of the additional black body, $F_{\rm PL}$. As self-consistent models for the X-ray spectra of accreting neutron stars are still under development an interpretation of the evolution of these phenomenological parameters is challenging. Recent work by Farinelli et al. (2012, 2016) solved the radiative transfer equations developed by BW07 (see Sect. 1.3.2) in order to fit the observational data of a few accreting neutron stars. Their implementation into *XSPEC* uses the mass accretion rate, $\dot{M}$, the electron temperature, $kT_{\rm e}$, the magnetic field strength, B, and the radius and height of the accretion column, r_0 and H, respectively. Finally, a normalization factor, $N_{\rm comp}$, is proportional to the source's distance and emission geometry including light bending effects[1]. This results in 6 parameters in total. From these parameters B and $N_{\rm comp}$ are not expected to vary with flux or even within a few decades. As found by Farinelli et al. (2016) the electron temperature, $kT_{\rm e}$, seems to scale with the magnetic field strength and determines the value of exponential roll-over, which is comparable to the folding energy, $E_{\rm fold}$, in the `cutoffpl` or `highecut` model (see Eqs. 1.45 and 1.46). Indeed, we find that all *RXTE* spectra of GRO J1008−57 are consistent with a constant folding energy, $E_{\rm fold}$ (see Table 5.2). As the mass accretion rate, $\dot{M}$, is proportional to the observed source's flux (combine Eq. 1.2 with 1.5), the only remaining parameters which can vary with flux are the height of the accretion column, H, and its radius, r_0. How they are associated to the phenomenological parameters, Γ and $F_{\rm BB}$, requires further investigation. Postnov et al. (2015a) expects that the X-ray spectrum starts to harden as soon as the accretion column increases in height. As the photon index, Γ, in GRO J1008−57 decreases with increasing flux this results in a hardening of the spectra, might point to a connection between the column height, H, and Γ. In any case, the fact that Γ and $F_{\rm BB}$ are tightly correlated with the source's flux suggests that **the accretion column's height and radius dynamically depend on the mass accretion rate**.

As mentioned above the spectrum is expected to harden with increasing column height. This behavior sets in once the accretion column gets optically thick, i.e., a radiation-dominated shock forms (Postnov et al., 2015a). The photon index, Γ, is a phenomenological indicator for the hardness of the spectrum. Since Γ seems to be constant below a certain flux level in GRO J1008−57 while it starts to decrease for higher flux (see Fig. 5.16) this behavior could be interpreted as **observational evidence for a transition from an optically thin to optically thick accretion column**. After Becker et al. (2012) this transition occurs at the Coulomb breaking luminosity, $L_{\rm coul}$. However, the luminosity of GRO J1008−57, where the change in the evolution of Γ with flux occurs, is inconsistent with $L_{\rm coul}$, which is not a satisfying answer to general question 3. Solving this inconsistency requires further investigation.

6.2 Outlook: Still Unanswered Questions

In summary, the key driver for the spin period evolution *and* the spectral evolution with the source's flux is the mass accretion rate. This is an important finding as it establishes the need to investigate physically motivated questions in future studies, such as

- *Since the theory after Ghosh & Lamb (1979b) is able to explain the observed spin-period evolutions of BeXRBs, can we determine neutron star parameters from the results?*

[1] This should be in principle equal to the $g(E)$ factor introduced in Eq. (5.9).

To answer this question a model implementing a full and recent accretion torque theory, such as, e.g., Perna et al. (2006), should be applied to the observed pulse period evolutions. The fit parameters of such a model would include the neutron star's mass, radius, magnetic field strength, and distance (to calculate luminosities). Since uncertain orbital parameters can mimic a spin-up or -down, precise orbital solution are crucial to investigate the intrinsic spin period evolution[2].

- *How do the height and radius of the accretion column change with luminosity?*

  The BeXRBs GRO J1008−57 and GX 304−1 are ideal candidates to apply self-consistent models for the X-ray spectrum of accreting neutron stars due to a tight correlation of the spectral shape on the luminosity of these sources. The results of such data analyses would provide important input to understand the theory of accretion columns.

- *What happens with the accreted matter on the surface of the neutron star?*

  As the spectral shape of accreting neutron stars in Be-systems seems not to change between outbursts, the matter accreted in previous outbursts does not have any (detectable) influence. Thus, it cannot remain in the accretion column.

- *Can we observe transitions between certain accretion regimes in the spectral evolution of neutron stars?*

  These regimes have been proposed by Becker et al. (2012) to explain the different correlations of the CRSF's energy with flux as observed in several sources. To my knowledge, no transition between these regimes have been observed yet. In GRO J1008−57 there is evidence for a transition in its spectral evolution. Thus, it is important to detect similar behaviors in other accreting neutrons stars

- *Will BeXRBs become new calibration sources?*

  The accretion mechanism onto neutron stars with Be companions seems to be stable over time and is driven by the mass accretion rate only. Thus, the response of an X-ray detector could be calibrated once the spectral evolution of a source with its flux is precisely known. Some of these systems even feature regular outbursts, which would simplify scheduling calibration observations.

[2]This answers specific question 7.

Acknowledgments

Certainly, doing my Ph.D. thesis would not have been possible without my supervisor, Jörn Wilms. Well, as already pointed out by several people before me, the word "supervisor" is not appropriate for him. As he cares for his students more than any professor I can think of[3], the German term "Doktorvater" could probably be defined on his example. I am very grateful for his commitment, support of and trust in my work, scientific expertise he likes to share with people, and the opportunity to do my Ph.D. in his group in the first place. Finally, living together with my fiancé despite our different scientific careers would have been much more difficult without Jörn's comprehension.

The analyses I have performed would not have been possible without the excellently maintained computers, for which I thank the administrators of the Remeis observatory. Especially, Ingo Kreykenbohm spends a tremendous amount of energy to ensure the stability of the computing system. Thank you for not turning into the BOFH despite this frustrating and often unnoticed work, your enlightened discussions about neutron stars, your personal library, and for proofreading. Don't let the hammer fall in the rack!

Collaborating on the world wide level is an important aspect in science, which I appreciate and enjoy. Thanks to the MAGNET group for the great regular discussions — to Katja Pottschmidt for providing extremely valuable comments, ideas, and proofreading at all times — to Richard E. Rothschild for the great time at UCSD, the GX 304−1 project, and showing me prototype parts of HEXTE — to Mark H. Finger for his constructive comments about the torque model and collaboration on XTE J1946+274, RX J0520.5−6932, and XTE J1859+083 — to Diana M. Marcu for scientific discussions and our collaboration on XTE J1946+274 — to Silvia Martínez-Núñez and José Miguel Torrejón for the various discussions and time at the Universidad de Alicante, for the collaboration meetings at the ISSI, and our work on Vela X-1 — to Peter Kretschmar for his support and ideas around the Be outbursts project and inviting me to ESAC at Madrid — to Herrn Staubert for supporting the Hercules X-1 project and sharing his office with me during the week at IAAT — to Michael A. Nowak for inviting me to collaborate on 4U 2129+47 — to Carlo Ferrigno and Gabriele Schönherr for providing ideas and comments — to Pere Blay and Jakob Stierhof for our work on XTE J1859+083 — to Atsuo T. Okazaki for the instructive discussions about Be outbursts and our recently established collaboration — to Felix Fürst and Victoria Grinberg for their contribution, ideas, and comments to my pet-source GRO J1008−57 and for the fun during their time in Bamberg — to Ralf Ballhausen and Sebastian Falkner for proofreading and the plenty conversations about neutron stars, life, the universe, and everything — to Manfred Hanke for infecting me with his enthusiasm on *ISIS* a few years ago — to Thomas Dauser for his work as computer administrator and support with *ISIS* — to Fritz-Walter Schwarm for installing and maintaining the TORQUE Resource Manager at the Remeis observatory, for showing me how to play the guitar in the first place, and for the workouts.

Thank you, Macarena Sagredo, for improving the German's language skills in form of the ECAP English Services and for proofreading most of my thesis in such a short time. Furthermore, I am glad that you have decided to do your Master's thesis with me as unofficial supervisor and, thus, became a Kniggerian office mate with all the tics.

[3]Especially since my induced interaction with the Jörn-antiparticle.

Special thanks to my former office mate Sebastian Müller. He has helped me a lot during my first contact with X-ray data years ago, we have worked together in various projects from their beginnings until their successful publications, and he has played a significant part in the friendly and funny working atmosphere in Bamberg. I am very happy for our friendship and I am glad that you accepted to become my best man!

I am very thankful for the opportunity to do my Ph.D. at the Remeis observatory in Bamberg as it is one of the best places to work due to two facts. First, its shared department consisting of Jörn Wilms, Ulrich Heber, and Horst Drechsel successfully organizes and maintains this convenient place. However, this would not be possible without a powerful women in the background, Edith Day, the best secretary in the world. Secondly, all colleagues aid one another, organize regular social activities, and create a friendly atmosphere, for which I would like to especially thank my former and current office mates in the Kniggeroom, which are among others and those mentioned above — Christian Heuser for the jam sessions and the discussions about how to rescue the world — Eugenia Fink né Litzinger for keeping the coffee machine running, for proofreading, and for reliably organizing many activities; you are the (unfortunately often unappreciated) good heart of the observatory — Stephan Geier, Lew Classen, Thomas Kupfer, Dominik Hertel, and quasi-Kniggerian Eva Ziegerer. For the friendly atmosphere and activities, not only in Bamberg, I further like to thank, besides all people above, Michael Wille for our observing nights in the domes, the writing sessions, and the coffee breaks — Alex Markowitz and Christina Gräfe for the jam sessions at UCSD and Bamberg — Jérôme Rodriguez for the judo training in Paris.

Owing to Markus Kuster, I have started a career in high energy astrophysics in the first place during my time at the Technical University of Darmstadt. He has ignited my fascination by drawing a sketch of Hercules X-1 with its tear-shaped companion. Thank you, also for bringing me into contact with the Bamberg group!

My research is based on observations by *RXTE*, *Swift*, *Suzaku*, *XMM-Newton*, *Chandra*, *NuSTAR*, and *Fermi*. I thank the respective teams for their great job and, especially, for accepting and scheduling the proposed observations. Furthermore, I appreciate using SAO/NASA's Astrophysics Data System (ADS) and NASA's High Energy Astrophysics Science Archive Research Center (HEASARC) for literature and observation queries, respectively. I thank John Houck and John E. Davis for the development of *ISIS* and `S-Lang` including the `SLxfig` package, respectively.

Finally, I acknowledge support by the Bundesministerium für Wirtschaft und Technologie through Deutsches Zentrum für Luft- und Raumfahrt grants 50OR1113 and 50OR1207. Furthemore, I appreciate support by the Deutscher Akademischer Austauschdienst for the RISE project with Elisabeth Matthews and for the establishment of a collaboration with the X-ray group at the Universidad de Alicante.

Last but not least, I would like to thank my family, especially my parents, who always supported my education in all aspects. Without you all this would not have been possible.

Kerstin, although my work is often close to be "kranker Physikscheiss", I'm grateful that you proofread my thesis. Thank you for supporting me during my thesis and for always staying behind me. Regardless of how long and detailed I'll observe the universe, I won't find anyone more beautiful and lovelier than you are. I don't even want to try, because I've found you and I'm indefinitely happy that you've said "yes"!

Thanks Danke Grazie どうもありがとう ¡Gracias! Спасибо Merci

Appendix A
List of Acronyms

2MASS	*Two Micron All Sky Survey*
ACIS	*Advanced CCD Imaging Spectrometer*
	instrument onboard *Chandra* (see Sect. 3.2.5)
ARF	ancillary response function
ASM	*All Sky Monitor*
	instrument onboard *RXTE* (see Sect. 3.2.1)
BAT	*Burst Alert Telescope*
	instrument onboard *Swift* (see Sect. 3.2.2)
BATSE	*Burst and Transient Source Experiment*
	instrument onboard *CGRO*
BeXRB	Be X-ray binary
BeppoSAX	*Beppo Satellite per Astronomia X*
	Italian X-ray mission in honor of Giuseppe "Beppo" Occhialini
BGO	bismuth germanate
	used as scintillator cyrstals in, e.g., *Suzaku*-HXD
BW07	spectral model for accreting neutron stars by Becker & Wolff (2007)
CALDB	calibration database
CC	continuous clocking
	Chandra-ACIS readout mode
CCD	charge coupled device
CGRO	*Compton Gamma Ray Observatory*
	NASA X-ray mission
CM	center of mass
CP	change point
	refers to Bayesian blocks (see Sect. 4.5.1)
CRSF	cyclotron resonant scattering feature
	component in the X-ray spectra of accreting neutron stars (see Sect. 1.3.3)
DSS	*Digitized Sky Survey*
ECAP	Erlangen Centre for Astroparticle Physics
EoS	equation of state
EPIC-pn	European Photon Imaging Camera Positive-Negative CCD
	instrument onboard *XMM-Newton* (see Sect. 3.2.4)
EPIC-MOS	European Photon Imaging Camera Metal Oxide Semi-conductor
	instrument onboard *XMM-Newton* (see Sect. 3.2.4)
ESA	*European Space Agency*
FFT	fast Fourier transform
FPM	*Focal Plane Module*
	two identical instruments onboard *NuSTAR* (see Sect. 3.2.6)

FWHM full width at half maximum
GBM *Gamma-ray Burst Monitor*
instrument onboard *Fermi* (see Sect. 3.2.7)
GL79 accretion torque theory by Ghosh & Lamb (1979a,b)
GR general relativity
GRXE galactic ridge X-ray emission
GSC *Gas Slit Camera*
instrument onboard MAXI
GSO gadolinium silicate
used as scintillator cyrstals in, e.g., *Suzaku*-HXD
HETG *High Energy Transmission Gratings*
gratings used in *Chandra* (see Sect. 3.2.5)
HEXTE *High Energy X-ray Timing Experiment*
instrument onboard *RXTE* (see Sect. 3.2.1)
HMXB high mass X-ray binary
HRC *HighResolution Camera*
instrument onboard *Chandra* (see Sect. 3.2.5)
HRMA *High Resolution Mirror Assembly*
X-ray focusing device onboard *Chandra* (see Sect. 3.2.5)
HXD *Hard X-ray Detector*
instrument onboard *Suzaku* (see Sect. 3.2.3)
ISIS *Interactive Spectral Interpretation System*
ISM interstellar medium
JAXA *Japan Aerospace eXploration Agency*
JPL *Jet Propulsion Laboratory*
institution at the California Institute of Technology
LAT *Large Area Telescope*
instrument onboard *Fermi* (see Sect. 3.2.7)
LETG *Low Energy Transmission Gratings*
gratings used in *Chandra* (see Sect. 3.2.5)
LMC Large Margellanic Cloud
LMXB low mass X-ray binary
MAXI *Monitor of All-sky X-ray Image*
X-ray instrument assembled at the International Space Station
MJD Modified Julian date
MW Milky Way
NASA *National Aeronautics and Space Administration*
NPEX Negative Positive power law EXponential
phenomenological continuum model (see Eq. 1.48)
NuSTAR *Nuclear Spectroscopic Telescope Array*
X-ray mission (see Sect. 3.2.6)
ObsID observation identifier
OGLE *Optical Gravitational Lensing Experiment*

OSSE	*Oriented Scintillation Spectrometer Experiment*
	instrument onboard *CGRO*
PC	photon counting
	Swift-XRT readout mode
PCA	*Proportional Counter Array*
	array of instruments onboard *RXTE* (see Sect. 3.2.1)
PCU	*Proportional Counter Unit*
	five identical instruments onboard *RXTE* (see Sect. 3.2.1)
PIN	PIN
	instrument as part of the HXD onboard *Suzaku* (see Sect. 3.2.3)
PNS	proto neutron star
PSD	power spectral density
PWN	pulsar wind nebular
QCD	quantum chromodynamics
RGS	Reflection Grating Spectrometers
	instrument onboard *XMM-Newton* (see Sect. 3.2.4)
RIAF	radiatively inefficient accretion flows
RXTE	*Rossi X-ray Timing Explorer*
	NASA X-ray mission (see Sect. 3.2.1)
RMF	redistribution matrix function
S/N	signal to noise ratio
SMC	Small Margellanic Cloud
SN	supernova explosion
SNR	supernova remnant
TE	timed exposure
	Chandra-ACIS readout mode
TP	tangent plane of the asky
ToA	(pulse) times of arrival
USNO	*United States Naval Observatory*
UVOT	*UV/Optical Telescope*
	instrument onboard *Swift* (see Sect. 3.2.2)
WFC	*Wide Field Camera*
	instrument onboard *BeppoSAX*
WT	windowed timing
	Swift-XRT readout mode (see Sect. 3.2.2)
XIS	*X-ray Imaging Spectrometer*
	instrument onboard *Suzaku* (see Sect. 3.2.3)
XMM-Newton	X-ray Multi-Mirror Mission
	ESA X-ray mission (see Sect. 3.2.4)
XRS	*X-ray Spectrometer*
	instrument onboard *Suzaku* (see Sect. 3.2.3)
XRT	*X-ray Telescope*
	instrument onboard *Swift* (see Sect. 3.2.2)
	X-ray focusing device onboard *Suzaku* (see Sect. 3.2.3)
XSPEC	*X-Ray Spectral Fitting Package*

Appendix B

Position of L_1

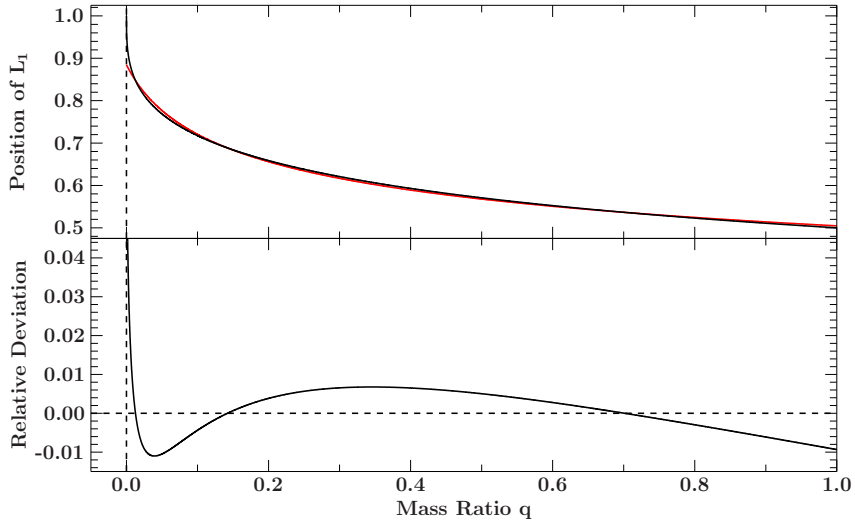

Figure B.1: Position of the first Lagrangian point L_1 in units of the binary separation as a function of mass ratio q (upper panel). The black line is the result of a numerical calculation of its position after Eq. (1.11). The red line is a fit of this result to $a(q+b)^c$, which gives $a = 0.509$, $b = 0.048$, and $c = -0.182$. The relative deviation of the fit to the numerical position is shown in the lower panel.

Appendix C

Estimating $a \sin i$ by eye

The observed, Doppler shifted pulse period after Eq. (1.17) is

$$P_{\mathrm{obs}}(t) = P(t)\left(1 - \frac{v(t)}{c}\right)$$

If we assume that the intrinsic spin period, $P(t)$, stays constant at P the difference between the maximum and minimum observed pulse period, ΔP, is given by

$$\Delta P = P\left(\frac{v_{\mathrm{max}}}{c} - \frac{v_{\mathrm{min}}}{c}\right)$$

where v_{max} and v_{min} are the maximum and minimum radial velocities. From its calculation after Eq. (1.18)

$$v(t) = \frac{2\pi a \sin i}{P_{\mathrm{orb}}\sqrt{(1-e)(1+e)}}\left(\cos(\theta+\omega) + e\cos(\omega)\right)$$

and assuming that $e \ll 1$ follows

$$\Delta P = P\frac{4\pi a \sin i}{cP_{\mathrm{orb}}}$$

Solving for the projected semi-major axis leads to

$$\frac{a\sin i}{c} = \frac{\Delta P P_{\mathrm{orb}}}{4\pi P}$$

To express $a \sin i$ in units of lt-s based on P_{orb} in days, P in seconds, and ΔP in ms, we end up with

$$a \sin i \approx 7\,\mathrm{lt\text{-}s}\left(\frac{\Delta P}{0.001\,\mathrm{s}}\right)\left(\frac{P_{\mathrm{orb}}}{1\,\mathrm{d}}\right)\left(\frac{1\,\mathrm{s}}{P}\right)$$

with an accuracy not better than 2% due to rounding and neglecting the eccentricity.

Appendix D

The Torque Model in *ISIS*

To use the implemented torque model in *ISIS* (see Sect. 2.3.2), the user needs to define the measured pulse period evolution using the `define_counts` function:

```
id = define_counts(
  time, make_hi_grid(time), periods, uncertainties
);
```

with the `periods` and their `uncertainties` in seconds given over `time` in MJD. The returned `id` is the identifier of the newly created dataset. Since the uncertainties are usually smaller than one second the `Mininum_Stat_Err` variable, which defines the smallest uncertainty allowed and is set to one (count) by default, has to be set accordingly. To evaluate the torque model the observed flux evolution, e.g., a light curve needs to be assigned as metadata information to the defined dataset containing the pulse period measurements:

```
set_dataset_metadata(id, struct {
  time = Double_Type[], flux = Double_Type[],
  eps = Double_Type, maxiter = Integer_Type
});
```

Here, `id` is the dataset ID, which is returned by `define_counts`. The `time` and `flux` fields correspond to the light curve given in MJD and an arbitrary flux unit, respectively. The optional field `eps` defines the convergence criteria of the iterative integration, which is set to the smallest numerical precision by default (`DOUBLE_EPSILON`). The maximum number of allowed iterations is defined by the optional `maxiter` field and set to ten by default. Afterwards, the torque model is set by

```
fit_fun("pulsarorbit");
```

and all usual *ISIS*-function for fitting and modifying the model parameters can be used. All parameters of the torque model are summarized in Table 2.2.

The measured flux evolution, $F(t)$, usually contains uncertainties as well. However, since it is used to calculate the modeled pulse period evolution, the uncertainties of the flux evolution propagate into the model. Thus, the model itself is uncertain. There are three possible ways to take these additional uncertainties in the final parameter uncertainties into account:

a) investigation of the changes of the model once the input flux evolution is randomized within its uncertainties by Monte Carlo simulations

b) error propagation of Eq. (2.24) and the resulting uncertainties are added directly to the fit-statistics

c) same as in a) but the distribution of the resulting fit-parameters is investigated

All analyses presented in Chapter 4 follow the Monte Carlo approach briefly described in a). A detailed description of this method is shown on the example of XTE J1946+274 in Sect. 4.1. For the same source, a proof of concept for the error propagation of the differential equation after b) is given, since this method was under development during the time this thesis was written.

Appendix E

ISIS Functions for Simultaneous Fits

In the following the implementation and handling of a simultaneous into *ISIS* described briefly. A full documentation is available by using the `help`-qualifier of a certain function and in the source code of the simultaneous fit package[1]. See Sect. 2.4 for a general description of a simultaneous fit and its terminology.

In principle, *ISIS* allows to load in as many datasets, e.g. spectra, as the memory of the machine allows. The model defined by the `fit_fun`-function is then evaluated for each dataset. Because the model is a string, which *ISIS* needs to interpret, it may contain further functions or variables.

Each model component, which is added to the string, is a function itself. To allow multiple instances of the same component, an integer is appended to its name. For instance, to realize the `NPEX`-model in *ISIS* (see Eq. 1.48) two cut-off power-laws are added to the model string, "`cutoffpl(1) + cutoffpl(2)`", which folding energies, E_{fold} (see Eq. 1.45), are tied together to have the same value.

One of the most useful variables within the model string is called `Isis_Active_Dataset`. Its value is set to the dataset ID, for which the model is currently evaluated. If the integer representing a component's instance is replaced by this variable, there will be the same number of instances of this particular component as datasets are defined. A simple application are detector calibration constants, which are realized by a multiplication of the continuum model with a parameter via "`constant(Isis_Active_Dataset)*...`". This is the key ingredient to perform a simultaneous fit in *ISIS*: each component in the model is appended by `Isis_Active_Dataset` such that all datasets have their own sets of parameters.

However, the parameters of the datasets defining a datagroup have to be tied together to be its group parameters. This tasks requires a careful handling of the user in order not to, e.g., tie wrong parameters. This has to be done for each datagroup, which is complicated further since each datagroup might consist of a different number of datasets. To handle this issues in a user-friendly and time-saving way, the following functions implemented into the *ISISscripts*[2] define and handle a simultaneous fit.

simultaneous_fit() This function initializes and returns a structure with all implemented functions handling the simultaneous fit. Furthermore, it contains the necessary informations needed internally, such as the definition of the datagroups and the corresponding lists of group and global parameters. In order to call the available functions the returned structure has to be assigned to a variable and then accessed in the same way as, e.g., the Xfig-objects of the `SLXfig` module. This solution was chosen to be able to use the same function names as already available in *ISIS*, like `set_par` (see below).

The descriptions of the functions below assume that they are called via the object assigned to the simultaneous fit structure, e.g., `simfit.function_name()`.

[1] http://www.sternwarte.uni-erlangen.de/git.public/?p=isisscripts;a=blob_plain;f=src/data/simultaneous_fit.sl;hb=HEAD

[2] The source code of all provided functions is available at http://www.sternwarte.uni-erlangen.de/git.public/?p=isisscripts;a=blob_plain;f=src/data/simultaneous_fit.sl;hb=HEAD

add_data(String_Type[] or Struct_Type[]) This function is used to define a new datagroup and to load the data into *ISIS*. It accepts a single filename to a spectrum or a structure containing another type of data. To load more datasets into a datagroup an array of filenames or structures have to be passed to the function.

fit_fun(String_Type) Like the internal *ISIS* function of the same name, the model gets defined by the given string. As addition, however, a placeholder in form of the percent-sign (%) for the `Isis_Active_Dataset`-variable is implemented. In more detail, actually, it should be used as a component's instance, e.g., `powerlaw(%)`. Then, the function internally adds the parameters of the power-law to the list of group parameters for each datagroup. Furthermore, it ties the parameters of all datasets within the group to those of its first dataset (because each dataset actually gets one set of parameters due to the use of `Isis_Active_Dataset`. Of course, the usual numeric expressions such as "(%+100)" can be used as the component's instance to allow multiple instances within the model.

set_par(String_Type) With the same usage as the corresponding function in *ISIS* a parameter can be set, with the addition that the %-placeholder as described above can be used in the parameter name. In that way, e.g., starting values for a certain group parameter can be set to all groups.

set_par_fun(String_Type, String_Type) Similar to the corresponding *ISIS* function, this function allows to define the value of a specific parameter to be calculated after the second given string, which can be understood as the parameter's function. Here, the name of the parameter may contain the %-placeholder again. The parameter's function can be of any complexity and may contain further parameter names. In particular, if it is equal to the name of a parameter, it will be interpreted to be a global parameter from now on. For example, the call `set_par_fun("cutoffpl(%).HighECut", "cutoffpl(1).HighECut")` ties the folding energies of all datagroups together, technically to the parameter of the first dataset. From now on, the folding energy is a global parameter and removed from the internal list of group parameters. It is also possible to implement more complex dependencies. For instance, the cyclotron line energy can be set to a linear function of the flux, such that its coefficients are the actual parameters to be fitted instead of the line energy of each datagroup.

set_global(String_Type), unset_global(String_Type) To simplify the handling of global parameters, the given group parameter name, e.g., `cutoffpl(%).HighECut`, is set (or unset) to be a global parameter using the `set_par_fun` function as explained above.

list_global(), list_groups([Integer_Type]) Lists the global/group parameters in the format as known from *ISIS*. In case of the group parameters the number of the datagroup can be provided optionally.

fit_global(), fit_groups([Integer_Type]) The runtime of the known `fit_counts`command in *ISIS*, which performs a fit of all parameters to the loaded datasets, is dramatically increased in case of a simultaneous fit with many datagroups. Thus, `fit_global` uses the internal information to perform a fit of the global parameters only, during which all datasets are taken into account. On the other hand, `fit_groups` excludes all datasets from the fit except those forming the datagroup of interest. Consequently, the corresponding

group parameters are fitted only, while the global parameters are kept fix. If a number of a specific datagroup is omitted all datagroups are fitted sequentially.

fit_smart() Because the global parameters most probably influence the group parameters, the above functions to speed up a simultaneous fit do not find the final best-fit. In good approximation, `fit_smart` alternates between fitting the group and the global parameters until the change in the quality of the fit, $\Delta\chi^2$, is below a certain threshold or until the maximum number of iterations is reached. As early applications have shown, the best-fit found using this function can still be worse by some percent in chi^2 than using the usual `fit_counts`, but the runtime is decreased significantly.

group_stats() As solution to the issue of missing failed fits of some datagroups (see Sect. 2.4.2) this function prints a histogram of the χ^2_{red}-values of all datagroups. To identify the datagroups with high a χ^2_{red}, the function returns an array with the number of datagroups sorted by their χ^2_{red}-values, beginning with the worst.

filter_groups([Integer_Type or String_Type]) Another way to identify failed fits is to call this function, which returns the number of the datagroup with the worst χ^2_{red} if no argument is provided. If an integer, n, is given an array of the worst n datagroups in terms of their fit statistic is returned. The optional string allows to apply more complex filters, such as returning the datagroups in a certain range of χ^2_{red}.

Appendix F

Summary of Observations and Data

Table F.1: X-ray observations in chronological order used for the timing analysis of XTE J1946+274 as presented in Sect. 4.1. The exposure times and start dates of the *RXTE* and *Swift* observations correspond to those given in Müller et al. (2012).

Satellite	Instrument	ObsID	Start (MJD)	Exposure (s)
RXTE	PCA	95032-12-01-00	55367.12	1584
RXTE	PCA	95032-12-01-01	55367.18	1408
RXTE	PCA	95032-12-01-02	55368.69	4080
RXTE	PCA	95032-12-01-03	55371.74	2880
RXTE	PCA	95032-12-02-00	55373.50	5776
RXTE	PCA	95032-12-02-03	55375.14	2800
RXTE	PCA	95032-12-02-01	55375.66	3184
RXTE	PCA	95032-12-02-02	55377.62	3200
RXTE	PCA	95032-12-03-00	55380.89	2000
RXTE	PCA	95032-12-03-01	55380.96	3056
RXTE	PCA	95032-12-03-02	55382.92	6368
RXTE	PCA	95032-12-03-03	55384.48	5872
RXTE	PCA	95032-12-04-00	55387.03	6144
RXTE	PCA	95032-12-04-01	55388.73	3184
RXTE	PCA	95032-12-04-02	55390.95	3200
RXTE	PCA	95032-12-05-00	55393.77	3248
RXTE	PCA	95032-12-05-01	55393.83	1392
Suzaku	PIN	405041010	55480.91	44123
RXTE	PCA	95032-12-06-02	55523.19	2640
RXTE	PCA	95032-12-06-01	55524.17	3200
RXTE	PCA	95032-12-06-00	55525.15	1392
RXTE	PCA	95032-12-07-00	55526.54	2000
Swift	XRT	0031888001	55526.60	2475
RXTE	PCA	95032-12-07-01	55528.36	2656
Swift	XRT	0031888002	55528.39	2630
Swift	XRT	0031888003	55530.39	2424
RXTE	PCA	95032-12-07-02	55530.58	2928
Swift	XRT	0031888004	55532.00	1442
RXTE	PCA	95032-12-08-00	55533.26	3168
RXTE	PCA	95032-12-08-01	55535.28	2432
RXTE	PCA	95032-12-08-02	55537.31	2624
Swift	XRT	0031888005	55552.49	2600
Swift	XRT	0031888006	55554.77	1838
Swift	XRT	0031888007	55556.90	663
Swift	XRT	0031888008	55558.31	2110

Table F.2: X-ray observations of the BeXRB GRO J1008−57 presented in this thesis. The column F indicates whether the data have been used during a timing (T; see Sect. 4.4) or spectral analysis (S; see Sect. 5.1). Data epochs, which have been combined during the spectral analysis, are marked in the last column E.

Satellite	Instrument	ObsID	Start (MJD)	Exposure (s)	F	E
Observations in quiescence (1996/1997)						
RXTE	PCA, HEXTE	20132-01-01-000	50412.49	9439	S	I
RXTE	PCA, HEXTE	20132-01-01-00	50412.80	6623	S	I
RXTE	PCA, HEXTE	20132-01-01-01	50413.05	8719	S	I
RXTE	PCA, HEXTE	20132-01-01-02	50413.21	1136	S	I
RXTE	PCA, HEXTE	20132-01-01-04	50413.69	4319	S	I
RXTE	PCA, HEXTE	20132-01-01-05	50413.84	1472	S	I
RXTE	PCA, HEXTE	20132-01-02-00	50466.74	17135	S	I
RXTE	PCA, HEXTE	20132-01-02-01	50467.09	4687	S	I
RXTE	PCA, HEXTE	20132-01-02-02	50467.22	5023	S	I
RXTE	PCA, HEXTE	20132-01-02-03	50467.38	3648	S	I
RXTE	PCA, HEXTE	20132-01-02-04	50467.64	7327	S	I
RXTE	PCA, HEXTE	20132-01-03-000	50514.36	13327	S	I
RXTE	PCA, HEXTE	20132-01-03-00	50514.67	9999	S	I
RXTE	PCA, HEXTE	20132-01-03-01	50514.87	10047	S	I
RXTE	PCA, HEXTE	20132-01-03-02	50515.02	11231	S	I
RXTE	PCA, HEXTE	20123-09-01-00	50519.20	4335	S	I
RXTE	PCA, HEXTE	20123-09-02-00	50537.48	4559	S	I
RXTE	PCA, HEXTE	20123-09-03-00	50565.90	5375	S	I
RXTE	PCA, HEXTE	20132-01-04-00	50567.38	15615	S	I
RXTE	PCA, HEXTE	20132-01-04-03	50568.36	9455	S	I
RXTE	PCA, HEXTE	20132-01-04-01	50569.52	7855	S	I
RXTE	PCA, HEXTE	20132-01-04-02	50569.68	9599	S	I
RXTE	PCA, HEXTE	20132-01-04-04	50569.95	1456	S	I
RXTE	PCA, HEXTE	20123-09-04-00	50602.11	4607	S	I
RXTE	PCA, HEXTE	20123-09-05-00	50619.11	4303	S	I
Outburst in 2005 February						
RXTE	PCA, HEXTE	90089-03-01-00	53421.56	832	T,S	
RXTE	PCA, HEXTE	90089-03-02-01	53426.01	2208	T,S	II
RXTE	PCA, HEXTE	90089-03-02-08	53426.29	863	T,S	II
RXTE	PCA, HEXTE	90089-03-02-07	53426.40	1232	T,S	II
RXTE	PCA, HEXTE	90089-03-02-02	53427.11	2912	T,S	III
RXTE	PCA, HEXTE	90089-03-02-000	53427.29	15536	T,S	III
RXTE	PCA, HEXTE	90089-03-02-00	53427.59	7792	T,S	III
RXTE	PCA, HEXTE	90089-03-02-03	53428.11	1808	T,S	IV
RXTE	PCA, HEXTE	90089-03-02-04	53428.27	5968	T,S	IV
RXTE	PCA, HEXTE	90089-03-02-05	53428.84	735	T,S	IV
RXTE	PCA, HEXTE	90089-03-02-06	53429.28	9808	T,S	
RXTE	PCA, HEXTE	90089-03-02-09	53430.33	7536	T,S	
RXTE	PCA, HEXTE	90089-03-02-10	53431.14	1376	T,S	V
RXTE	PCA, HEXTE	90089-03-02-12	53431.20	2896	T,S	V
RXTE	PCA, HEXTE	90089-03-02-14	53431.56	1248	T,S	V
RXTE	PCA, HEXTE	90089-03-02-11	53431.66	1360	T,S	V
RXTE	PCA, HEXTE	90089-03-02-15	53431.72	624	T,S	V
RXTE	PCA, HEXTE	90089-03-02-16	53432.12	1616	T,S	V
RXTE	PCA, HEXTE	90089-03-02-13	53432.18	1584	T,S	V

Table F.2: continued

Satellite	Instrument	ObsID	Start (MJD)	Exposure (s)	F	E
Outburst in 2007 December						
RXTE	PCA	93032-03-01-00	54426.00	560	T,S	
Swift	XRT	00031030001	54427.69	2892	T,S	
RXTE	PCA, HEXTE	93032-03-02-00	54427.81	2832	T,S	
RXTE	PCA, HEXTE	93032-03-02-01	54429.84	2016	T,S	
RXTE	PCA, HEXTE	93032-03-02-02	54431.61	2592	T,S	
RXTE	PCA, HEXTE	93032-03-02-03	54433.05	1712	T,S	
RXTE	PCA, HEXTE	93032-03-03-00	54434.24	1520	T,S	
Suzaku	XISs, PIN, GSO	902003010	54434.48	34385	T,S	
RXTE	PCA, HEXTE	93032-03-03-01	54435.50	863	T,S	
RXTE	PCA, HEXTE	93032-03-03-02	54437.14	560	T,S	
RXTE	PCA, HEXTE	93032-03-03-03	54438.17	768	T,S	
RXTE	PCA, HEXTE	93032-03-03-04	54439.92	1760	T,S	
RXTE	PCA, HEXTE	93032-03-04-01	54442.12	832	T,S	VI
RXTE	PCA, HEXTE	93032-03-04-02	54443.10	591	T,S	VI
RXTE	PCA, HEXTE	93032-03-04-00	54443.79	927	T,S	VI
RXTE	PCA, HEXTE	93032-03-04-04	54445.23	1200	T,S	VII
RXTE	PCA, HEXTE	93032-03-04-03	54446.33	1184	T,S	VII
RXTE	PCA, HEXTE	93032-03-04-06	54447.02	1360	T,S	VII
RXTE	PCA, HEXTE	93423-02-01-00	54449.18	1168	T,S	VIII
RXTE	PCA, HEXTE	93423-02-01-01	54451.98	1712	T,S	VIII
RXTE	PCA, HEXTE	93423-02-01-02	54454.87	1616	T,S	VIII
RXTE	PCA, HEXTE	93423-02-02-00	54457.16	1136	T,S	VIII
Outburst in 2011 April						
RXTE	PCA	96368-01-03-04	55647.35	655	S	IX
RXTE	PCA	96368-01-03-03	55648.39	671	S	IX
RXTE	PCA	96368-01-03-02	55649.62	688	S	
RXTE	PCA	96368-01-03-01	55650.72	944	S	
RXTE	PCA	96368-01-03-00	55651.97	768	S	
RXTE	PCA	96368-01-02-06	55652.55	1104	S	
RXTE	PCA	96368-01-02-05	55653.66	688	S	
RXTE	PCA	96368-01-02-04	55654.50	719	S	
RXTE	PCA	96368-01-02-03	55655.48	671	S	
RXTE	PCA	96368-01-02-02	55656.59	704	S	
RXTE	PCA	96368-01-02-01	55657.64	495	S	
RXTE	PCA	96368-01-02-07	55658.23	1840	S	
RXTE	PCA	96368-01-02-08	55658.37	2352	S	
RXTE	PCA	96368-01-02-09	55658.43	13024	S	
RXTE	PCA	96368-01-02-00	55658.72	15744	S	
RXTE	PCA	96368-01-01-08	55659.15	1584	S	
RXTE	PCA	96368-01-01-05	55659.55	6448	S	
RXTE	PCA	96368-01-01-03	55659.67	16863	S	
RXTE	PCA	96368-01-01-00	55660.32	14464	S	
RXTE	PCA	96368-01-01-02	55660.65	17695	S	
RXTE	PCA	96368-01-01-07	55661.37	2432	S	
RXTE	PCA	96368-01-01-01	55661.43	14224	S	
RXTE	PCA	96368-01-01-06	55661.96	655	S	

Table F.2: continued

Satellite	Instrument	ObsID	Start (MJD)	Exposure (s)	F	E
Type II Outburst in 2012 April						
Suzaku	XISs, PIN, GSO	907006010	56251.63	9061	S	
NuSTAR	FPMA, FPMB	80001001002	56261.36	14767	S	
Swift	XRT	00031030018	56261.53	1716	S	
Outburst in 2014 January						
Suzaku	XISs, PIN, GSO	408044010	56660.66	15322	S	
Triple-peaked outburst in 2014/2015						
NuSTAR	FPMA, FPMB	90001003002	56994.82	26861	S	
Swift	XRT	00081425001	56995.00	2263	S	
NuSTAR	FPMA, FPMB	90001003004	57049.74	17260	S	
Swift	XRT	00081425002	57049.79	1943	S	

Table F.3: List of X-ray observations of the hierarchic triple system candidate 4U 2129+47 performed by *XMM-Newton* and *Chandra*. The analysis of this observations is given in Sect. 4.5.

Satellite	Instrument	ObsID	Start (MJD)	Lifetime[a] (s)
Chandra	ACIS	1925	51879.03	37846
XMM-Newton	EPIC-pn	0307120101	53505.65	30269
XMM-Newton	EPIC-pn	0307120201	53527.41	42639
XMM-Newton	EPIC-pn	0502460101	54433.20	40017
XMM-Newton	EPIC-pn	0502460201	54454.85	54983
XMM-Newton	EPIC-pn	0502460301	54469.49	40055
XMM-Newton	EPIC-pn	0502460401	54483.09	41256
Chandra	ACIS	13681	55956.08	24296
Chandra	ACIS	13682	56025.22	24121
Chandra	ACIS	13683	56091.20	22252
Chandra	ACIS	16751	57281.29	21921

Notes. [a] the difference between the start and stop of the observation

Table F.4: List of *RXTE* observations of the BeXRB GX 304−1 used during the spectral analysis of the source (see Sect. 5.2). For observations marked with * systematic uncertainties were added to the analysis.

Satellite	Instrument	ObsID	Start (MJD)	Exposure (s)
Observations in 2010 March				
RXTE	PCA, HEXTE	95417-01-01-00	55282.34	2880
RXTE	PCA, HEXTE	95417-01-01-01	55282.61	2192
RXTE	PCA, HEXTE	95417-01-02-00	55292.68	3296
Observations in 2010 August				
RXTE	PCA, HEXTE	95417-01-03-03	55421.15	2304
RXTE	PCA, HEXTE	95417-01-03-00*	55421.20	3712
RXTE	PCA, HEXTE	95417-01-03-01	55422.07	5408
RXTE	PCA, HEXTE	95417-01-03-02*	55423.09	6096
RXTE	PCA, HEXTE	95417-01-04-00*	55426.10	3328
RXTE	PCA, HEXTE	95417-01-04-01	55427.08	3216
RXTE	PCA, HEXTE	95417-01-04-02	55427.99	64

Table F.4: continued

Satellite	Instrument	ObsID	Start (MJD)	Exposure (s)
RXTE	PCA, HEXTE	95417-01-05-00	55428.00	3120
RXTE	PCA, HEXTE	95417-01-05-01	55429.85	992
RXTE	PCA, HEXTE	95417-01-05-02	55431.00	2016
RXTE	PCA, HEXTE	95417-01-05-03	55432.11	3408
RXTE	PCA, HEXTE	95417-01-05-04	55433.24	1184
RXTE	PCA, HEXTE	95417-01-05-05	55434.03	1328
RXTE	PCA, HEXTE	95417-01-06-00	55435.26	1696
RXTE	PCA, HEXTE	95417-01-06-01	55436.03	1984
RXTE	PCA, HEXTE	95417-01-06-02	55437.35	1568
RXTE	PCA, HEXTE	95417-01-06-03	55438.20	2336
RXTE	PCA, HEXTE	95417-01-06-04	55439.07	1440
RXTE	PCA, HEXTE	95417-01-06-06	55439.13	1344
RXTE	PCA, HEXTE	95417-01-06-05	55440.75	832
Observations in 2010 December/2011 January				
RXTE	PCA, HEXTE	95417-01-07-00	55547.16	16400
RXTE	PCA, HEXTE	95417-01-07-01	55549.83	2944
RXTE	PCA, HEXTE	95417-01-07-02*	55550.22	12210
RXTE	PCA, HEXTE	95417-01-07-03	55551.27	7744
RXTE	PCA, HEXTE	95417-01-07-04	55552.33	2848
RXTE	PCA, HEXTE	95417-01-07-05*	55553.12	8880
RXTE	PCA, HEXTE	95417-01-07-06	55553.30	3664
RXTE	PCA, HEXTE	95417-01-07-07	55553.37	3200
RXTE	PCA, HEXTE	95417-01-08-00	55554.16	3408
RXTE	PCA, HEXTE	95417-01-08-01	55555.07	3520
RXTE	PCA, HEXTE	95417-01-08-02	55556.18	3344
RXTE	PCA, HEXTE	95417-01-08-03	55557.35	768
RXTE	PCA, HEXTE	95417-01-08-04	55558.27	2736
RXTE	PCA, HEXTE	95417-01-08-05	55558.92	5760
RXTE	PCA, HEXTE	95417-01-08-06	55559.92	5136
RXTE	PCA, HEXTE	95417-01-08-07	55560.95	3344
RXTE	PCA, HEXTE	96369-01-01-00	55562.80	9939
RXTE	PCA, HEXTE	96369-01-01-01	55566.91	2524
RXTE	PCA, HEXTE	96369-01-02-00	55569.59	1744
RXTE	PCA, HEXTE	96369-01-02-01	55571.66	2544
RXTE	PCA, HEXTE	96369-01-02-02	55573.82	2528
Observations in 2011 May				
RXTE	PCA, HEXTE	96369-01-03-00	55684.49	1280
RXTE	PCA, HEXTE	96369-01-03-01	55684.76	960
RXTE	PCA, HEXTE	96369-01-03-02	55685.00	1168
RXTE	PCA, HEXTE	96369-01-04-00	55685.53	1984
RXTE	PCA, HEXTE	96369-01-05-00	55686.31	3584
RXTE	PCA, HEXTE	96369-01-05-01*	55686.44	6272
RXTE	PCA, HEXTE	96369-01-05-02	55686.96	1136
RXTE	PCA, HEXTE	96369-02-01-00	55687.00	32
RXTE	PCA, HEXTE	96369-02-01-000*	55687.00	17730
RXTE	PCA, HEXTE	96369-02-01-02	55787.77	1056
RXTE	PCA, HEXTE	96369-02-01-03	55687.84	768
RXTE	PCA, HEXTE	96369-02-01-04	55687.94	1104
RXTE	PCA, HEXTE	96369-02-01-01G*	55688.00	18300
RXTE	PCA, HEXTE	96369-02-01-05	55688.54	3072

Table F.4: continued

Satellite	Instrument	ObsID	Start (MJD)	Exposure (s)
RXTE	PCA, HEXTE	96369-02-01-06	55698.68	1344
RXTE	PCA, HEXTE	96369-01-06-00*	55689.26	2064
RXTE	PCA, HEXTE	96369-01-06-01*	55689.32	2912
RXTE	PCA, HEXTE	96369-01-06-02	55690.27	96
RXTE	PCA, HEXTE	96369-01-06-03	55691.34	656
RXTE	PCA, HEXTE	96369-01-06-04	55691.47	1344
RXTE	PCA, HEXTE	96369-01-07-00	55691.68	1728
RXTE	PCA, HEXTE	96369-01-07-01	55692.25	4076
RXTE	PCA, HEXTE	96369-01-08-00	55694.31	7056
RXTE	PCA, HEXTE	96369-01-08-01	55695.29	1136
RXTE	PCA, HEXTE	96369-01-09-00	55696.34	3760
RXTE	PCA, HEXTE	96369-01-09-01	55617.31	832
RXTE	PCA, HEXTE	96369-01-10-00	55698.40	3104
RXTE	PCA, HEXTE	96369-01-10-01	55700.28	480

Appendix G

Outbursts of GRO J1008−57

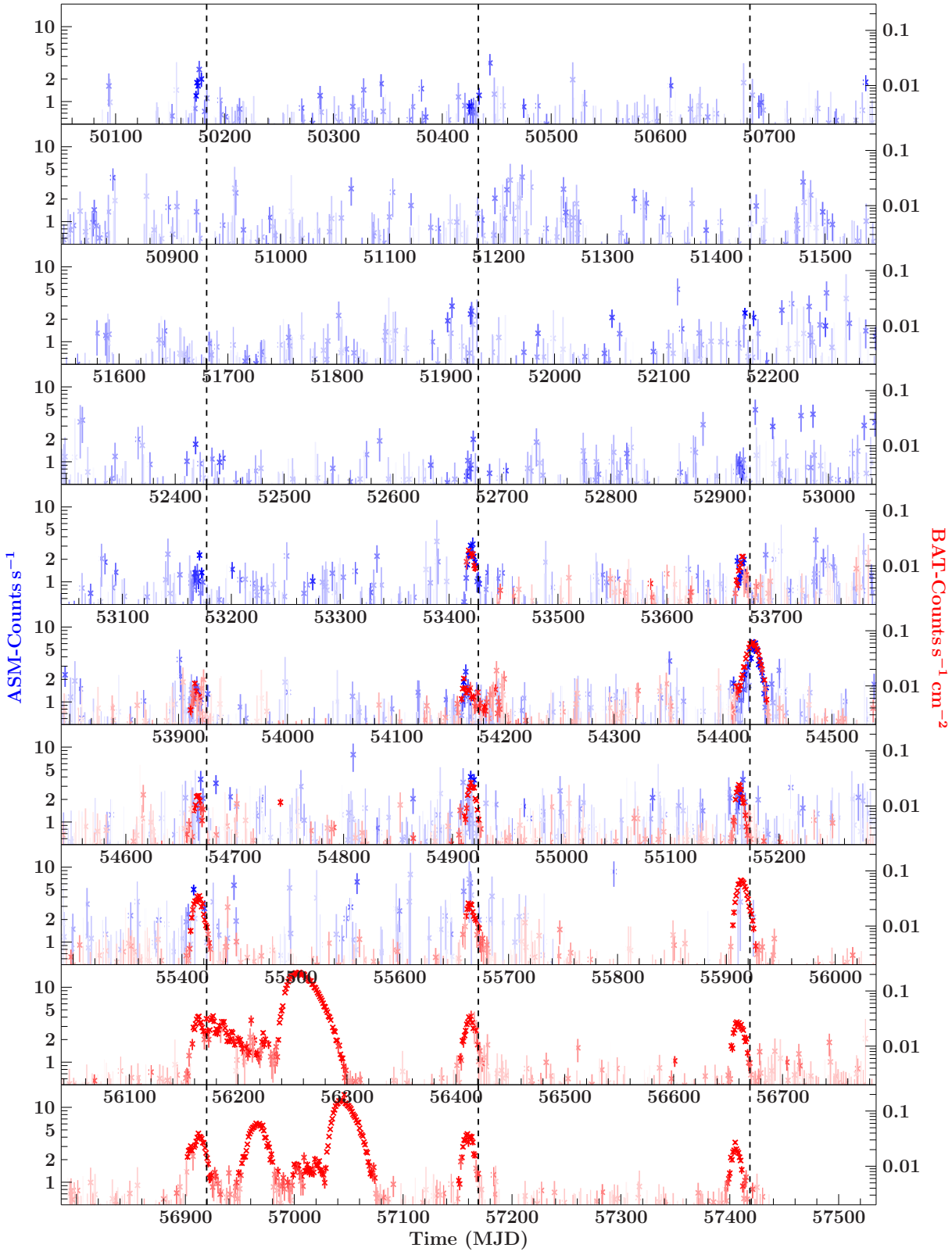

Figure G.1: Outburst history of GRO J1008−57 in *RXTE*-ASM (blue) and *Swift*-BAT (red). The S/N of the data are represented by the saturation of the 1 d-binned datapoints (with a maximum S/N of 5). The time range of each panel is set to three times the orbital period of the binary to emphasize the regular outbursts around the periastron passages (vertical dashed lines).

Bibliography

Adams W.S., 1915, PASP 27, 236
Anders E., Ebihara M., 1982, Geochim. Cosmochim. Acta 46, 2363
Anders E., Grevesse N., 1989, Geochim. Cosmochim. Acta 53, 197
Andersen J., 1983, The Observatory 103, 165
Ando S., Beacom J.F., Yüksel H., 2005, Physical Review Letters 95, 171101
Araya R.A., Harding A.K., 1999, ApJ 517, 334
Araya-Góchez R.A., Harding A.K., 2000, ApJ 544, 1067
Arnaud K.A., 1996, In: Jacoby G.H., Barnes J. (eds.) Astronomical Data Analysis Software and Systems V, Vol. 101. Astron. Soc. of the Pacific Conf. Series, p. 17
Arons J., Burnard D.J., Klein R.I., et al., 1984, In: Woosley S.E. (ed.) American Institute of Physics Conference Series, Vol. 115. American Institute of Physics Conference Series, p.215
Asplund M., Grevesse N., Sauval A.J., Scott P., 2009, ARA&A 47, 481
Atwood W.B., Abdo A.A., Ackermann M., et al., 2009, ApJ 697, 1071
Baade W., Zwicky F., 1934, Physical Review 46, 76
Balucinska-Church M., McCammon D., 1992, ApJ 400, 699
Baron E., Cooperstein J., 1990, ApJ 353, 597
Barthelmy S.D., Barbier L.M., Cummings J.R., et al., 2005, Space Sci. Rev. 120, 143
Basko M.M., Sunyaev R.A., 1976, MNRAS 175, 395
Becker P.A., Klochkov D., Schönherr G., et al., 2012, A&A 544, A123
Becker P.A., Wolff M.T., 2005a, Astrophys. J., Lett. 621, L45
Becker P.A., Wolff M.T., 2005b, ApJ 630, 465
Becker P.A., Wolff M.T., 2007, ApJ 654, 435
Begelman a.M.C., McKee C.F., 1983, ApJ 271, 89
Bellm E.C., Fürst F., Pottschmidt K., et al., 2014, ApJ 792, 108
Bethe H.A., 1939, Physical Review 55, 434
Bethe H.A., 1990, Reviews of Modern Physics 62, 801
Bethe H.A., Critchfield C.L., 1938, Physical Review 54, 248
Bevington P.R., Robinson D.K., 2003, Data reduction and error analysis for the physical sciences, McGraw-Hill Education, Boston, MA, USA
Bildsten L., Chakrabarty D., Chiu J., et al., 1997, ApJS 113, 367
Blondin J.M., Kallman T.R., Fryxell B.A., Taam R.E., 1990, ApJ 356, 591
Blondin J.M., Stevens I.R., Kallman T.R., 1991, ApJ 371, 684
Böck M., 2012, Ph.D. thesis, Friedrich-Alexander-Universität Erlangen-Nürnberg
Boldin P.A., Tsygankov S.S., Lutovinov A.A., 2013, Astron. Lett. 39, 375
Boltzmann L., 1884, Annalen der Physik 258, 291
Bonanno A., Urpin V., Belvedere G., 2005, A&A 440, 199
Bondi H., Hoyle F., 1944, MNRAS 104, 273
Bothwell M.S., Torres M.A.P., Garcia M.R., Charles P.A., 2008, A&A 485, 773
Bozzo E., Falanga M., Papitto A., et al., 2007, A&A 476, 301
Bradshaw C.F., Fomalont E.B., Geldzahler B.J., 1999, Astrophys. J., Lett. 512, L121
Bradt H., Levine A.M., Morgan E.H., Remillard R., 2007, In: di Salvo T., Israel G.L., Piersant L., Burderi L., Matt G., Tornambe A., Menna M.T. (eds.) The Multicolored

Landscape of Compact Objects and Their Explosive Origins, Vol. 924. American Institute of Physics Conference Series, p.481
Brinkman A.C., Gunsing C.J., Kaastra J.S., et al., 1997, In: Hoover R.B., Walker A.B. (eds.) Grazing Incidence and Multilayer X-Ray Optical Systems, Vol. 3113. Society of Photo-Optical Instrumentation Engineers (SPIE) Conference Series, p.181
Burbidge E.M., Burbidge G.R., Fowler W.A., Hoyle F., 1957, Reviews of Modern Physics 29, 547
Burrows D.N., Hill J.E., Nousek J.A., et al., 2005, Space Sci. Rev. 120, 165
Burrows D.N., Park S., Helder E.A., et al., 2012, In: Roming P., Kawai N., Pian E. (eds.) Death of Massive Stars: Supernovae and Gamma-Ray Bursts, Vol. 279. IAU Symposium, p.71
Caballero I., Pottschmidt K., Marcu D.M., et al., 2013, Astrophys. J., Lett. 764, L23
Camero-Arranz A., Finger M.H., Ikhsanov N.R., et al., 2010, ApJ 708, 1500
Camero-Arranz A., Finger M.H., Wilson-Hodge C.A., et al., 2012, ApJ 754, 20
Cameron A.G.W., Mock M., 1967, Nat 215, 464
Campana S., Israel G., Stella L., 1999, A&A 352, L91
Canizares C.R., Davis J.E., Dewey D., et al., 2005, PASP 117, 1144
Canuto V., Ventura J., 1977, Fundam. Cosmic Phys. 2, 203
Case G.L., Cherry M.L., Wilson-Hodge C.A., et al., 2011, ApJ 729, 105
Chandrasekhar S., 1931a, MNRAS 91, 456
Chandrasekhar S., 1931b, ApJ 74, 81
Chandrasekhar S., 1935, MNRAS 95, 207
Chevalier C., Ilovaisky S.A., Motch C., et al., 1989, A&A 217, 108
Chiappini C., Matteucci F., Romano D., 2001, ApJ 554, 1044
Claerbout J., 1990, Stanford Exploration Project Report 67, 139
Coburn W., Heindl W.A., Rothschild R.E., et al., 2002, ApJ 580, 394
Coe M.J., Bird A.J., Hill A.B., et al., 2007, MNRAS 378, 1427
Coe M.J., Negueruela I., Buckley D.A.H., et al., 2001, MNRAS 324, 623
Coe M.J., Roche P., Everall C., et al., 1994, MNRAS 270, L57
Colgate S.A., 1971, ApJ 163, 221
Colgate S.A., White R.H., 1966, ApJ 143, 626
Corbet R.H.D., 1986, MNRAS 220, 1047
Corbet R.H.D., in't Zand J.J.M., Levine A.M., Marshall F.E., 2009, ApJ 695, 30
Corbet R.H.D., Krimm H.A., 2013, ApJ 778, 45
Cowley A.P., Schmidtke P.C., 1990, AJ 99, 678
Daltabuit E., Cox D.P., 1972, ApJ 177, 855
D'Angelo C.R., Spruit H.C., 2012, MNRAS 420, 416
Davidson K., 1973, Nature Physical Science 246, 1
Davidson K., Ostriker J.P., 1973, ApJ 179, 585
Davies R.E., Pringle J.E., 1981, MNRAS 196, 209
Deák I., 1990, Random Number Generators and Simulation, Mathematical Methods of Operations Research, Akadémiai Kiadó, Budapest (transl. of Véletlenszám generátorok és alkalmazásuk)
den Herder J.W., Brinkman A.C., Kahn S.M., et al., 2001, A&A 365, L7
Dickey J.M., Lockman F.J., 1990, ARA&A 28, 215
Diehl R., Siegert T., Hillebrandt W., et al., 2014, Science 345, 1162
Doppler C.J., 1843, Abhandlungen der Königl. Böhm. Gesellschaft der Wissenschaften 5, 465
Doppler C.J., 1852, Weitere Mittheilungen, meine Theorie des farbigen Lichtes der Doppelsterne betreffend. In: Poggendorff J.C. (ed.) Annalen der Physik und Chemie,

Vol. 161. Verlag von Johann Ambrosius Barth, Lepizig, Germany, p.371
Dove J.B., Wilms J., Maisack M., Begelman M.C., 1997, ApJ 487, 759
Ebisawa K., Yamauchi S., Tanaka Y., et al., 2007, Prog. Theo. Phys. Suppl. 169, 121
Eikmann W., Wilms J., Lee J., 2012, In: An INTEGRAL view of the high-energy sky (the first 10 years). PoS
Eikmann W., Wilms J., Smith R.K., Lee J.C., 2014, Ac. Polytechnica 54, 177
Elsner R.F., Lamb F.K., 1977, ApJ 215, 897
Enoto T., Sasano M., Yamada S., et al., 2014, ApJ 786, 127
Falkner S., et al., 2016, in prep.
Farinelli R., Ceccobello C., Romano P., Titarchuk L., 2012, A&A 538, A67
Farinelli R., Ferrigno C., Bozzo E., Becker P.A., 2016, A&A 591, A29
Feldman U., 1992, Physica Scripta 46, 202
Ferrigno C., Becker P.A., Segreto A., et al., 2009, A&A 498, 825
Ferrigno C., Falanga M., Bozzo E., et al., 2011, A&A 532, A76
Fewell M.P., 1995, American Journal of Physics 63, 653
Finger M.H., 2010, Renewed Activity from XTE J1946+274, ATel 2847
Finger M.H., Beklen E., Narayana Bhat P., et al., 2009, ArXiv Astrophysics e-prints 0912.3847
Finger M.H., Bildsten L., Chakrabarty D., et al., 1999, ApJ 517, 449
Finger M.H., Camero-Arranz A., Kretschmar P., et al., 2006, In: AAS/High Energy Astrophysics Division #9, Vol. 38. Bulletin of the American Astronomical Society, p. 359
Finger M.H., Prince T.A., 1997, In: Dermer C.D., Strickman M.S., Kurfess J.D. (eds.) Proceedings of the Fourth Compton Symposium, Vol. 410. AIP Conf. Proc., p.57
Forman W., Jones C., Cominsky L., et al., 1978, ApJS 38, 357
Fossey J., Cooke B., Pollack G., et al., 2014, Central Bureau Electronic Telegrams 3792, 1
Fowler R.H., 1926, MNRAS 87, 114
Frank J., King A., Raine D.J., 2002, Accretion Power in Astrophysics: Third Edition, Cambridge University Press, Cambridge, United Kingdom
Fransson C., Fabian A.C., 1980, A&A 87, 102
Freire P.C.C., Ransom S.M., Bégin S., et al., 2008, ApJ 675, 670
Fürst F., 2011, Ph.D. thesis, Friedrich-Alexander-Universität Erlangen-Nürnberg
Fürst F., Kreykenbohm I., Pottschmidt K., et al., 2010, A&A 519, A37
Fürst F., Suchy S., Kreykenbohm I., et al., 2011, A&A 535, A9
García J.A., McClintock J.E., Steiner J.F., et al., 2014, ApJ 794, 73
Garcia M.R., Bailyn C.D., Grindlay J.E., Molnar L.A., 1989, Astrophys. J., Lett. 341, L75
Garcia M.R., Grindlay J.E., 1987, Astrophys. J., Lett. 313, L59
Garmire G.P., Bautz M.W., Ford P.G., et al., 2003, In: Truemper J.E., Tananbaum H.D. (eds.) X-Ray and Gamma-Ray Telescopes and Instruments for Astronomy., Vol. 4851. Society of Photo-Optical Instrumentation Engineers (SPIE) Conference Series, p.28
Gehrels N., Chincarini G., Giommi P., et al., 2005, ApJ 621, 558
Gehrels N., Chincarini G., Giommi P., et al., 2004, ApJ 611, 1005
Gerend D., Boynton P.E., 1976, ApJ 209, 562
Ghosh P., Lamb F.K., 1979a, ApJ 232, 259
Ghosh P., Lamb F.K., 1979b, ApJ 234, 296
Ghosh P., Pethick C.J., Lamb F.K., 1977, ApJ 217, 578
Giacconi R., Gursky H., Kellogg E., et al., 1971, Astrophys. J., Lett. 167, L67
Giacconi R., Gursky H., Paolini F.R., Rossi B.B., 1962, Phys. Rev. Lett. 9, 439
Giacconi R., Murray S., Gursky H., et al., 1972, ApJ 178, 281
Ginzburg V.L., 1964, Soviet Physics Doklady 9, 329

González-Galán A., Kuulkers E., Kretschmar P., et al., 2012, A&A 537, A66
Gould H., Tobochnik J., Christian W., 2006, An introduction to computer simulation methods: Applications to Physical Systems (third edition), Addison-Wesley, San Francisco, USA
Green D.A., 2014, Bulletin of the Astronomical Society of India 42, 47
Grevesse N., Sauval A.J., 1998, Space Sci. Rev. 85, 161
Grove J.E., Kurfess J.D., Phlips B.F., et al., 1995, In: Iucci N., Lamanna E. (eds.) 24th International Cosmic Ray Conference, Vol. 2. International Union of Pure and Applied Physics, p.1
Gvaramadze V.V., 2001, A&A 374, 259
Hanke M., 2011, Ph.D. thesis, Friedrich-Alexander-Universität Erlangen-Nürnberg
Hansen C.J., Kawaler S.D., 1994, Stellar Interiors, Springer-Verlag, New York, USA
Hansen C.J., Primas F., Hartman H., et al., 2012, A&A 545, A31
Hanuschik R.W., 1996, A&A 308, 170
Harrison F.A., Craig W.W., Christensen F.E., et al., 2013, ApJ 770, 103
Hayakawa S., Matsuoka M., 1964, Progress of Theoretical Physics Supplement 30, 204
Hessels J.W.T., Ransom S.M., Stairs I.H., et al., 2006, Science 311, 1901
Hilditch R.W., 2001, An Introduction to Close Binary Stars, Cambridge University Press, Cambridge, United Kingdom
Houck J.C., Denicola L.A., 2000, In: Manset N., Veillet C., Crabtree D. (eds.) Astronomical Data Analysis Software and Systems IX, Vol. 216. Astron. Soc. of the Pacific Conf. Series, p. 591
Hoyle F., Lyttleton R.A., 1939, Proceedings of the Cambridge Philosophical Society 35, 405
Illarionov A.F., Sunyaev R.A., 1975, A&A 39, 185
Inno L., Matsunaga N., Bono G., et al., 2013, ApJ 764, 84
Isenberg M., Lamb D.Q., Wang J.C.L., 1998, ApJ 505, 688
Jahoda K., Markwardt C.B., Radeva Y., et al., 2006, ApJS 163, 401
Janka H.T., Langanke K., Marek A., et al., 2007, Phys. Rep. 442, 38
Jansen F., Lumb D., Altieri B., et al., 2001, A&A 365, L1
Jenkins G.M., Watts D.G., 1969, Spectral analysis and its applications, Holden-Day, London, United Kingdom
Kalberla P.M.W., Burton W.B., Hartmann D., et al., 2005, A&A 440, 775
Kargaltsev O., Pavlov G.G., 2008, In: Bassa C., Wang Z., Cumming A., Kaspi V.M. (eds.) 40 Years of Pulsars: Millisecond Pulsars, Magnetars and More, Vol. 983. AIP Conf. Proc., p.171
Kato S., Fukue J., Mineshige S., 2008, Black-Hole Accretion Disks — Towards a New Paradigm —, Kyoto University Press, Koto, Japan
Kelley R.L., Mitsuda K., Allen C.A., et al., 2007, PASJ 59, 77
Kendziorra E., Kretschmar P., Pan H.C., et al., 1994, A&A 291, L31
Kepler J., 1609, Astronomia Nova ΑΙΤΙΟΛΟΓΗΤΟΣ seu physica coelestis, tradita commentariis de motibus stellæ Martis, Ex observationibus G.V. Tychonis Brahe
Kepler J., 1621, Epitome Astronomiæ Copernicanæ usitata formâ quaestionum & responsionum conscriptæ, liber quartus, doctrinæ theoricæ primus: quo physica coelestis, hoc est, omnium in coelo magnitudinum, motuum, proportionumque causæ vel naturales vel archetypicæ explicantur, et sic principia doctrinæ theoricæ demonstrantur. Qui quodvice supplementi librorum Aristotelis de caelo esset, certo consilio seorsim est editus, Johannes Plancus, Lentiis ad Danubium (Linz, Austria)
Ketsaris N.A., Kuster M., Postnov K.A., et al., 2000, ArXiv Astrophysics e-prints 0010035
Kippenhahn R., Weigert A., 1990, Stellar Structure and Evolution, Springer-Verlag, Berlin

Heidelberg, Germany
Kirsch M.G., Briel U.G., Burrows D., et al., 2005, In: Siegmund O.H.W. (ed.) UV, X-Ray, and Gamma-Ray Space Instrumentation for Astronomy XIV. SPIE Conf. Ser. 5898, p. 22
Klochkov D., Doroshenko V., Santangelo A., et al., 2012, A&A 542, L28
Knigge C., Coe M.J., Podsiadlowski P., 2011, Nat 479, 372
Knödlseder J., Vedrenne G., 2001, In: Gimenez A., Reglero V., Winkler C. (eds.) Exploring the Gamma-Ray Universe, Vol. 459. ESA Special Publication, p.23
Knoll G.F., 1999, Radiation Detection and Measurement, John Wiley & Sons, Inc., New York, USA
Koester D., Chanmugam G., 1990, Reports on Progress in Physics 53, 837
Kokubun M., Makishima K., Takahashi T., et al., 2007, PASJ 59, 53
Kompaneets A.S., 1957, Sov. Phys.-JETP 4, 730
Kortright J.B., Thompson A.C., 2009, X-Ray Emission Energies. In: Thompson A.C. (ed.) X-Ray Data Booklet. Lawrence Berkeley National Laboratory, Berkeley, CA, USA
Kotze M.M., Charles P.A., 2012, MNRAS 420, 1575
Kouveliotou C., Dieters S., Strohmayer T., et al., 1998, Nat 393, 235
Koyama K., Tsunemi H., Dotani T., et al., 2007, PASJ 59, 23
Kraft R.P., Chappell J.H., Kenter A.T., et al., 2000, In: Truemper J.E., Aschenbach B. (eds.) X-Ray Optics, Instruments, and Missions III, Vol. 4012. Society of Photo-Optical Instrumentation Engineers (SPIE) Conference Series, p.493
Kraus U., Zahn C., Weth C., Ruder H., 2003, ApJ 590, 424
Kreykenbohm I., Mowlavi N., Produit N., et al., 2005, A&A 433, L45
Kreykenbohm I., Wilms J., Kretschmar P., et al., 2008, A&A 492, 511
Krimm H.A., Barthelmy S.D., Baumgartner W., et al., 2010, Swift/BAT detects renewed hard X-ray activity from XTE J1946+274, ATel 2663
Krimm H.A., Barthelmy S.D., Baumgartner W., et al., 2015, Swift/BAT detection of the current outburst of XTE J1859+083, ATel 7037
Kühnel M., 2009, Bachelor's thesis, Technische Universität Darmstadt
Kühnel M., 2011, Masters's thesis, Friedrich-Alexander-Universität Erlangen-Nürnberg
Kühnel M., Falkner S., Grossberger C., et al., 2016a, Acta Pol. 56(1), 41
Kühnel M., Finger M.H., Fürst F., et al., 2014, Orbital parameters and spin evolution of RX J0520.5-6932, ATel 5856
Kühnel M., Fürst F., Pottschmidt K., et al., 2016b, Evidence for different accretion regimes in GRO J1008 57, submitted to A&A
Kühnel M., Kretschmar P., Nespoli E., et al., 2015a, In: Proceedings of the 10th INTEGRAL Workshop "A Synergistic View of the High Energy Sky" (INTEGRAL 2014). PoS, p. 78
Kühnel M., Müller S., Kreykenbohm I., et al., 2013, A&A 555, A95
Kühnel M., Müller S., Kreykenbohm I., et al., 2015b, Acta Pol. 55(2), 123
Kühnel M., Rothschild R.E., Müller S., et al., 2016c MNRAS, in prep.
Kurtz D.W., 1983, Information Bulletin on Variable Stars 2285, 1
La Barbera A., Burderi L., Di Salvo T., et al., 2001, ApJ 553, 375
Lai D., 2001, Reviews of Modern Physics 73, 629
Lamb F.K., Pethick C.J., Pines D., 1973, ApJ 184, 271
Lamers H.J.G., Pauldrach A.W.A., 1991, A&A 244, L5
Lampton M., Margon B., Bowyer S., 1976, ApJ 208, 177
Landau L., 1938, Nat 141, 333
Larsson S., 1996, A&AS117, 197
Latal H.G., 1986, ApJ 309, 372

Lattimer J.M., 2012, Annual Review of Nuclear and Particle Science 62, 485
Leahy D.A., Darbro W., Elsner R.F., et al., 1983, ApJ 266, 160
Leahy D.A., Kostka M., 2008, MNRAS 384, 747
Levenberg K., 1944, Quart. Appl. Math. 2(2), 164
Levine A.M., Bradt H., Cui W., et al., 1996, Astrophys. J., Lett. 469, L33
Levine A.M., Bradt H.V., Chakrabarty D., et al., 2011, ApJS 196, 6
Levine A.M., Corbet R., 2006, Detection of Additional Periodicities in RXTE ASM Light Curves, ATel 940
Lewin W.H.G., Clark G.W., Smith W.B., 1968a, Nat 219, 1235
Lewin W.H.G., Clark G.W., Smith W.B., 1968b, Astrophys. J., Lett. 152, L49
Li K.L., Kong K.H., 2015, Swift follow-up observation of XTE J1859+083, ATel 7067
Lin J., Nowak M.A., Chakrabarty D., 2009, ApJ 706, 1069
Liu Q.Z., van Paradijs J., van den Heuvel E.P.J., 2006, A&A 455, 1165
Liu Q.Z., van Paradijs J., van den Heuvel E.P.J., 2007, A&A 469, 807
Lodders K., 2003, ApJ 591, 1220
Lovelace R.V.E., Romanova M.M., Bisnovatyi-Kogan G.S., 1995, MNRAS 275, 244
Lynds C.R., 1967, Astrophys. J., Lett. 149, L41
Lyne A.G., Manchester R.N., Taylor J.H., 1985, MNRAS 213, 613
Makishima K., Mihara T., Ishida M., et al., 1990, Astrophys. J., Lett. 365, L59
Malacaria C., Klochkov D., Santangelo A., Staubert R., 2015, A&A A121
Maloney P.R., Begelman M.C., 1997, Astrophys. J., Lett. 491, L43
Manchester R.N., 2007, In: Immler S., Weiler K., McCray R. (eds.) Supernova 1987A: Twenty Years After: Supernovae and Gamma-Ray Bursters, Vol. 937. AIP Conf. Proc., p.134
Manousakis A., Beckmann V., Bianchin V., et al., 2008, INTEGRAL hard X-ray detection of HMXB GX 304-1 and H 1417-624, ATel 1613
Manousakis A., Walter R., Blondin J.M., 2012, A&A 547, A20
Marcu D.M., Pottschmidt K., Gottlieb A.M., et al., 2015, In: Proceedings of the 10th INTEGRAL Workshop "A Synergistic View of the High Energy Sky" (INTEGRAL 2014). PoS
Marcu-Cheatham D.M., Pottschmidt K., Kühnel M., et al., 2015, ApJ 815, 44
Marquardt D., 1963, J. Soc. Indust. Appl. Math. 11(2), 431
Marshall F.E., in 't Zand J.J.M., Strohmayer T., Markwardt C.B., 1999, IAU Circ. 7240, id. 2
Martínez-Núñez S., Kretschmar P., Bozzo E., et al., 2016, Towards a unified view of inhomogeneous stellar winds in isolated supergiant stars and supergiant high mass X-ray binaries, submitted to Space Science Reviews
Martínez-Núñez S., Torrejón J.M., Kühnel M., et al., 2014, A&A 563, A70
Mason K.O., Murdin P.G., Parkes G.E., Visvanathan N., 1978, MNRAS 184, 45P
McClintock J.E., London R.A., Bond H.E., Grauer A.D., 1982, ApJ 258, 245
McClintock J.E., Nugent J.J., Li F.K., Rappaport S.A., 1977, Astrophys. J., Lett. 216, L15
McClintock J.E., Ricker G.R., Lewin W.H.G., 1971, Astrophys. J., Lett. 166, L73
Meegan C., Bhat N., Connaughton V., et al., 2007, In: Ritz S., Michelson P., Meegan C.A. (eds.) The First GLAST Symposium, Vol. 921. AIP Conf. Proc., p.13
Meegan C., Lichti G., Bhat P.N., et al., 2009, ApJ 702, 791
Mészáros P., 1992, High-energy radiation from magnetized neutron stars, The University of Chicago Press, Chicago, USA
Mészáros P., Nagel W., 1985a, ApJ 298, 147
Mészáros P., Nagel W., 1985b, ApJ 299, 138

Michel F.C., 1991, Theory of neutron star magnetospheres, The University of Chicago Press, Chicago, USA
Mihara T., 1995, Ph.D. thesis, Univ. of Tokyo
Miller K.A., Stone J.M., 2000, ApJ 534, 398
Mitsuda K., Bautz M., Inoue H., et al., 2007, PASJ 59, 1
Moritani Y., Nogami D., Okazaki A.T., et al., 2013, PASJ 65, 83
Morrison P., 1967, ARA&A 5, 325
Morton D.C., 1964, ApJ140, 460
Mowlavi N., Kreykenbohm I., Shaw S.E., et al., 2006, A&A 451, 187
Müller H., Serot B.D., 1996, Nuclear Physics A 606, 508
Müller S., 2013, Ph.D. thesis, Friedrich-Alexander-Universität Erlangen-Nürnberg
Müller S., Ferrigno C., Kühnel M., et al., 2013, A&A 551, A6
Müller S., Kühnel M., Caballero I., et al., 2012, A&A 546, A125
Müller S., Obst M., Kreykenbohm I., et al., 2010, In: Proceedings of the 8th INTEGRAL Workshop "The Restless Gamma-ray Universe" (INTEGRAL 2010). PoS, p. 116
Murray S.S., Austin G.K., Chappell J.H., et al., 2000, In: Truemper J.E., Aschenbach B. (eds.) X-Ray Optics, Instruments, and Missions III, Vol. 4012. Society of Photo-Optical Instrumentation Engineers (SPIE) Conference Series, p.68
Nagel W., 1981a, ApJ 251, 278
Nagel W., 1981b, ApJ 251, 288
Naik S., Paul B., Kachhara C., Vadawale S.V., 2011, MNRAS 413, 241
Nakajima M., Mihara T., Makishima K., Niko H., 2006, ApJ 646, 1125
Nakajima M., Mihara T., Sugizaki M., et al., 2012, MAXI/GSC detection of an outburst from Be/X-ray binary pulsar GX 304-1, ATel 4420
Negoro H., Suzuki K., Namba T., et al., 2015, MAXI/GSC detection of a new X-ray outburst from XTE J1859+083/MAXI J1859+082, ATel 7035
Nowak M., Kuehnel M., Chakrabarty D., Wilms J., 2014, In: Ness J.U. (ed.) The X-ray Universe 2014., p. id. 154
Nowak M.A., Hanke M., Trowbridge S.N., et al., 2011, ApJ 728, 13
Nowak M.A., Heinz S., Begelman M.C., 2002, ApJ 573, 778
Nowak M.A., Paizis A., Rodriguez J., et al., 2012, ApJ 757, 143
Oertel M., 2013, Diploma thesis, Friedrich-Alexander-Universität Erlangen-Nürnberg
Okazaki A.T., 1991, PASJ 43, 75
Okazaki A.T., Bate M.R., Ogilvie G.I., Pringle J.E., 2002 337, 967
Okazaki A.T., Hayasaki K., Moritani Y., 2013, PASJ 65, 41
Okazaki A.T., Negueruela I., 2001, A&A 377, 161
Oppenheimer J.R., Volkoff G.M., 1939, Physical Review 55, 374
Özbey Arabacı M., Camero-Arranz A., Zurita C., et al., 2015, A&A 582, A53
Özel F., Freire P., 2016, ARA&A 54, 401
Paczyński B., 1977, ApJ 216, 822
Palmeri P., Mendoza C., Kallman T.R., et al., 2003, A&A 410, 359
Parkes G.E., Murdin P.G., Mason K.O., 1980, MNRAS 190, 537
Perlmutter S., Aldering G., Goldhaber G., et al., 1999, ApJ 517, 565
Perna R., Bozzo E., Stella L., 2006, ApJ 639, 363
Petterson J.A., 1978, ApJ 224, 625
Plummer W.E., 1881, MNRAS 42, 56
Poeckert R., Marlborough J.M., 1978, ApJS 38, 229
Pols O.R., Cote J., Waters L.B.F.M., Heise J., 1991, A&A 241, 419
Postnov K.A., Gornostaev M.I., Klochkov D., et al., 2015a, MNRAS 452, 1601
Postnov K.A., Mironov A.I., Lutovinov A.A., et al., 2015b, MNRAS 446, 1013

Pottschmidt K., Rothschild R.E., Gasaway T., et al., 2006, In: AAS/High Energy Astrophysics Division #9, Vol. 38. Bulletin of the American Astronomical Society, p. 384
Predehl P., Braeuninger H.W., Brinkman A.C., et al., 1997, In: Hoover R.B., Walker A.B. (eds.) Grazing Incidence and Multilayer X-Ray Optical Systems, Vol. 3113. Society of Photo-Optical Instrumentation Engineers (SPIE) Conference Series, p.172
Predehl P., Schmitt J.H.M.M., 1995, A&A 293
Prendergast K.H., Burbidge G.R., 1968, Astrophys. J., Lett. 151, L83
Priedhorsky W.C., Holt S.S., 1987, Space Sci. Rev. 45, 291
Priedhorsky W.C., Terrell J., 1983, ApJ 273, 709
Puls J., Vink J.S., Najarro F., 2008, Astron. Astrophys. Rev. 16, 209
Rajoelimanana A.F., Charles P.A., Udalski A., 2011, MNRAS 413, 1600
Ransom S.M., Stairs I.H., Archibald A.M., et al., 2014, Nat 505, 520
Rappaport S., Clark G.W., Cominsky L., et al., 1978, Astrophys. J., Lett. 224, L1
Rappaport S., van den Heuvel E.P.J., 1982, In: Jaschek M., Groth H.G. (eds.) Be Stars, Vol. 98. IAU Symposium, p.327
Reig P., Nespoli E., 2013, A&A 551, A1
Revnivtsev M., Sazonov S., Churazov E., et al., 2009, Nat 458, 1142
Riquelme M.S., Torrejón J.M., Negueruela I., 2012, A&A 539, A114
Rivinius T., Carciofi A.C., Martayan C., 2013, Astron. Astrophys. Rev. 21, 69
Roche E.A., 1849a, Mém. Acad. Sci. Montpellier 1, 243
Roche E.A., 1849b, Mém. Acad. Sci. Montpellier 1, 333
Roche E.A., 1851, Mém. Acad. Sci. Montpellier 2, 21
Roming P.W.A., Hunsberger S.D., Mason K.O., et al., 2004, In: Flanagan K.A., Siegmund O.H.W. (eds.) X-Ray and Gamma-Ray Instrumentation for Astronomy XIII, Vol. 5165. Society of Photo-Optical Instrumentation Engineers (SPIE) Conference Series, p.262
Rothschild R.E., Blanco P.R., Gruber D.E., et al., 1998, ApJ 496, 538
Rothschild R.E., Kuehnel M., Pottschmidt K., et al., 2016, Discovery and Modeling of a Flattening of the Positive Cyclotron Line/Luminosity Relation in GX 304-1 with RXTE, MNRAS in press, ArXiv Astrophysics e-prints 1610.08944
Rothschild R.E., Markowitz A., Hemphill P., et al., 2013, ApJ 770, 19
Sako M., Kahn S.M., Paerels F., et al., 2003, ArXiv Astrophysics e-prints 0309503
Salpeter E.E., 1964, ApJ 140, 796
Sandage A., Osmer P., Giacconi R., et al., 1966, ApJ 146, 316
Scargle J.D., Norris J.P., Jackson B., Chiang J., 2013, ApJ 764, 167
Schandl S., Meyer F., 1994, A&A 289
Schmidtke P.C., Cowley A.P., Frattare L.M., et al., 1994, PASP 106, 843
Schönherr G., Wilms J., Kretschmar P., et al., 2007, A&A 472, 353
Schwarm F.W., 2010, Diploma thesis, Friederich-Alexander Universität Erlangen-Nürnberg
Schwarm F.W., Schoenherr G., Falkner S., et al., 2016, Cyclotron resonant scattering feature simulations. I. Thermally averaged cyclotron scattering cross sections, mean free photon-path tables, and electron momentum sampling, A&A in press, ArXiv Astrophysics e-prints 1609.05030
Schwartz D.A., David L.P., Donnelly R.H., et al., 2000, In: Truemper J.E., Aschenbach B. (eds.) X-Ray Optics, Instruments, and Missions III, Vol. 4012. Society of Photo-Optical Instrumentation Engineers (SPIE) Conference Series, p.28
Schwarzenberg-Czerny A., 1989, MNRAS 241, 153
Serlemitsos P.J., Soong Y., Chan K.W., et al., 2007, PASJ 59, 9
Seward F.D., Harnden, Jr. F.R., Murdin P., Clark D.H., 1983, ApJ 267, 698
Sguera V., Bazzano A., Ubertini P., et al., 2014, INTEGRAL observations of GRO

J1008-57 in outburst provide hint of a cyclotron absorption line at $\sim$ 79 keV, ATel 6664
Shakura N.I., 1975, Soviet Astronomy Letters 1, 223
Shakura N.I., Prokhorov M.E., Postnov K.A., Ketsaris N.A., 1999, A&A 348, 917
Shakura N.I., Sunyaev R.A., 1973, A&A 24, 337
Shipman H.L., 1972, ApJ 177, 723
Shklovsky I.S., 1967, Astrophys. J., Lett. 148, L1
Shrader C.R., Sutaria F.K., Singh K.P., Macomb D.J., 1999, ApJ 512, 920
Siemiginowska A., 2011, Statistics. In: Keith A. Arnaud K.A., Smith R.K., Siemiginowska A. (eds.) Handbook of X-ray Astronomy. Cambridge University Press, New York, NY, USA, p.140
Silverman J.M., Filippenko A.V., Cenko S.B., 2011, PTF Discovery of a Type II Supernova in M51, ATel 3398
Smith D.A., Takeshima T., 1998, XTE J1946+274 Transient 15.8-s Pulsar (= 3A 1942+274 ?), ATel 36
Staubert R., Klochkov D., Postnov K., et al., 2009, A&A 494, 1025
Staubert R., Klochkov D., Wilms J., et al., 2014, A&A 572, A119
Staubert R., Shakura N.I., Postnov K., et al., 2007, A&A 465, L25
Stefan J., 1879, Sitzungzberichte der mathematisch-naturwissenschaftlichen Classe der Kaiserlichen Akademie der Wissenschaften 79, 391 Abteilung II
Stella L., White N.E., Davelaar J., et al., 1985, Astrophys. J., Lett. 288, L45
Sterne T.E., 1941, Proceedings of the National Academy of Science 27, 175
Stollberg M.T., Finger M.H., Wilson R.B., et al., 1993, IAU Circ. 5836
Stoner E.C., 1929, Phil. Mag. 7, 63
Strom S.E., Strom K.M., 1961, PASP 73, 43
Strüder L., Briel U., Dennerl K., et al., 2001, A&A 365, L18
Sugizaki M., Mihara T., Nakajima M., Yamaoka K., 2015a, In: Fifth Fermi Symposium Proceedings., 1502.04461
Sugizaki M., Yamamoto T., Mihara T., et al., 2015b, PASJ 67, 73
Takagi T., Mihara T., Sugizaki M., et al., 2016, PASJ
Takahashi T., Abe K., Endo M., et al., 2007, PASJ 59, 35
Tananbaum H., Gursky H., Kellogg E.M., et al., 1972, Astrophys. J., Lett. 174, L143
Tendulkar S.P., Fürst F., Pottschmidt K., et al., 2014, ApJ 795, 154
Thorstensen J., Charles P., Bowyer S., et al., 1979, Astrophys. J., Lett. 233, L57
Thorstensen J., Charles P., Bowyer S., et al., 1980, Astrophys. J., Lett. 237, L25
Timmes F.X., Woosley S.E., 1997, ApJ 489, 160
Tomsick J.A., Nowak M.A., Parker M., et al., 2014, ApJ 780, 78
Townsend L.J., Coe M.J., Corbet R.H.D., Hill A.B., 2011, MNRAS 416, 1556
Tremblay P.E., Ludwig H.G., Steffen M., Freytag B., 2013, A&A 559, A104
Tsujimoto M., Guainazzi M., Plucinsky P.P., et al., 2011, A&A 525, A25
Tsygankov S.S., Lutovinov A.A., Churazov E.M., Sunyaev R.A., 2007, Astron. Lett. 33, 368
Tsygankov S.S., Lutovinov A.A., Serber A.V., 2010, MNRAS 401, 1628
Turner M.J.L., Abbey A., Arnaud M., et al., 2001, A&A 365, L27
Turolla R., Zane S., Watts A.L., 2015, Reports on Progress in Physics 78, article id. 116901
Ulmer M.P., Shulman S., Yentis D., et al., 1980, Astrophys. J., Lett. 235, L159
Vacca W.D., Garmany C.D., Shull J.M., 1996, ApJ 460, 914
van den Heuvel E.P.J., 1983, In: Lewin W.H.G., van den Heuvel E.P.J. (eds.) Accretion-Driven Stellar X-ray Sources., p. 303
van der Klis M., 1988, In: Ögelman H., van den Heuvel E.P.J. (eds.) Timing Neutron Stars. NATO ASI Series C 262, Kluwer Academic Publishers, Dortrecht, the Netherlands, p.27

Vasco D., Klochkov D., Staubert R., 2011, A&A 532, A99
Vasilopoulos G., Haberl F., Sturm R., et al., 2014a, A&A 567, A129
Vasilopoulos G., Maggi P., Sturm R., et al., 2013a, X-ray outburst of RX J0520.5-6932, confirmed as a Be/X-ray binary, ATel 4748
Vasilopoulos G., Sturm R., Maggi P., Haberl F., 2013b, Discovery of the spin period and a new bright outburst of RXJ0520.5-6932, ATel 5673
Vasilopoulos G., Sturm R., Maggi P., Haberl F., 2014b, The X-ray outburst of RX J0520.5-6932 is reaching the Eddington luminosity, ATel 5760
Vedrenne G., Roques J.P., Schönfelder V., et al., 2003, A&A 411, L63
Verbunt F., Phinney E.S., 1995, A&A 296, 709
Verbunt F., van den Heuvel E.P.J., 1995, In: Lewin W.H.G., van Paradijs J., van denH euvel E.P.J. (eds.) X-ray binaries., Cambridge University Press, p.457
Verner D.A., Ferland G.J., Korista K.T., Yakovlev D.G., 1996, ApJ 465, 487
Verrecchia F., Israel G.L., Negueruela I., et al., 2002, A&A 393, 983
Vink J., 2012, Astron. Astrophys. Rev. 20, 49
von Kienlin A., Meegan C.A., Lichti G.G., et al., 2004, In: Hasinger G., Turner M.J.L. (eds.) UV and Gamma-Ray Space Telescope Systems. Society of Photo-Optical Instrumentation Engineers (SPIE) Conference Series, p.763
Watanabe S., Sako M., Ishida M., et al., 2006, ApJ 651, 421
Waters L.B.F.M., van Kerkwijk M.H., 1989, A&A 223, 196
Westphal J.A., Sandage A., Kristian J., 1968, ApJ 154, 139
Wien W., 1893, In: Sitzungsberichte der Königlich Preussischen Akadamie der Wissenschaften zu Berlin., Verlag der Königlichen Akademie der Wissenschaften, p. 55
Wien W., 1896, Annalen der Physik 294, 662
Wilms J., Allen A., McCray R., 2000, ApJ 542, 914
Wilms J., Juett A.M., Schulz, N. S. Nowak M.A., 2016, in prep.
Wilms J., Nowak M.A., Pottschmidt K., et al., 2006, A&A 447, 245
Wilson C.A., Finger M.H., Coe M.J., Laycock S., 2001, In: Ritz S., Gehrels N., Shrader C.R. (eds.) Gamma 2001: Gamma-Ray Astrophysics, Vol. 587. AIP Conf. Proc., p.34
Wilson C.A., Finger M.H., Coe M.J., Negueruela I., 2003, ApJ 584, 996
Wilson R.B., Harmon B.A., Fishman G.J., et al., 1994, In: Holt S., Day C.S. (eds.) The Evolution of X-ray Binaries, Vol. 308. American Institute of Physics Conference Series, p. 451
Wilson-Hodge C.A., Cherry M.L., Case G.L., et al., 2011, Astrophys. J., Lett. 727, L40
Winkler C., Courvoisier T.J.L., Di Cocco G., et al., 2003, A&A 411, L1
Wisniewski J.P., Draper Z.H., Bjorkman K.S., et al., 2010, ApJ 709, 1306
Wolff M.T., Becker P.A., Gottlieb A.M., et al., 2016, The NuSTAR X-ray Spectrum of Hercules X-1: A Radiation-Dominated Radiative Shock, ApJ in press, ArXiv Astrophysics e-prints 1608.08978
Wolff M.T., Ray P.S., Wood K.S., Hertz P.L., 2009, ApJS 183, 156
Woltjer L., 1964, ApJ 140, 1309
Woosley S.E., Heger A., Weaver T.A., 2002, Reviews of Modern Physics 74, 1015
Woosley S.E., Wilson J.R., Mathews G.J., et al., 1994, ApJ 433, 229
Yamamoto T., Mihara T., Sugizaki M., et al., 2013, Discovery of cyclotron-line feature at 76 keV from Be/X-ray binary pulsar, GRO J1008-57, ATel 4759
Yamamoto T., Sugizaki M., Mihara T., et al., 2011, PASJ 63, S751
Yamauchi S., Ebisawa K., Tanaka Y., et al., 2009, PASJ 61, 225
Yan M., Sadeghpour H.R., Dalgarno A., 1998, ApJ 496, 1044
Zamanov R.K., Reig P., Martí J., et al., 2001, A&A 367, 884
Zwicky F., 1938, ApJ 88, 522